Study if the semileptonic decay D+ –> K- pi+ e+ nu with the BaBar experiment

J. Firmino da Costa

LAL 09-94

THÈSE

présentée le 6 Juillet 2009
par

João Firmino da Costa

pour obtenir le grade de
Docteur ès sciences
de l'Université Paris XI Orsay

Étude de la désintégration semileptonique $D^+ \to K^-\pi^+e^+\nu_e$ dans l'expérience *BABAR* .

Study of the semileptonic decay $D^+ \to K^-\pi^+e^+\nu_e$ with the BaBar experiment

soutenue devant la commission d'examen composée de:

M.	S.	Descotes-Genon	
M.	J.	Dingfelder	Rapporteur
M.	M.	Rotondo	Rapporteur
M.	P.	Roudeau	Directeur de thèse
M.	G.	Wormser	Président

Contents

Etude de la désintégration $D^+ \rightarrow K^-\pi^+e^+\nu_e$ dans l'expérience *BABAR*

Intérêt de l'analyse Cette thèse présente l'étude de la désintégration $D^+ \rightarrow K^-\pi^+e^+\nu_e$ (et de son état conjugué de charge) effectuée à l'aide des données recueillies par le détecteur *BABAR* placé au point d'interaction e^+e^- du collisionneur PEP-II à SLAC National Accelerator Laboratory.
Nous avons étudié une luminosité intégrée de 347,5 fb^{-1}, ce qui correspond à 451 millions de paires $c\bar{c}$ produites. En profitant de cette grande statistique, nous avons pu évaluer avec précision le système $K\pi$ d'isospin 1/2 dans les états de moment angulaire S et P.
Le mode dominant de la désintégration étudiée $D^+ \rightarrow K^-\pi^+e^+\nu_e$ est le $D^+ \rightarrow \bar{K^{*0}}e^+\nu_e$, avec le $\bar{K^{*0}}$ donnant $K^-\pi^+$. L'étude du système $K\pi$ en onde P est intéressante car elle permet de déterminer avec précision les facteurs de forme hadroniques intervenant dans cette réaction. Ces résultats permettront de valider ou d'affiner les méthodes de calcul d'interaction forte sur réseau "lattice QCD" qui permettent, en discrétisant l'espace-temps, d'évaluer les interactions fortes à partir des principes fondamentaux de QCD.
L'étude du système $K\pi$ en onde S est également intéressante car elle permet a priori d'extraire des observables - notamment la longueur de diffusion - directement comparables aux prévisions de la théorie QCD à basse énergie, c'est-à-dire la théorie des perturbations chirales (χPT). On peut extraire expérimentalement la longueur de diffusion pour l'onde S $K\pi$ I=1/2 en mesurant la variation de la phase de cette onde à basse masse. Cette théorie est encore peu testée expérimentalement pour les systèmes contenant une particule étrange car la mesure de la phase à basse masse $K\pi$ n'était possible que de manière indirecte.
Dans cette analyse, la variation de la phase de l'onde S $K\pi$ I=1/2 est mesurée directement à partir du seuil d'énergie du système $K\pi$. Les résultats de l'expérience LASS, obtenus à partir de l'étude de la production diffractive de systèmes $K\pi$ sont confirmés. Cependant les incertitudes de mesure sont encore trop élevées pour que l'on puisse mesurer directement la longueur de diffusion du système $K\pi$.

Etat actuel de la compétition pour l'onde S L'étude du système $K\pi$ en onde S est un sujet d'actualité. Les données disponibles relatives à la variation de la phase de l'onde S proviennent de deux types de réactions : des collisions du type $K^-p \rightarrow K^-\pi^+n$ [43],[17], relativement anciennes réalisées en 1976 et 1986, et des désintégrations hadroniques $D^+ \rightarrow K^-\pi^+\pi^+$ [22],[23],[65], plus récentes voire très récentes. Dans ce dernier cas, l'interaction du pion spectateur avec le système $K\pi$ lors des désintégrations hadroniques introduit des difficultés supplémentaires en induisant une modification de la valeur de la phase $K\pi$. Notons que les deux processus indiqués ne sont pas directement sensibles à l'amplitude d'isospin I=1/2 et doivent prendre en compte la présence de l'amplitude I=3/2. Pour mention, l'expérience FOCUS [26] a également étudié l'onde S à partir de la désintégration $D^+ \rightarrow K^-\pi^+\mu^+\nu_{mu}$ mais n'a pu obtenir que la fraction d'onde S et n'était pas sensible à la variation de la phase de l'onde S avec l'énergie.

Sélection et reconstruction Le signal étudié correspond à des mésons D^+ se désintégrant en $K^-\pi^+e^+\nu_e$ issus de l'hadronisation de paires $c\bar{c}$. L'énergie dans le centre de masse des collisions dans *BABAR* étant égale à la masse du Υ(4S), les mésons charmés apparaissent dans des jets et sont accompagnés par d'autres particules. On définit un axe de thrust qui correspond à la direction qui maximise la somme des valeurs absolues des impulsions des traces reconstruites, projetées sur cet axe. Un plan perpendiculaire à cet axe et passant par le point d'interaction définit alors deux hémisphères contenant chacun l'un des jets. L'hémisphère du signal est celui dans lequel on repère trois traces identifiées aux trois particules K^-, π^+ et e^+ (l'ensemble de ces trois traces est appelé « candidat signal »). Si la probabilité que les trois particules proviennent d'un même vertex est inférieure à 10^{-7}, alors le candidat est éliminé.

La principale étape de la reconstruction consiste à estimer la direction du D et l'énergie du neutrino à l'aide de toutes les traces spectatrices mesurées dans l'évènement. On effectue alors un fit cinématique pour contraindre la masse du candidat $K^-\pi^+e^+\nu_e$ à la masse du D^+.

Diminution du bruit de fond Pour réaliser cette analyse, on a effectué essentiellement trois jeux de coupures :

- le premier (présélection) revient à enrichir l'échantillon de données avec des désintégrations semileptoniques ;
- le second et le troisième consistent principalement à utiliser des variables discriminantes de Fisher pour supprimer respectivement les bruits de fond $b\bar{b}$ et $c\bar{c}$ (notées Fbb et Fcc).

Les évènements de type $b\bar{b}$ qui correspondent aux désintégrations de l'Υ(4S) sont caractérisés par une topologie plus sphérique que les évènements $c\bar{c}$ (« jet-like ») et engendrent, en moyenne, un plus grand nombre de particules. La variable de Fisher Fbb est définie à partir de ces différences de topologie et de multiplicité et permet d'éliminer environ 85 % du bruit de fond $b\bar{b}$ en conservant 70 % du signal.

Une fois cette coupure effectuée, la principale source de bruit de fond restant correspond à des candidats dont le K^- et le e^+ viennent de désintégrations semileptoniques d'un méson D, alors que le π^+ provient, le plus souvent, de la fragmentation des quarks. Pour éliminer ces candidats, on définit la variable de Fisher Fcc à partir de certaines caractéristiques du méson D^+ et de la vraisemblance de sa reconstruction. Cette variable permet d'éliminer environ 94 % du bruit de fond $c\bar{c}$ et conserve 40 % du signal précédent.

Une fois toute la procédure de sélection/reconstruction/réduction de bruit de fond réalisée, on reconstruit environ 3 % du signal initial et on atteint un rapport signal sur bruit supérieur à 2.

Amélioration de l'accord data/simulation Une partie importante de cette analyse consiste à améliorer la description faite par la simulation du signal et du bruit de fond.

Pour améliorer la simulation du signal, on utilise des échantillons de données et de simulation des désintégrations hadroniques $D^+ \rightarrow K^-\pi^+\pi^+$, ou le D^+ est complètement reconstruit. Ces évènements sont utilisés pour comparer les résolutions obtenues sur la reconstruction de la direction du D^+ et de l'énergie manquante, dans les données et la simulation, lorsqu'on applique l'algorithme utilisé pour la mesure des désintégrations

semileptoniques. Ils permettent aussi de corriger les différences sur les distributions des différentes variables qui entrent dans la définition des discriminants de Fisher.

Pour améliorer la simulation du bruit de fond $b\bar{b}$, on corrige les distributions obtenues avec la simulation en les comparant aux données enregistrées à l'Υ(4S) auxquelles on a soustrait les évènements issus du continuum.

Pour améliorer la simulation du bruit de fond $c\bar{c}$, on corrige les taux de désintégration semileptonique des mésons D ainsi que la production des particules issues de la fragmentation qui accompagnent les mésons D au sein d'un évènement. On vérifie l'accord entre les données et la simulation du fond à l'aide d'évènements reconstruits du type $K^-\pi^-e^+$ qui ont, pour la plupart, la même origine et les mêmes caractéristiques que le bruit de fond de l'analyse et ne contiennent pas le signal étudié.

Procédure de fit La désintégration $D^+ \rightarrow K^-\pi^+e^+\nu_e$ peut être entièrement définie en utilisant cinq variables cinématiques :

- le carré du quadrimoment transféré (q^2),
- la masse invariante du système $K\pi$ ($m_{K\pi}$),
- le cosinus de l'angle entre la direction du pion dans le centre de masse $K\pi$ et celle du système $K\pi$ dans le centre de masse du D^+ ($cos\theta_\pi$),
- le cosinus de l'angle entre la direction du e^+ dans le centre de masse du système $e^+\nu_e$ et celle du système $e^+\nu_e$ dans le centre de masse du D^+ ($cos\theta_e$),
- l'angle entre les plans de désintégration des systèmes hadronique et leptonique, dans le centre de masse du D (χ).

Les valeurs des paramètres physiques pertinents pour notre analyse ainsi que le niveau du bruit de fond sont extraits en utilisant une méthode de maximum de vraisemblance. L'espace des 5 variables cinématiques est divisé en 2800 "bins" et, dans chacun d'eux, les nombres d'évènements mesurés et attendus sont comparés. La proportion de bruit de fond est ajustée à partir de la distribution de la variable Fcc. Le nombre d'évènements de signal attendu dans chaque "bin" depend des valeurs de différents paramètres qui sont ainsi determinés.

Résultats Grâce à toutes les étapes précédentes, on peut accéder pour la première fois à la variation de la phase de l'onde S du système $K\pi$ I=1/2 depuis le seuil. On détermine également avec une grande précision la contribution de l'onde S pour notre canal et on caractérise en détail l'onde P au niveau de sa structure en masse (Breit-Wigner) et de ses facteurs de forme. Le résultat de l'ajustement sur les 5 variables est présenté dans la Figure 9.1 et les paramètres correspondants pour l'onde S, pour l'onde P ainsi que pour le nombre d'événements signal et fond sont données dans le Tableau 10.5 :

Nous avons aussi mesuré la variation de la phase de l'onde S en plusieurs bins en masse et ceci est présenté dans la Figure 2.

variable	Résultat
r_S	$0.477 \pm 0.025 \pm 0.022$
$r_S^{(1)}$	$0.15 \pm 0.06 \pm 0.06$
$a_S(GeV/c)^{-1}$	$1.78 \pm 0.15 \pm 0.19$
$b_S(GeV/c)^{-1}$	$-1.93 \pm 0.69 \pm 0.69$
$\Gamma^0(K^*)(GeV/c^2)$	$0.0457859 \pm 0.00023 \pm 0.00021$
$m(K^*)(GeV/c^2)$	$0.8950 \pm 0.0001 \pm 0.0005$
$r_{BW}(GeV/c)^{-1}$	4.20 ± 0.23
$m_A(GeV/c^2)$	$2.68^{+0.11}_{-0.10}$
r_V	1.480 ± 0.016
r_2	0.824 ± 0.020
N_S	244619 ± 697
N_B	106602 ± 567

Table 1: *Résultat de l'ajustement aux données de BABAR*

On étudie l'éventuelle existence d'un autre état $J^P = 1^-$, le $K^*(1410)$, et on détermine sa normalisation et sa phase par rapport au $K^*(892)$.

En normalisant le canal semileptonique étudié par rapport à la désintégration $D^+ \to K^-\pi^+\pi^+$, que nous avons reconstruite, et en utilisant la valeur publiée du rapport d'embranchement pour ce dernier canal, nous avons obtenu les rapports d'embranchement $D^+ \to K^-\pi^+e^+\nu_e$ et $D^+ \to \bar{K^{*0}}e^+\nu_e$. Finalement on déduit la valeur du facteur de forme A_1 à $q^2 = 0$ qui sert de normalisation à l'ensemble des facteurs de forme étudiés.

On compare alors nos résultats à ceux obtenus par d'autres expériences et à des prédictions de modèles théoriques.

Nos mesures, ainsi que celles de l'expérience LASS, sont sensibles à la différence entre les phases des ondes S et P. Les résultats de ces deux expériences peuvent donc être directement comparés à partir de la mesure de cette différence en fonction de la masse $K\pi$. Ceci est illustré sur la Figure 3.

L'accord entre nos mesures et celles de LASS montre que les données issues de l'analyse des distributions de Dalitz des désintégrations du D, comme $D^+ \to K^-\pi^+\pi^+$, ne permettent pas de mesurer précisément la diffusion $K\pi$ dans l'onde S.

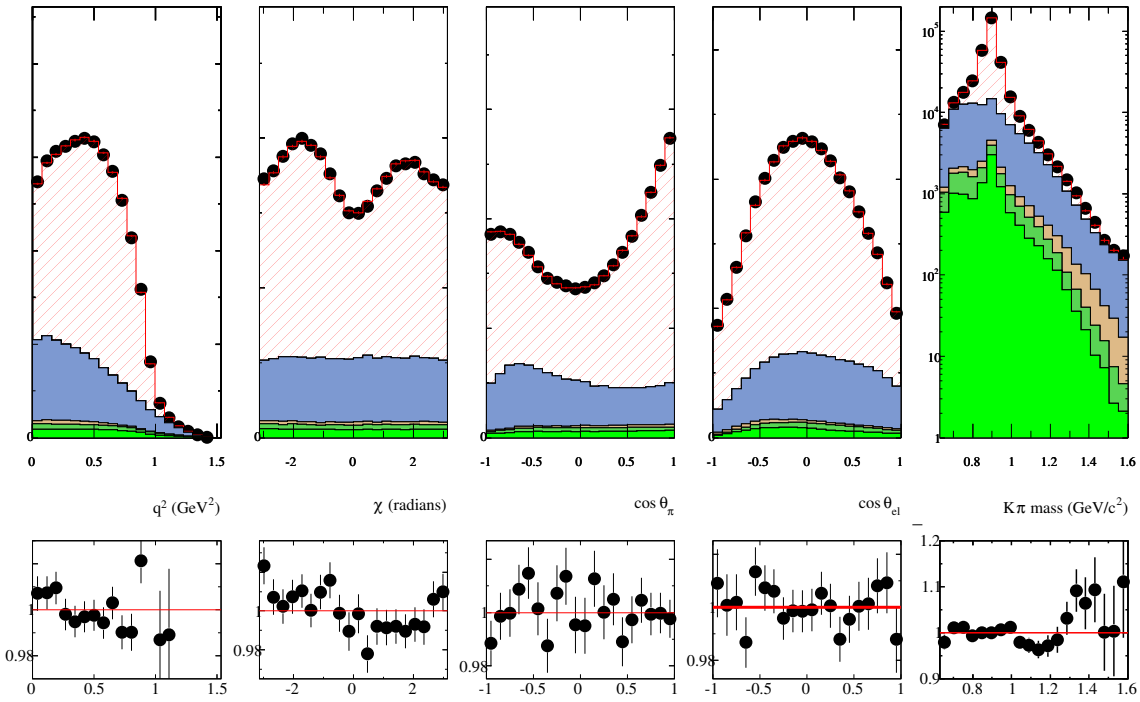

Figure 1: *Figures du haut: Projections des données et de la simulation après l'ajustement sur chacune des 5 variables cinématiques. Code couleur: rouge(signal),bleu(fond charme), marron (fond uds), vert foncé (fond B^+B^-), vert clair (fond $B^0\bar{B}^0$). Figures du bas: rapports data/MC des figures en haut.*

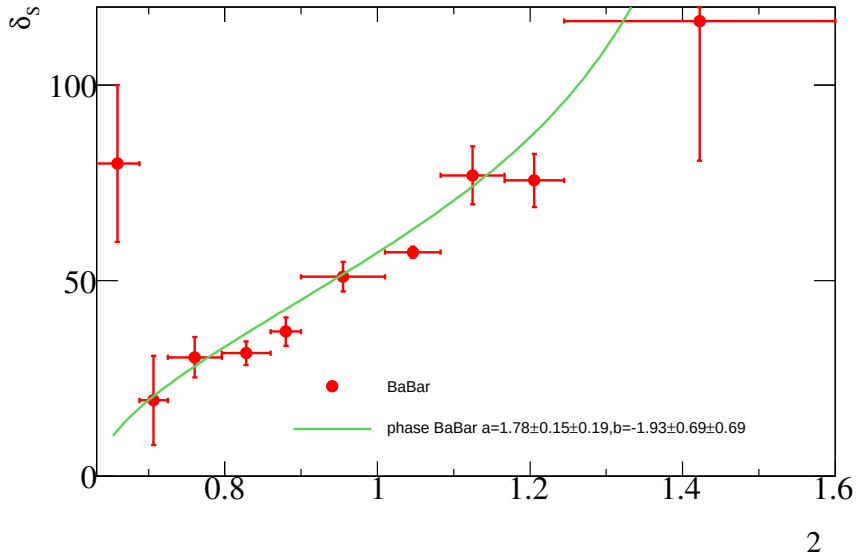

Figure 2: *Variation de la phase de l'onde S mesurée en plusieurs bins en masse $K\pi$ (points rouges) ainsi que la valeur centrale de la phase trouvée avec la paramétrisation de LASS (ligne verte).*

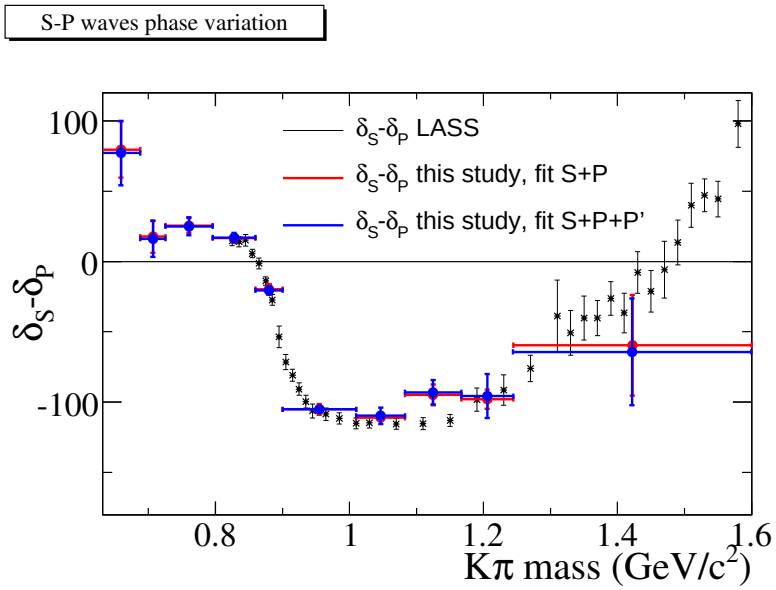

Figure 3: *Variation de la difference de phase entre les ondes S et P mesurée en plusieurs bins en masse $K\pi$ (points rouges et bleus) ainsi que les valeurs trouvées par LASS [19]. Les points rouges indiquent le fit où l'onde P est constituée par le $K^{*0}(892)$ tandis que, pour les points bleus, le $K^*(1410)$ est inclus.*

Chapter 1

Introduction

Mesons are the simplest particles generated by QCD, from the combination of a quark-antiquark pair. With baryons, made of three quarks (or three antiquarks) they are considered as the only two types of colourless objects which can be observed (more complex structures with four quarks or more are not completely excluded but lack of experimental confirmation).

Low energy meson-meson interactions are generally described using chiral perturbation theory which explains the low energy limit of QCD in terms of few fundamental parameters. In the other limit, at high energy and short distances, processes governed by strong interactions can be described in terms of quark-gluon interactions and corresponding processes are computed using perturbative expansions in terms of the strong coupling constant α_S. In between these two domains, processes depending on QCD can be best evaluated using Lattice QCD which makes use of a space-time discretization. In this approach, configurations of the QCD vacuum are generated using Monte-Carlo techniques and different -but rather simple- reactions are evaluated using these configurations. Lattice methodes are used, at present, to compute meson decay constants ($K,\ D$ and B) parameters, entering in neutral meson oscillations and hadronic form factors in semileptonic decays. These are only few examples which are related, mainly for the latter, to the physics considered in the present work. Lattice QCD cannot yet compute a decay process into hadrons and for this reason it is still difficult to simulate a resonance on the lattice (as the $K^*(892)$). Part of the measurements obtained in this thesis can be compared with LQCD expectations for hadronic form factors in the process $D^+ \to \bar{K}^{*0}(892)e^+\nu_e$ whereas results on the $K\pi$ S-wave can be related with expectations from Chiral perturbation theory.

The D_{e4} decay channel is an important laboratory for the study of the $K\pi$ hadronic system as there is no extra hadron contributing in the final state. This is considered to be the best place to study the S-wave $I = 1/2$ $K\pi$ system at low mass values.

In practice these studies have not been acomplished yet because they require the measurement of the full differential decay distribution (which depends on 5 variables) and large statistics are needed. The present analysis gives the progress that have been achieved in this direction using the large event sample registered by the BaBar experiment. Improvements on the determination of the parameters governing the dominant decay channel, $D^+ \to \overline{K}^{*0}e^+\nu_e$, are also obtained and search for other excited hadrons contributing to the $K\pi$ final state is considered.

resonance	J^P	BR to $K\pi$ %	mass $\mathrm{MeV/c^2}$	width $\mathrm{MeV/c^2}$
$K_0^*(800)$ (?)	0^+	$100(?)$	672 ± 40	550 ± 34
$K^*(892)$	1^-	100	896.00 ± 0.25	50.3 ± 0.6
$K_1(1270)$	1^+	0	1272 ± 7	90 ± 20
$K_1(1400)$	1^+	0	1403 ± 7	174 ± 13
$K^*(1410)$	1^-	6.6 ± 1.3	1414 ± 15	232 ± 21
$K_0^*(1430)$	0^+	93 ± 10	1425 ± 50	270 ± 80
$K_2^*(1430)$	2^+	49.9 ± 1.2	1432.4 ± 1.3	109 ± 5
$K^*(1680)$	1^-	38.7 ± 2.5	1717 ± 27	322 ± 110

Table 1.1: *Possible resonances contributing in Cabibbo favoured D^+ semileptonic decays [14].*

In Table 1.1 are listed strange particle resonances which can appear in Cabibbo favoured D^+ semileptonic decays. $J^P = 1^+$ states are not decaying into $K\pi$ and cannot be observed in the present analysis. The $K^*(1410)$ is a 1^- radial excitation and has a rather small branching fraction into $K\pi$. The $K^*(1680)$ has a mass close to the kinematic limit and its production is disfavoured by the available phase space. Above the $K^*(892)$ one is thus left with possible contributions from the $K_0^*(1430)$, $K^*(1410)$ and $K_2^*(1430)$ which are decaying into $K\pi$ through S, P and D-waves respectively. At low $K\pi$ mass values one expects also an S-wave contribution which can be resonant ($\kappa = K_0^*(800)$) or not.

1.1 Theory aspects

1.1.1 S-wave $K\pi$: theory aspects

Some basic definitions

$K\pi$ scattering involves two isospin amplitudes with respectively $I = 1/2$ and $I = 3/2$.

The amplitude in isospin channel I can be written as:

$$A\left[\pi(p_1)K(p_2) \to \pi(p_3)K(p_4)\right] = T^I(s,t,u) \tag{1.1}$$

s, t, u are the ususal Mandelstam variables:

$$s = (p_1 + p_2)^2,\ t = (p_1 - p_3)^2 \text{ and } u = (p_1 - p_4)^2. \tag{1.2}$$

The two isospin amplitudes are related via $s \leftrightarrow u$ crossing which yields[1]:

$$T^{1/2}(s,t,u) = -\frac{1}{2}T^{3/2}(s,t,u) + T^{3/2}(u,t,s) \tag{1.3}$$

The various amplitudes are expanded into partial waves via:

$$T^I(s,t,u) = 16\pi \sum_{l=0}^{\infty} (2l+1) P_l(\cos\theta) t_l^I(s) \tag{1.4}$$

and, near threshold, the amplitude $t_l^I(s)$ can be expressed in a Taylor series:

$$t_l^I(s) = \frac{1}{2}\sqrt{s}\,(p^*_{\pi K})^{2l} \left(a_l^I + b_l^I\,(p^*_{\pi K})^2 + ... \right) \tag{1.5}$$

a_l^I is a scattering length and b_l^I an effective range parameters.

The amplitude $t_l^I(s)$ can be also expressed in terms of its modulus and phase; if, in the considered energy domain, the process remains elastic this gives:

$$t_l^I(s) = \frac{\sqrt{s}}{2p^*_{\pi K}} \frac{1}{2i} \left(e^{2i\delta_l^I(s)} - 1 \right) = \frac{\sqrt{s}}{2p^*_{\pi K}} \sin\delta_i^l(s) e^{i\delta_i^l(s)} \tag{1.6}$$

Depending on the considered physics process, the measured amplitude corresponds to different combinations of the two isospin amplitudes. In the reactions considered in this thesis we will have:

- $K^+\pi^+$ scattering: $A(K^+\pi^+ \to K^+\pi^+) = T^{3/2}$;
- $K^+\pi^-$ scattering: $A(K^+\pi^- \to K^+\pi^-) = \frac{1}{3}\left(2T^{1/2} + T^{3/2}\right)$;
- $K^-\pi^+$ produced in $D^+ \to K^-\pi^+e^+\nu_e$ decays: it involves only $T^{1/2}$ because the weak transition between the c and s quarks is not changing isospin.

Charm semileptonic decays, and also τ decays into strange particles, are thus a privileged way to access $T^{1/2}$.

Elastic scattering and the Watson theorem

The Watson theorem [2] tells us that, for a given angular momentum and Isospin, the phase measured in $K\pi$ elastic scattering is the same as the phase of the wave describing the $K\pi$ system produced in a decay process as long as one remains in the elastic regime.

Following [3], the principle of demonstration is presented below.

A reaction is usually described using the S matrix which is unitary to conserve the probability between the initial and the final state. The T matrix is introduced to distinguish between particles having or not interacted: $S = 1 + iT$. The unitarity of the S matrix reads:

$$T - T^\dagger = iT \cdot T^\dagger. \tag{1.7}$$

Consider that some final state $|\phi_k>$ is produced from the vacuum ($|0>$) then:

$$<0|T|\phi_k> - <0|T^\dagger|\phi_k> = i<0|T\cdot T^\dagger|\phi_k> . \tag{1.8}$$

If this expression is applied in a domain where there is only a contribution from the elastic scattering: $|\phi_k> = |\phi_{el.}>$, then inserting also this state in the right hand side of Equation 1.8 one gets:

$$<0|T|\phi_{el.}> - <0|T^\dagger|\phi_{el.}> = i<0|T|\phi_{el.}>\cdot<\phi_{el.}|T^\dagger|\phi_{el.}> . \tag{1.9}$$

If one express: $<0|T|\phi_{el.}> = a_D \exp(i\phi_D)$ for the decay channel and $<\phi_{el.}|T|\phi_{el.}> = a_{el.}\exp(i\phi_{el.})$ then Equation 1.9 becomes:

$$a_D \sin(\phi_D) = a_D \cdot a_{el.}\left[\cos(\phi_D - \phi_{el.}) + i\sin(\phi_D - \phi_{el.})\right] \tag{1.10}$$

This implies:

- the equality of the two phases: $\phi_D = \phi_{el.}$;
- the amplitude $a_{el.} = \sin(\phi_{el.})$, which is verified in case of elastic scattering;
- no condition on a_D.

This theorem concerns only the phase and implies no condition on the amplitude for the decay process.

Chiral Perturbation Theory

We give a short summary of the main ideas on which is based chiral perturbation theory of strong interactions. We have used references [4],[5],[6] which provide an introduction to this field.

In the absence of quark masses, the QCD Lagrangian:

$$\mathcal{L}_{QCD} = \sum_{q=u,d,s} \bar{q}\gamma_\mu(iD^\mu)q - \frac{1}{4}G^c_{\mu\nu}G_c^{\mu\nu} \tag{1.11}$$

is invariant under the independent transformations of the right and left-handed quark fields:

$$q_R \to Rq_R,\ q_L \to Lq_L, \tag{1.12}$$

with $R \in SU(n_f)_R$ and $L \in SU(n_f)_L$, with $n_f = 3$ corresponding to the number of light quark flavours.

In Equation (1.11) the sum has been restricted to the three families of light quarks. $iD^\mu = i\partial^\mu + g_S G_c^\mu \frac{\lambda_c}{2}$ is the covariant derivative and λ_c are Gell-Mann matrices. G_c is a gluon field of colour index c. The fields $q_{R,L}$ have definite chirality:

$$q_{R,L} = \frac{1}{2}(1 \pm \gamma_5)q \tag{1.13}$$

The invariance of the massless QCD Lagrangian is referred to as the $SU(3)_L \times SU(3)_R$ chiral symmetry.

$$\mathcal{L}_{QCD} = \sum_{q=u,d,s} [\bar{q}_L \gamma_\mu (iD^\mu) q_L + \bar{q}_R \gamma_\mu (iD^\mu) q_R] - \frac{1}{4} G^c_{\mu\nu} G^{\mu\nu}_c \tag{1.14}$$

As a result of E. Noether's theorem, this invariance implies the existence of conserved currents which can be obtained from the generators of the corresponding symmetry groups:

$$J^{c\mu}_{R,L} = \bar{q}_{R,L} \gamma^\mu \frac{\lambda^c}{2} q_{R,L}. \tag{1.15}$$

The corresponding charges $Q^c_{R,L} = \int d^3x J^{c0}_{R,L}(x)$ are time independent and satisfy commutation relations which are the starting point of Current Algebras methods [7].

It is useful to define the combinations:

$$Q^c_V = Q^c_R + Q^c_L \text{ and } Q^c_A = Q^c_R - Q^c_L \tag{1.16}$$

which have a different behaviour under parity:

$$Q^c_V \to Q^c_V \text{ and } Q^c_A \to -Q^c_A. \tag{1.17}$$

If $|\psi>$ is an eigenstate of the massless QCD Hamiltonian, the states $Q^c_V|\psi>$ and $Q^c_A|\psi>$ have the same energy and opposite parity. But degenerate $SU(3)$ multiplets with opposite parity do not exist in nature. The light pseudoscalar ($J^P = 0^-$) mesons have much lower mass than the scalar ($J^P = 0^+$) mesons. This can be realized by considering that the ground state of the theory is not symmetric under the chiral group. If the QCD vacuum is not invariant under the action of the axial charge:

$$Q^c_V|0> = 0 \text{ and } Q^c_A|0> \neq 0. \tag{1.18}$$

Then, the $SU(3)_L \times SU(3)_R$ symmetry spontaneously breaks down to $SU(3)_{V=L+R}$ and, according to Goldstone theorem, an octet of pseudoscalars massless bosons appears in the theory, which are identified to the octet of pseudoscalar mesons.

Operators which are not invariant under the chiral transformation will have a non-zero value on the new ground state. This is the case for operators entering in mass terms as:

$$u\bar{u} = u_L \bar{u}_R + u_R \bar{u}_L. \tag{1.19}$$

The average value of this operator is named the quark condensate, and by $SU(3)$ symmetry it has the same value for the three light flavours [8]:

$$<\psi_0|u\bar{u}|\psi_0> = <\psi_0|d\bar{d}|\psi_0> = <\psi_0|s\bar{s}|\psi_0> \sim (250MeV)^3 \tag{1.20}$$

The theory is expected to be valid for low energies up to the resonant states (ρ, K^*), therefore up to an energy scale of around 800 MeV.

Instead of using the initial QCD Lagrangian it is possible to construct an effective theory in terms of the Goldstone bosons fields and the initial symmetry defines the allowed interaction terms between these fields.

The Lagrangian is expressed as an expansion in terms corresponding to different orders related to terms violating the chiral symmetry as quark masses. In this expansion quark masses enter as $(p^*)^2$ contributions.

$$\mathcal{L}_{QCD} = \mathcal{L}^{(2)}_{QCD} + \mathcal{L}^{(4)}_{QCD} + \mathcal{L}^{(6)}_{QCD} \tag{1.21}$$

The leading order ($\mathcal{L}^{(2)}_{QCD}$) corresponds to results from current algebra in the sixties.

Calculations of the πK scattering amplitude at NLO were done in 1991 [9]. NNLO expressions can be found in [10].

Some expectations from Chiral Perturbation Theory for the $K\pi$ amplitude

Chiral perturbation theory expectations have been compared with experiment for $\pi\pi$ scattering. High accuracy has been obtained and agreement was found with recent high statistics experiments on $Ke4$ decays.

Corresponding tests envolving three flavours are not yet available at a similar accuracy. It is not clear either if $SU(3)$ chiral expectations are valid because the strange quark mass $m_s \sim 100\ MeV/c^2$ is much higher than $m_{u,d} \sim 5 - 10\ MeV/c^2$, and also because the threshold for $K\pi$ scattering ($m_K + m_\pi = 633.3\ MeV/c^2$) is a lot higher than $2m_\pi$.

At leading order, the scattering length and effective range parameters can be expressed simply in terms of hadron masses and the pion decay constant $F_\pi = (92.21 \pm 0.15)\ MeV$.

The S-wave scattering length is, in this approximation [11], equal to:

$$a_0^{1/2} = \frac{1}{4\pi}\frac{m_K m_\pi}{m_K + m_\pi}\frac{1}{f_\pi^2} = 1.02\ GeV^{-1} = 0.142\ m_\pi^{-1}. \tag{1.22}$$

The convergence of the chiral expansion is illustrated in Table 1.2 [10]. For the S-wave scattering length the convergence seems fine whereas for the effective range parameter, higher order terms are large:

parameter	$\mathcal{L}^{(2)}$	$\mathcal{L}^{(4)}$	$\mathcal{L}^{(6)}$
$a_0^{1/2}$	0.142	0.035	0.022
$10 \cdot b_0^{1/2}$	0.664	0.311	0.112
$10 \cdot a_1^{1/2}$	0.100	0.006	0.056

Table 1.2: *Contributions from leading and higher order terms in the evaluation of scattering length and effective range parameters. Units are m_π^{-1} for $a_0^{1/2}$, and m_π^{-3} for $b_0^{1/2}$ and $a_1^{1/2}$.*

In Table 1.3 are summarized present expectations for scattering length and effective range parameters of the S and P waves for the $T^{1/2}$ amplitude:

parameter	[10]	[18]
$a_0^{1/2}$	1.58	1.60 ± 0.16
$b_0^{1/2}$	0.93	0.61 ± 0.03
$a_1^{1/2}$	6.62	6.99 ± 0.37

Table 1.3: *Expected values for scattering length and effective range parameters. Units are GeV^{-1} for $a_0^{1/2}$ and GeV^{-3} for $a_1^{1/2}$ and $b_0^{1/2}$.*

1.1.2 Form Factors in heavy hadron semileptonic decays

Lattice QCD

Quantum Chromodynamics (QCD) is the theory of strong interactions. It consists, at its fundamental level, of interactions between quarks and gluons. It works well in the regime of high energies (large moment transfer) where using perturbation theory one can solve the QCD equations.
At small momentum transfer this is not possible and one uses non-perturbative methods. Lattice QCD is a non-perturbative computation whose aim is to solve numerically QCD equations in the non-perturbative regime from first principles.
This applies for charm semileptonic decays. Here, the matrix element of the weak interaction Hamiltonian between the initial D meson and the final hadron has large QCD corrections (exchange of soft gluons, this is illustrated in Figure 1.1) which cannot be estimated from perturbative QCD. Here lies the connection with the measurement of semileptonic decays of the D mesons, since these provide crucial experimental inputs of the values of hadronic matrix elements that are compared to the lattice estimates.

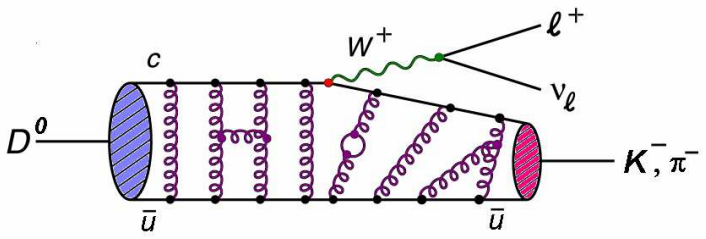

Figure 1.1: *Illustration of QCD corrections in a Feynman diagram for a generic semileptonic decay of a charm meson. The QCD corrections are illustrated by the gluons exchanged between the initial and final hadron states. The leptonic vertex is calculated precisely analytically, while the hadronic vertex requires non-perturbative calculations*

The lattice QCD method consists in the use of the formalism of path integrals, these being calculated numerically over a discretized euclidean space-time[16]. The lattice consists of a hypercube with lattice spacing a and a linear extension L. The typical characteristics of actual lattices are $L \sim 2\ fm$ and $a \sim 0.1\ fm$.. The finite spacing of the lattice itself provides an ultraviolet cut-off. Results for physical observables are found by calculating the expectation values of:

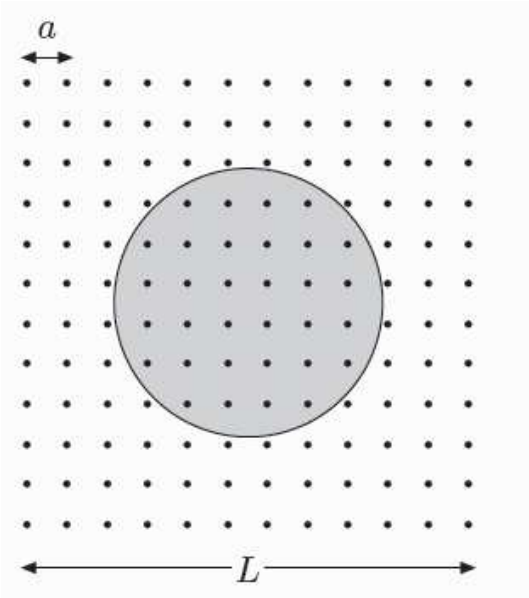

Figure 1.2: *Representation of a lattice scheme with spacing a and length L. The circle illustrates the typical scale of the hadrons analysed.*

$$< 0|Q(x_1,..,x_n)|0 >= \frac{1}{Z}\int DA_\mu D\bar{\psi}D\psi exp[-S^{latt}]Q(x_1,..,x_n)$$
$$Z = \int DA_\mu D\bar{\psi}D\psi exp[-S^{latt}] \tag{1.23}$$

where S^{latt} is the lattice QCD action,

$$S^{latt} = a^4 \sum([F_{\mu\nu}F^{\mu\nu}]^{latt} + \bar{\psi}M\psi) \tag{1.24}$$

M is the Dirac operator, A_μ the gluon fields, $\psi, \bar{\psi}$ the fermion fields (Grassman variables). Integrating overthe Grassman variables one gets:

$$< 0|Q(x_1,..,x_n)|0 >= \frac{1}{Z}\int DA_\mu D\bar{\psi}D\psi exp[-S^{glue}]det[M]\tilde{Q}(x_1,..,x_n) \tag{1.25}$$

To reduce the computing time which is mainly determined by the calculation of the determinant $det[M]$ corresponding to internal fermion loops (the sea quarks), one approximation is to assume that these are infinitely heavy, ($det[M] = 1$). This is the quenched approximation, which induces large, and difficult to quantify, uncertainties on the computed physical quantities (10 to 20%).
Results that take into account sea quark effects exist for charm semileptonic decays into pseudoscalar states, however decays into resonant states still use the "quenched" approximation.

1.2 S-wave $K\pi$: experimental measurements

1.2.1 In $K\pi$ production at small transfer

The LASS (Large Aperture Solenoid Spectrometer) experiment has analyzed data from 11 GeV/c kaon scattering on hydrogen: $K^- p \rightarrow K^- \pi^+ n$ [15]. They do a partial wave analysis of 151,000 events with a missing mass squared to the $K^-\pi^+$ system below 1.2 $(GeV/c^2)^2$ and $m_{K^-\pi^+} < 2.6\ GeV/c^2$ which satisfy $|t'| < 0.2\ GeV^2$, $m_{n\pi^+} > 1.7$ GeV/c^2 and $m_{K^-\pi^+} < 2.6$ GeV/c^2. The first cut is to ensure $K\pi$ production dominated by pion exchange and the second is to suppress events in which the target is excited into a baryonic resonance.

The $K\pi$ S-wave, $I = 1/2$, is taken as the sum of a background term and the $K_0^*(1430)$. At masses higher than 1.7 GeV/c^2 another resonance, with a mass around 1.9 GeV/c^2, contributes. Considering only the first two components, which are relevant in D semileptonic decays, their total amplitude is written:

$$\begin{aligned} A_S^{1/2} &= A_{BG} \sin(\delta_{BG}^{1/2} + \phi_{BG}) \exp i(\delta_{BG}^{1/2} + \phi_{BG}) \\ &+ A_{K_0^*(1430)} \exp i(\phi_{K_0^*(1430)}) \exp 2i(\delta_{BG}^{1/2} + \phi_{BG}) \sin \delta_{K_0^*(1430)} \exp i\delta_{K_0^*(1430)}. \end{aligned} \tag{1.26}$$

A_{BG}, A_K, ϕ_{BG} and ϕ_K are constants, while $\delta_{BG}^{1/2}$ and $\delta_{K_0^*(1430)}$ depend on the $K\pi$mass.

The mass dependence of $\delta_{BG}^{1/2}$ is described by means of an effective range parameterization:

$$\cot(\delta_{BG}^{1/2}) = \frac{1}{a_S^{1/2} p^*} + \frac{b_S^{1/2} p^*}{2}, \tag{1.27}$$

where $a_S^{1/2}$ is the scattering length and $b_S^{1/2}$ is the effective range, p^* indicates the momentum of the emitted particles in the $K\pi$ c.m. system.

The mass dependence of $\delta_{K_0^*(1430)}$ is obtained assuming that the $K_0^*(1430)$ decay amplitude is a Breit-Wigner distribution:

$$\cot(\delta_{K_0^*(1430)}) = \frac{m_{K_0^*(1430)}^2 - m^2}{m_{K_0^*(1430)} \Gamma_{K_0^*(1430)}(m)}, \tag{1.28}$$

where $m_{K_0^*(1430)}$ is the pole mass resonance and $\Gamma_{K_0^*(1430)}(m)$ its mass-dependent total width.

The $K\pi$ scattering S-wave, $I = 1/2$, remains elastic up to the $K\eta$ threshold but, since the coupling to this channel is weak, it is considered in practice to be elastic up to the $K\eta\prime$ threshold. This implies that the amplitude is described by a vector with origin at zero and extremity that remains on the circumference of a unit diameter circle in the complex plane having centre at (0, 1/2). Using the parameterization given in Eq. 1.27, this condition

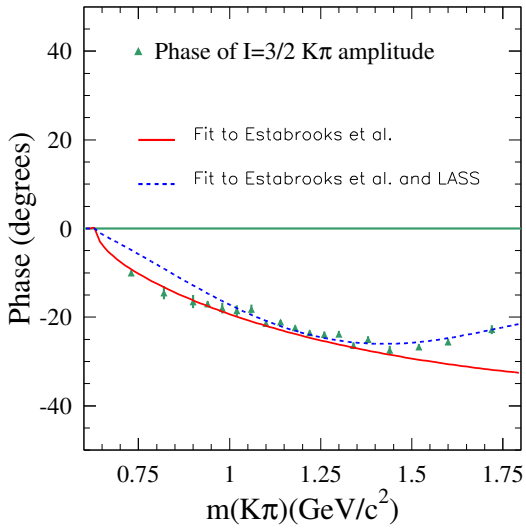

Figure 1.3: *The points correspond to a fit on the measurements of the phase of the $I = 3/2$ $K\pi$ amplitude and are given in the original publication [17]. The full line curve is the result of a fit to the sample of these data obtained with a recoiling neutron (the other data set corresponds to a recoiling Δ). The dashed curve is the result of a fit [22] including all these data points and the measurements by LASS on $K^-\pi^+$ scattering.*

is satisfied with $A_{BG} = A_K = 1$ and $\phi_{BG} = \phi_K = 0$. This gives:

$$\begin{aligned} A_S^{1/2} &= \sin\delta_{BG}^{1/2} \exp i(\delta_{BG}^{1/2}) + \exp 2i(\delta_{BG}^{1/2}) \sin\delta_{K_0^*(1430)} \exp i\delta_{K_0^*(1430)} \\ &= \sin(\delta_{BG}^{1/2} + \delta_{K_0^*(1430)}) \exp i(\delta_{BG}^{1/2} + \delta_{K_0^*(1430)}). \end{aligned}$$

It must be noted that the measured amplitude in $K^-\pi^+$ scattering is the sum of two isospin amplitudes:

$$A_S = A_S^{1/2} + \frac{1}{2} A_S^{3/2} \tag{1.29}$$

whereas, in charm semileptonic decays, only the $I = 1/2$ component contributes.
LASS measurements are based on the fits of moments of angular distributions which depend on the interference between S, P, D...waves. S wave characteristics are thus dependent on P wave measurements.

Measurement of the $I = 3/2$ component This component has been measured in $K^+p \to K^+\pi^+n$ scattering [17]. The experiment was done at SLAC with a 13 GeV K^+ beam impigging on a one meter long hydrogen target. Phase measurements are obtained selecting data produced at small transfer to have enhancement from

the pion exchange mechanism. Fitting data with an effective range parameterization:

$$\cot\left(\delta_{BG}^{3/2}\right) = \frac{1}{a_S^{3/2} p^*} + \frac{1}{2} b_S^{3/2} p^*, \tag{1.30}$$

they obtain:

$$a_S^{3/2} = -(1.03 \pm 0.10)\ GeV^{-1} \text{ and } b_S^{3/2} = -(0.94 \pm 0.5)\ GeV^{-1}. \tag{1.31}$$

The measured amplitude is compatible with an elastic wave:

$$A_S^{3/2} = \left|\sin \delta_{BG}^{3/2}\right| \exp i\delta_{BG}^{3/2}. \tag{1.32}$$

Measured value for the phase $\delta_{BG}^{3/2}$ and the curve corresponding to the values of the parameters given in Equation 1.31 are diplayed in Figure 1.3. Another fit done by M. Pennington [22] which includes in addition measurements from LASS is also given using a dashed line.

Determination of the $I = 1/2$ component To obtain the S-wave, $I = 1/2$, $K^-\pi^+$ amplitude, the fitted parameterization obtained for the $I = 3/2$ component is subtracted from the LASS measurement following Equation 1.29. It can be noted that A_S is not an elastic amplitude even if it is the combination of two amplitudes which are elastic. Then these data are fitted using an effective range parameterization at low energy complemented by the $K_0^*(1430)$ amplitude and considering that the resulting amplitude is elastic up to $1.5\ \mathrm{GeV/c^2}$; corresponding results [19] are given in Table 1.4.

parameters	34 points fit	37 points fit
$m_{K_0^*(1430)}$ $(\mathrm{MeV/c^2})$	1435 ± 5	1415 ± 3
$\Gamma_{K_0^*(1430)}$ $(\mathrm{MeV/c^2})$	279 ± 6	300 ± 6
$a_S^{1/2}$ (GeV^{-1})	1.95 ± 0.09	2.07 ± 0.10
$b_S^{1/2}$ (GeV^{-1})	1.76 ± 0.36	3.32 ± 0.34

Table 1.4: *Fit results to LASS data [19].*

Values of these parameters, obtained using 34 measurements (which correspond to a range of $K\pi$ mass between 0.825 and $1.53\ \mathrm{GeV/c^2}$) are used essentially in all fits to Dalitz distributions for rare charmless B meson decays with a possible S-wave $K\pi$ in the final state.

Few comments The $I = 3/2$ measurements date from 1978 and are not in good agreement with a global fit of the two isospin amplitudes done in [18]. The same experiment [17] provides also a fit of the effective range

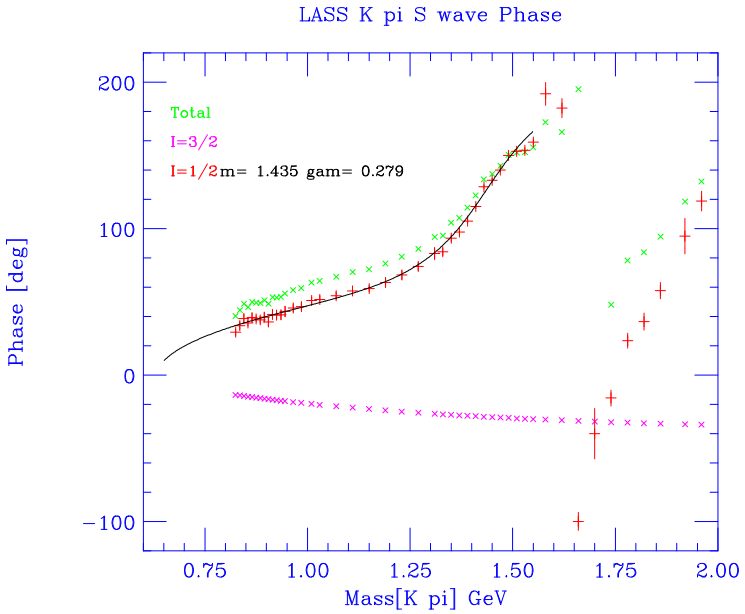

Figure 1.4: *LASS S-wave phase results [19]. Green crosses show the total S-wave phase, the magenta crosses show the I=3/2 behaviour, and the red points with error bars show the I=1/2 phase which results after subtraction of the complex I=3/2 contribution from the complex total S-wave amplitude measured. The black curve is the fit to the 34 points below 1.52 GeV.*

parameterization for the $I = 1/2$ amplitude:

$$a_S^{1/2}([17]) = (2.4 \pm 0.1)\ GeV^{-1} \text{ and } b_S^{1/2}([17]) = -(1.7 \pm 0.3)\ GeV^{-1}. \tag{1.33}$$

One can note the sign of the $b_S^{1/2}([17])$ parameter which is opposite to LASS or to present determinations.

There is not, at present, a direct measurement of the $I = 1/2$ amplitude. Present results reported in Table 1.4 differ from values given in the LASS original publication and have not been published officially.

1.2.2 In $\tau \to K\pi\nu_\tau$ decays

The Belle collaboration [40] has analyzed the $K_S\pi$ mass distribution in $\tau^- \to K_S\pi^-\nu_\tau$ in terms of vector and scalar components. Each component is taken as the sum of Breit-Wigner mass distributions. In τ decays, only the $I = 1/2$ $K\pi$ final state contributes as it originates, from vacuum, through a $s\bar{u}$ weak current. They find that another contribution, in addition to the $K^*(892)$, is needed to fit the data but they obtain a similar χ^2 fit probability using:

- $K_0^*(800) + K^*(892) + K^*(1410)$ or
- $K_0^*(800) + K^*(892) + K_0^*(1430)$.

A fit using for the scalar component an amplitude corresponding to the LASS parameterization has been also tried. They take:

$$a_S^{1/2} = \lambda \times \frac{m}{p^*} \sin\left(\delta_{BG} + \delta_{K_0^*(1430)}\right) \exp i(\delta_{BG} + \delta_{K_0^*(1430)}). \tag{1.34}$$

The m/p^* term is needed to compensate the invariant phase in the decay. Using the values of the a and b parameters measured by LASS for the $I = 1/2$ component, corresponds to a fit probability of 10^{-10}. Finally, they do not express firm conclusions about the composition of the measured hadronic $K\pi$ final state.

The same data has been analyzed in [21] considering simultaneous contributions from scalar and vector components (including the $K^*(1410)$ for the latter). They use a model for the scalar contribution which describes correctly also measurements from LASS. They obtain a good fit of Belle mesurements.

In conclusion, a good description of $\tau^- \to K_S\pi^-\nu_\tau$ decays requires, in addition to the $K^*(892)$:

- a contribution from the $K^*(1410)$ to the vector form factor. Using the value of the corresponding parameter fitted on Belle data, its relative importance in our analyzed decay channel is evaluated to be of the order of 0.5% of the total $K^-\pi^+e^+\nu_e$ decay rate.

- a scalar contribution, with a mass dependence compatible with LASS measurements but the corresponding branching fraction is not yet given in τ decays.

To be able to separate scalar and vector contributions in τ decays the analysis of angular distributions is needed.

1.2.3 In hadronic D meson decays

$K\pi$ interactions can be studied in several Dalitz analyses of three-body D decays. As there is another hadron in the final state which interacts with the K and the π, differences are expected as compared with a purely isolated $K\pi$ system. Let's consider, as an example, $D^+ \to K^-\pi^+\pi^+$ measured by FOCUS [22]. This final state is known to have a large S-wave component because the $\pi^+\pi^+$ system being exotic, there is no resonant $\pi\pi$ contributions.

For the parameterization of the S-wave amplitude they use a K-matrix having the following characteristics:

- it generates a pole for the S-matrix that corresponds to the $K_0^*(1430)$;

- two possible decay channels are considered: $K^-\pi^+$ and $K^0\eta'$;

- parameters have been fitted on LASS data for $I = 1/2$ and $I = 3/2$ amplitudes and $K^-\pi^-$ scattering data is used also for $I = 3/2$;

- predictions from Chiral Perturbation Theory are included to extrapolate expressions at threshold as measurements from LASS start at $m_{K\pi} > 0.825$ GeV/c^2.

The two I-spin amplitudes used to fit the Dalitz plot have been expressed according to:

$$\begin{aligned} \mathcal{A}(1/2)_1 &= [I - iK(1/2)\rho]^{-1}_{1j} P(1/2)^j,\ j = 1,2 \\ \mathcal{A}(3/2) &= [I - iK(3/2)\rho_1]^{-1} P(3/2). \end{aligned} \tag{1.35}$$

$K(1/2)$ and ρ are 2×2 matrices. ρ is diagonal, of elements $\rho_{1,2} = 2p^*_{1,2}/m_{Kpi}$. $p^*_{1,2}$ are the breakup momenta in the decays into $K^-\pi^+$ and $K^0\eta'$, respectively, of a system of mass equal to m. For values of the mass below the second threshold, ρ_2 has to be taken as imaginary (not zero !). For the $I = 3/2$ amplitude only the first channel contributes.

Elements of the K matrices are channel independent and are determined, in the FOCUS paper, from fits to $K\pi$ scattering. These elements are parameterized as:

$$\begin{aligned} K(1/2)_{11} &= \left(\frac{s - s_0^{1/2}}{s_{norm.}}\right)\left(\frac{g_1^2}{s_1 - s} + c_{110} + c_{111}\tilde{s} + c_{112}\tilde{s}^2\right) \\ K(1/2)_{12} &= \left(\frac{s - s_0^{1/2}}{s_{norm.}}\right)\left(\frac{g_1 g_2}{s_1 - s} + c_{120} + c_{121}\tilde{s} + c_{122}\tilde{s}^2\right) \\ K(1/2)_{22} &= \left(\frac{s - s_0^{1/2}}{s_{norm.}}\right)\left(\frac{g_2^2}{s_1 - s} + c_{220} + c_{221}\tilde{s} + c_{222}\tilde{s}^2\right) \\ K(3/2) &= \left(\frac{s - s_0^{3/2}}{s_{norm.}}\right)\left(d_{110} + d_{111}\tilde{s} + d_{112}\tilde{s}^2\right). \end{aligned} \tag{1.36}$$

In these expressions $s = m^2_{K\pi}$ and $s_{norm.} = m_K^2 + m_\pi^2$ is introduced so that the K-matrix elements are dimensionless. Values for $s_0^{1/2} = 0.23\ GeV^2$ and $s_0^{3/2} = 0.27\ GeV^2$ are related to the position of Adler zeros. The expansion parameter is $\tilde{s} = s/s_{norm.} - 1$.

For completeness values of the different parameters are given in Table 1.5.

pole (GeV^2)	couplings (GeV)	c_{11i}	c_{12i}	c_{22i}	d_{11i}
$s_1 = 1.7919$	$g_1 = 0.31072$	$c_{110} = 0.79299$	$c_{120} = 0.15040$	$c_{220} = 0.17054$	$d_{110} = -0.22147$
	$g_2 = -0.02323$	$c_{111} = -0.15099$	$c_{121} = -0.038266$	$c_{221} = -0.0219$	$d_{111} = 0.026637$
		$c_{112} = 0.00811$	$c_{122} = 0.0022596$	$c_{222} = 0.00085655$	$d_{112} = -0.00092057$

Table 1.5: *Values of the parameters entering into the elements of the $K(1/2)$ and $K(3/2)$ matrices. [22]*

The element $K(3/2)$ has no pole as it corresponds to an exotic final state.

P-vectors give the production of the different states in the considered process and have the same singularities as the K-matrix elements. They are thus process dependent and parameters giving their functional forms have been fitted on FOCUS data [22]:

$$\begin{aligned} P(1/2)_1 &= \frac{\beta g_1 e^{i\theta}}{s_1 - s} + \left(c_{10} + c_{11}\hat{s} + c_{12}\hat{s}^2\right) e^{i\gamma_1} \\ P(1/2)_2 &= \frac{\beta g_2 e^{i\theta}}{s_1 - s} + c_{20} e^{i\gamma_2} \\ P(3/2) &= c_{30} e^{i\gamma_3}. \end{aligned} \tag{1.37}$$

This parameterization is obtained versus $\hat{s} = s - 2\ GeV^2$, a quantity which is close to zero in the centre of the Dalitz plane.

Values measured by FOCUS for the different parameters are given in Table 1.6 [22].

parameter	phase (degrees)
$\beta = 3.389 \pm 0.152 \pm 0.002 \pm 0.068$	$\theta = 246 \pm 4 \pm 0.3 \pm 3.0$
$c_{10} = 1.655 \pm 0.156 \pm 0.010 \pm 0.101$ $c_{11} = 0.780 \pm 0.096 \pm 0.003 \pm 0.090$ $c_{12} = -0.954 \pm 0.058 \pm 0.0015 \pm 0.025$	$\gamma_1 = 304 \pm 6 \pm 0.4 \pm 5.8$
$c_{20} = 17.182 \pm 1.036 \pm 0.023 \pm 0.362$	$\gamma_2 = 126 \pm 3 \pm 0.6 \pm 1.2$
$c_{30} = 0.734 \pm 0.080 \pm 0.005 \pm 0.030$	$\gamma_3 = 211 \pm 10 \pm 0.7 \pm 7.8$

Table 1.6: *Values measured by FOCUS for the parameters entering into the P vectors elements.*

Few remarks are in order:

- from the Watson theorem one expects to measure the same phases for the $I = 1/2$ and $I = 3/2$ amplitudes, separately, in $K\pi$ scattering and in $D \to K\pi\pi$ if the third hadron does not play an important role. The presence of this hadron can produce in any case an overall phase difference.

- for the $I = 3/2$ amplitude the adopted parameterization includes only a global phase (γ_3) in addition to the $K(3/2)$ element. For this amplitude the Watson theorem is thus satisfied by construction.

- for the $I = 1/2$ amplitude, the P-vector has three phases, and the phase of its elements varies across the Dalitz plane. One thus expects some violation of the Watson theorem in this case. This is illustrated in Figure 1.5. In this comparison the phase at threshold is put to zero.

- the total S wave fit fraction measured by FOCUS is $(83 \pm 2)\%$ whereas the $I = 1/2$ and $I = 3/2$ components are equal to $(207 \pm 30)\%$ and $(40 \pm 10)\%$, respectively. There is thus a large effect from interference between these two waves. Is this really physical or due to an artefact of the parameterization?

It is also possible to compare (see Figure 1.6) the value of the $I = 1/2$ S wave amplitude measured by FOCUS with the "naive" estimate given in Equation 1.34, derived from the elastic amplitude. Whereas the latter has a small variation with $m_{K\pi}$, below $1.4\ \mathrm{GeV/c^2}$, a steep behaviour, close to threshold, is observed in the former. Above $1.4\ \mathrm{GeV/c^2}$, the two amplitudes sharply decrease to become rather small around $1.5\ \mathrm{GeV/c^2}$.

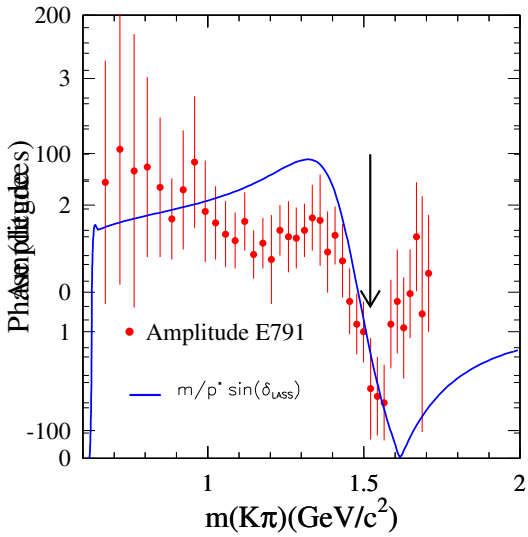

Figure 1.5: *The points correspond to the values obtained by LASS for the phase of the $I = 1/2$ amplitude. The continuous line is a fit of these data provided also by LASS and using the first 34 points ($m_{K\pi} < 1.53$ GeV/c^2). The dashed line is the corresponding phase obtained by FOCUS [22] from their fit to $D^+ \to K^-\pi^+\pi^+$ where the phase at threshold has been imposed to be equal to zero.*

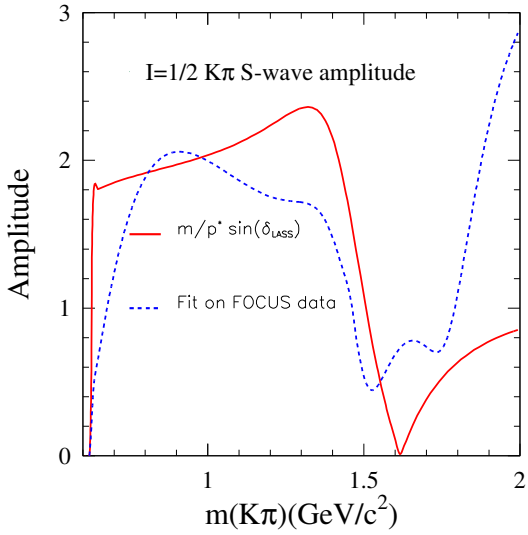

Figure 1.6: *The continuous line is the value of the amplitude equal to $m/p^* \sin\delta_{LASS}$, in which δ_{LASS} is the phase given in Figure 1.5 corresponding to LASS measurements. The dashed line is the corresponding amplitude fitted by FOCUS.*

E791 analysis The E791 collaboration has also analyzed the $D^+ \to K^-\pi^+\pi^+$ decay channel [23]. Several differences are observed as compared with the FOCUS approach:

- they do not separate between $I = 1/2$ and $I = 3/2$ $K\pi$ S-waves but expect, in their article that the $I = 1/2$ dominates (this is not in agreement with findings from FOCUS);
- they measure a total S-wave fraction of $(78.6 \pm 2.3)\%$ in agreement with FOCUS;
- they measure the S-wave amplitude and phase in several bins of the Dalitz plane without using any specific parameterization;
- in the parameterization of the partial waves the presence of the second pion results in the presence of a form factor $\mathcal{F}_D(q)$ where q is the momentum of the bachelor pion in the $K\pi$ rest frame. For S-waves, this form factor is assumed to have a Gaussian behaviour: $\mathcal{F}_D(q) = e^{-(rq)^2/12}$, with $r = 5\ GeV^{-1}$. This quantity varies from 0.25 for values of the $K\pi$ mass close to threshold to unity at maximal value of this mass.

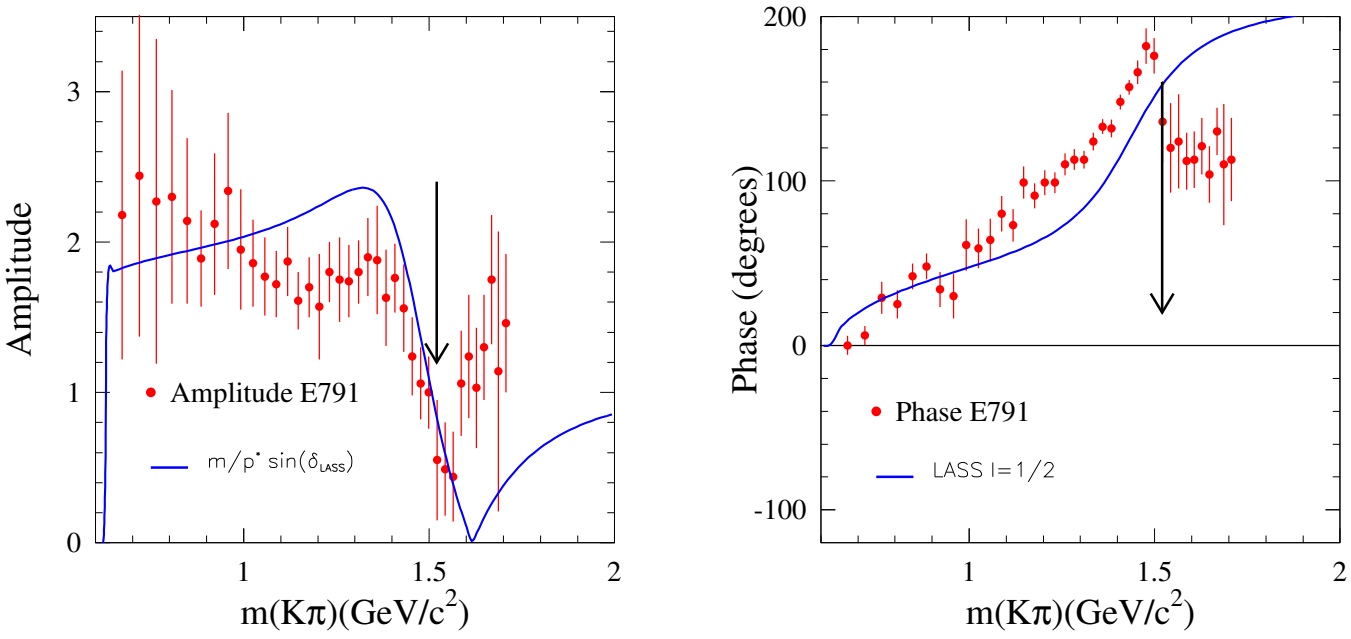

Figure 1.7: *Comparison between the amplitude and the phase measured by E791 for the total $K\pi$ S-wave and the fitted results obtained by LASS for the I=1/2 component. The arrow indicates the maximum value of the mass used in the fit to LASS data. The phase measured by E791 has been shifted by $+102°$ to be zero at the first measured point, close to threhold.*

In Figure 1.7 have been compared the phase and the amplitude of the measured quantity:

$$\mathcal{F}_D(q)|C_0(m_{K\pi})|e^{i\phi(m_{K\pi})} \tag{1.38}$$

for different values of the $K\pi$ mass, with the "naive" estimate given in Equation 1.34, derived from the elastic ($I = 1/2$) amplitude. This comparison, which contains some degree of arbitrariness, is the same as the one given in their publication. The phase measured by E791 has been shifted by 102° so that its value at the first measured point is equal to zero.

CLEO analysis The CLEO-c experiment has also published an analysis of the $D^+ \to K^-\pi^+\pi^+$ decay channel; as compared with the FOCUS measurement one can note the following differences:

- as in the E791 analysis they do not separate the $I = 1/2$ and $I = 3/2$ components;
- they determine the amplitude and the phase of the S-wave in different bins of the Dalitz plane, without using a specific parameterization. The fitted amplitude corresponds to the product $\mathcal{F}_D(q)\mathcal{A}_S$. They have not included the contribution from the $K_0^*(1430)$ into their model independent fit but have preferred to add it separately as a resonance using the isobar approach. They have provided a S-wave complex ampltitude which includes this component.
- they add a $\pi^+\pi^+$ component and measure a corresponding rate fraction equal to $(15 \pm 3)\%$;
- the $K\pi$ S-wave rate fraction, not including the $K_0^*(1430)$, is equal to $(84 \pm 4)\%$. The fitted fraction for the $K_0^*(1430)$ amounts to $(13.3 \pm 0.6)\%$. They do not provide the rate fraction for the S-wave, including the $K_0^*(1430)$ so it is not possible to do a comparison with previous experiments.

Summary of results on the $K\pi$ S-wave from $D^+ \to K^-\pi^+\pi^+$

- the Watson theorem is expected to be valid, separately for the $I = 1/2$ and $I = 3/2$ components and applies only to the corresponding phases of these amplitudes. The relative importance of $I = 1/2$ and $I = 3/2$ components can thus be different in $K\pi$ scattering and in a Dalitz decay. In E791 and CLEO-c they measure the total $K\pi$ S-wave amplitude and compare their results with the $I = 1/2$ component from LASS. FOCUS, using the phase of the $I = 3/2$ amplitude measured in scattering experiments, has fitted separately the two components and finds large effects from the $I = 3/2$ part.
- measured phases in Dalitz analyses have a global shift as compared with the scattering case (in which phases are expected to be zero at threshold). Once having corrected for this effect (with some arbitrariness) the variation measured for the phase in Dalitz decays and in $K\pi$ scattering behaves roughly in a similar way but it is difficult to give a quantitative comparison. Differences between the two approaches, versus the value of $m(K\pi)$, are much larger than quoted uncertainties. They can come from the comparison itself which considers the total $K\pi$ S-wave in one case and only the $I = 1/2$ component for scattering. It can be due also to the effect of the bachelor pion in Dalitz decays which creates violations of the Watson theorem.
- for measured amplitudes, in Dalitz decays, there is the presence of the form factor $\mathcal{F}_D(q)$ which has numerically large effects. Experiments are sensitive to the product of this form factor by the S-wave amplitude.

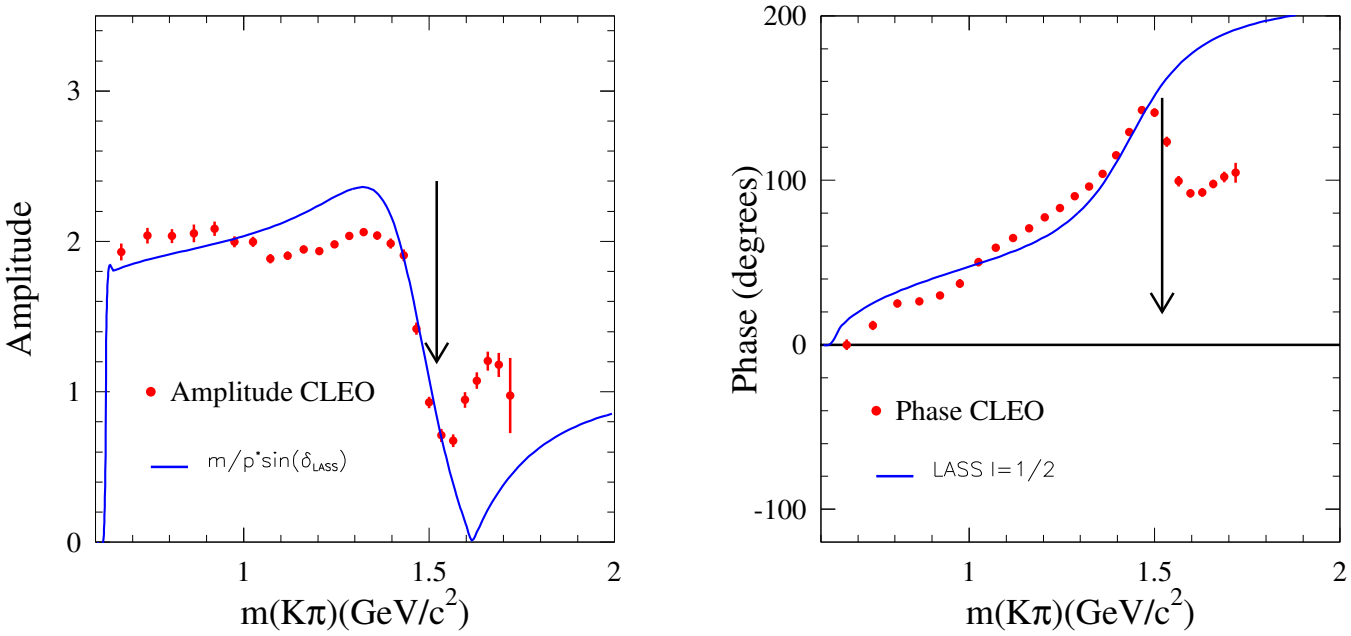

Figure 1.8: *Comparison between the amplitude and the phase measured by CLEO-c for the total $K\pi$ S-wave and the fitted results obtained by LASS for the I=1/2 component. The arrow indicates the maximum value of the mass used in the fit to LASS data. The phase measured by CLEO-c has been shifted by $+66^\circ$ to be zero at the first measured point, close to threhold. The measured amplitude by CLEO in arbitrary unit has been scaled by 0.1.*

In their comparison with $K\pi$ scattering they take this product and compare its values with the amplitude derived from unitarity: $m/p^* \sin\delta_{LASS}$. E791 and CLEO-c find a similar behaviour for these two quantities versus $m(K\pi)$. FOCUS, having separated the $I = 3/2$ contribution measures a large variation close to threshold which is not seen in the scattering $I = 1/2$ amplitude.

It is thus difficult to draw quantitative conclusions from results obtained with $D^+ \to K^-\pi^+\pi^+$ decays. Qualitatively one can say that the phase of the S-wave behaves in a similar way, versus $m(K\pi)$, as the phase measured by LASS. Below the $K_0^*(1430)$, the S-wave amplitude has a smooth variation versus $m(K\pi)$. At the $K_0^*(1430)$ mass and above, the S-wave amplitude has a sharp decrease with the mass.

1.2.4 In D_{e4} decays

The dominant hadronic contribution in the D_{e4} decay channel comes from the (J^P =1^-) K^*(892) resonant state. E687 [24] gives a first suggestion that there is another component in addition to the K^*. FOCUS, few years later, obtains the real evidence for an S-wave contribution from the asymmetry of the angular distribution of the K in the $K\pi$ rest frame [25]. They conclude that the phase difference between S and P-waves is compatible with a constant equal to $\pi/4$, over the K^* mass region.

In a second publication [26] they find that the asymmetry can be explained if they use for the phase of the

S-wave the variation versus the $K\pi$ mass measured by the LASS collaboration [43]. They do not fit to their data the two parameters that govern this phase variation and take LASS results:

$$\cot(\delta_{LASS}) = \frac{1}{a_S p^*} + \frac{b_S p^*}{2} \quad , \quad a_S = 4.03 \pm 1.72 \pm 0.06 \text{ GeV}^{-1}$$
$$b_S = 1.29 \pm 0.63 \pm 0.67 \text{ GeV}^{-1}. \tag{1.39}$$

These values correspond to the total S-wave amplitude measured by LASS which is the sum of $I = 1/2$ and $I = 3/2$ contributions whereas only the former component is present in charm semileptonic decays. A new analysis of LASS data [19], extracting the $I = 1/2$ component gives quite different values for the parameters a_S and b_S and for their corresponding uncertainties (Table 1.4).

For the corresponding S-wave amplitude they use an empirical parameterization derived from the LASS measurement, taken to be elastic and corrected for the decay phase space factor (p^*/m):

$$A_{NR} = a_{NR} \frac{m}{p^*} \sin(\delta_{LASS}) e^{i\delta_{LASS}}. \tag{1.40}$$

If, according to Watson theorem, the phase measured in diffractive $K\pi$ scattering is expected to be the same as the one entering in $D \to K\pi e\nu_e$ decays, there is no similar condition to relate the S-wave amplitude in these two processes. So there is no real justification for Eq. 1.40.

They fit the values of the pole mass, the width and the Blatt-Weisskopf damping parameter for the $K^*(892)$. These values from FOCUS [26] are given in Table 1.7 and compared with previous measurements averaged in [13].

The corresponding P-wave amplitude they use is parameterized as [1] :

$$A_{K^*(892)} = \frac{m_{K^*(892)} \Gamma^0_{K^*(892)}}{m^2 - m^2_{K^*(892)} + i m_{K^*(892)} \Gamma_{K^*(892)}(m)} F_1(m). \tag{1.41}$$

In this expression:

- m is the $K\pi$ mass;
- $m_{K^*(892)}$ is the $K^*(892)$ pole mass;
- $\Gamma^0_{K^*(892)}$ is the nominal width of the $K^*(892)$ for $m = m_{K^*(892)}$;
- $\Gamma_{K^*(892)}(m)$ is the mass dependent $K^*(892)$ width. $\Gamma_{K^*(892)}(m) = \Gamma^0_{K^*(892)} \frac{p^*}{p^*_0} \frac{m_{K^*(892)}}{m} F_1^2(m)$;
- $F_1(m) = \frac{p^*}{p^*_0} \frac{B(p^*)}{B(p^*_0)}$ where B is the Blatt-Weisskopf damping factor: $B = 1/\sqrt{1 + r^2_{BW} p^{*2}}$.

[1] It has to be noted, and this is indicated in the FOCUS paper, that the convention used to define the Breit-Wigner amplitude in Eq (3) differs by a (-) sign from the "usual" expression. By "usual" it is meant a phase which grows from zero to π when the mass increases and which is equal to $\pi/2$ at the pole. In the present analysis we adopt this "usual" definition which is also used in [13].

Parameter	FOCUS results [26]	PDG
m_{K^*} MeV/c^2	$895.41 \pm 0.32^{+0.35}_{-0.43}$	896.00 ± 0.25 [13]
$\Gamma^0_{K^*}$ MeV/c^2	$47.79 \pm 0.86^{+1.32}_{-1.06}$	50.3 ± 0.6 [13]
r_{BW} GeV^{-1}	$3.96 \pm 0.54^{+1.31}_{-0.90}$	3.40 ± 0.67 [43]

Table 1.7: *Parameters of the K^{*0} measured by FOCUS are compared with world averaged values.*

Channel	FOCUS results [26] (%)
$\frac{\Gamma(D^+\to K^-\pi^+\mu^+\nu_\mu)_{NR}}{\Gamma(D^+\to K^-\pi^+\mu^+\nu_\mu)}$	$5.30 \pm 0.74^{+0.99}_{-0.96}$
$\frac{\Gamma(D^+\to K^-\pi^+\mu^+\nu_\mu)_{K^*_0(1430)}}{\Gamma(D^+\to K^-\pi^+\mu^+\nu_\mu)}$	$< 0.64\%$ at 90% C.L.
$\frac{\Gamma(D^+\to K^-\pi^+\mu^+\nu_\mu)_{K^*(1680)}}{\Gamma(D^+\to K^-\pi^+\mu^+\nu_\mu)}$	$< 4.0\%$ at 90% C.L.

Table 1.8: *Measured fraction of the non-resonant S-wave component and limits on contributions from $K^*_0(1430)$ and $K^*(1680)$ in the decay $D^+ \to K^-\pi^+\mu^+\nu_\mu$, obtained by FOCUS [26].*

They also compare [26] the measured angular asymmetry of the K in the $K\pi$ rest frame versus the $K\pi$ mass with expectations from a κ resonance and conclude that the presence of a κ can be neglected. They take a Breit-Wigner distribution for the κ amplitude using values measured by the E791 collaboration [35] for the mass and width of the resonance. ($m_\kappa = 797 \pm 19 \pm 43$ MeV/c^2, $\Gamma_\kappa = 410 \pm 43 \pm 87$ MeV/c^2). This approach to search for a κ does not seem to be appropriate. Adding a κ in this way violates the Watson theorem as the phase of the fitted $K\pi$ amplitude will differ much from the one measured by LASS. In addition the interpretation of LASS measurements in [18] concluded on the presence of a κ. FOCUS has simply excluded their naive parameterization of the S-wave amplitude when including a κ.

In addition to the $K^*(892)$ they measure the rate for the NR S-wave contribution and place limits on other components (Table 1.8).

Analyzing $D^+ \to K^-\pi^+e^+\nu_e$ events from a sample corresponding to 281 pb^{-1} integrated luminosity, the CLEO-c collaboration has confirmed the FOCUS result of an S-wave interference but does not provide an independent measurement of the phase [33].

1.3 D_{e4} decay formalism

As there are 4 particles in the final state, the differential decay rate for the channel $D^+ \to K^-\pi^+e^+\nu_e$ depends on five variables:

- m^2 the mass squared of the $K\pi$ system;
- q^2 the mass squared of the $e^+\nu_e$ system;
- $\cos(\theta_\pi)$, where θ_π is the angle formed by the π three-momentum in the $K\pi$ rest frame and the line of flight of the $K\pi$ in the D rest frame;

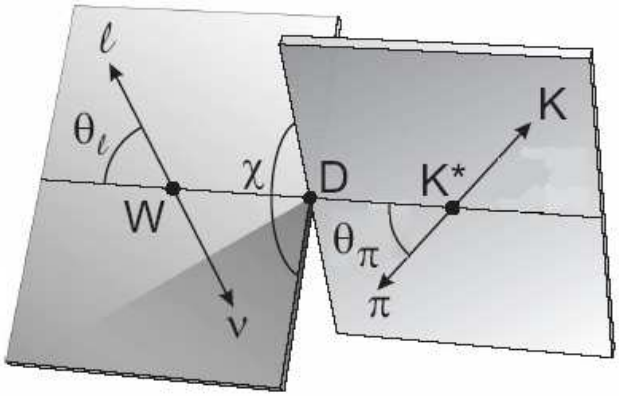

Figure 1.9: *Definition of angular variables.*

- $\cos(\theta_e)$, where θ_e is the angle formed by the charged lepton three-momentum in the $e\nu$ rest frame and the line of flight of the $e\nu$ in the D rest frame;

- χ, the angle between the normals to the planes defined in the D rest frame by the $K\pi$ pair and the $e\nu$ pair. The sense of the angle is from the normal to the $K\pi$ plane to the normal to the $e\nu$ plane. χ is defined between $-\pi$ and $+\pi$.

It has to be noted that, when analyzing D^- decays, the sign of the χ angle has to be changed.

In order to specify the above variables more precisely, we define k_-, k_+, k_e, k_ν to be respectively the K^-, π^+, e^+ and ν_e four-momenta.
$\vec{K_+}$ is the π^+ three-momentum in the $K\pi$ c.m. and $\vec{K_e}$ is the three-momentum of the positron in the virtual W center of mass. Let $\hat{v}$ be the unit vector along the $K\pi$ direction in the D rest frame, $\hat{c}$ the unit vector along the projection of $\vec{K_+}$ perpendicular to $\hat{v}$ and $\hat{d}$, the unit vector along the projection of $\vec{K_e}$ perpendicular to $\hat{v}$. We have:

$$\begin{aligned} m^2 = (k_+ + k_-)^2;\ \ q^2 = (k_e + k_\nu)^2 \\ cos(\theta_\pi) = \frac{\hat{v}.\vec{K_+}}{|\vec{K_+}|};\ \ cos(\theta_e) = -\frac{\hat{v}.\vec{K_e}}{|\vec{K_e}|} \\ cos(\chi) = \hat{c}.\hat{d};\ \ sin(\chi) = (\hat{c} \times \hat{v}).\hat{d} \end{aligned} \tag{1.42}$$

These variables have been introduced by N. Cabibbo and A. Maksymowicz [36] when studying $Ke4$ decays and the corresponding differential decay distribution was obtained by A. Pais and S.B. Treiman [37].

For the differential decay partial width, we use the formalism given in [38], which generalizes to 5 variables the decay rate given in ([39]) in terms of q^2, $\cos\theta_\pi$, $\cos\theta_e$ and χ variables. In addition it provides a partial wave decomposition for the hadronic system.

Any dependence versus the lepton mass has been neglected as electrons or positrons have been used.

$$d^5\Gamma = \frac{G_F^2 \left|V_{cs}\right|^2}{(4\pi)^6 m_D^3} X\beta\mathcal{I}(m^2, q^2, \theta_K, \theta_e, \chi) dm^2 dq^2 d\cos(\theta_K) d\cos(\theta_e) d\chi. \tag{1.43}$$

In this expression, $X = p_{K\pi} * m_D$ where $p_{K\pi}$ is the momentum of the $K\pi$ system in the D rest frame and $\beta = 2p^*/m$. As usual, p^* is the breakup momentum of the $K\pi$ system in its rest frame.

The dependence of $\mathcal{I}$ on θ_e and χ is given by:

$$\begin{aligned} \mathcal{I} &= \mathcal{I}_1 + \mathcal{I}_2 \cos 2\theta_l + \mathcal{I}_3 \sin^2\theta_l \cos 2\chi \\ &\quad + \mathcal{I}_4 \sin 2\theta_l \cos\chi + \mathcal{I}_5 \sin\theta_l \cos\chi \\ &\quad + \mathcal{I}_6 \cos\theta_l + \mathcal{I}_7 \sin\theta_l \sin\chi \\ &\quad + \mathcal{I}_8 \sin 2\theta_l \sin\chi + \mathcal{I}_9 \sin^2\theta_l \sin 2\chi \end{aligned} \tag{1.44}$$

where $\mathcal{I}_{1,\ldots,9}$ depend on $m^2,\ q^2$ and θ_π. These quantities can be expressed in terms of three form factors, $\mathcal{F}_{1,2,3}$.

$$\begin{aligned} \mathcal{I}_1 &= \frac{1}{4}\left\{ |\mathcal{F}_1|^2 + \frac{3}{2}\sin^2\theta_\pi \left(|\mathcal{F}_2|^2 + |\mathcal{F}_3|^2 \right) \right\} \\ \mathcal{I}_2 &= -\frac{1}{4}\left\{ |\mathcal{F}_1|^2 - \frac{1}{2}\sin^2\theta_\pi \left(|\mathcal{F}_2|^2 + |\mathcal{F}_3|^2 \right) \right\} \\ \mathcal{I}_3 &= -\frac{1}{4}\left\{ |\mathcal{F}_2|^2 - |\mathcal{F}_3|^2 \right\} \sin^2\theta_\pi \\ \mathcal{I}_4 &= \frac{1}{2} Real\left(\mathcal{F}_1^* \mathcal{F}_2\right) \sin\theta_\pi \\ \mathcal{I}_5 &= Real\left(\mathcal{F}_1^* \mathcal{F}_3\right) \sin\theta_\pi \\ \mathcal{I}_6 &= Real\left(\mathcal{F}_2^* \mathcal{F}_3\right) \sin^2\theta_\pi \\ \mathcal{I}_7 &= Im\left(\mathcal{F}_1 \mathcal{F}_2^*\right) \sin\theta_\pi \\ \mathcal{I}_8 &= \frac{1}{2} Im\left(\mathcal{F}_1 \mathcal{F}_3^*\right) \sin\theta_\pi \\ \mathcal{I}_9 &= -\frac{1}{2} Im\left(\mathcal{F}_2 \mathcal{F}_3^*\right) \sin^2\theta_\pi \end{aligned} \tag{1.45}$$

We can expand the form factors $\mathcal{F}_{1,2,3}$ into partial waves to have their explicit dependence on θ_π. If we keep only S, P and D-waves, this gives:

$$\begin{aligned}\mathcal{F}_1 &= \mathcal{F}_{10} + \mathcal{F}_{11}\cos\theta_\pi + \mathcal{F}_{12}\frac{3\cos^2\theta_\pi - 1}{2} \\ \mathcal{F}_2 &= \frac{1}{\sqrt{2}}\mathcal{F}_{21} + \sqrt{\frac{3}{2}}\mathcal{F}_{22}\cos\theta_\pi \\ \mathcal{F}_3 &= \frac{1}{\sqrt{2}}\mathcal{F}_{31} + \sqrt{\frac{3}{2}}\mathcal{F}_{32}\cos\theta_\pi\end{aligned} \tag{1.46}$$

Form factors $\mathcal{F}_{ij}$ depend only on m^2 and q^2. $\mathcal{F}_{10}$ characterizes the S-wave contribution whereas $\mathcal{F}_{i1}$ and $\mathcal{F}_{i2}$ correspond to the P- and D-wave, respectively.

1.3.1 Connexion with the usual decay formalism in $D \to K^* e\nu$

In [39] they provide an expression with no dependence on the $K\pi$ mass, the $\overline{K^{*0}}$ being considered at its pole mass value, which, in addition, gives the correspondance between helicity and Lorentz-invariant form factors.

$$d^4\Gamma = \frac{3G_F^2\left|V_{cs}\right|^2}{\left(4\pi\right)^4 m_D^3} X q^2 B(V \to P_1P_2)\mathcal{I}_R(q^2,\theta_\pi,\theta_e,\chi)dq^2 d\cos\left(\theta_\pi\right)d\cos\left(\theta_e\right)d\chi. \tag{1.47}$$

The dependence of $\mathcal{I}_R$ on θ_e and χ is given by:

$$\begin{aligned}\mathcal{I}_R &= (1+\cos\theta_l)^2\sin^2\theta_\pi\left|H_+(q^2)\right|^2 \\ &\quad +(1-\cos\theta_l)^2\sin^2\theta_\pi\left|H_-(q^2)\right|^2 \\ &\quad +4\sin^2\theta_l\cos^2\theta_\pi\left|H_0(q^2)\right|^2 \\ &\quad +4\sin\theta_l(1+\cos\theta_l)\sin\theta_\pi\cos\theta_\pi\cos\chi H_+(q^2)H_0(q^2) \\ &\quad -4\sin\theta_l(1-\cos\theta_l)\sin\theta_\pi\cos\theta_\pi\cos\chi H_-(q^2)H_0(q^2) \\ &\quad -2\sin^2\theta_l\sin^2\theta_\pi\cos 2\chi H_+(q^2)H_-(q^2).\end{aligned} \tag{1.48}$$

The helicity amplitudes $H_{+,-,0}(q^2)$ can in turn be related to the two axial-vector form factors $A_{1,2}(q^2)$, and to the vector form factor $V(q^2)$:

$$\begin{aligned}H_0(q^2) &= \frac{1}{2m_{K\pi}q}\left[\left(m_D^2 - m_{K\pi}^2 - q^2\right)\left(m_D + m_{K\pi}\right)A_1(q^2) - 4\frac{m_D^2 p_{K*}^2}{m_D + m_{K\pi}}A_2(q^2)\right] \\ H_\pm(q^2) &= \left(m_D + m_{K\pi}\right)A_1(q^2) \mp \frac{2m_D p_{K*}}{m_D + m_{K\pi}}V(q^2).\end{aligned} \tag{1.49}$$

Integrating Eq. (1.43) over dm^2, assuming that the K^* is the only contribution ($\mathcal{F}_{10} = 0$ and $\mathcal{F}_{i2} = 0$), it is possible to get the correspondance between $\mathcal{F}_{i1},\ i = 1, 2, 3$ and the helicity and invariant form factors.

$$\begin{aligned} \mathcal{F}_{11} &= \alpha 2\sqrt{2} q H_0 \\ \mathcal{F}_{21} &= \alpha 2q\left(H_+ + H_-\right) \\ \mathcal{F}_{31} &= \alpha 2q\left(H_+ - H_-\right) \end{aligned} \tag{1.50}$$

The value of α is not fixed yet, it depends on the way the Breit-Wigner for the K^* has been parameterized.

1.3.2 Partially integrated decay rates

Integrating over all angular variables, the decay rate is proportional to:

$$\begin{aligned} < \mathcal{I} >_{\cos\theta_e,\chi,\cos\theta_\pi} &= \frac{8\pi}{3}\left[|\mathcal{F}_{10}|^2 + \frac{1}{3}\left\{|\mathcal{F}_{11}|^2 + |\mathcal{F}_{21}|^2 + |\mathcal{F}_{31}|^2\right\}\right. \\ &+ \left.\frac{1}{5}\left\{|\mathcal{F}_{12}|^2 + |\mathcal{F}_{22}|^2 + |\mathcal{F}_{32}|^2\right\}\right]. \end{aligned} \tag{1.51}$$

This expression shows that the differential decay rate, versus q^2 and m^2, is an incoherent sum over the contributions from S, P and D-waves.

1.3.3 Interference between S and P-waves

P and S-waves are the dominant contributions to the measured decay rate. In the following we consider in more detail how they interfere and how these interferences allow to measure the S-wave component.

Integrating over all angular variables but $\cos\theta_\pi$, it remains only a dependence through $\mathcal{I}_1$ and $\mathcal{I}_2$:

$$< \mathcal{I} >_{\cos\theta_e,\chi} = \frac{4\pi}{3}\left\{|\mathcal{F}_1|^2 + \sin^2\theta_\pi\left(|\mathcal{F}_2|^2 + |\mathcal{F}_3|^2\right)\right\} \tag{1.52}$$

or

$$\begin{aligned} < \mathcal{I} >_{\cos\theta_e,\chi} &= \frac{4\pi}{3}\left\{|\mathcal{F}_{10}|^2 + \cos^2\theta_\pi|\mathcal{F}_{11}|^2 + 2\cos\theta_\pi Real\left(\mathcal{F}_{10}\mathcal{F}_{11}^*\right)\right. \\ &\left. + \frac{1}{2}\sin^2\theta_\pi\left(|\mathcal{F}_{21}|^2 + |\mathcal{F}_{31}|^2\right)\right\} \end{aligned} \tag{1.53}$$

The asymmetry observed by FOCUS in the $\cos\theta_\pi$ distribution is generated by the product of the form factors $\mathcal{F}_{10}\mathcal{F}_{11}^*$.

In [26], FOCUS has also studied the variation of the asymmetry versus the mass of the $K\pi$ system. Using Eq. (1.53) and computing the average value for $\cos\theta_\pi$ one obtains:

$$< \cos\theta_\pi >_{\cos\theta_e,\chi,\cos\theta_\pi} (q^2, m^2) = \frac{2}{3} \frac{Real\left(\mathcal{F}_{10}\mathcal{F}_{11}^*\right)}{|\mathcal{F}_{10}|^2 + \frac{1}{3}\left\{|\mathcal{F}_{11}|^2 + |\mathcal{F}_{21}|^2 + |\mathcal{F}_{31}|^2\right\}}. \tag{1.54}$$

The S-wave contribution appears through the $\mathcal{F}_1$ form factor and it is thus present also in $\mathcal{I}_{4,5,7,8}$ which contribute to the χ angular distribution. These contributions can be measured using the following moments:

$$\begin{aligned} < \sin\chi\cos\theta_e > &\sim \frac{\pi^3}{16\sqrt{2}} Im\left(\mathcal{F}_{10}\mathcal{F}_{31}^*\right) \\ < \cos\chi > &\sim \frac{\pi^3}{4\sqrt{2}} Real\left(\mathcal{F}_{10}^*\mathcal{F}_{31}\right) \\ < \sin\chi > &\sim \frac{\pi^3}{4\sqrt{2}} Im\left(\mathcal{F}_{10}\mathcal{F}_{21}^*\right) \\ < \cos\chi\cos\theta_e > &\sim \frac{\pi^3}{16\sqrt{2}} Real\left(\mathcal{F}_{10}^*\mathcal{F}_{21}\right) \end{aligned} \tag{1.55}$$

By taking ratios of these quantities it is possible to eliminate the effects from hadronic form factors and amplitudes and be sensitive only to the hadronic phase difference between S and P-waves.
Unfortunately this approach is not accurate statistically as it uses averages of distributions which are almost flat over their variation domain. It is more appropriate to do a complete fit of data using the full information in five dimensions.

We have verified that the signs of all asymmetries observed in data (Figure 1.11) agree with those expected from the decay rate expression that we use to generate "toy" event samples (Figure 1.10).

These tests demonstrate that a consistent set of conventions is used to define the angles (θ_e, θ_π and χ) and the phases of the S and P hadronic amplitudes.

To illustrate the importance of changing the sign for χ when going from a D^+ to a D^- we display, in Figure 1.12, the χ angle distributions for $D^\pm$ when this change is applied or not.

1.3.4 P-wave form factor parameterization

As we are considering resonances which have an extended mass distribution, form factors entering in Eq.(1.49) can have also a mass dependence. We have assumed that the q^2 and m dependence of the form factors factorize:

$$(V, A_1, A_2)(q^2, m) = (V, A_1, A_2)(q^2) \times A(m) \tag{1.56}$$

where $A(m)$ is, in case of a resonance, a Breit-Wigner distribution.

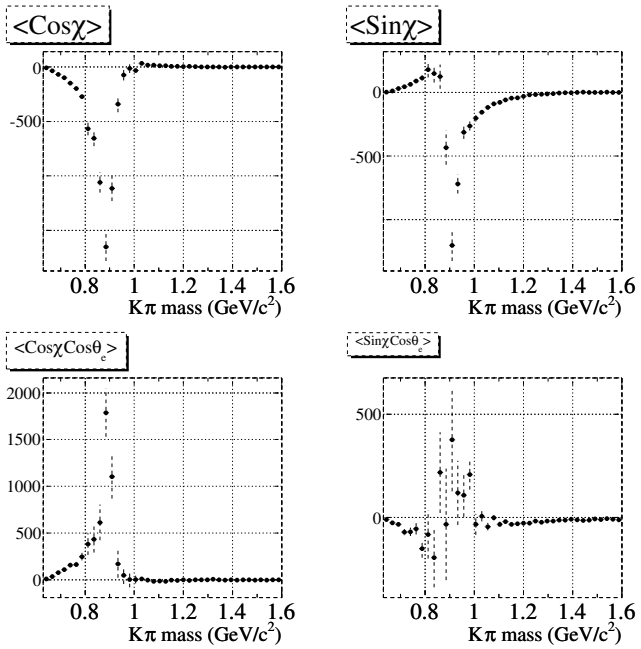

Figure 1.10: *Toy simulation of $K\pi$ mass distributions for interfering S+P-waves, obtained by weighting each event using different factors which depend on angular variables. No detector effect is included. Upper Left:*$<\cos\chi>$*. Upper Right:*$<\sin\chi>$*.Down Left:*$<\cos\chi\cos\theta_e>$*.Down Right:*$<\sin\chi\cos\theta_e>$*.*

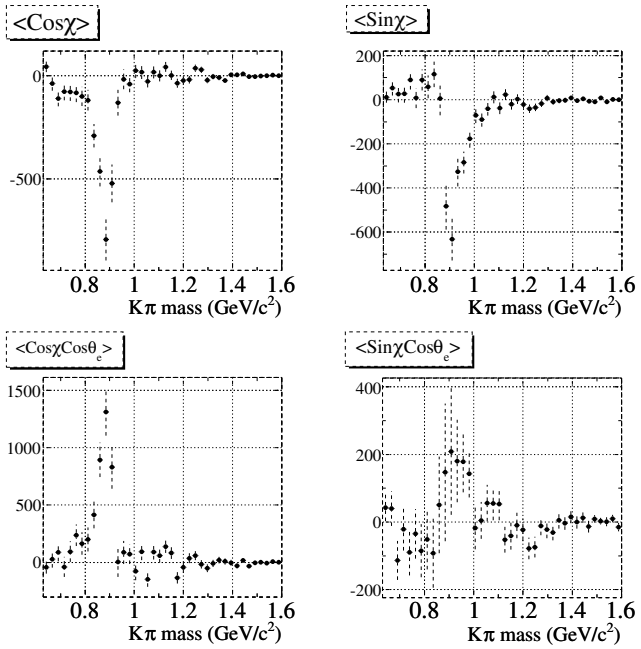

Figure 1.11: *Distributions versus the $K\pi$ mass for data events weighted by quantities that depend on angular variables, as in Figure 1.10. Upper Left:*$<\cos\chi>$*. Upper Right:*$<\sin\chi>$*.Down Left:*$<\cos\chi\cos\theta_e>$*. Down Right:*$<\sin\chi\cos\theta_e>$*.*

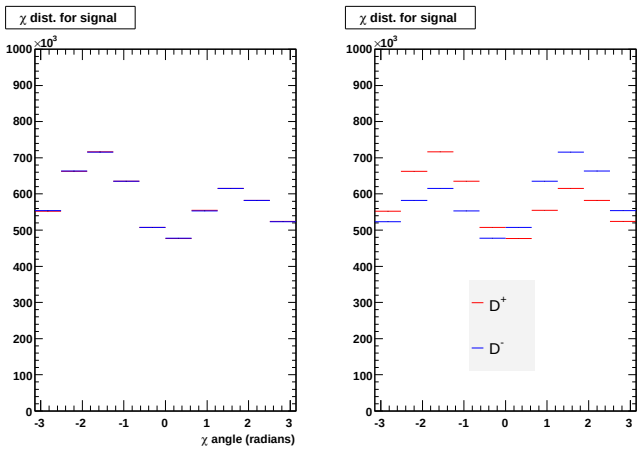

Figure 1.12: *Distribution of the χ angle for D^+ and D^- mesons. On the left plot, the sign of χ has been changed when analyzing D^- whereas it is left unchanged for the plot on the right.*

This factorized expression can be justified by the fact the q^2 dependence of the form factors is expected to be determined by the singularities which are nearest to the physical region defined by $q^2 \in [0,\ q^2_{max}]$. These singularities are poles or cuts situated at $M_H \sim$ 2.1-2.5GeV/c^2, depending on the form factor. In addition the variation range of q^2 is limited for the considered channel to $q^2 \simeq 1\ GeV^2$. Thus the proposed approach is equivalent to an expansion in $q^2/M_H^2 < 0.2$.

For the q^2 dependence we take a pole parameterization and try to determine the effective pole mass.

$$\begin{aligned} V(q^2) &= \frac{V(0)}{1-\frac{q^2}{m_V^2}} \\ A_1(q^2) &= \frac{A_1(0)}{1-\frac{q^2}{m_A^2}} \\ A_2(q^2) &= \frac{A_2(0)}{1-\frac{q^2}{m_A^2}} \end{aligned} \tag{1.57}$$

where $m_V = m_{D_s^*} = 2.112$ GeV/c^2 is the D_s^* mass and m_A is expected to be close to the $D_{s1} \sim 2.5$ GeV/c^2 mass.

In the following we measure ratios of these form factors evaluated at $q^2 = 0$: $r_V = \frac{V(0)}{A_1(0)}$ and $r_2 = \frac{A_2(0)}{A_1(0)}$, by studying the variation of the differential decay rate with the kinematic variables. The value of $A_1(0)$ is determined by measuring the $D^+ \to \bar{K^{*0}} e^+ \nu_e$ branching fraction.

For the mass dependence, in case of the $K^*(892)$, we use a Breit-Wigner distribution (note that it has a sign opposite to the one used by FOCUS, reminded in Eq. (1.41)).

$$A_{K^*(892)} = \frac{m_{K^*(892)}\Gamma^0_{K^*(892)} F_1(m)}{m^2_{K^*(892)} - m^2 - i m_{K^*(892)}\Gamma_{K^*(892)}(m)}. \tag{1.58}$$

In this expression:

- m is the $K\pi$ mass;
- $m_{K^*(892)}$ is the $K^*(892)$ pole mass;
- $\Gamma^0_{K^*(892)}$ is the total width of the $K^*(892)$ for $m = m_{K^*(892)}$;
- $\Gamma_{K^*(892)}(m)$ is the mass dependent $K^*(892)$ width:
  $\Gamma_{K^*(892)}(m) = \Gamma^0_{K^*(892)} \frac{p^*}{p_0^*} \frac{m_{K^*(892)}}{m} F_1^2(m)$;
- $F_1(m) = \frac{p^*}{p_0^*} \frac{B(p^*)}{B(p_0^*)}$ where B is the Blatt-Weisskopf damping factor: $B = 1/\sqrt{1 + r_{BW}^2 p^{*2}}$. r_{BW} is the barrier factor. p^* and p_0^* are evaluated at the mass m and $m_{K^*(892)}$ respectively and depend also on the masses of the $K^*(892)$ decay products.

In the denominator of Eq. (1.58) the width $\Gamma_{K^*(892)}(m)$ is the total width of the resonance whereas, in the numerator, only appears the dependence related to the studied decay channel. Thus, considering that according to isospin conservation the $K^*(892)$ decays into a charged pion in 2/3 of the cases:

$$\Gamma_{K^*(892)}(m) = \Gamma^0_{K^*(892)} \left[\frac{2}{3} \frac{p^*}{p_0^*} \frac{m_{K^*(892)}}{m} F_1^2(m) + \frac{1}{3}(\text{ now for } K^0\pi^0) \right] \tag{1.59}$$

(1.60)

1.3.5 S-wave parameterization for $\mathcal{F}_{10}$

In a similar way as for the P-wave we would like to have the correspondance between $\mathcal{F}_{10}$ and the invariant form factor.

In an S-wave, only the helicity H_0 form factor is contributing and we take:

$$\mathcal{F}_{10} = p_{K\pi} m_D r_S \frac{1}{1 - \frac{q^2}{m_A^2}} A_S(m^2). \tag{1.61}$$

The fact that $\mathcal{F}_{10}$ is proportional to $p_{K\pi}$ is needed to ensure that the corresponding decay rate varies as $p^3_{K\pi}$ as expected from the L=1 angular momentum between the virtual W and the S-wave $K\pi$ hadronic state.
Because the q^2 variation of the form factor is expected to be determined by the contribution of $J^P = 1^+$ $c\bar{s}$ states, we use the same q^2 dependence as for A_1 and A_2.

$A_S(m^2)$ corresponds to the mass dependent amplitude (LASS expression, Breit-Wigner...).

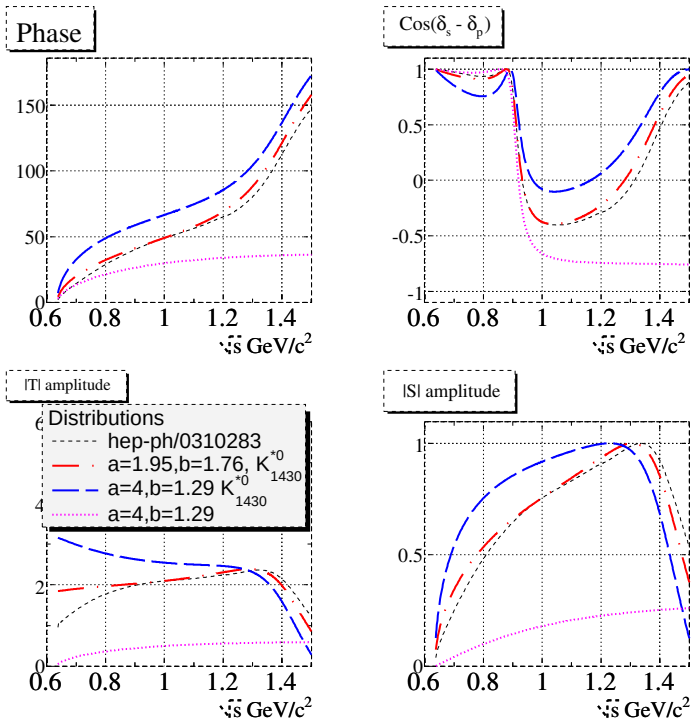

Figure 1.13: *Upper left: S-wave phase variation with energy for several values of LASS parameters. Upper right: Variation of the cosine of the phase difference between S and P-waves versus the $K\pi$ mass. Lower left: Variation of the $|T|$ amplitude. Lower Right: Variation of unitary S-wave amplitude*

We introduce a dimensionless constant, r_S, which measures, in our notations, the importance of the S-wave amplitude.

- *LASS expression*

  When used in a decay process, where the 2-body phase space factor p^*/m is already explicit in the differential decay rate, the amplitude S measured by LASS has to be replaced by:

$$A_S = r_S \frac{m}{p^*} \sin\delta \exp i\delta. \tag{1.62}$$

  The phase is taken as the sum of two terms : $\delta = \delta^{1/2}_{BG} + \delta_{K^*_0(1430)}$ whose parameterizations are given in Eq. (1.27) and (1.28). In this approach it is considered that not only the phase but also the amplitude are the same in diffractive scattering and in charm semileptonic decays.

  In Figure 1.13, we show how the phase and the amplitude of the S-wave are expected to vary for different values of the parameters used in the LASS parameterization and also using the results from reference [18].

  In the present analysis as we observe very few events at large mass (above 1 $\mathrm{GeV/c^2}$), we have fixed the $K^*_0(1430)$ mass and width to 1.412 and 0.294 GeV/c^2 respectively.

- *A more general parameterization for the S-wave* The phase of the S-wave can be also measured in several

independent intervals (j) of the $K\pi$ mass without using an explicit parameterization:

$$A_S^j = r_S \frac{m}{p^*} \sin\delta_j \exp i\delta_j. \tag{1.63}$$

where the phase δ_j is expected to be constant within a given range (j) of the $K\pi$ mass.

- *Model independent parameterization for the S-wave*

  According to the Watson theorem, only the phase of the elastic scattering amplitude is the same as the phase measured in the corresponding decay process; there is no constraint on the amplitude.

  We have thus considered the following parameterization for the S-wave:

$$\begin{aligned} A_S^j &= r_S P(m) \exp i\delta_j,\ m(K\pi) < m_{K_0^*(1430)}; \\ A_S^j &= r_S P(m_{K^{*0}(1430)}) \sqrt{\frac{(m_{K_0^*(1430)}\Gamma_{K_0^*(1430)})^2}{(m^2_{K_0^*(1430)} - m^2)^2 + (m_{K_0^*(1430)}\Gamma_{K_0^*(1430)})^2}} \exp i\delta_j,\ m(K\pi) > m_{K_0^*(1430)}. \end{aligned} \tag{1.64}$$

  where $P(m) = 1 + r_S^{(1)} \times x + r_S^{(2)} \times x^2 + ...$ and $x = \sqrt{(\frac{m(K\pi)}{m_K + m_\pi})^2 - 1}$. The coefficients $r_S^{(i)}$ have no dimension. This amplitude has a polynomial variation with the $K\pi$ mass below the $K_0^*(1430)$ and it decreases, above, according to the behaviour given by the $K_0^*(1430)$ Breit-Wigner expression. This last hypothesis is not crucial as few events are present in this mass region. The phase is measured in several intervals of the $K\pi$ mass and coefficients of the polynomial expression are also fitted.

1.3.6 D-wave parameterization

Expressions for the form factors $\mathcal{F}_{i,2}$ entering in Eq. 1.47 are given below[27]:

$$\begin{aligned} \mathcal{F}_{12} &= \frac{m_D p_{K\pi}}{3} \left[\left(m_D^2 - m_{K\pi}^2 - q^2\right)(m_D + m_{K\pi})\, T_1(q^2) - \frac{4m_D^2 p_{K\pi}^2}{m_D + m_{K\pi}} \left(T_2(q^2) + T_3(q^2)\right) \right], \\ \mathcal{F}_{22} &= \sqrt{\frac{2}{3}} m_D m_{K\pi} q p_{K\pi} (m_D + m_{K\pi})\, T_1(q^2), \\ \mathcal{F}_{32} &= \sqrt{\frac{2}{3}} \frac{2m_D^2 m_{K\pi} q p_{K\pi}^2}{(m_D + m_{K\pi})} T_V(q^2). \end{aligned} \tag{1.65}$$

These expressions are multiplied by a relativistic Breit-Wigner amplitude which corresponds to the $K_2^*(1430)$:

$$A_{K_2^*(1430)} = \frac{m_{K_2^*(1430)} \Gamma^0_{K_2^*(1430)} F_2(m)}{m^2_{K_2^*(1430)} - m^2 - i m_{K_2^*(1430)} \Gamma_{K_2^*(1430)}(m)}. \tag{1.66}$$

In this expression:

- m is the $K\pi$ mass;
- $m_{K_2^*(1430)}$ is the $K_2^*(1430)$ pole mass;
- $\Gamma^0_{K_2^*(1430)}$ is the total width of the $K_2^*(1430)$ for $m = m_{K_2^*(1430)}$;
- $\Gamma_{K_2^*(1430)}(m)$ is the mass dependent $K_2^*(1430)$ width:
  $\Gamma_{K_2^*(1430)}(m) = \Gamma^0_{K_2^*(1430)} \frac{p^*}{p_0^*} \frac{m_{K_2^*(1430)}}{m} F_2^2(m)$;
- $F_2(m) = \left(\frac{p^*}{p_0^*}\right)^2 \frac{B_2(p^*)}{B_2(p_0^*)}$ where B_2 is the Blatt-Weisskopf damping factor:

$$B_2 = 1/\sqrt{\left(r_{BW}^2 p^{*2} - 3\right)^2 + 9 r_{BW}^2 p^{*2}}, \tag{1.67}$$

  r_{BW} is the barrier factor. p^* and p_0^* are evaluated at the mass m and $m_{K_2^*(1430)}$ respectively.

The form factors $T_i(q^2)$ (i=1,2,3,V) are parameterized assuming the Single pole model with corresponding axial or vector poles. Furthermore, at present, we assume (improperly) that $T_3(0) = 0$ [2].

1.4 Comparison with $Ke4$ decays

We have used the same basic formalism developed for $Ke4$ [36, 37] to analyze $De4$ decays. There are two main differences between the two decay channels:

- the hadronic system is $K\pi$ instead of $\pi\pi$ but, over essentially all the accessible mass distribution in the corresponding decays, the two systems remain in the elastic regime. The hadronic phase measured in elastic scattering or in semileptonic decays is thus expected to be the same;
- pions emitted in $Ke4$ decays remain rather soft and results from chiral perturbation theory can be used. In $De4$ decays, the available phase space is larger, chiral perturbation theory remains valid in the region close to threshold but hadronic resonances are also produced.

In 1977, 30,000 $Ke4$ decays of charged kaons were measured at CERN [28] . Recent experiments have analyzed about half a million of such decays. At BNL, the E865 experiment, measures 400,000 decays [29] and at CERN, NA48/2 has published results based on 670,000 decays [30].

For sake of clarity we present the definition of the angular variables in this analysis in Figure 1.14

[2] In practice the D-wave analysis was not completed in time for this document.

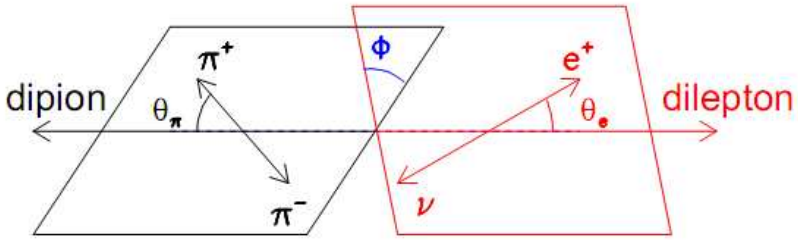

Figure 1.14: *Definition of the angular variables for Ke4 analysis.*

Form factors used generally in these analyses are labeled F, G and H. They can be related to those defined in Equation 1.47:

$$\begin{aligned} \mathcal{F}_1 &= XF + \beta\frac{1}{2}(m_K^2 - m^2 - q^2)\cos\theta_\pi G \\ \mathcal{F}_2 &= \beta m q G \\ \mathcal{F}_3 &= \beta X m q \frac{H}{m_K^2} \end{aligned} \tag{1.68}$$

G and H form factors define the P-wave contribution whereas the F form factor determines the S-wave: $\mathcal{F}_{10} = XF$. Variables $\beta,\ X,\ q$ have the same definition as in Section 1.3 whereas $m = m(\pi\pi)$. As the phase space available in K semileptonic decays is small and as the physical region, in terms of $m(\pi\pi)$ or q^2, is far from singularities (poles in the q^2 variation of form factors or in Breit-Wigner mass distributions), form factors are expanded in terms of these variables. For the F form factor, this gives:

$$F = \left[f_s + f_s'\left(\frac{p^*}{m_\pi}\right)^2 + f_s''\left(\frac{p^*}{m_\pi}\right)^4 + f_l\frac{q^2}{4m_\pi^2}\right]e^{i\delta_0^0(m_{\pi\pi}^2)} \tag{1.69}$$

f_s, f_s', f_s'' and f_l are dimensionless constants. δ_0^0 is the scattering phase shift in the S-wave with I=0.

We can define δ_0^0 in the following way [29],[31]:

$$\tan\delta_l^I = \sqrt{1 - \frac{4m_\pi^2}{m_{\pi\pi}^2}q^{2l}(A_l^I + B_l^I q^2 + ...)} \times \left(\frac{4m_\pi^2 - s_l^I}{s_\pi - s_l^I}\right) \tag{1.70}$$

where $s_\pi = m_{\pi\pi}^2$. From the so-called Roy equations, one can express the parameters (A_l^I, B_l^I) as a function of the I=0 and I=2 S-wave $\pi-\pi$ scattering lengths [32]. The other parameter, s_0^0, slowly varies with the scattering length and can be taken as constant[32].

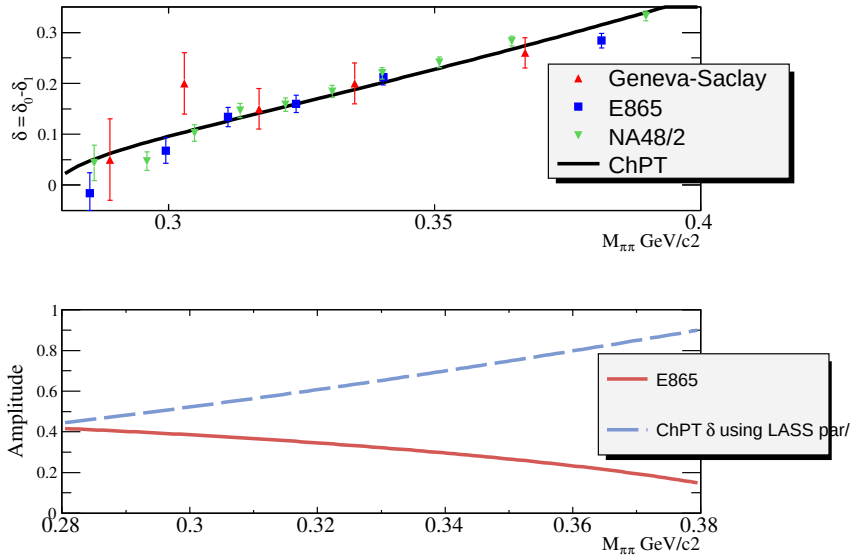

Figure 1.15: Upper plot: Ke4 results for the phase shift variation and estimations coming from ChPT for $\pi\pi$ scattering. Lower plot: Comparison of the measured S-wave amplitude (=XF,using eq. 1.68) as compared to amplitude used often in D decays ($\frac{m_{\pi\pi}}{p^*}\sin\delta_0^0$)

The validation of Watson's theorem in this decay channel is presented in the upper plot of Figure 1.15, where the predictions of Chiral Perturbation Theory for the phase variation in $\pi-\pi$ scattering are compared to the phase variation of the S-wave in Ke4 decays[3]. In the lower plot we compare the E865 measured S-wave amplitude to the one expected using equation 1.40.

It can be noted that the amplitude for the S-wave measured by the Ke4 experiments is incompatible with the amplitude using equation 1.40. These experiments validate Watson's theorem and show that there is no direct connexion between the moduli of the $\pi-\pi$ scattering amplitude and the $\pi-\pi$ S-wave amplitude in Ke4 decays.

1.5 Expected distributions for P and S+P components

In Figure 1.16 have been compared projected distributions over the 5 kinematic variables obtained for a pure P-wave and an S+P-wave. For the P-wave we use $R_V = 1.6$, $R_2 = 0.8$, $m_V = 2.1$ GeV/c^2 and $m_A = 2.5$ GeV/c^2. For the S-wave we use the LASS parameterization with $a_S = 2\ GeV^{-1}$ and $b_S = 3\ GeV^{-1}$. The assumed S-wave decay rate fraction, 4.16%, is close to the final measurement and corresponds to $r_S = 0.25$.

In the mass distribution, an excess of events corresponding to the S-wave is observed below the $K^*(892)$ and around 1.4 GeV/c^2, the latter originating from the $K_0^*(1430)$. The enhancement at large mass is expected to be difficult to measure as the decay rate is rapidly decreasing versus the $K\pi$ mass and also because of the background level (in real data). Distributions of the other variables are dominated by contributions from events situated in the $K^*(892)$ region. To illustrate how these distributions are expected to change versus the mass of

[3]The ChPT phase curve corresponds only to δ_0^0. Although non zero, the δ_1^1 phase variation is quite small in this mass range and we neglect it.

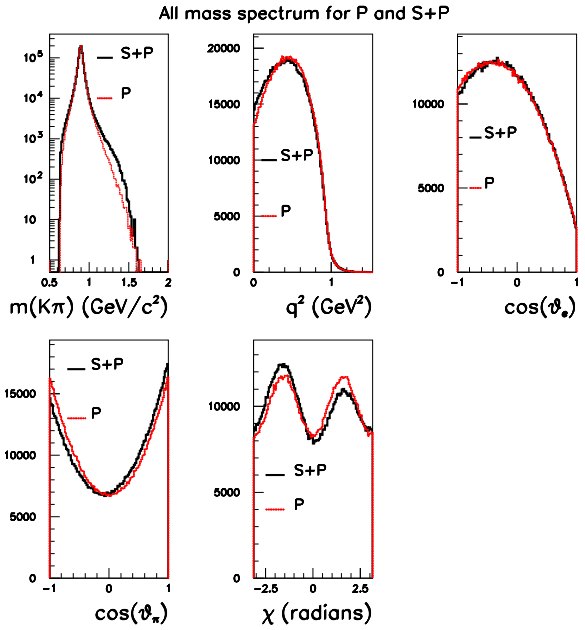

Figure 1.16: *Comparison between decay rates expected for a pure P-wave and an S+P-wave. Projections over the 5 kinematic variables are given. The presence of the S-wave creates asymmetries in* $\cos(\theta_\pi)$ *and* χ *distributions.*

the $K\pi$ system, five mass intervals have been considered:

- $m < 0.85$ GeV/c^2: below the $K^*(892)$ region;
- $m \in [0.85,\ 0.896]$ GeV/c^2: in the $K^*(892)$ region, below the mass pole;
- $m \in [0.896,\ 0.95]$ GeV/c^2: in the $K^*(892)$ region, above the mass pole;
- $m \in [0.95,\ 1.20]$ GeV/c^2: between the two K^* resonances;
- $m \in [1.20,\ 1.43]$ GeV/c^2: in the $K^*(1430)$ region, below its mass pole;
- $m > 1.43$ GeV/c^2: in the $K^*(1430)$ region, above its mass pole;

q^2 distributions obtained for the different mass intervals are displayed in Figure 1.17. The S-wave gives more events at low q^2 values for two reasons. There could be an S-wave component at large mass, corresponding to the $K^*(1430)$, for which the q^2 distribution is restricted to low values by kinematics. The second reason is that the differential decay rate corresponding to the S-wave component has a $p^{*3}_{K\pi}$ dependence and is thus maximal at $q^2 = 0$.

$\cos(\theta_e)$ distributions are given in Figure 1.18. The S-wave component gives more events around zero, as expected from its variation, proportional to $\sin^2\theta_e$.

Interference between the S and P-waves creates asymmetries in the distributions of $\cos(\theta_\pi)$ (Figure 1.19) and χ (Figure 1.20) variables.

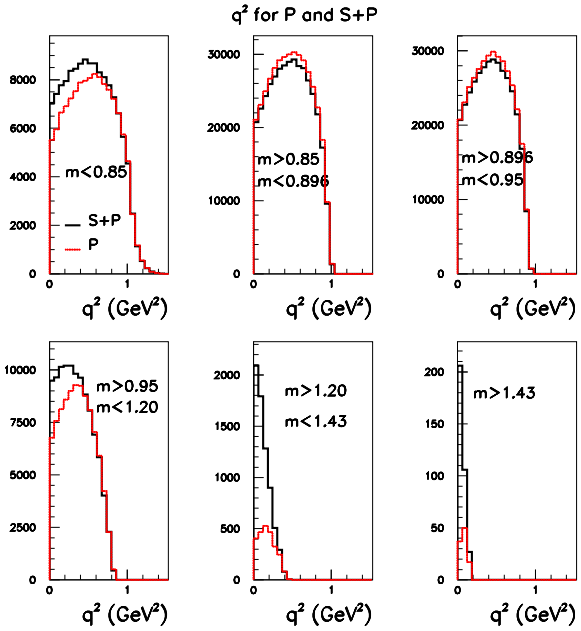

Figure 1.17: *Comparison between P and S+P waves: q^2 distributions expected for different $K\pi$ mass intervals.*

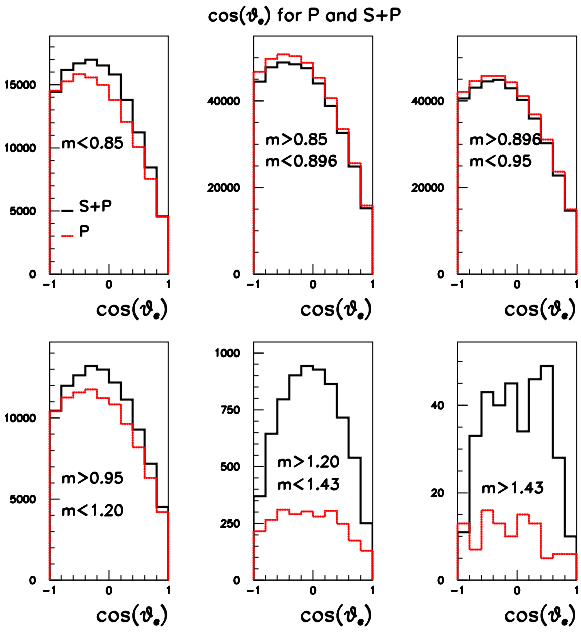

Figure 1.18: *Comparison between P and S+P waves: $\cos(\theta_e)$ distributions expected for different $K\pi$ mass intervals.*

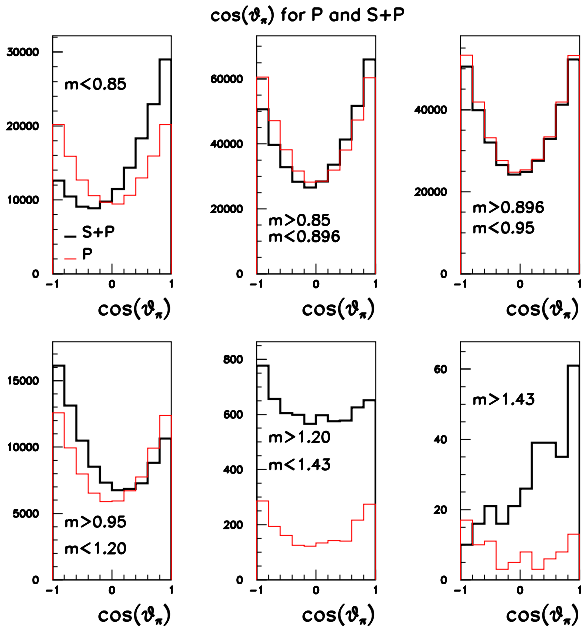

Figure 1.19: *Comparison between P and S+P waves:* $\cos(\theta_\pi)$ *distributions expected for different* $K\pi$ *mass intervals.*

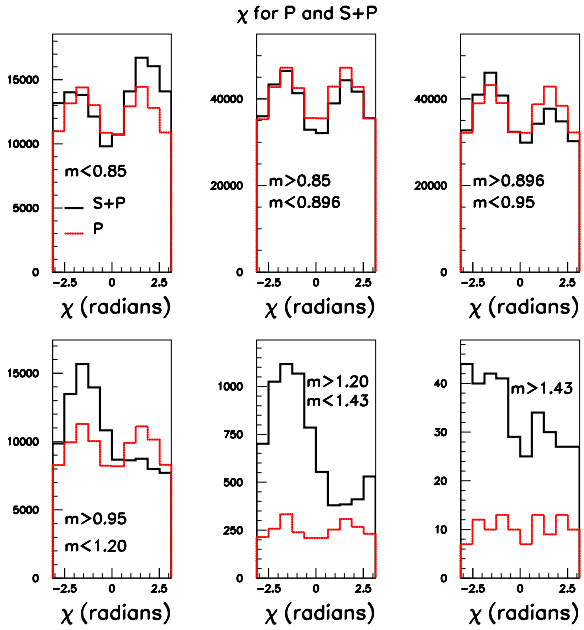

Figure 1.20: *Comparison between P and S+P waves:* χ *distributions expected for different* $K\pi$ *mass intervals.*

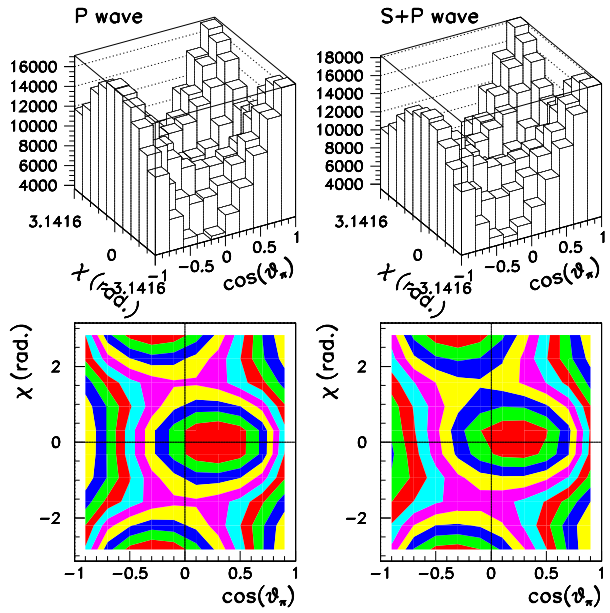

Figure 1.21: *2d-distributions of the differential decay rate on the plane* $(\cos\theta_\pi - \chi)$*. On the left only a P-wave is considered whereas, on the right, the S-wave is added.*

The effect of the S-wave is illustrated in Figure 1.21 which gives the projection of the differential decay rate on the plane $(\cos\theta_\pi - \chi)$. Plots on the left correspond to a pure P-wave whereas those on the right include the S-wave component.

1.6 Expected distributions for S+P and S+P+P′ components

The P-wave amplitude is taken as the sum of the $K^*(892)$ and $K^*(1410)$.

$$A(m) = A_{K^*(892)} + r_{01} \exp i(\phi_{01}) * A_{K^*(1410)} \tag{1.71}$$

and it is assumed that the form factors $H_{\pm,0}$ are the same for the two resonances. As the $K^*(1410)$ is a vector state, the helicity form factors contain the same kinematic terms as for the $K^*(892)$. The present hypothesis is thus equivalent in assuming that form factors $A_{1,2}$ and V are the same for the two resonances.

For the modulus of the $K^*(1410)$ amplitude and its phase, relative to the $K^*(892)$, we have first considered measurements obtained in τ decays [40]. They have measured a relative phase of $\phi_{01} = (1.44 \pm 0.15)\ rad.$ between the two states (this value is compatible with 90 degrees). Correcting for the difference in normalisation for Breit-Wigner amplitudes used in [40] and in the present analysis we estimate that 0.05% of $D^+ \to K^-\pi^+e^+\nu_e$ events can originate from $K^*(1410)$ decays.

In the following, to illustrate the possible effect of the $K^*(1410)$ amplitude we have increased its contribution, relative to the $K^*(892)$, such that it corresponds to a 0.5% rate fraction for $\phi_{01} = 90^\circ$ (an order of magnitude

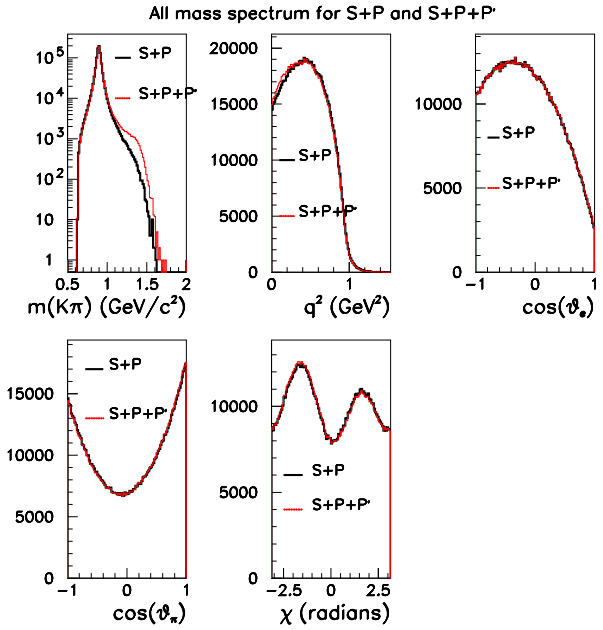

Figure 1.22: *Comparison between the decay rates expected for a S+P-wave and an S+P+P′ wave. Projections over the 5 kinematic variables are given. The presence of the P′ wave is mainly visible in the mass projection.*

ϕ_{01} (degrees)	-180	-135	-90	-45	0	45	90	135	180
P′ fraction (%)	1.01	0.41	0.54	1.22	1.03	0.37	0.46	1.06	1.01
S fraction (%)	4.09	4.31	4.45	4.35	4.12	3.93	3.80	3.87	4.09
P fraction (%)	94.92	95.31	95.04	94.46	94.88	95.73	95.77	95.09	94.92

Table 1.9: *Expected relative rates for S and P′ components for different values of the relative hadronic phase between the $K^*(892)$ and $K^*(1410)$ resonances.*

higher than expected from τ decays).

In Figure 1.22 have been compared projected distributions over the 5 kinematic variables when the first radial $s\bar{d}$ excitation is added to the S+P-wave. Apart for the mass all other distributions are rather similar. This is expected because the $K^*(1410)$ having the same $J^P = 1^-$ as the dominant $K^*(892)$, all helicity amplitudes have the same structure. The effect of the radial excitation can be observed in angular distributions if one selects events at large mass ($> 1.$ GeV/c^2 typically). Interference between the S and P′ waves generates asymmetries in $\cos(\theta_\pi)$ and χ distributions as given in Figure 1.23 and 1.24 respectively.

These distributions, obtained with $\phi_{01} = 90°$, depend on the value of the global hadronic phase (ϕ_{01}) between the $K^*(892)$ and the $K^*(1410)$ as illustrated in Figure 1.25, 1.26 which are obtained for events with a $K\pi$ mass selected between 1.20 and 1.43 GeV/c^2. Table 1.9 gives the variation of the fraction of the decay rate corresponding to the $K^*(1410)$ with this phase.

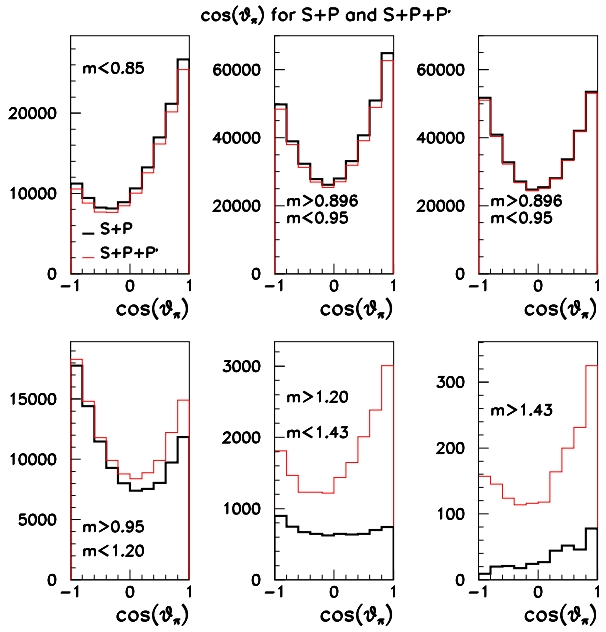

Figure 1.23: *Comparison between S+P and S+P+P′ waves:* $\cos(\theta_\pi)$ *distributions expected for different* $K\pi$ *mass intervals.*

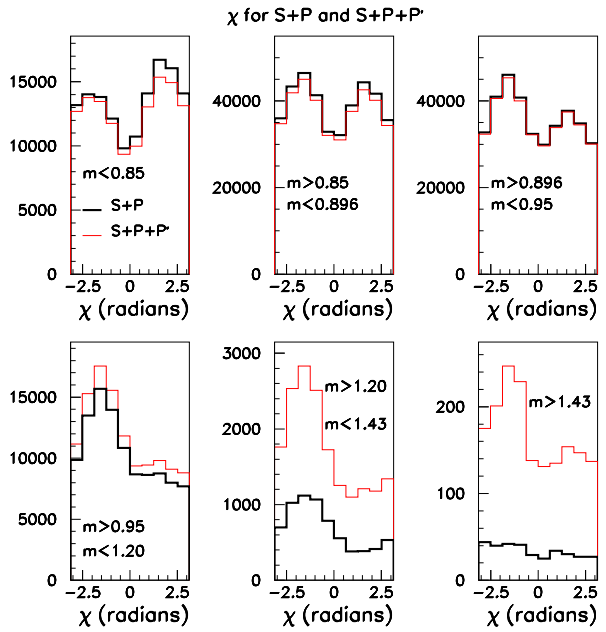

Figure 1.24: *Comparison between S+P and S+P+P′ waves:* χ *distributions expected for different* $K\pi$ *mass intervals.*

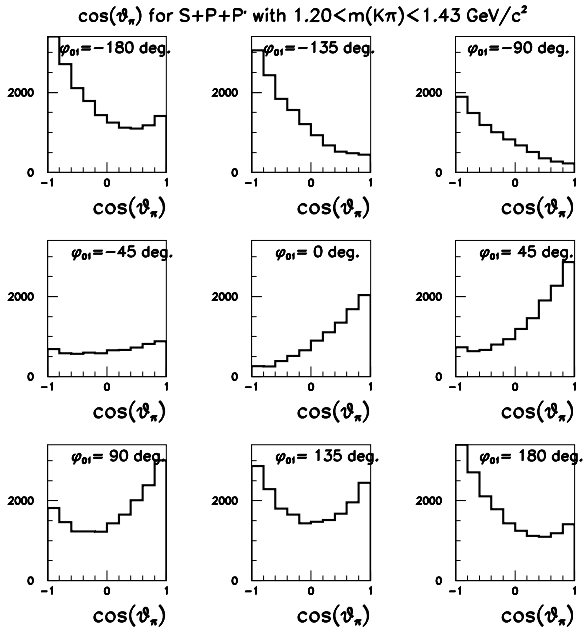

Figure 1.25: *Comparison between S+P and S+P+P′ waves:* $\cos(\theta_\pi)$ *distributions for events with an invariant* $K\pi$ *mass between 1.20 and 1.43* $\mathrm{GeV/c^2}$ *and for different values of the hadronic phase between the two* K^* *states.*

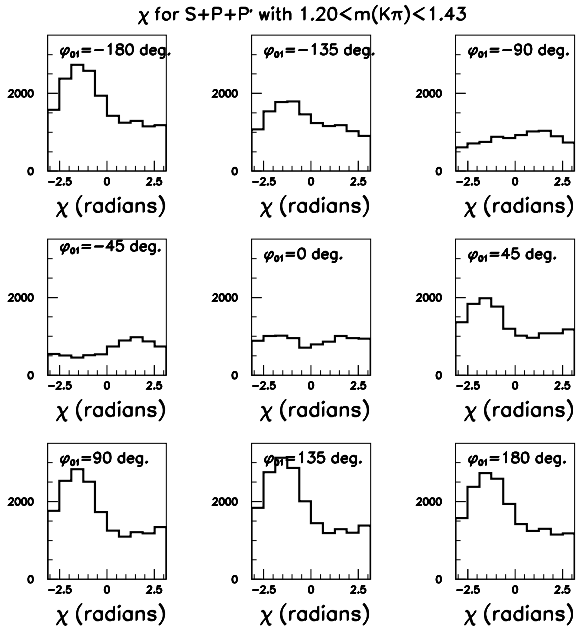

Figure 1.26: *Comparison between S+P and S+P+P′ waves:* χ *angle distributions for events with an invariant* $K\pi$ *mass between 1.20 and 1.43* $\mathrm{GeV/c^2}$ *and for different values of the hadronic phase between the two* K^* *states.*

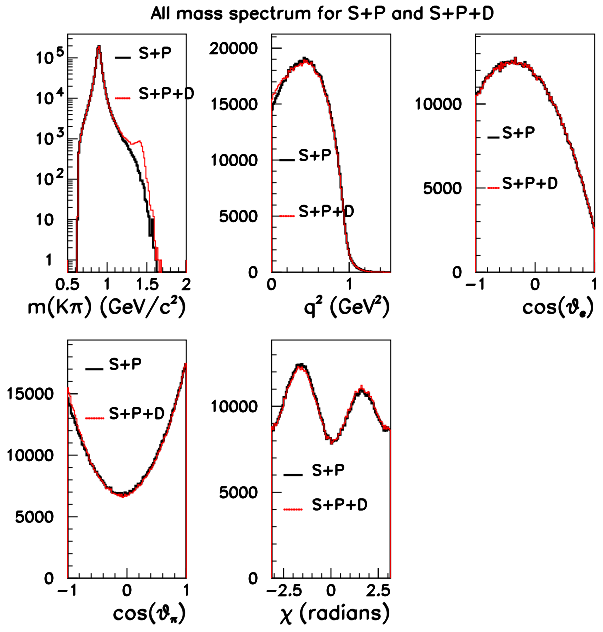

Figure 1.27: *Comparison between the decay rates expected for a S+P-wave and an S+P+D-wave. Projections over the 5 kinematic variables are given. The presence of the D-wave is mainly visible in the mass projection.*

1.7 Expected distributions for S+P and S+P+D components

Conversely to the P′, the three form factors $\mathcal{F}_{i2}$ have expressions that differ from those corresponding to Eq. (1.49, 1.51). They are given in Eq. (1.66).

In the following, it is assumed that the D-wave, originating from the $K_2^*(1430)$, has 1% contribution to the considered $K^-\pi^+$ final state. It is assumed also that the global phase ϕ_{02} of this state, relative to the $K^*(892)$, is equal to zero. This is justified by the fact that, at threshold, S, P and D-wave phases are expected to be zero.

In Figure 1.27 have been compared projected distributions over the 5 kinematic variables when the D-wave is added to the S+P-wave. In this case also, Apart for the mass, all other projected distributions are rather similar. This comes from the fact that the effect of the D-wave enters essentially at high values of the $K\pi$ mass.

The effect of the D-wave can be observed in angular distributions if one selects events at large mass ($>$ 1. $\mathrm{GeV/c^2}$ typically). Interference between the S and D-waves generates asymmetries in $\cos(\theta_\pi)$ and χ distributions as given in Figure 1.28 and 1.29 respectively.

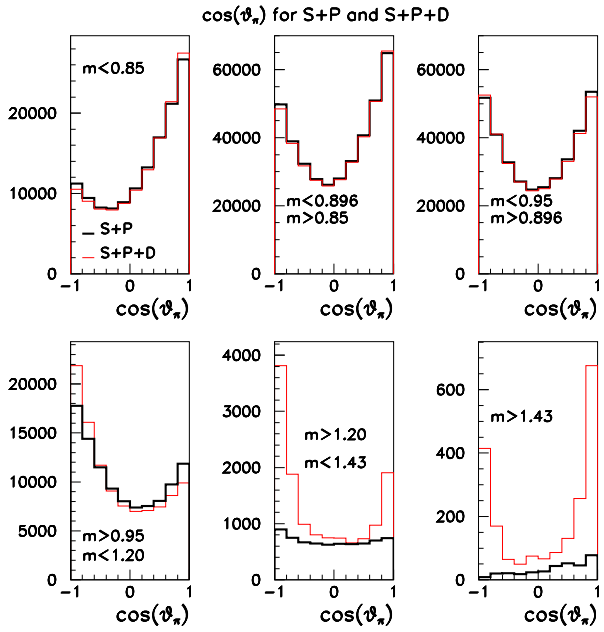

Figure 1.28: *Comparison between S+P and S+P+D waves:* $\cos(\theta_\pi)$ *distributions expected for different* $K\pi$ *mass intervals.*

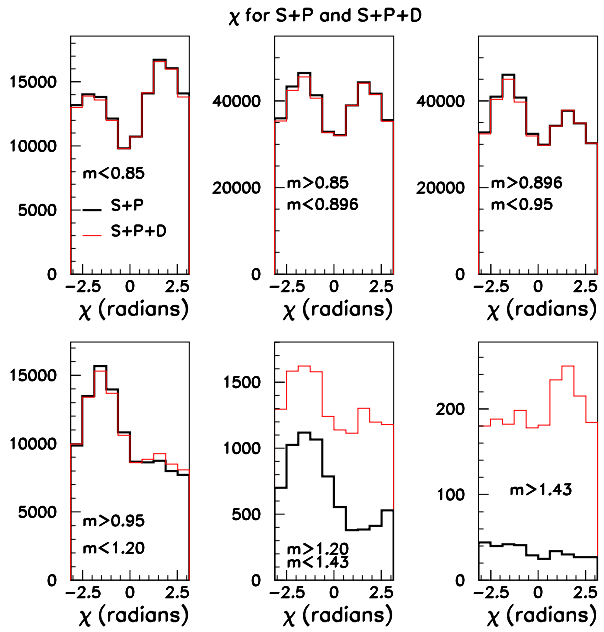

Figure 1.29: *Comparison between S+P and S+P+D waves:* χ *distributions expected for different* $K\pi$ *mass intervals.*

Chapter 2

The *BABAR* Experiment

The *BABAR* experiment, located at the SLAC National Accelerator Laboratory (SLAC) in California, has been optimized for the systematic study of *CP* violation in the B meson system. The experiment consists of a detector [45] built around the interaction region of the high luminosity e^+e^- asymmetric collider PEP-II [46]. The geometry of the detector as well as the technical requirements of its main components have been designed in order to obtain the cleanest environment and the best efficiency to reconstruct the B meson decays.
Despite being optimized for this purpose the experiment is responsible for a wide variety of analysis. The scientific program of BaBar consists of, besides CP violation studies in the B sector, analysis ranging from searches for rare B decays, CP violation studies in the D sector, meson spectroscopy searches, semileptonic decays in the B and D sector, just to name some important examples.

In this chapter we describe the main features and performances of PEP-II and the *BABAR* detector.

2.1 The PEP-II accelerator

The PEP-II B-Factory is an asymmetric-energy e^+e^- collider designed to operate at a center of mass energy of $E_{CM} = 10.58\,\mathrm{GeV}$, corresponding to the mass of the $\Upsilon(4S)$ vector meson resonance. The $\Upsilon(4S)$ has a mass slightly above the $B\bar{B}$ threshold, and thus it decays almost exclusively into $B\overline{B}^0$ or B^+B^- pairs.
The e^+e^- collisions create either pairs of quark-antiquark continuum events as well as lepton pairs. The cross sections for the main physics processes in PEP-II are listed in Table 2.1. There is a large amount of charm quark pairs produced at the energy of the $\Upsilon(4S)$. All the events created at this energy are from now on called On-Peak events.
To study specifically processes coming from continuum events, part of the data is collected at a center of mass energy 40 MeV below the $\Upsilon(4S)$ peak, where $B\bar{B}$ production is not allowed. This data sample corresponds to about $1/10$ of the sample taken at the $\Upsilon(4S)$ peak. We call these Off-Peak events.

If the $\Upsilon(4S)$ is produced at rest, then the B mesons would have an average residual momentum of the order of $\sqrt{(M_{\Upsilon(4S)}/2)^2 - M_B^2} \sim 325\,\mathrm{MeV}/c$ [1]. With this momentum, the average distance covered by a B meson would be of the order of [2] $\beta\gamma c\tau_B \sim 30\mu m$ and it would be experimentally very difficult to measure the separation

[1] We use $M_{\Upsilon(4S)}$ =10.58 GeV/c^2 and $M_B = 5.28$ GeV/c^2.
[2] The factor $\beta\gamma$ arising from a momentum of the B of 325 MeV/c is $\beta\gamma \sim 0.061$ and the B meson lifetime is $\tau_B = (1.530 \pm 0.009) \times$

between the decay points of the two B mesons.

The PEP-II machine collides a 9.0 GeV electron beam head-on with a 3.1 GeV positron beam. In this way the Lorentz boost of the $\Upsilon(4S)$ is $\beta\gamma = \frac{E_{e^-} - E_{e^+}}{E_{CM}} \sim 0.56$, resulting in an average separation between the two B meson of the order of 250 μm, compatible with the *BABAR* vertex resolution, as shown in the following.

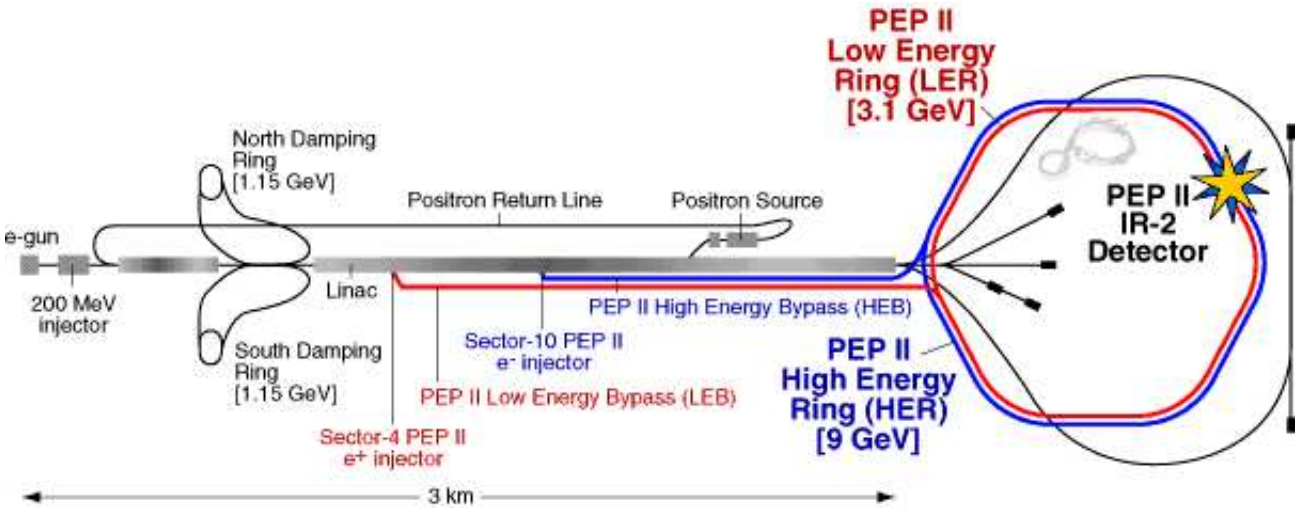

Figure 2.1: Overview of the PEP-II B-Factory. *BABAR* is situated at the IR2 position

An overview of the accelerator is shown in Fig. 2.1.

Electrons and positrons are accelerated in the 3.2 km long SLAC linac and accumulated into two 2.2 km long storage rings, called HER (high-energy ring, in which the electrons circulate) and LER (low-energy ring, in which the positrons, produced in the linac by collisions of 30 GeV electrons on a target, circulate).

In proximity of the interaction region the beams are focused by a series of offset quadrupoles (labelled Qx) and bent by means of a pair of dipole magnets, which allow the bunches to collide head-on and then to separate. The tapered B1 dipoles, located at $\pm$ 21 cm on either side of the interaction point (IP), and the Q1 quadrupoles operate inside the field of the *BABAR* superconducting solenoid, while Q2, Q4, and Q5, are located outside or in the fringe field of the solenoid (Fig. 2.2). The interaction region is enclosed in a water-cooled beam pipe consisting of two thin layers of beryllium with a water channel in between. Its outer radius is about 28 mm. The total thickness of the central beam pipe section at normal incidence corresponds to 1.06 % of a radiation length.

The beam pipe, the permanent magnets and the Silicon Vertex Tracker (SVT) are assembled, aligned and then enclosed in a 4.5 m long support tube. This rigid structure is inserted into the *BABAR* detector, spanning the IP.

The *BABAR* data taking, started with the first collisions in PEP-II at the end of 1999 and ended April 7th 2008. *BABAR* has recorded an integrated luminosity of about 531 fb^{-1}, including about 54 fb^{-1} just below the $\Upsilon(4S)$ resonance, 433 fb^{-1} recorded at the $\Upsilon(4S)$ and 44 fb^{-1} at other Υ resonances. The *BABAR* recorded luminosity until the end of data taking is shown in Fig. 2.3.

$10^{-12} s$[14].

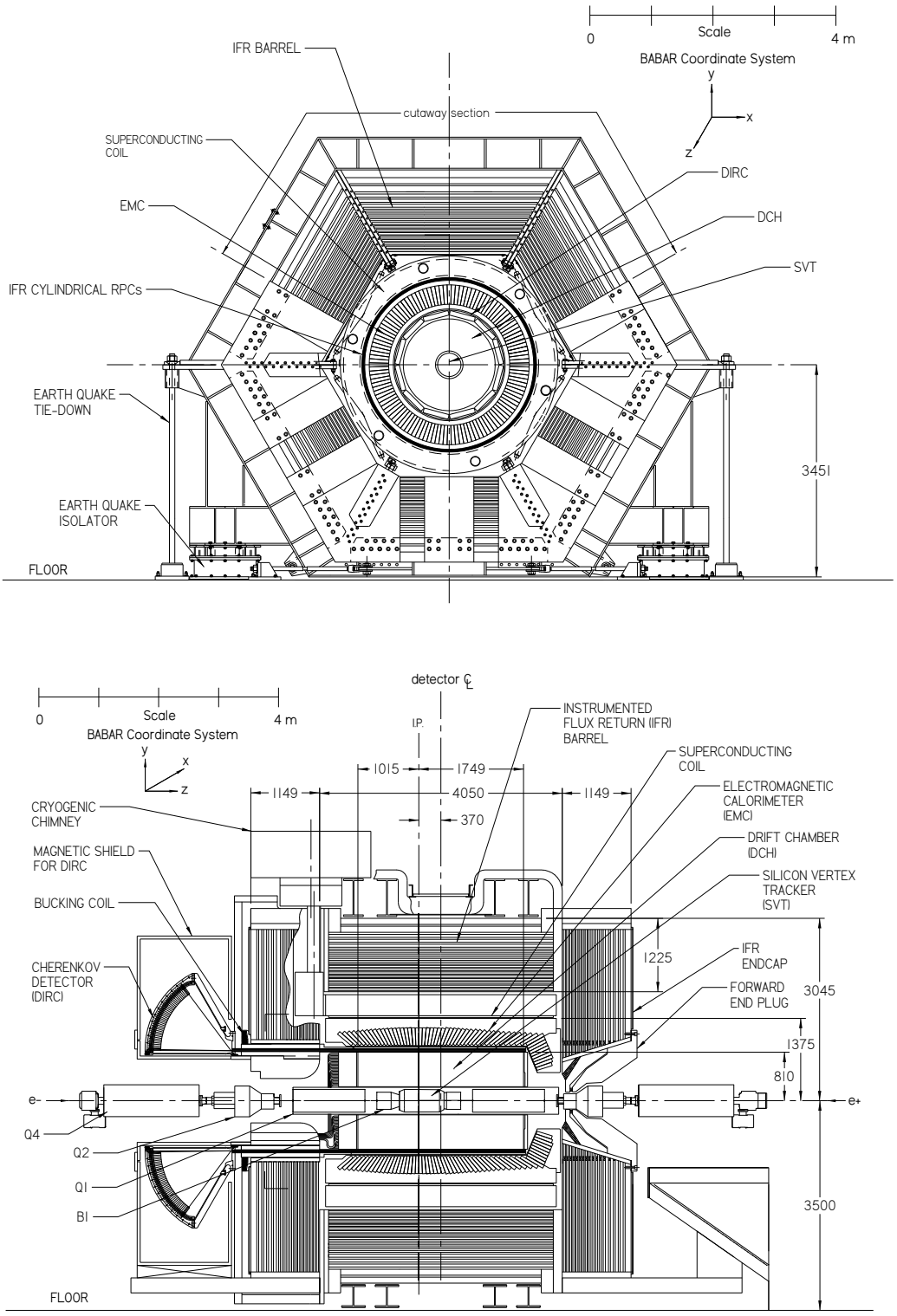

Figure 2.2: *BABAR* detector front view (top) and side view (bottom).

Event	Cross section (nb)
$b\bar{b}$	1.05
$c\bar{c}$	1.30
$s\bar{s}$	0.35
$u\bar{u}$	1.39
$d\bar{d}$	0.35
e^+e^-	∼53
$\mu^+\mu^-$	1.16
$\tau^+\tau^-$	0.94

Table 2.1: *Cross sections of the main physics processes at the $\Upsilon(4S)$. The cross section for e^+e^- refers to events with at least one charged track $e^{\pm}$ inside the electromagnetic calorimeter detection volume.*

Parameters	Design	2008 Records
Energy HER/LER (GeV)	9.0/3.1	9.0/3.1
Current HER/LER (A)	0.75/2.15	2.1/3.2
# of bunches	1658	1722
Bunch length (mm)	15	11–12
Peak Luminosity ($10^{33} cm^2/s$)	3	12
Integrated luminosity (pb^{-1}/day)	135	911

Table 2.2: PEP beam parameters. Values are given both for the design and for the records achieved during 2008.

PEP-II surpassed its design performances, both in terms of the instantaneous luminosity and the daily integrated luminosity (see Tab. 2.2), achieving a peak value of $1.2 \times 10^{34}\ cm^{-2}\ s^{-1}$ during Run 6. A significant improvement to the integrated luminosity has been achieved between December 2003 and March 2004 with the implementation of a novel mode of operation of PEP-II, called "trickle injection". Until the end of 2003, PEP-II typically operated in a series of 40-minute fills during which the colliding beams coasted: at the end of each fill, three to five minutes were needed to replenish the beams for the next fill. During this period, the *BABAR* data acquisition system had to be turned off for detector safety. With the new technique, the *BABAR* detector can keep taking data virtually uninterrupted while the linac continuously injects electron and positron bunches (at a rate up to 10 Hz in the HER and 20Hz in the LER) into the two PEP-II storage rings. This novel mode of operation allows an increase of 20 to 30% of the integrated luminosity. Moreover, the continuous injection makes the storage of particles more stable, so that PEP-II rings are easier to operate and beam losses are far less frequent than with the previous operational mode. This result is very important since, after a loss of the stored beams, it takes approximately 15 minutes to refill the two beams during which obviously no data taking is allowed.
The luminosity is measured by PEP-II with radiative Bhabha scattering, while BaBar measures it offline, taking advantage of QED processes, like $e^+e^-, \mu^+\mu^-$ pairs.

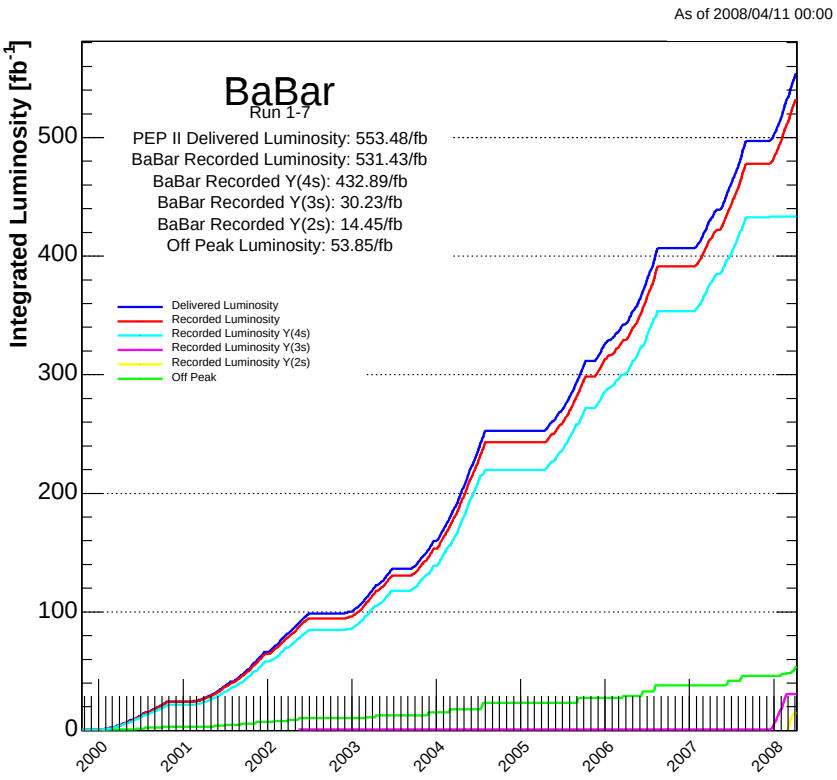

Figure 2.3: Approximate PEP-II delivered and *BABAR* recorded integrated luminosity in Run 1 to Run 7 (from October 1999 to April 2008).

2.2 The *BABAR* detector

The design of the *BABAR* detector is optimized for CP violation studies, but it is also well suited to do precision measurements in other B and non B physics. To achieve the goal of performing accurate measurements there are many requirements:

- a large and uniform acceptance, in particular down to small polar angles relative to the boost direction, to avoid particle losses. Although the boost originated by the asymmetric beams is not a big one, optimizing the detector acceptance leads to an asymmetric detector;
- a good vertex resolution;
- an excellent detection efficiency and an excellent precision on the momentum measurement for charged particles with transverse momentum ranging between 60 MeV/c and 4 GeV/c ;
- excellent energy and angular resolution for photons and π^0 s with energy down to 20 MeV and up to 5 GeV ;

- a good discrimination between e, μ, π, K and p over a wide kinematic range;
- some neutral hadrons identification capability.

Since the average momentum of charged particles produced in B meson decays is below 1 GeV/c, the errors on the measured track parameters are dominated by multiple Coulomb scattering rather than by the intrinsic spatial resolution of the detectors. Similarly, the detection efficiency and energy resolution of low energy photons are severely impacted by material in front of the calorimeter. Thus, special care has been given to keep the material in the active volume of the detector to a minimum.

A schematic view of the *BABAR* detector is shown in Fig. 2.2. The *BABAR* superconducting solenoid, which produces a 1.5 T axial magnetic field, contains a set of nested detectors, which are – going from inside to outside – a five-layers double sided Silicon Vertex Tracker (SVT), a central Drift Chamber (DCH) for charged particles detection and momentum measurement, a fused-silica Cherenkov radiation detector (DIRC) for particle identification, and a CsI(Tl) crystal electromagnetic calorimeter for detection of photons and electrons. The calorimeter has a barrel and an end-cap which extends asymmetrically into the forward direction (e^- beam direction), where many of the collision products emerge. All the detectors located inside the magnet have practically full acceptance in azimuth (ϕ). The flux return outside the cryostat is composed of 18 layers of steel, which increase in thickness outwards, and are instrumented (the IFR) with 19 layers of planar resistive plate chambers (RPCs) or limited streamer tubes (LSTs) in the barrel and 18 in the forward and backward end-caps. The IFR allows the muon identification, and also detects penetrating neutral hadrons. The *BABAR* right-handed coordinate system is indicated in Fig. 2.2. The z axis corresponds to the magnetic field axis and is offset relative to the beam axis by about 20 mrad in the horizontal plane. It is oriented in the direction of electrons. The positive y-axis points upward and the positive x-axis points away from the center of the PEP-II storage rings. A schematic view of the interaction region is shown in Fig. 2.4.

The next sections are dedicated to a description of each subsystem.

2.2.1 The Silicon Vertex Tracker

The Silicon Vertex Tracker (SVT) provides a precise measurement of the decay vertices and of the charged particle trajectories near the interaction region. The mean vertex resolution along the z-axis for a fully reconstructed B decay must be better than 80 μm in order to avoid a significant impact on the time-dependent CP asymmetry measurement precision; a 100μm resolution in the $x - y$ transverse plane is necessary in reconstructing decays of bottom and charm mesons, as well as τ leptons. The SVT also provides standalone tracking for particles with transverse momentum too low to reach the drift chamber, like soft pions from D^* decays and many charged particles produced in multi-body B meson decays.

Finally, the SVT supplies particle identification (PID) information both for low and high momentum tracks. It provides stand-alone tracking for low momentum particles that do not reach the drift chamber, with an efficiency estimated to be 20% for particles with transverse momenta of 50 MeV/c, rapidly increasing to over 80% at 70 MeV/c. Limited particle ID information for low momentum particles that do not reach the drift chamber and the Cherenkov detector is provided by the SVT through the measurement of the specific ionization loss, dE/dx,

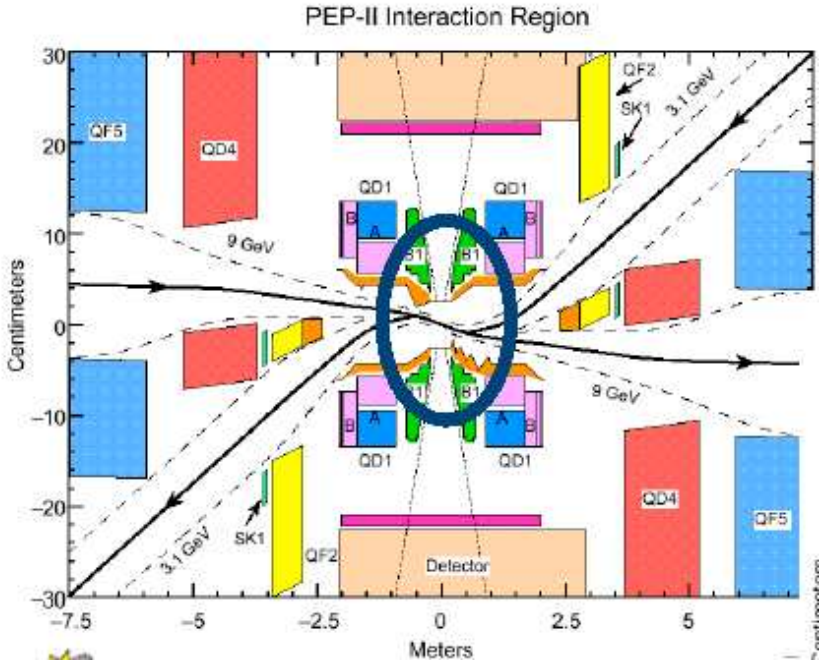

Figure 2.4: *Transverse view of the interaction region.. Vertical axis in centimeters, horizontal axis in meters. Electrons flow from left to right, positrons from right to left.*

as derived from the total charge deposited in each silicon layer. For high momentum tracks the SVT provides the best measurement of the track angles, required to achieve the design resolution on the Cherenkov angle measured by the DIRC.

The design of the SVT is constrained by the components of the storage rings which have been arranged so as to allow maximum SVT coverage in the forward direction: the SVT extends down to 20° (30°) in polar angle from the beam line in the forward (backward) direction. Furthermore, it must have a small amount of material, to reduce multiple scattering which would affect the performance of the outer subdetectors. The solution which was adopted is a five-layer device with 340 double-sided silicon wafers mounted on a carbon-fiber frame (see Fig. 2.5). On the inner (outer) face of each wafer, strip sensors are located running orthogonal (parallel) to the beam direction, measuring the z (ϕ) coordinate of the tracks. The wafers are organized in modules split into forward and backward sections: they are read out on their respective ends and the charge deposited by a particle is determined by the time over threshold of the signal on each strip. In total, 150,000 read-out channels are present. The inner three layers, containing six modules each, are placed close to the beam pipe (at 3.3, 4 and 5.9 cm from it) and dominate the determination of track positions and angles. The outer two layers, containing 16 and 18 modules respectively, are arch-shaped, thus minimizing the amount of silicon needed to cover the solid angle, and placed close to the DCH (at 9.1 and 14.6 cm from the beam pipe) to help the track matching between the two detectors.

The total active silicon area is 0.96 m^2 and the geometrical acceptance is 90% of the solid angle in the center-

of-mass frame. The material traversed by particles corresponds to $\sim 4\%$ of a radiation length.

The SVT efficiency is calculated for each section of the modules by comparing the number of associated hits to the number of tracks crossing the active area of the module and is found to be 97%. The spatial resolution of SVT hits is determined by measuring the distance between the track trajectory and the hit for high-momentum tracks in two-prong events: it is generally better than $40\mu m$ in all layers for all track angles, allowing a precise determination of decay vertices to better than $70\mu m$ (see Fig. 2.6).

2.2.2 The Drift Chamber

The Drift Chamber (DCH) is the main tracking device for charged particles with transverse momenta p_T above $\sim 120\,\mathrm{MeV}/c$, providing the measurement of p_T from the curvature of the particle's trajectory inside the 1.5 T solenoidal magnetic field. The DCH also allows the reconstruction of secondary vertices located outside the silicon detector volume, such as those from $K_S \to \pi^+\pi^-$ decays. For this purpose, the chamber is able to measure not only the transverse coordinate, but also the longitudinal (z) position of tracks with good resolution (about 1 mm). Good z resolution also aids in matching DCH and SVT tracks, and in projecting tracks to the DIRC and the calorimeter. For low momentum particles the DCH provides particle identification by measurement of dE/dx, thus allowing for K/π separation up to $\approx 600\,\mathrm{MeV}/c$. This capability is complementary to that of the DIRC in the barrel region, while it is the only mean to discriminate between different particle hypotheses in the extreme backward and forward directions which fall outside of the geometric acceptance of the DIRC. Finally, the DCH provides real-time information used in the first level trigger system. The DCH is a 2.80 m long cylinder with an inner radius of 23.6 cm and an outer radius of 80.9 cm (Fig. 2.7). Given the asymmetry of the beam energies, the DCH center is displaced by about 37 cm with respect to the interaction point in the forward direction. The active volume provides charged particle tracking over the polar angle range $-0.92 < \cos\theta < 0.96$.

The drift system consists of 7104 hexagonal cells, approximately 1.8 cm wide by 1.2 cm high, arranged in 10 superlayers of 4 layers each, for a total of 40 concentric layers (Fig. 2.8). Each cell consists of one sense wire surrounded by six field wires. The sense wires are 20 μm Rh-W gold-plated wires operating nominally around 1930 V. The field wires are 120 μm Al wires operating at 340 V. Within a given superlayer, the sense and field wires are organized with the same orientation. For measuring also the z coordinate, the superlayers alternate in orientation: first an axial view, then a pair of small angle stereo views (one with positive, one with negative angle) and finally axial view again, as indicated in Fig. 2.8.

The layers are housed between a 1 mm beryllium inner wall and a 9 mm carbonfiber outer wall (corresponding to 0.28% and 1.5% radiation lengths, respectively) both to facilitate the matching between the SVT and DCH tracks and to minimize the amount of material in front of the DIRC and the calorimeter. The counting gas is a 80:20 mixture of helium: isobutane, which again satisfies the requirement of keeping the multiple scattering at minimum. Overall, the multiple scattering inside the DCH is limited by less than 0.2% radiation lengths of material.

The drift chamber reconstruction efficiency has been measured on data in selected samples of multi-track events by exploiting the fact that tracks can be reconstructed independently in the SVT and the DCH. The absolute drift chamber tracking efficiency is determined as the fraction of all tracks detected in the SVT which are also

reconstructed by the DCH when they fall within its acceptance. Its dependency on the transverse momentum and polar angle is shown in Fig. 2.9 [45]. At the design voltage of 1960V the reconstruction efficiency of the drift chamber averages $98 \pm 1\%$ for tracks above 200 MeV/c and polar angle $\theta > 500$ mrad (29°).

The p_T resolution is measured as a function of p_T in cosmic ray studies:

$$\frac{\sigma_{p_T}}{p_T} = (0.13 \pm 0.01)\% \cdot \frac{p_T}{1\ GeV/c} + (0.45 \pm 0.03)\%, \tag{2.1}$$

where p_T is expressed in GeV/c. The first contribution, dominating at high p_T, comes from the curvature error due to finite spatial measurement resolution; the second contribution, dominating at low momenta, is due to multiple Coulomb scattering.

The specific ionization loss dE/dx for charged particles traversing the drift chamber is derived from the total charge deposited in each drift cell. The resolution achieved to date is typically about 7.5% (as shown in Fig. 2.10 for $e^{\pm}$ from Bhabha scattering). A 3σ separation between kaons and pions can be achieved up to momenta of about 700 MeV/c [54].

2.2.3 The Cherenkov detector

The particle identification (PID) at low momenta exploits primarily the dE/dx measurements in the DCH and SVT. However, above the threshold of 700 MeV/c, the dE/dx information does not allow to separate pions and kaons. The Detector of Internally Reflected Cherenkov radiation (DIRC) is employed primarily for the separation of pions and kaons from about 500 MeV/c to the kinematic limit of 4 GeV/c reached in rare B decays like $B \to \pi^+\pi^-/K^+K^-$. The principle of the DIRC is based on the detection of Cherenkov light generated by a charged particle in a medium of refractive index n, when its velocity v is greater than c/n. The photons are emitted on a cone of half-angle θ_c with respect to the particle direction, where $cos\theta_c = 1/\beta n,\ \beta = v/c$. Knowing the particle momentum thanks to the SVT and the DCH, the measurement of θ_c allows the mass measurement, so the particle identification, with the relation:

$$m^2c^2 = \frac{1-\beta^2}{\beta^2}p^2 \tag{2.2}$$

Fig. 2.11 illustrates the principles of light production, transport, and imaging in the DIRC.

The radiator material of the DIRC is synthetic fused silica (refraction index $n = 1.473$) in the form of 144 long, thin bars with regular rectangular cross section. The bars, which are 17 mm thick, 35 mm wide and 4.9 m long, are arranged in a 12-sided polygonal barrel, each side being composed of 12 adjacent bars placed into sealed containers called bar boxes. Dry nitrogen gas flows through each bar box, and humidity levels are monitored to check that the bar box to water interface remains sealed. The solid angle subtended by the radiator bars corresponds to 94% of the azimuth and 83% of the cosine of the polar angle in the center-of-mass system. The bars serve both as radiators and as light pipes for the portion of the light trapped in the radiator by total internal reflection. For particles with $\beta \approx 1$, some photons will always lie within the total internal reflection limit, and will be transported to either one or both ends of the bar, depending on the particle incident angle. To avoid having to instrument both bar ends with photon detectors, a mirror is placed at the forward end, perpendicular

to the bar axis, to reflect incident photons to the backward (instrumented) bar end.

Once photons arrive at the instrumented end, most of them emerge into an expansion region filled with 6000 litres of purified water ($n = 1.346$), called the stand-off box (see Fig. 2.12). A fused silica wedge at the exit of the bar reflects photons at large angles and thereby reduces the size of the required detection surface. The photons are detected by an array of densely packed photo-multiplier tubes (PMTs), each surrounded by reflecting "light catcher" cones to capture light which would otherwise miss the PMT active area. The PMTs, arranged in 12 sectors of 896 phototubes each, have a diameter of 29 mm and are placed at a distance of about 1.2 m from the bar end. The expected Cherenkov light pattern at this surface is essentially a conic section, whose cone opening-angle is the Cherenkov production angle modified by refraction at the exit from the fused silica window. By knowing the location of the PMT that observes a Cherenkov photon and the charged particle direction from the tracking system, the Cherenkov angle can be determined. In addition, the time taken for the photon to travel from its point of origin to the PMT is used to effectively suppress hits from beam-generated background and from other tracks in the same event, and also to resolve some ambiguities in the association between the PMT hits and the track (for instance, the forward-backward ambiguity between photons that have or have not been reflected by the mirror at the forward end of the bars).

The relevant observable to distinguish between signal and background photons is the difference between the measured and expected photon time, δt_γ. It is calculated for each photon using the track time-of-flight, the measured time of the candidate signal in the PMT and the photon propagation time within the bar and in the water filled standoff box. The resolution on this quantity, as measured in dimuon events, is 1.7 ns, close to the intrinsic 1.5 ns transit time spread of the photoelectrons in the PMTs. Applying the time information substantially improves the correct matching of photons with tracks and reduces the number of accelerator induced background hits by approximately a factor 40, as can be seen in Fig. 2.13 [56]. The reconstruction routine provides a likelihood value for each of the five stable particle types ($e,\ \mu,\ \pi,\ K,\ p$) if the track passes through the active volume of the DIRC. These likelihoods are calculated in an iterative process by maximising the likelihood value for the entire event while testing different hypotheses for each track. If enough photons are found, a fit of θ_c and the number of observed signal and background photons are calculated for each track.

The DIRC uses two independent and complementar approaches for a calibration of the unknown PMT time response and the delays introduced by the electronic and the fast control system. The first one is a conventional pulser calibration: 1 ns duration light pulses are emitted from 12 blue LEDs (one per sector), with a rate of 2 kHz. A calibration run requires a few minutes and is taken about three times a week. The second calibration system uses reconstructed tracks from the collision data ("rolling calibration"). It performs a calibration of the global time delay, and the time delay sector by sector.

Fig. 2.14 shows the number of photons detected as a function of the polar angle in di-muons events. It increases from a minimum of about 20 at the center of the barrel ($\theta \approx 90^\circ$) to well over 50 in the forward and backward directions, corresponding to the fact that the path-length in the radiator is longer for tracks emitted at large dip angles (therefore the number of Cherenkov photons produced in the bars is greater) and the fraction of photons trapped by total internal reflection rises. This feature is very useful in the *BABAR* environment, where, due to the boost of the center-of-mass, particles are emitted preferentially in the forward direction. The bump at

$\cos\theta = 0$ is a result of the fact that for tracks at small angles internal reflection of the Cherenkov photons occurs in both the forward and backward direction. The small decrease of the number of photons from the backward direction to the forward one is a consequence of the photon absorption along the bar before reaching the stand-off box in the backward end. The combination of the single photon Cherenkov angle resolution, the distribution of the number of detected photons versus polar angle and the polar angle distribution of charged tracks yields a typical track Cherenkov angle resolution which is about 2.5 $mrad$ in di-muon events.

The pion-kaon separation power is defined as the difference of the mean Cherenkov angles for pions and kaons divided by the measured track Cherenkov angle resolution, assuming a Gaussian-like distribution. As shown in Fig. 2.15, left, the separation between kaons and pions at 3 GeV/c is about 4.3 σ. The use of the DIRC to identify kaons improves greatly the removal of background, as presented in the right plot of Figure 2.15.

2.2.4 The Electromagnetic Calorimeter

The *BABAR* electromagnetic calorimeter (EMC) is designed to detect and measure electromagnetic showers with high efficiency and very good energy and angular resolution over a wide energy range: from 20 MeV to 9 GeV. This allows the reconstruction of $\pi^0 \to \gamma\gamma$ and $\eta \to \gamma\gamma$ decays where the photons can have very low energy, as well as the reconstruction of Bhabha events and processes like $e^+e^- \to \gamma\gamma$, important for luminosity monitoring and calibration, where electron and photon energies can be very large. The EMC also provides the primary information for electron identification and electron-hadron separation.

Energy deposit clusters in the EMC with lateral shape consistent with the expected pattern from an electromagnetic shower are identified as photons when they are not associated to any charged tracks extrapolated from the SVT and the drift chamber, and as electrons if they are matched to a charged track and if the ratio between the energy E measured in the EMC and the momentum p measured by the tracking system is $E/p \approx 1$.

The EMC contains 6580 CsI crystals doped with Tl (Fig. 2.16). CsI(Tl) has a high light yield (50,000 photons/ MeV) and a small Molière radius (3.8 cm), which provide the required energy and angular resolution; its radiation length of 1.86 cm guarantees complete shower containment at the *BABAR* energies.

Each crystal is a truncated trapezoidal pyramid and ranges from 16 to 17.5 radiation lengths in thickness. The front faces are typically about 5 cm in each dimension. The crystals are arranged to form a barrel and a forward endcap giving a 90% solid-angle coverage in the center-of-mass frame. The barrel has 48 rows of crystals in θ and 120 in ϕ; the forward endcap contains 8 rings in θ. Overall the EMC extends from an inner radius of 91 cm to an outer radius of 136 cm and is displaced asymmetrically with respect to the interaction point.

The crystals are read out by two independent $1\ cm^2$ PIN photodiodes, glued to their rear faces, which are connected to low-noise preamplifiers that shape the signal with a short shaping time (400 ns) so to reduce soft beam-related photon backgrounds.

For the purpose of precise calibration and monitoring, use is made of a neutron activated fluorocarbon fluid, which produces a radioactive source (^{16}N) originating a 6.1 MeV photon peak in each crystal. A light pulser system injecting light into the rear of each crystal is also used. In addition, signals from data, including π^0 decays and $e^+e^- \to e^+e^-/\gamma\gamma/\mu^+\mu^-$ events, provide energy calibration and resolution determination.

The efficiency of the EMC exceeds 96% for the detection of photons with energy above 20 MeV. The energy

resolution is usually parameterized by

$$\frac{\sigma_E}{E} = \frac{\sigma_1}{E^{1/4}(\,\mathrm{GeV})} \oplus \sigma_2, \tag{2.3}$$

where $\sigma_1 = 2.32 \pm 0.30\%$ and $\sigma_2 = 1.85 \pm 0.12\%$, as determined using the above mentioned sources. The first term in Eq. 2.3 arises from fluctuations in photon statistics and is dominant for energies below about 2.5 GeV, while the constant term takes into account several effects, such as fluctuations in shower containment, non-uniformities, calibration uncertainties and electronic noise.

The decays of π^0 and η candidates in which the two photons have approximately equal energy are used to infer angular resolution. It varies between about 12 mrad at low energies and 3 mrad at high energy. The data fit the empirical parameterization:

$$\sigma_{\theta,\phi} \;=\; \left(\frac{(3.87 \pm 0.07)}{\sqrt{E(\,\mathrm{GeV})}} + (0.00 \pm 0.04) \right) mrad \tag{2.4}$$

Fig. 2.17 [57] shows the energy and angular resolution measured as a function of the photon energy.

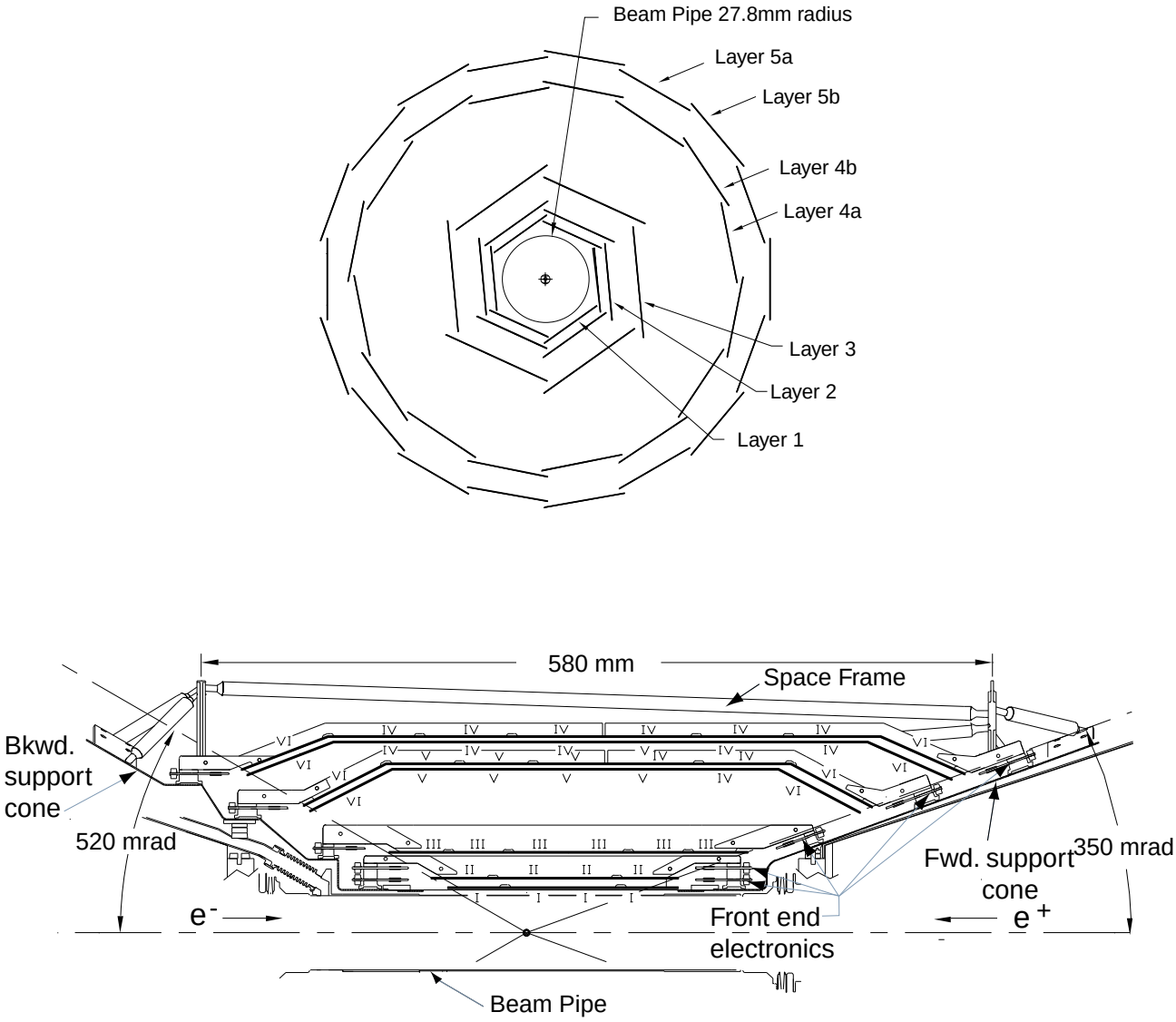

Figure 2.5: Schematic view of the SVT, transverse section (upper plot) and longitudinal section (bottom plot).

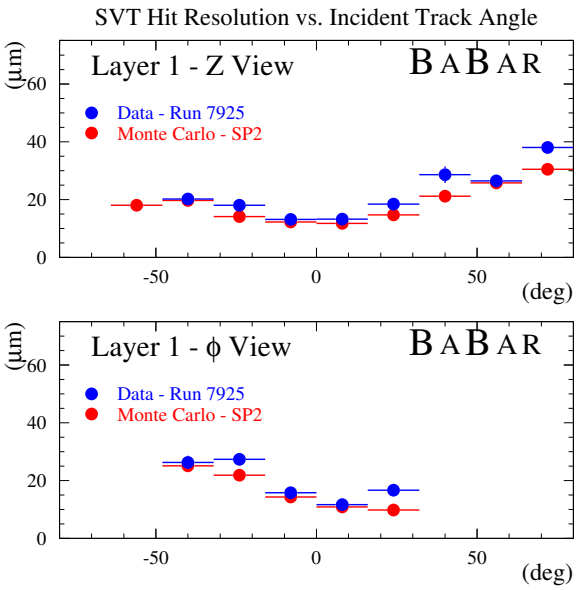

Figure 2.6: SVT resolution (layer 1) on the single hit, as a function of the track angle.

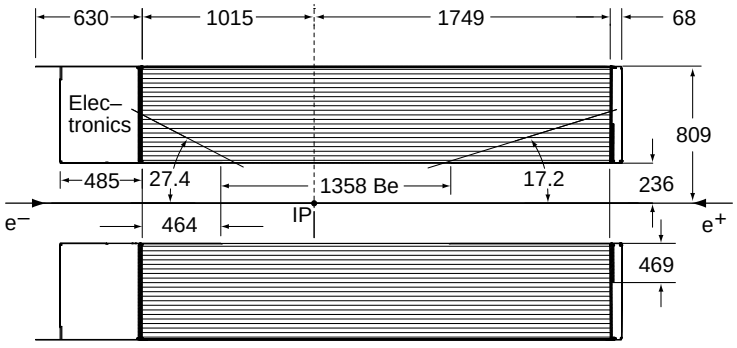

Figure 2.7: Schematic view of the DCH (longitudinal section).

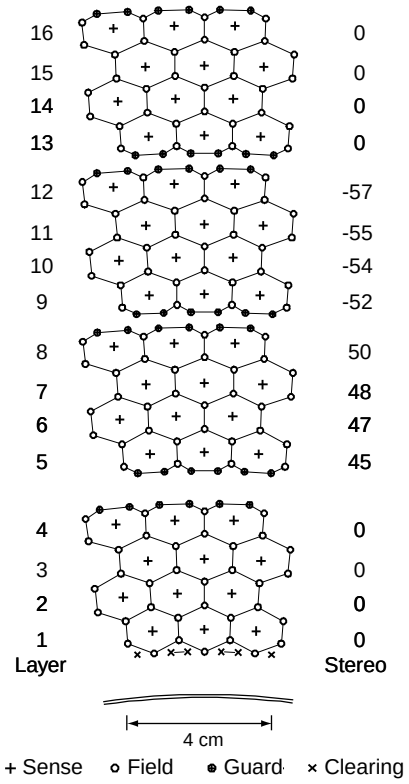

Figure 2.8: Schematic layout of the drift cells for the four innermost superlayers. The numbers on the right side give the stereo angles (mrad) of sense wires in each layer.

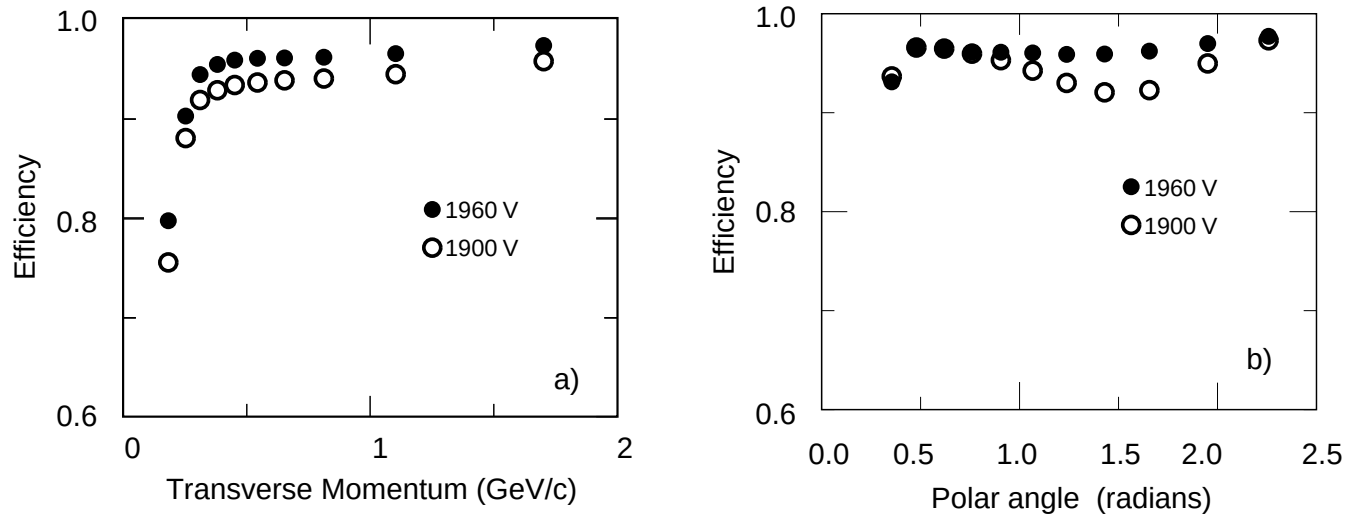

Figure 2.9: Track reconstruction efficiency in the DCH at operating voltages of 1900 V and 1960 V, as a function of transverse momentum (a) and polar angle (b).

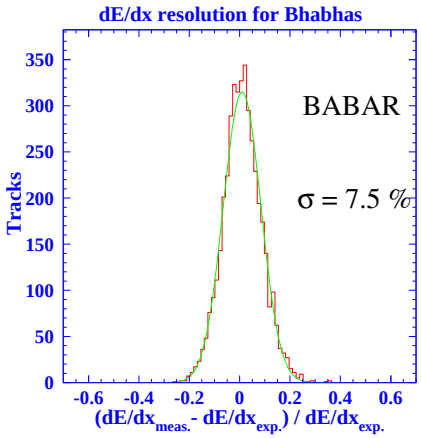

Figure 2.10: DCH Resolution on dE/dx for $e^{\pm}$ from Bhabha scattering.

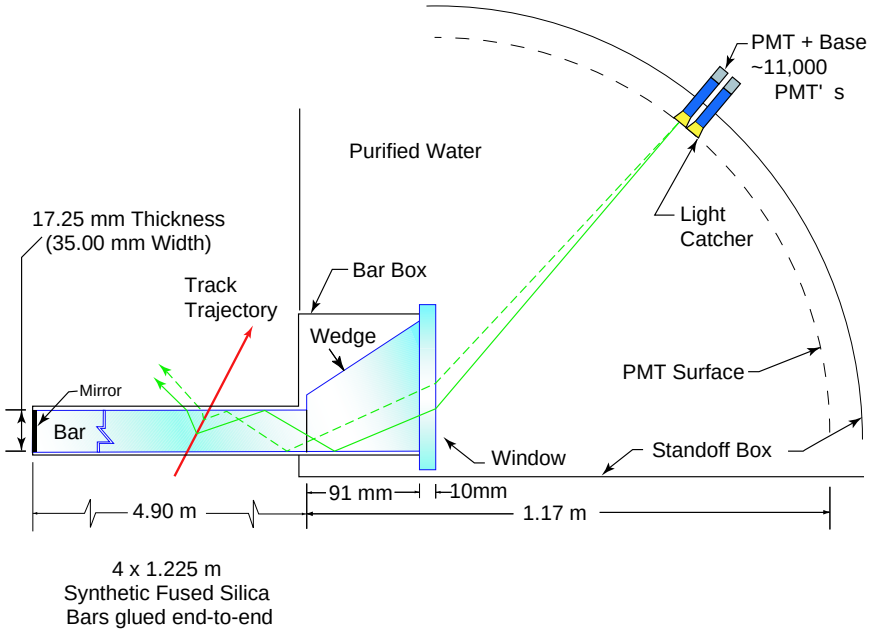

Figure 2.11: Schematics of the DIRC fused silica radiator bar and imaging region. In this scheme the forward region is to the left and the backward regio is to the right.

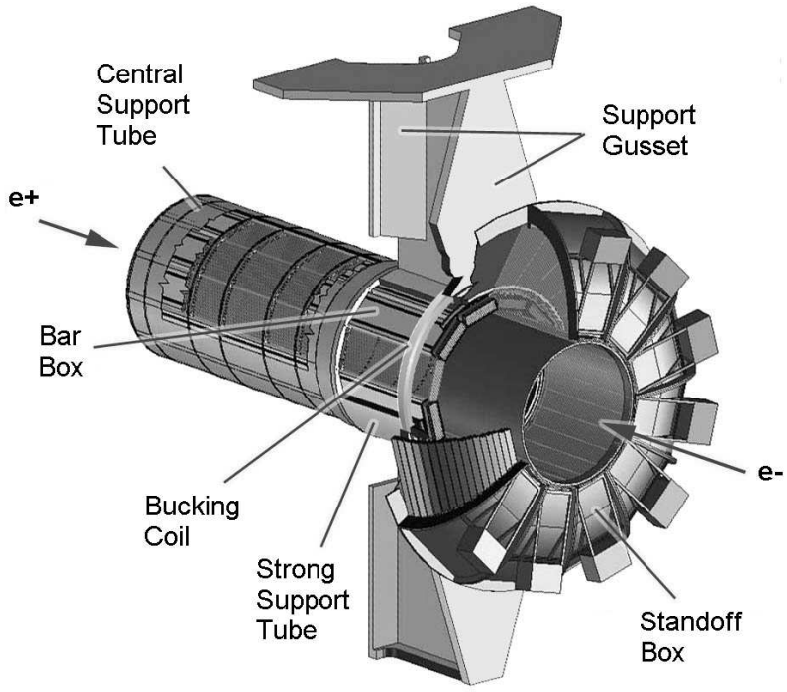

Figure 2.12: Schematic view of the DIRC.

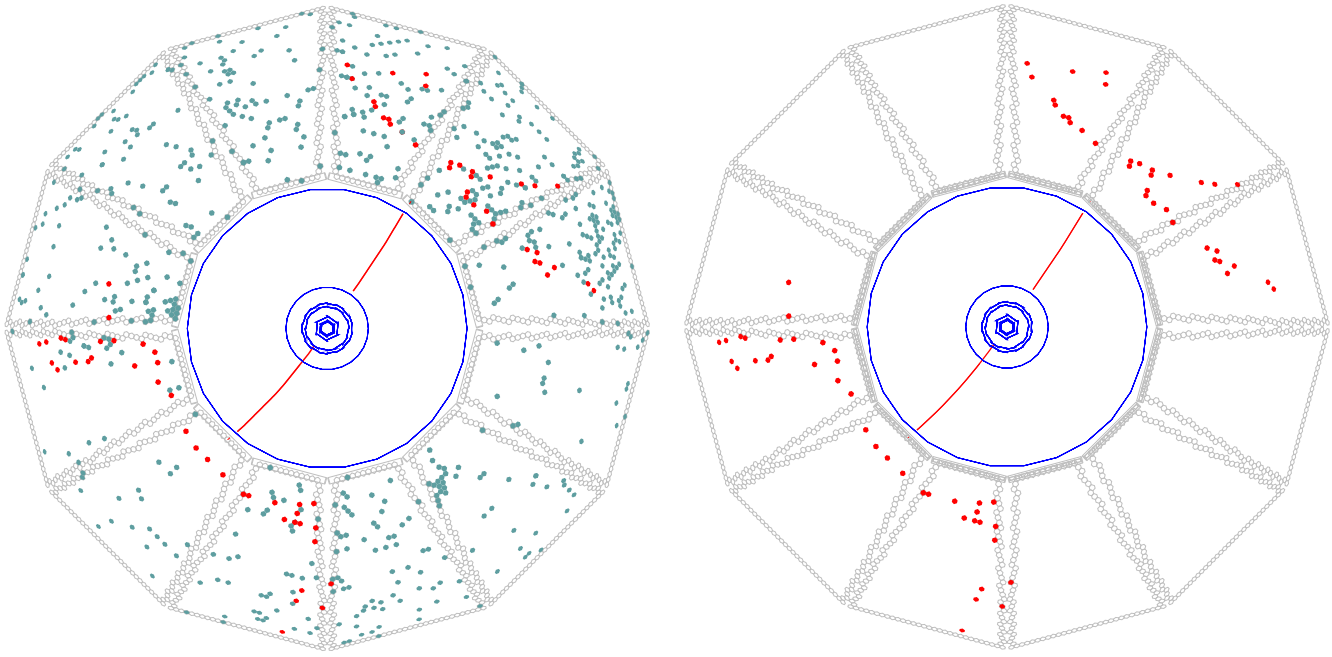

Figure 2.13: Display of one $e^+e^- \to \mu^+\mu^-$ event reconstructed in *BABAR* with two different time cuts. On the left, all DIRC PMTs that were hit within the $\pm 300\ ns$ trigger window are shown. On the right, only those PMTs that were hit within 8 ns of the expected Cherenkov photon arrival time are displayed.

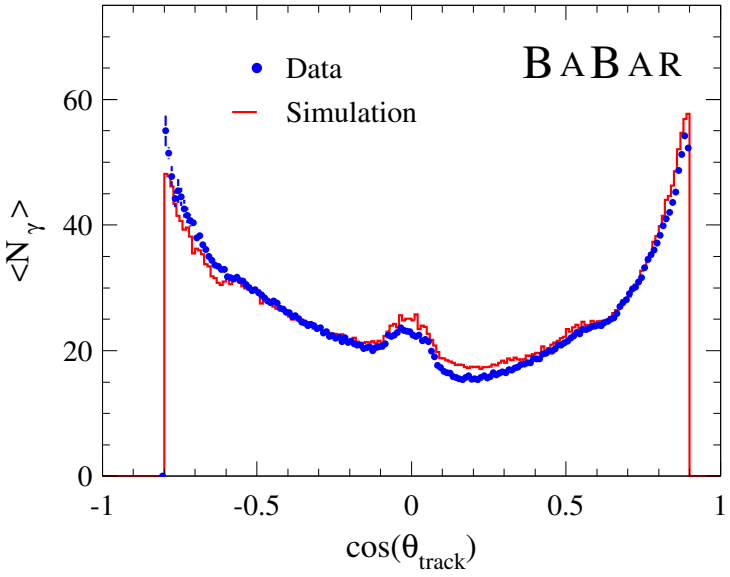

Figure 2.14: Number of detected photoelectrons versus track polar angle for reconstructed di-muon events in data and simulation.

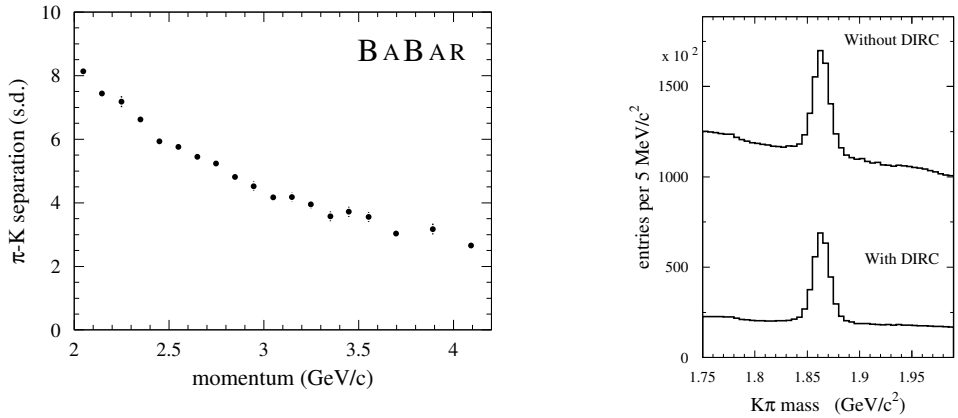

Figure 2.15: Left plot:DIRC π-K separation versus track momentum measured in $D^0 \to K^-\pi^+$ decays selected kinematically from inclusive D^* production. Right plot: Invariant $K^+\pi^-$ mass spectrum for kinematically reconstructed D^0 mesons in the decay $D^* \to D^0\pi$ without (top) and with (bottom) the use of the DIRC to identify the kaon.

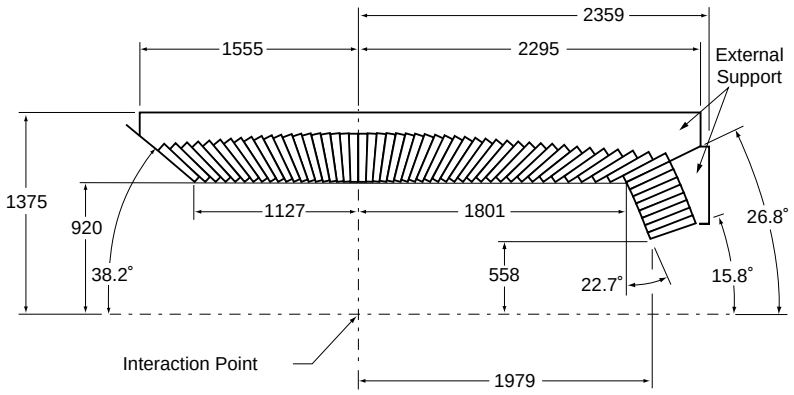

Figure 2.16: Longitudinal section of the top half of the EMC (barrel and forward). Dimensions are in mm.

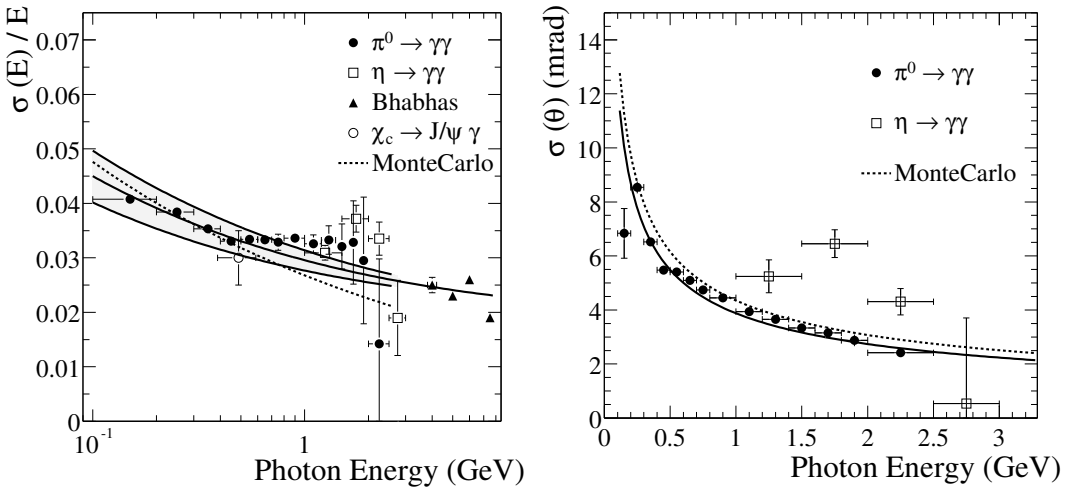

Figure 2.17: Energy (left) and angular (right) resolutions measured using a variety of data. The solid curves represent a fit to the data using Equation 2.3 and 2.4 respectively.

2.2.5 The Instrumented Flux Return

The Instrumented Flux Return (IFR) is designed to identify muons and neutral hadrons (primarily K_L and neutrons). Muons are important for tagging the flavor of neutral B mesons via semi-leptonic decays, for the reconstruction of vector mesons, like the J/ψ, and the study of semi-leptonic and rare decays involving leptons from B and D mesons and τ leptons. K_L detection allows for the study of exclusive B decays, in particular CP eigenstates. The principal requirements for IFR are large solid angle coverage, good efficiency and high background rejection for muons down to momenta below 1 GeV/c. For neutral hadrons, high efficiency and good angular resolution are most important. The IFR uses the steel flux return of the magnet as muon filter and hadron absorber, limiting pion contamination in the muon identification. Originally single gap resistive plate chambers (RPC) with two-coordinate readout, operated in limited streamer mode constituted the active part of the detector [58], with 19 layers in the barrel and 18 in each endcap. The RPC were installed in the gaps of the finely segmented steel of the six barrel sectors and the two end-doors of the flux return, as illustrated in Fig. 2.18. The steel segmentation has been optimized on the basis of Monte Carlo studies of muon penetration and charged and neutral hadron interactions. In addition, two layers of cylindrical RPCs were installed between the EMC and the magnet cryostat to detect particles exiting the EMC. RPCs contain a 2 mm Bakelite gap with ~ 8 kV across it. Ionizing particles which cross the gap create streamers of ions and electrons in the gas mixture (Argon, freon and isobutane), which in turn creates signals via capacitive coupling on the strips mounted on each side of the RPC. Soon after the installation (which took place in Summer 1999), the efficiency of a significant fraction of

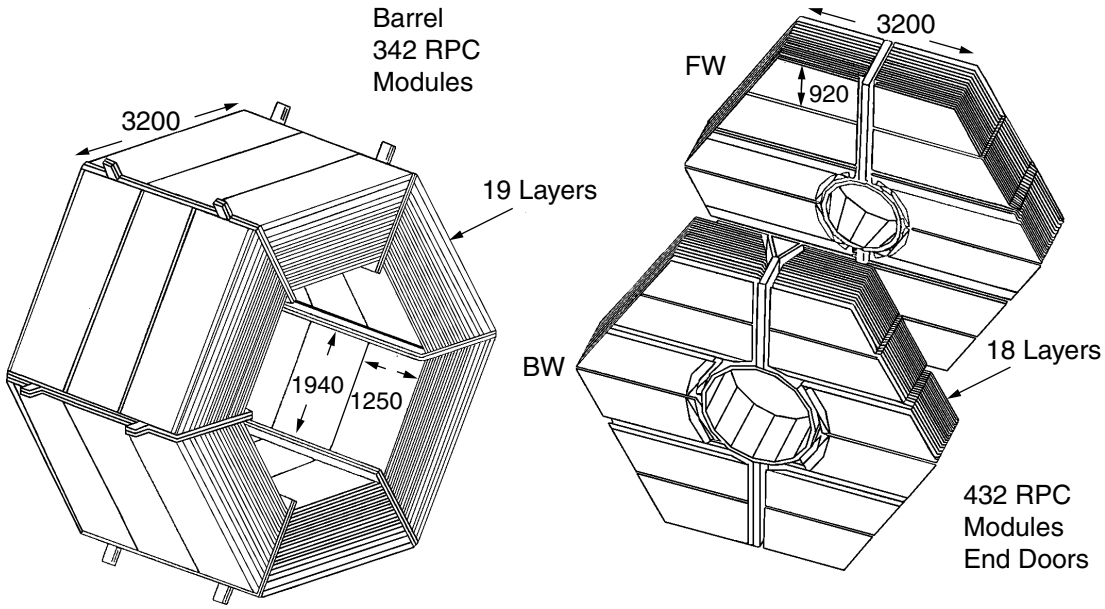

Figure 2.18: Overview of the IFR Barrel sectors and forward and backward end-doors; the shape of the RPC modules and the way they are stratified is shown.

the chambers (initially greater then 90%) has started to deteriorate at a rate of 0.5-1%/month. In order to solve

some of the inefficiency problems, an extensive improvement program has been developed. The forward endcap was retrofitted with new improved RPCs in 2002, their efficiency has not significatly decreased since then. In the barrel, the RPCs have been replaced in 2004 and 2006 by 12 layers of limited streamer tube (LST) detectors and 6 layers of brass have been added to improve hadron absorption. The tubes have performed well since their installation with an efficiency of all layers at the geometrically expected level of 90%. The pion rejection versus muon efficiency is shown in Fig. 2.19 for the LSTs and RPCs. The LSTs efficiency is better than the efficiency that the RPCs had, even during the Run 1.

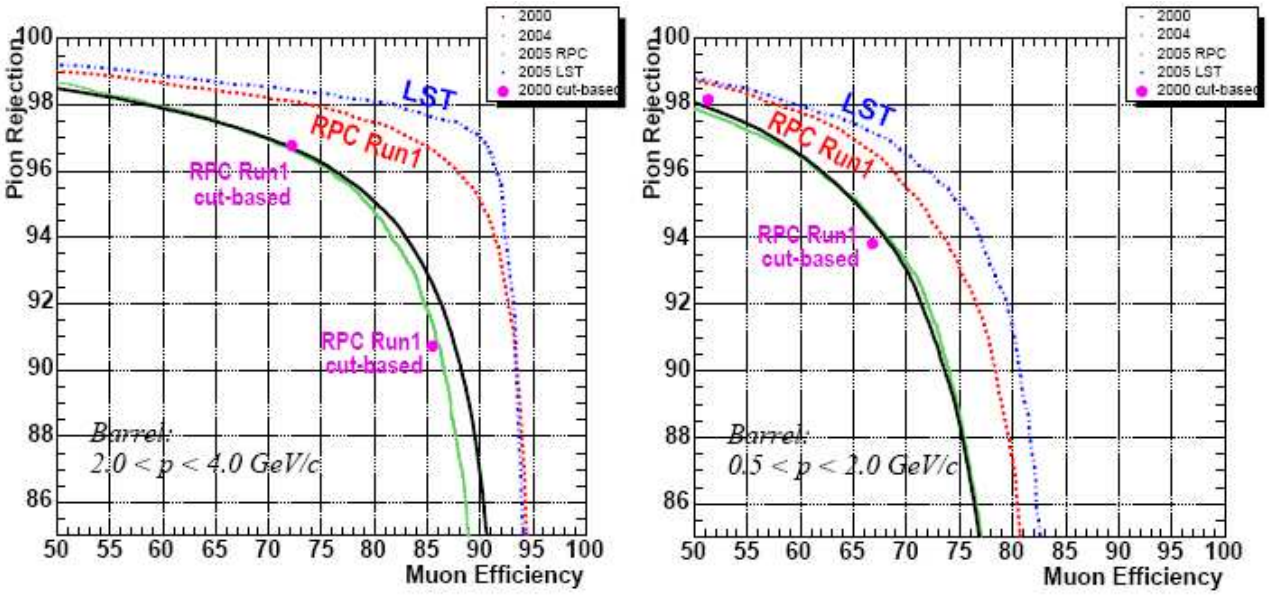

Figure 2.19: Pion rejection versus muon efficiency for two different momentum ranges (left: $2 < p < 4$ GeV/c, right $0.5 < p < 2$ GeV/c). The LST efficiency (blue) is compared with the RPC one for different Runs. We see the deterioration of the RPC performance between 2000 (red) and 2005 (green).

2.2.6 Trigger

The *BABAR* trigger is designed to select a large variety of physics processes (efficiency greater than 99% for $B\bar{B}$ events) while keeping the output rate below 400 Hz to satisfy computing limitations of the offline processing farms (beam induced background rates with at least one track with $p_t > 120$ MeV/c or at least one EMC cluster with $E > 100$ MeV are typically 20 kHz). The trigger accepts also 95 % of continuum hadronic events and more than 90 % of $\tau^+\tau^-$ events. It is implemented as a two level hierarchy, the hardware Level 1 (L1) followed by the software Level 3 (L3).

The L1 trigger has an output rate of the order of 1 kHz to 3 kHz, depending on the luminosity and background conditions. It is based on charged tracks in the DCH above a preset transverse momentum, showers in the EMC, and track detected in the IFR. L3 operates by refining and augmenting the selection methods used in L1. Based on both the complete event and L1 trigger information, the L3 software algorithm selects events of interest allowing

L3 Trigger	$\epsilon_{b\bar{b}}$	$\epsilon_{B\to\pi^0\pi^0}$	$\epsilon_{B\to\tau\nu}$	$\epsilon_{c\bar{c}}$	ϵ_{uds}	$\epsilon_{\tau\tau}$
Combined DCH filters	99.4	89.1	96.6	97.1	95.4	95.5
Combined EMC filters	93.5	95.7	62.3	87.4	85.6	46.3
Combined DCH+EMC filters	>99.9	99.3	98.1	99.0	97.6	97.3
Combined L1+L3	>99.9	99.1	97.8	98.9	95.8	92.0

Table 2.3: L3 trigger efficiency (%) for various physics processes, derived from Monte Carlo simulation.

them to be transferred to mass storage data for further analysis. It uses an algorithm based on the drift chamber tracking, which rejects beam-induced charged particle background produced in the material close to the IP, and a second algorithm based on the calorimeter clustering. Then, based on the L3 tracks and clusters, a variety of filters perform event classification and background reduction. Tab. 2.3 shows the L3 and L1+L3 trigger efficiency for some relevant physics processes, derived from simulated events.

2.3 Particle identification

After having described the different components of the detector, we will explain more specifically what is the information used in the reconstruction of the $D^+ \to K^-\pi^+e^+\nu_e$ channel. In this analysis, we have to reconstruct one charged kaon, one charged pion and one electron, which requires the explicit identification of these particles. As the neutrino is not measured, we use the charged and neutral particles produced in the rest of the event to evaluate the missing energy and the D^+ direction.

2.3.1 Charged particle reconstruction

The charged particle tracks are reconstructed by processing information from both tracking systems, the SVT and the DCH. Charged tracks are defined by five parameters shown in Figure 2.20 ($d_0, \phi_0, \omega, z_0, tan\lambda$) and their associated error matrix, measured at the point of closest approach to the z-axis. d_0 and z_0 are the distances between the point and the origin of the coordinate system in the x-y plane and along the z-axis respectively. The angle ϕ_0 is the azimuth of the track, λ is the angle between the transverse plane and the track tangent vector at the point of closest approach and the x-axis, and $\omega = 1/p_t$ is the curvature of the track. d_0 and ω are signed variables and their sign depends on the charge of the track. The track finding and the fitting procedures use the *Kalman filter algorithm* [59] that takes into account the detailed distribution of material in the detector and the full magnetic field map.

The identified tracks are then organized in different categories depending on requirements on specific quantities. In the study of the $D^+ \to K^-\pi^+e^+\nu_e$ decay channel, we start from the list *GoodTrackVeryLoose* which is composed of charged tracks with momentum below 10 GeV/c (to remove tracks not compatible with the beam energy), distance of closest approach to the beam spot in the x-y plane below 1.5 cm, and below 10 cm along the z axis. The pion mass is associated by default to the candidate for each track.

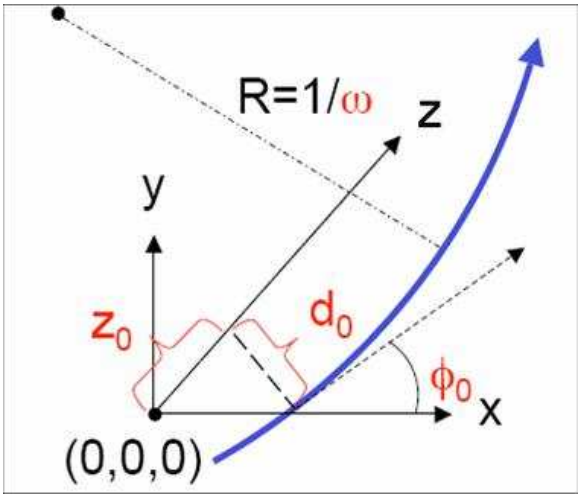

Figure 2.20: *Definition of the parameters d_0, ϕ_0, ω and z_0 used to define charged tracks.*

2.3.2 Neutral particles reconstruction

Neutral particles (photons, π^0, neutral hadrons) are detected in the EMC as clusters of close crystals where energy has been deposited. They are required not to be matched to any charged track extrapolated from the tracking volume to the inner surface of the EMC. The lateral distribution of energy within a cluster depends heavily of the nature of the incident particle. The lateral moment, LAT, is defined as :

$$LAT = \frac{\sum_{i=3}^{N} E_i r_i^2}{\sum_{i=3}^{N} E_i r_i^2 + E_1 r_0^2 + E_2 r_0^2}, \tag{2.5}$$

where N is the number of crystals associated with the electromagnetic shower, r_0 is the average distance between two crystals, which is approximately 5 cm for the *BABAR* calorimeter, E_i is the energy deposited in the i-th crystal, numbering them such that $E_1 > E_2 > \ldots > E_N$ and r_i, ϕ_i are the polar coordinates in the plane perpendicular to the line pointing from the interaction point to the shower cluster centroid. Considering that the summations start from $i = 3$, they omit the two crystals containing the highest amounts of energy. Since electrons and photons deposit most of their energy in two or three crystals, the value of LAT is small for electromagnetic showers. Multiplying the energies by the squared distances enhances the effect for hadronic showers, compared with electromagnetic ones.

In this analysis, neutral particles are required to have an energy greater than 100 MeV and a lateral moment smaller than 0.8.

2.3.3 Particle identification

The particle identification is done by several algorithms with different levels of purity and efficiency. They allow the identification of stable particles: $e^{\pm}$, $\mu^{\pm}$, $\pi^{\pm}$, $K^{\pm}$, $p^{\pm}$ and K_L^0.

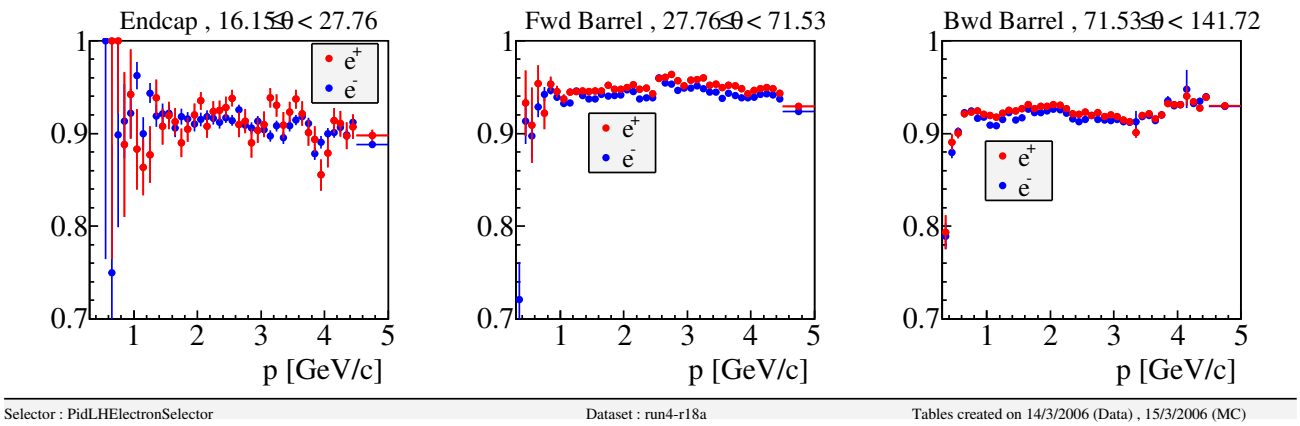

Figure 2.21: *Electron identification efficiency for the likelihood-based electron selector as function of momentum, for three different angular regions.*

The identification of electrons is done using information predominantly from the electromagnetic calorimeter, but also coming from the DIRC and dE/dx in the tracking devices at low momenta. In this analysis, for the electron identification, we use an algorithm called *PidLHElectrons* based on a likelihood [61]. An electron candidate is accepted or rejected if it has a value higher than 0.95 for the following likelihood ratio:

$$f_L = \frac{p_e L(e)}{p_e L(e) + p_\pi L(\pi) + p_K L(K) + p_P L(P)}$$

Where the L(x) (x=$K, \pi, e, P = proton$) are products of likelihoods using information such as the following variables:

- For the EMC: the ratio E/p of the energy deposited in the EMC and the momentum in the laboratory frame; LAT, the lateral shape of the calorimeter deposit; $\Delta\Phi$, a quantity characterizing the longitudinal energy distribution; and the number of crystals in the EMC cluster.
- For the DIRC: the Cherenkov angle and the number of measured photons in the DIRC.
- For the DCH: the specific energy loss dE/dx.

The efficiency of the likelihood-based electron identification algorithm is shown in Figure 2.21 as function of the momentum for three different polar angle regions: the forward endcap, the forward barrel and the backward barrel [60]. The rate of pions and kaons misidentified as electrons is shown in Figure 2.22. This algorithm allows the selection of more than 90% of electron with momentum above 500 MeV, while the rate of misidentified hadrons is below 0.3% and 0.5% for pions and kaons with momentum above 1 GeV/c, respectively, cutting at $f_L > 0.95$.

The kaon selection is based on information from the SVT, the DCH and the DIRC. The efficiency of kaons as funtion of their momentum are shown in Figure 2.23. It uses subdetector likelihoods with a neural network approach. The kaon efficiency is on average bigger than 80% and there are some charge asymmetries efficiencies

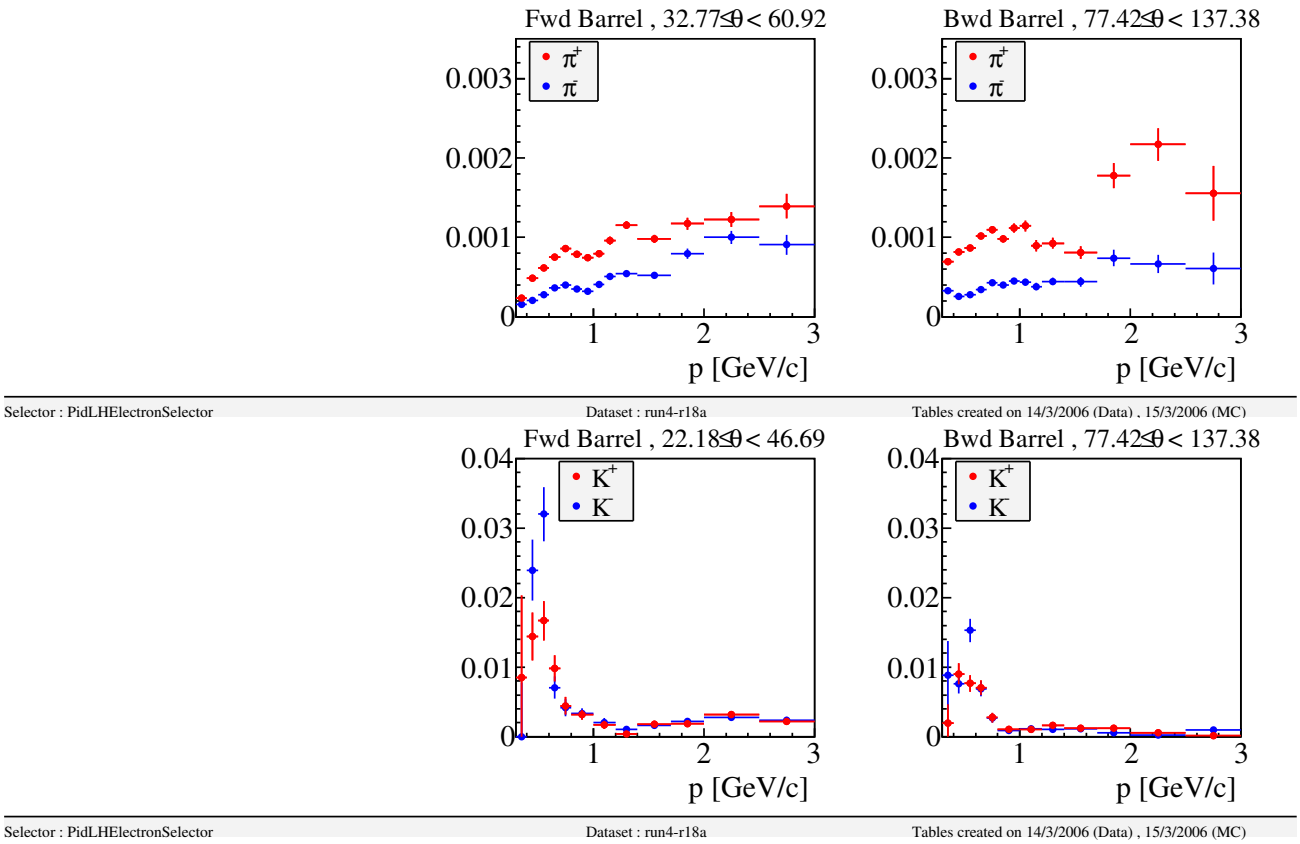

Figure 2.22: *Hadron misidentification probability for the likelihood-based electron selector in two barrel regions.*

which are at most of order $2-4\%$ below 1.5 GeV/c momentum. The pion fake rate ranges between 0.1% and 4% and is on average smaller than 2%.

Protons are identified using a similar method as electrons, their efficiency as funtion of their momentum is shown in Figure 2.24.

In the present analysis, the data/MC agreement for tracking efficiency and particle identification has been studied and corrected using standard tools developped in *BABAR* . To correct neutral particle efficiencies, the central value and resolution of the measured energy are corrected. These corrections depend on the run period and are relatively small. For the PID, we correct for the data/MC efficiency differences in the following way. For a given particle selector, and using the PID efficiency tables derived from data and MC, the PID correction algorithm:

- rejects an accepted track with the probability $\epsilon_{data}/\epsilon_{MC}$ if $\epsilon_{data} < \epsilon_{MC}$,
- accepts a rejected track with the probability $(\epsilon_{data} - \epsilon_{MC}) \,/\, (1 - \epsilon_{MC})$ if $\epsilon_{data} > \epsilon_{MC}$,

where $\epsilon_{data(MC)}$ is the data (MC) efficiency of the given selector. This procedure is applied to the main selectors of the analysis (kaon and electron selectors).

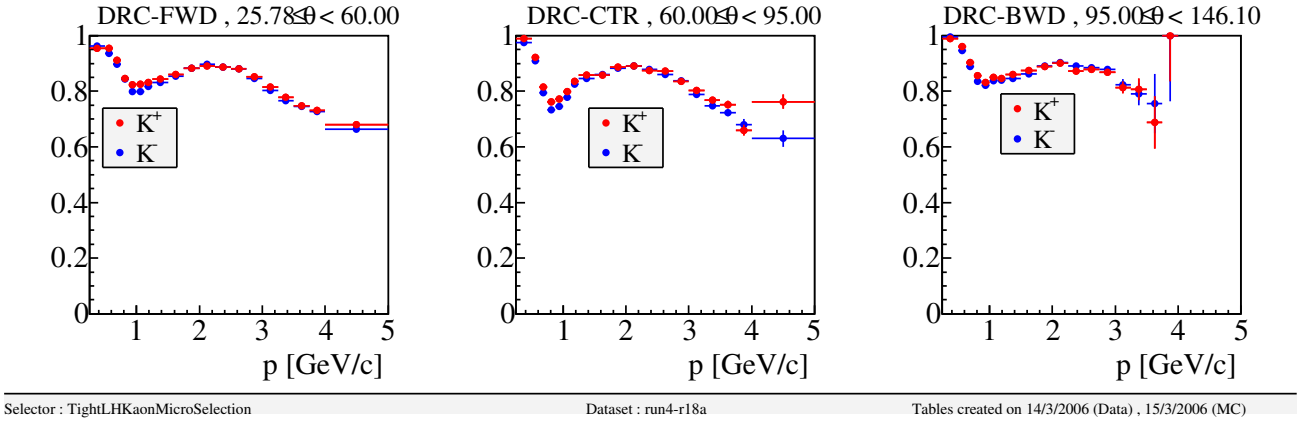

Figure 2.23: *Kaons identification efficiency for the neural network based kaons selector as function of momentum, for three different angular regions.*

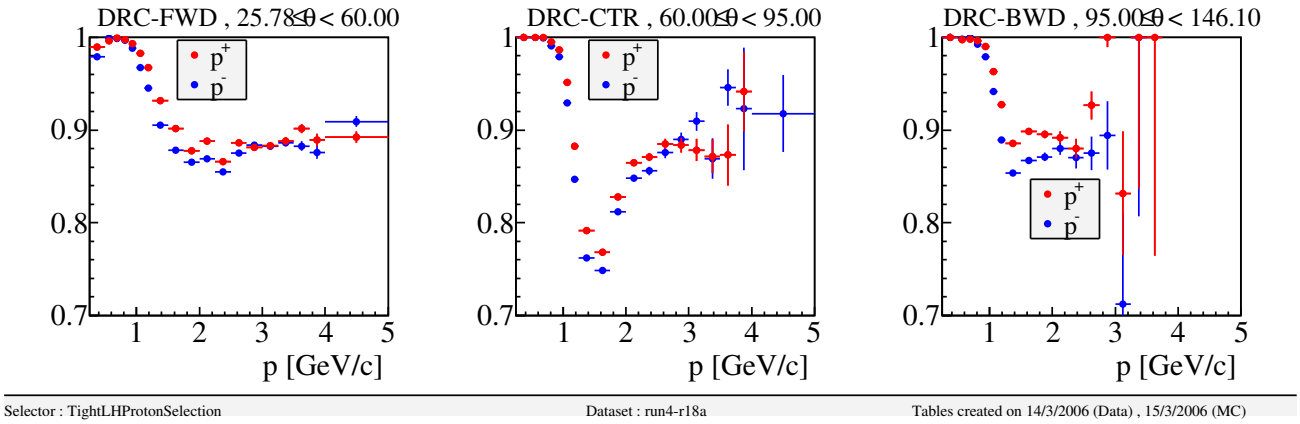

Figure 2.24: *Protons identification efficiency for the likelihood-based protons selector as function of momentum, for three different angular regions.*

Chapter 3

Event reconstruction and background rejection

3.1 Pre-selection and reconstruction

Events are selected using a skim dedicated to charm semileptonic decays and corresponding selection criteria are explained. We then consider the reconstruction of signal candidates and give the expected resolution on the different kinematic variables.

3.1.1 Event samples

We have analyzed data from Runs 1-5 which correspond to a total integrated luminosity of 347 fb^{-1}. Generic samples of simulated events corresponding to similar conditions of data taking have been used for background estimates. Table 3.1 gives the ratios between MC and data for each flavour.

Dedicated samples of $D^+ \to K^-\pi^+e^+\nu_e$ have been generated using phase space and SLPOLE decay models. They amount to at least five times the data statistics and are in proportion with the integrated luminosities analyzed for the different runs.

3.1.2 Skim selection

We verify that a charged particle is not a member of several lists by selecting particle signatures using the following priority order: electron>kaon>pion.
The first step for the selection of signal candidates is to use the skim selector CharmSL which consists of the cuts listed in the following. Some of the selection criteria refer to event hemispheres. These hemispheres contain,

run	B^0B^0	B^+B^-	$c\bar{c}$	uds
123	3.68	3.74	2.19	1.20
4	3.15	3.17	1.20	1.
5	2.99	3.15	1.60	1.14

Table 3.1: *Available generic Monte Carlo samples for each type of flavour and for the different runs. Values presented are the proportion of MC as compared to the real data luminosity for the same run.*

respectively, the particles which are on each side of the plane passing through the beam interaction point and perpendicular to the thrust axis.

- the momentum of the lepton in the c.m. frame.
  Choosing a lepton removes most of hadronic backgrounds. Cutting its momentum at 500 MeV removes low energetic leptons originating from, for instance, pair production.

- the Fox-Wolfram moment h_2h_0.
  It helps to separate events from continuum and those originated from $\Upsilon(4S)$ decays. It is defined by the expression:

$$\frac{\sum_{ij} \frac{|p_i||p_j|}{E_{vis}^2} \times P_2(\cos\theta_{ij})}{\sum_{ij} \frac{|p_i||p_j|}{E_{vis}^2} \times P_0(\cos\theta_{ij})} \tag{3.1}$$

  where P_l are Legendre polynomials, E_{vis} is the detected energy, θ_{ij} is the opening angle between particles i and j and $p_{i,j}$ is the momentum of particle i or j respectively. Events with $h_2h_0 > 0.2$ are kept. This rejects a large fraction of B events which have a more spherical topology with respect to charm events.

- the invariant mass of the hemisphere opposite to the one where the candidate is situated(m_{opp}). We accept events with $m_{opp} > 0.5\ GeV/c^2$. This cut rejects lepton pairs and two-photon events.

- the invariant mass of the system (electron+leading)(m_{tag}).
  Here leading stands for the most energetic particle in the hemisphere of the candidate. Events are accepted if $m_{tag} > 0.13\ GeV/c^2$. This cut removes events where the lepton is the only particle in the hemisphere.

Fractions of events selected by the skim in data and in different simulation samples are given in Table 3.2. The fraction of events selected in data appears to be lower than for events selected in simulation because of the presence, in data, of additional background sources.

Type	remainder
Data	2%
Charm Events	9%
$B\bar{B}$ Events	6%
Light Quark Events	3%
Signal	62%

Table 3.2: *Events remaining after the CharmSL skim selection (%).*

3.1.3 Event reconstruction

The approach used to reconstruct D^+ mesons decaying into $K^-\pi^+e^+\nu_e$ is similar to the one used in previous analyses studying $D^0 \to K^-e^+\nu_e$ [41] and $D_s^+ \to K^+K^-e^+\nu_e$ [42].

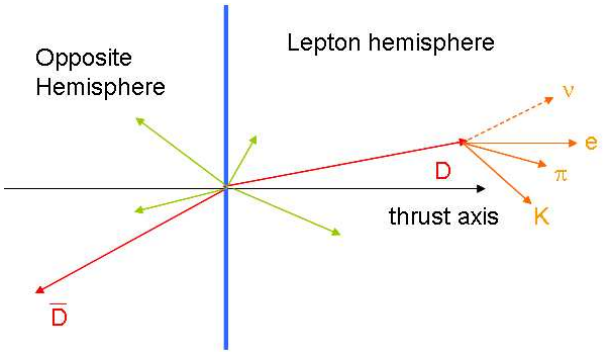

Figure 3.1: *Determination of the two hemispheres.*

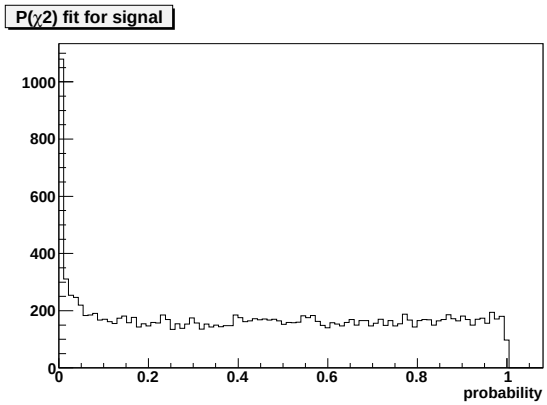

Figure 3.2: χ^2 *vertex fit probability for* K^-, π^+, e^+ *tracks in signal events*

Charged and neutral particles are boosted to the center of mass system and the event thrust axis is determined. A plane perpendicular to this axis is used to define two hemispheres.

A candidate corresponds to a positron, a charged kaon and a pion, present in the same hemisphere. One reconstructs a vertex using these 3 tracks. We only accept events with χ^2 probability for the vertex bigger than 10^{-7}. Figure 3.2 presents the χ^2 probability for signal events passing this condition.

All other tracks, in the hemisphere, are defined as "spectators". They most probably originate from the beam interaction point and are emitted during hadronisation of the created c and $\overline{c}$ quarks. The "leading" is the spectator particle having the highest momentum. Information from the spectator system is used, to reduce the contribution from the combinatorial background. As charm hadrons take a large fraction of the charm quark energy, charm decay products have, on average, higher energies than spectator particles.

To estimate the neutrino (ν_e) momentum, a constrained fit, imposing the D^+ mass to the $(K^-\pi^+e^+\nu_e)$ system, is applied. In this fit, estimates of the D^+ direction and of the neutrino energy are included from measurements obtained from all tracks registered in the event. The D^+ direction estimate is taken as the direction of the vector opposite to the momentum sum of all reconstructed particles but the kaon, the pion and the positron. The neutrino energy is evaluated by subtracting from the hemisphere energy, the energy of reconstructed particles

contained in that hemisphere. The energy of each hemisphere is evaluated by considering that the total center of mass energy is distributed in two objects of mass corresponding to the measured hemisphere masses [1].
As a D^+ is expected to be present in the analyzed hemisphere and as at least a D meson is produced in the opposite hemisphere, minimum values for hemisphere masses have been imposed.

For an hemisphere i, the energy $E^{(i)}_{hem}$ and the mass $m^{(i)}_{hem}$ are defined as:

$$E^{(i)}_{hem} = \frac{1}{2}\left[\sqrt{s} + \frac{m^2_{(i),hem} - m^2_{(j),hem}}{\sqrt{s}}\right] \tag{3.2}$$

$$m^{(i)}_{hem} = max(m^i_{hem}(measured), m_D). \tag{3.3}$$

The missing energy in an hemisphere is the difference between the hemisphere energy and the sum of the energy of the particles contained in this hemisphere ($E^{miss}_{hem} = E_{hem} - \sum_{i=1}^{n_hem} E_i$). In a given collision, some of the resulting particles might take a path close to the beam line, being therefore undetected. In such cases, as one uses all reconstructed particles in an event to estimate the D meson direction, this direction is poorly determined. The removal of these events is made by only accepting those where the cosine of the angle between the thrust axis and the beam line ($\cos(\theta_{thrust})$) is smaller than 0.7. In cases where there is a loss of a large fraction of the energy contained in the opposite hemisphere, the reconstruction of the D is also damaged. To minimize the impact of these cases, events with a missing energy in the opposite hemisphere higher than 3 GeV are rejected.

In the mass constrained fit, estimates of the uncertainties on the angles defining the D^+ direction and on the missing energy have to be also provided. The estimates are parameterized versus the energy missing in the opposite hemisphere which is used to quantify the quality on the reconstruction for a given event. Parameterizations of these uncertainties are obtained in data and in the simulation using $D^+ \to K^-\pi^+\pi^+$ for which we can compare the measured D^+ direction with its estimate using the algorithm applied in semileptonic decays. These events allow also to control the missing energy estimate and the estimate of the corresponding uncertainty (see Section 4.1.3).

3.1.4 Resolution on kinematic variables for signal

Simulated events used for this study correspond to reconstructed $D^+ \to \overline{K^{*0}}e^+\nu_e$ decays, generated using the SLPole EvtGen [62] option. Measured particles are matched to the simulated ones. Distributions of differences between reconstructed and generated values for the 5 dynamical variables are shown in Figure 3.3 and in 2D plots in Figure 3.4 . These distributions are only indicative as the full migration of events in 5D is included, event-by-event, in the fit procedure.

[1] The hemisphere mass is the mass of the system corresponding to the sum of the 4-vectors of particles contained in that hemisphere.

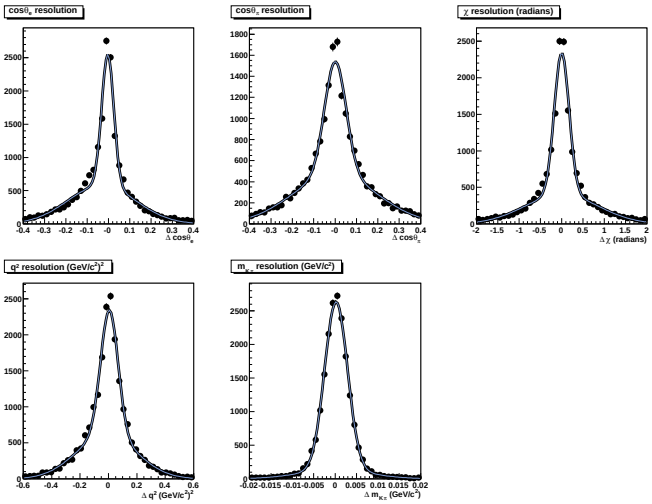

Figure 3.3: *Distributions of the difference between reconstructed and generated values of the five dynamical variables. These distributions are normalized to unity. They have been fitted using a double Gaussian. Table 3.3 provides the values of the fitted standard deviations and of the fraction of events contained in the broad component.*

variable resolution	σ_1	σ_2	fraction of events in broadest Gaussian
$\cos\theta_e$	0.028	0.159	0.621
$\cos\theta_\pi$	0.050	0.159	0.633
χ	0.174	0.860	0.508
$q^2\ (GeV^2)$	0.061	0.213	0.546
$m_{K\pi}\ (\mathrm{GeV/c^2})$	0.0027	0.0085	0.138

Table 3.3: *Resolutions for all five variables. They are obtained by fitting the sum of two Gaussians on the distributions of the difference between reconstructed and generated values of a given variable. The fraction of events fitted in the broad component is given in the last column.*

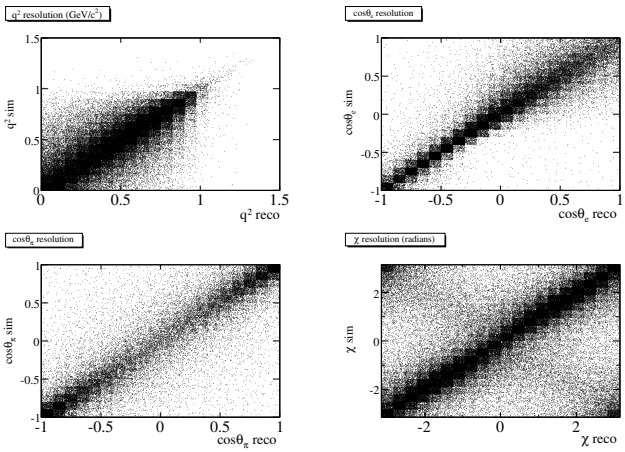

Figure 3.4: *2D distributions presenting the resolution effect for all dynamical variables but $m_{K\pi}$ as this last variable as very high resolution. The horizontal and vertical axis correspond to the reconstructed and the simulated values of each variable.*

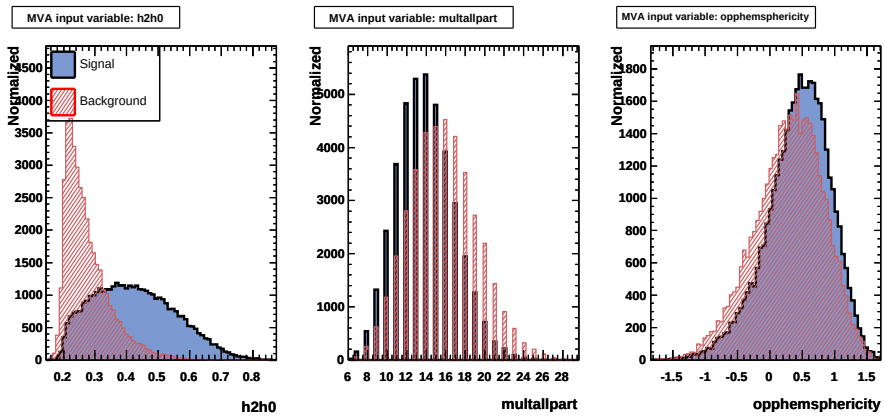

Figure 3.5: *Distributions for signal and $\Upsilon(4S)$ background events of variables used in F_{bb}.*

3.2 Background rejection

Definitions of the different variables used to decrease the background level are explained.
These variables consist mainly of Fisher discriminant variables. This discriminant is a linear combination of input variables which allows for a maximisation of the separation between signal and background distributions. The Fisher discriminant takes into account up to linear correlations between input variables.
We use TMVA (Toolkit for multivariate analysis) [63] to perform the construction of these discriminant variables. If most of the quantities entering in the discriminants are similar to those used already in previous charm semileptonic analyses, new informations are introduced to benefit from the measurable decay distance of the D^+ meson.

At this level the background rejection has not been really optimized as this requires the evaluation of systematic uncertainties, especially on background control.

It has to be noted also that events have already been selected by cuts applied at the CharmSL skim level and values quoted, in the following for rejection and efficiency are relative to this first selection.

3.2.1 $B\bar{B}$ background rejection

The main differences between $\Upsilon(4S)$ and $e^+e^- \rightarrow c\bar{c}$ events are the topology (the former have a spherical distribution of tracks whereas the latter are more jet-like) and the mean number of particles (B decays have more tracks on average than continuum events).

These differences are used to define a Fisher discriminant variable (F_{bb}) in order to separate signal from $\Upsilon(4S)$ decays.

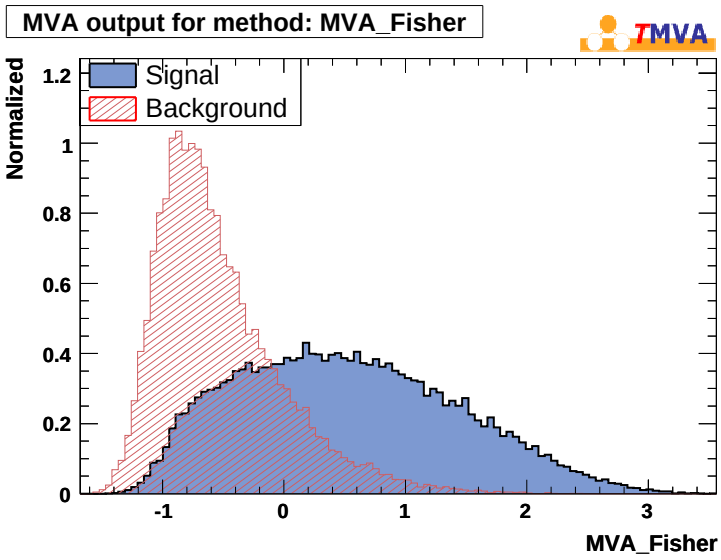

Figure 3.6: *Distributions of F_{bb} for signal and for $\Upsilon(4S)$ background events.*

$$F_{bb} = 1.21897 + 2.55276 * h_2h_0 - 0.221978 * mult - 0.3393 * opphemsphericity \quad (3.4)$$

where $mult$ is the event particle multiplicity and $opphemsphericity$ is equal to $\log(-1 \times \log(sphericity))$ [2] measured with particles contained in the hemisphere opposite to the candidate. When used in Eq. (3.4), these variables must be normalized such that they vary between 0 and 1 over their variation range: $x^{Fisher} = 2 * \frac{x - x_{min}}{x_{max} - x_{min}} - 1$. The values for x_{max} and x_{min} are given in Table 3.4.

Distributions for signal and $\Upsilon(4S)$ background events are given in Figure 3.5, for each variable entering in the expression of F_{bb}. Distributions of F_{bb} for the two event categories are displayed in Figure 3.6.

variable	x_{min}	x_{max}
h_2h_0	0.163936	0.846598
$mult$	6	28
$opphemsphericity$	-1.87648	1.61012

Table 3.4: *Minimum and maximum values of the variables entering in the Fisher discriminant variable against the $B\bar{B}$ background.*

Remaining fractions of signal and background events of different origin, obtained for several values of the

[2] Instead of the sphericity variable itself, this quantity is transformed as indicated in the expression of $opphemsphericity$ to have a bell-shape like distribution.

cut on F_{bb} are given in Table 3.5:

cut value	$signal$	$\Upsilon(4S)$	$c\bar{c}\ bkg$	$uds\ events$
> -0.3	80%	26%	71%	70%
> 0	70%	15%	59%	59%
> 0.25	60%	10%	49%	49%

Table 3.5: *Efficiency on signal and background for different values of the cut on F_{bb}. These values do not include the skim efficiency.*

The variation of the $\Upsilon(4S)$ background rejection versus the efficiency to signal is displayed in Figure 3.7. A

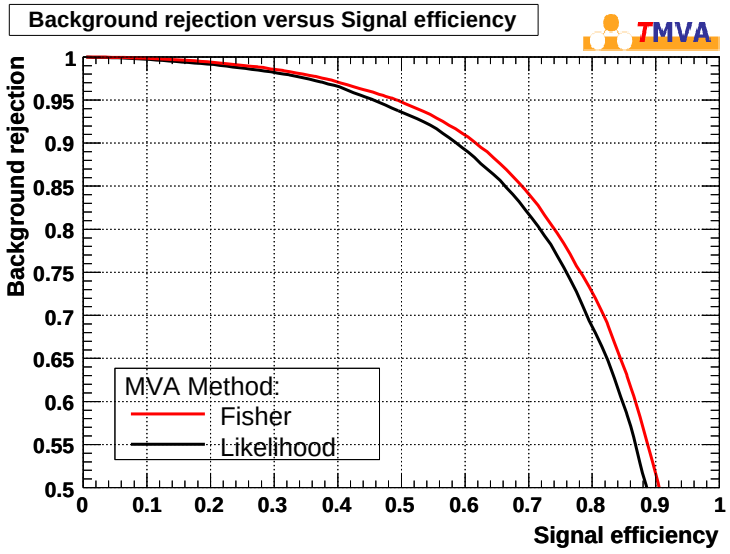

Figure 3.7: $\Upsilon(4S)$ *background rejection versus the efficiency to signal when cutting on F_{bb}.*

cut at 0 retains 70% of signal and removes 85% of the $\Upsilon(4S)$ background. The corresponding value for the ratio signal/background (S/B) is 0.23, where B stands for the sum all background sources.

3.2.2 $c\bar{c}$ background rejection

The charm background suppression is obtained using two procedures. From this point onwards a cut on F_{bb} at 0 is applied on all distributions. The main source of charm background comes from the association of charm meson decay products (for instance $D^0 \to K^- e^+ \nu_e$) with fragmentation particles (in this example a π) or decay particles from excited charm states (π from the decay $D^{*+} \to D^0 \pi^+$).

Rejection of events $D^{*+} \to D^0 \pi^+$, with $D^0 \to K^- e^+ \nu_e$

One component of this background can be isolated and eliminated efficiently. It comes from $D^{*+} \to D^0 \pi^+$, $D^0 \to K^- e^+ \nu_e$ decays. For each $(K\ \pi\ e)$ candidate, we determine if the $(K,\ e)$ pair can originate from a $D^0 \to K^- e^+ \nu_e$ decay with the D^0 cascading from a $D^{*+} \to D^0 \pi^+$. In this purpose we do the same analysis as for the $D^0 \to$

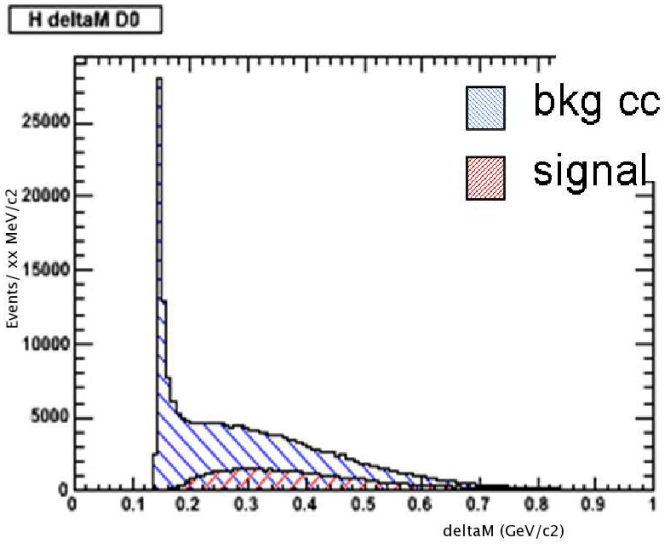

Figure 3.8: *Distributions of the invariant mass difference $\delta m = m(D^0\pi) - m(D^0)$ for signal and charm background events. The peak close to threshold corresponds to $D^{*+} \to D^0\pi^+,\ D^0 \to K^-e^+\nu_e$.*

$K^-e^+\nu_e$ channel [41]. A mass constrained fit is applied to reconstruct the D^0 momentum and we evaluate the mass difference $\delta m = m(D^0\pi^+) - m(D^0)$. Here $m(D^0\pi^+)$ is measured by combining a charged pion, of correct charge, with the fitted D^0 momentum and $m(D^0)$ is the physical mass of the D^0. This variable has a sizeable peak induced by $D^{*+} \to D^0\pi^+$ events. Figure 3.8 gives the δm distributions for background and signal events. Events with $\delta m > 0.18\ GeV/c^2$ are selected. This removes a negligible fraction of signal and eliminates 27% of the charm background and 93% of this particular background.

Rejection of fake electrons

There are some events where the electron candidate is in fact a mis-identified pion. In this case, no semileptonic desintegration occurs and the event has a particular topology, namely the q^2 value is very low and $cos\theta_e$ is preferably high, peaking near 1. The distribution for these events versus these two variables and the $K\pi$ mass are shown in Figure 3.9.
We exclude around 40% of this background rejecting all events with $q^2 < 0.06\ GeV^2$ and $cos\theta_e > 0.85$. This cut removes virtually no signal events.

Fisher discriminant variable for charm background removal

To reduce the charm background from other origins we have used the fact that D decay products have on average a larger energy than particles from fragmentation and that the D^+ has a relatively large lifetime as compared to other charm hadrons.

Variables exploiting the first property are similar to those used in previous analyses of charm semileptonic decays. The other property is exploited using the χ^2 probability of the $K\pi e$ secondary vertex and the fact that a

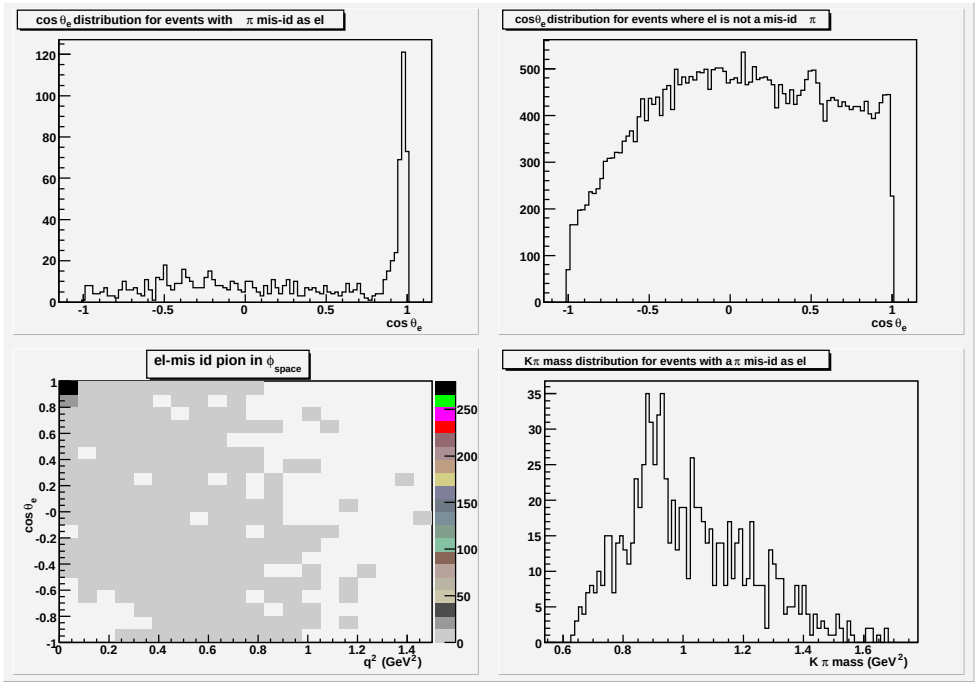

Figure 3.9: *Several distributions for charm background events where the electron candidate is(or is not) a mis-identified π.Upper left plot: distribution of events versus $cos\theta_e$ where electron is a mis-id π, Upper right plot:distribution of events versus $cos\theta_e$ where electron is not a mis-id π. Lower left plot: 2D distribution in $(q^2, cos\theta_e)$ where the eletron candidate is a mis-id π. Lower right plot: $K\pi$ mass distribution for events where electron candidate is a mis-id π.*

large fraction of the background is coming from pions from fragmentation which originate from the beam interaction region. We have thus compared also the distance of closest of approach of the pion to the primary and to the secondary vertex.

The following variables have been used:

- *specmass*: the spectator system mass, which has lower values for signal events;
- *plead*: the momentum of the leading spectator particle;
- *Pchi2*: equal to $\log(-\log P(\chi^2))$, where $P(\chi^2)$ is the χ^2 probability of the D^+ mass constrained fit;
- *Pchi2kepi*: equal to $\log(-\log(P(\chi^2_{K\pi e})))$ where $P(\chi^2_{K\pi e})$ is the χ^2 vertex fit probability of the $K,\ \pi,\ e$ trajectories;
- *pd01*: the D^+ momentum after the D^+ mass constrained fit;
- *chi2Dflight*: the logarithm of the D^+ flight significance. This last quantity is equal to the square of the distance between the secondary and the interaction vertex, projected along the D^+ momentum direction and divided by the uncertainty on the measured flight distance. Events are kept if this quantity is positive;
- *rRatio*: the logarithm of the ratio between the absolute value of the XY-offset of the pion track to the beam spot divided by its error and the absolute value of the XY-offset of the π track to the decay vertex divided by its error.

Distributions of these variables obtained for signal and background are given in Figure 3.10 and 3.11.
In the *specmass* distribution, the peak at zero corresponds to events with no spectator particle or a single photon (or electron). The other peak on the right is for events with a single spectator pion. Events at zero in the *plead* distribution have no spectator particle. The two peaks in the *chi2Dflight* distribution result from the transition between two regimes for the flight significance variable, which are presented in Figure 3.12. The left peak originates from events where the resolution is comparable to the D flight, while the right peak corresponds to events where the two vertices are well separated

The expression for the Fisher discriminant, F_{cc}, is:

$$\begin{aligned} F_{cc} \;=\; 3.109 \;+\; 1.339 * pd01 \;+\; 2.139 * plead \;+\; 1.542 * chi2Dflight \\ -\; 0.837 * Pchi2 - \; 1.063 * Pchi2kepi \;+\; 0.04427 * specmass \\ +\; 1.44 * rRatio\,. \end{aligned} \tag{3.5}$$

and distributions of F_{cc} obtained for signal and background are given in Figure 3.13.

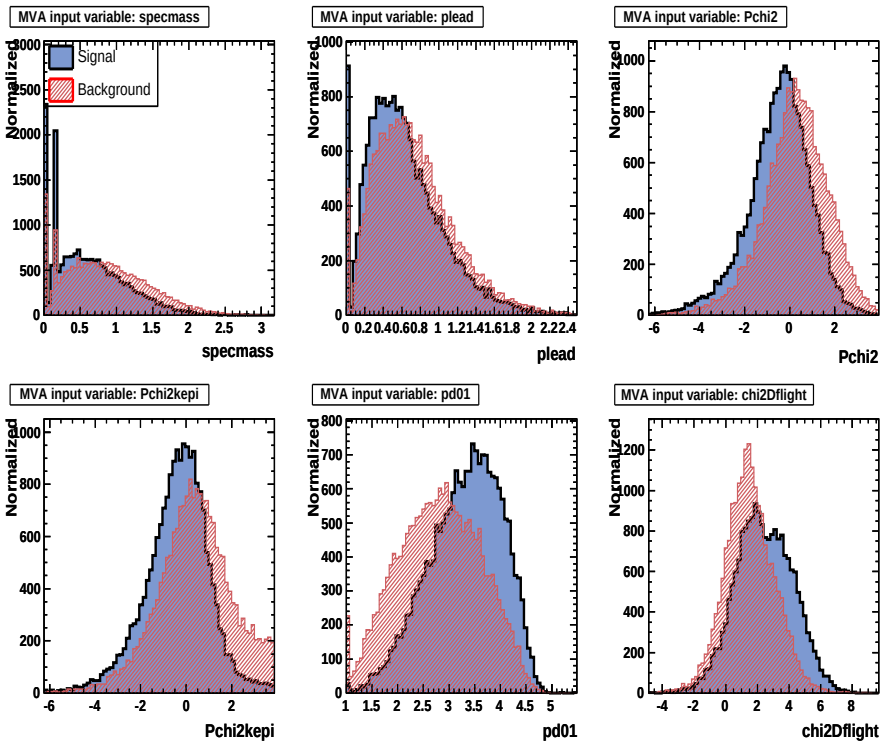

Figure 3.10: *Distributions of several variables used in the Fisher discriminant against the charm background.*

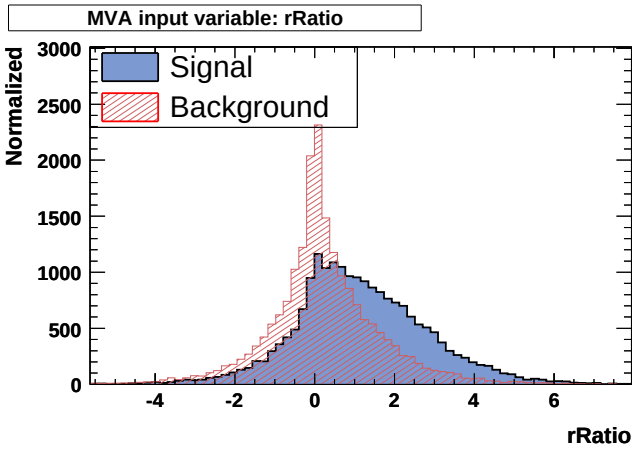

Figure 3.11: *Distributions of the values of the variable rRatio for signal and charm background events.*

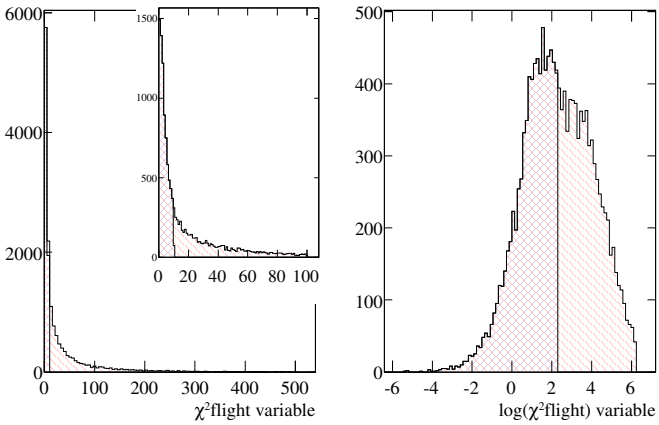

Figure 3.12: *Left: D flight significance (χ^2) distribution for signal. Right: chi2Dflight distribution for signal. Distributions on the left and right with the same color correspond to the same events.*

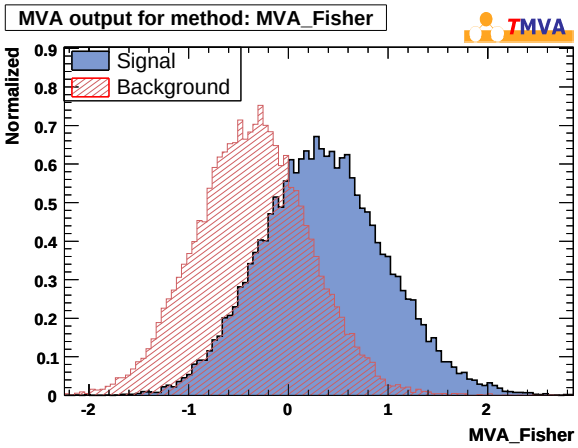

Figure 3.13: *Fisher discriminant variable distribution for charm background and signal events.*

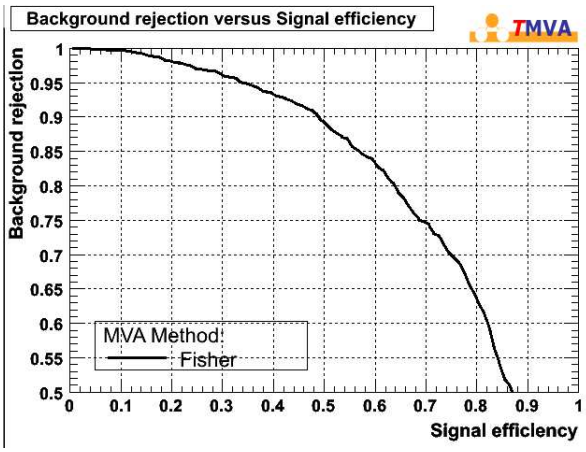

Figure 3.14: *$c\bar{c}$ background rejection versus the efficiency to signal when cutting on F_{cc}.The skim selection and the cut $F_{bb} > 0$ are already applied.*

One can note again that variables used in Eq. (3.5) must be written in the form $x^{Fisher} = 2 * \frac{x - x_{min}}{x_{max} - x_{min}} - 1$, where the values for x_{max} and x_{min} are given in Table 3.6.
Some events may fall outside the limits stated in Table 3.6. Bringing those out of boundaries events back to the limits does not change the results. We have quantified this using BaBar Runs1-5, observing that with this procedure we collect only 14 more events out of around 350k events.

variable	x_{min}	x_{max}
$pd01$	> 1	5.48123
$pLead$	0	8.33906
$chi2Dflight$	-5.75711	13.5797
$Pchi2$	-9.49346	3.95776
$Pchi2kepi$	-9.71384	3.86912
$specmass$	0	3.84566
$rRatio$	-10.3017	13.3444

Table 3.6: *Minimum and maximum values of the variables used in F_{cc}.*

We present in Table 3.7 the efficiency to signal and background for different values of the cut on the Fisher variable F_{cc}.

cut point	$signal\ remaining$	$bkg\ remaining$
> 0.4	50%	10%
> 0.5	40%	6%
> 0.7	30%	3.5%

Table 3.7: *Efficiency for signal and $c\bar{c}$ background for different cuts on the F_{cc} discriminant variable. The skim selection and the cut $F_{bb} > 0$ are already applied.*

The variation of the $c\bar{c}$ background rejection versus the efficiency to signal is displayed in Figure 3.14.

3.2.3 uds background rejection

As light quark events are not expected to contain prompt electrons, the corresponding background rejection is improved by eliminating events in which the candidate electron belongs to the electron list and also to the gamma conversion daughters list. Efficiencies of this selection, against converted photons, for uds and other event samples are given in Table 3.8.

event sample	efficiency
$c\bar{c}$ bkg	90%
$B^0\bar{B}^0$	95%
B^+B^-	92%
light $q\bar{q}$	53%
generic signal	98%
$data$	92%

Table 3.8: *Fraction of background, signal and data events remaining after removal of candidate electrons from gamma conversion.*

3.2.4 Summary on background rejection

The cumulative efficiency for background events obtained after applying the different cuts is given in Table 3.9.

sample	ϵ_{skim}	$\otimes\epsilon_{precuts}$	$\otimes\epsilon_{Fbb}$	$\otimes\epsilon_{Fcc+\delta_M)}$	$\otimes\epsilon_{missid-\pi}$
$c\bar{c}\ bkg$	1	0.356	0.223	0.012	0.012
B^0B^0	1	0.343	0.056	0.025	0.025
B^+B^-	1	0.313	0.049	0.016	0.016
$light\ q\bar{q}$	1	0.092	0.057	0.017	0.017
$generic\ signal$	1	0.641	0.460	0.198	0.198
$data$	1	0.309	0.151	0.018	0.018

Table 3.9: *Cumulative efficiency for signal and background events selected with $F_{bb} > 0$ and $F_{cc} > 0.5$.*

These values do not include the skim selection efficiency (ϵ_{skim}). Values quoted in Table 3.9 include the removal of badly reconstructed events and conversion electrons(column 3), effects from the cut on Fisher discriminant variables ($F_{bb} > 0$, $F_{cc} > 0.5$) and the removal of fake electron candidates (last column).

3.3 Signal selection efficiency

Efficiency for the generic signal simulation is also given in Table 3.9. Including the skim selection, it is on average equal to 2.9%. Its variation projected over the 5 kinematic variables, and including the skim selection efficiency, is given in Figure 3.15. It is rather uniform over these projections.

The observed decrease in efficiency at negative $\cos\theta_e$ comes from the effect of the semileptonic skim selection. If one removes the cut on $p_e > 0.5$ GeV/c the trend would disappear.

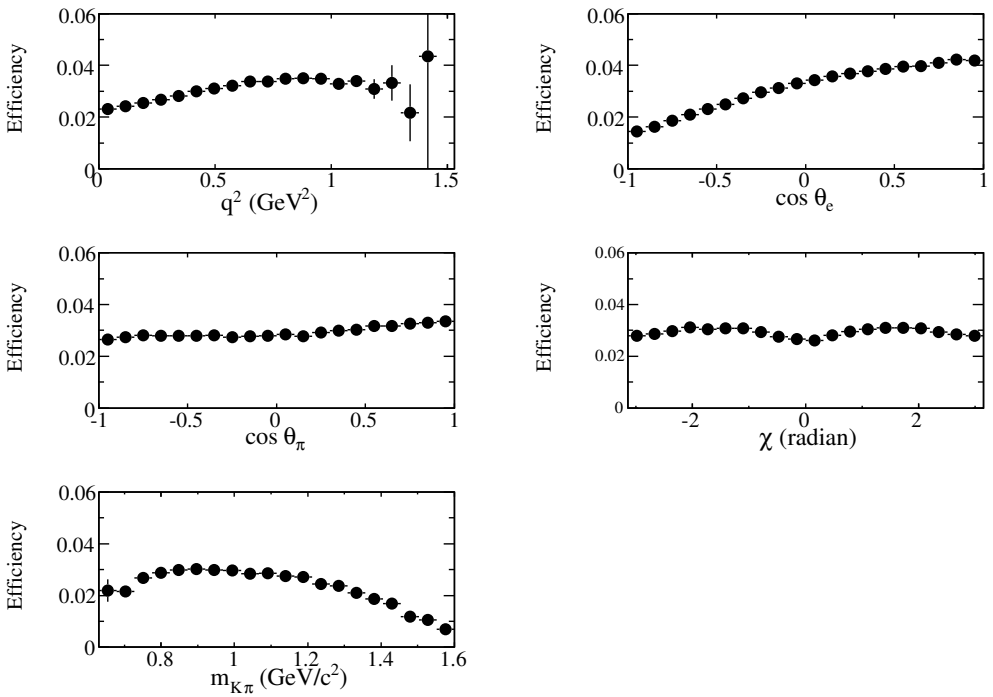

Figure 3.15: *Efficiency for signal reconstruction and selection after all cuts applied, including the skim and the cuts* $F_{bb} > 0$ *and* $F_{cc} > 0.5$.

2-D plots of efficiency which corresponds to $\cos\theta_e$ versus q^2 and to $\cos\theta_\pi$ versus $m(K\pi)$ are presented in Figure 3.16.

One can observe that the region at low q^2 and low $\cos\theta_e$ has a lower efficiency. This is just a direct consequence of cutting events with a lepton momentum lower than 500 MeV/c.

The efficiency in 5D is presented in Figure 3.17, where the phase space is divided in 2800 bins (these are those used in the fits done in this analysis). It corresponds to a coverage over the full decay phase space.

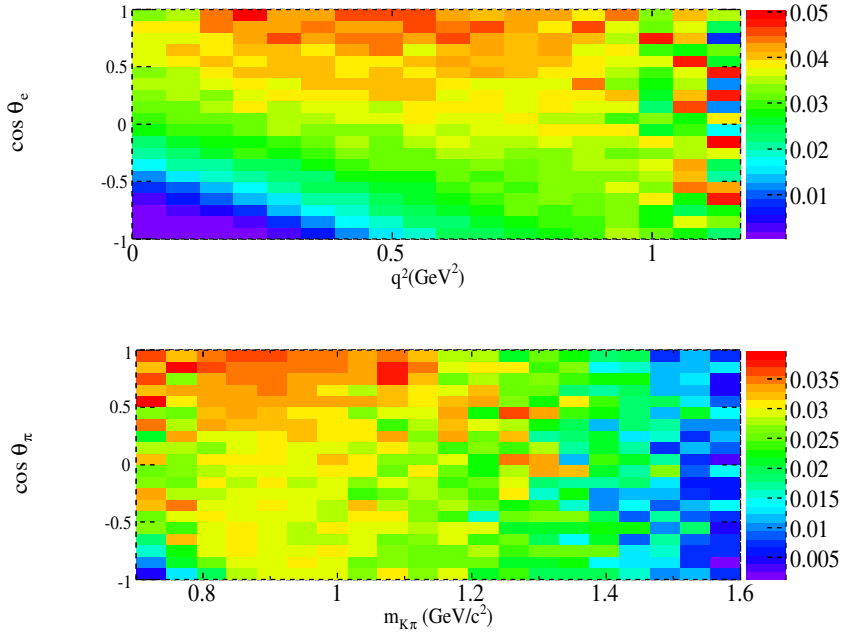

Figure 3.16: *2-D efficiency distributions for signal reconstruction after all cuts applied, including* $F_{bb} > 0$ *and* $F_{cc} > 0.5$. *Top: Efficiency for the leptonic sector variables* ($\cos\theta_e$ *versus* q^2). *Bottom: Efficiency for the hadronic sector variables* ($\cos\theta_\pi$ *versus* $m(K\pi)$).

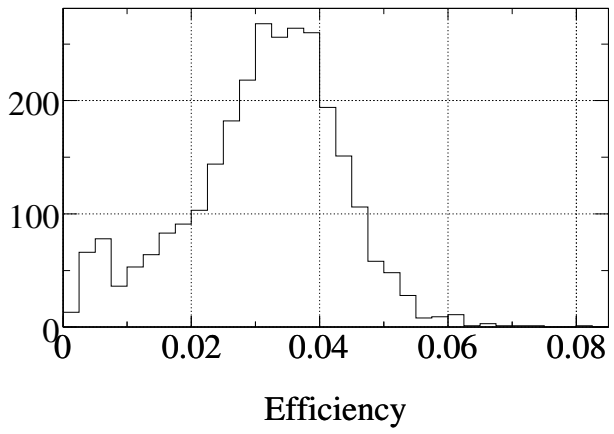

Figure 3.17: *Distribution of efficiency over the 2800 bins containing the physical phase space. The efficiency of signal reconstruction is found after all cuts are applied, including* $F_{bb} > 0$ *and* $F_{cc} > 0.5$.

Chapter 4

Adjustments applied to the simulation

This chapter presents several controls and adjustments applied to the simulation. First we present the tuning applied to the signal simulation, followed by the tuning on the $B\bar{B}$ and $c\bar{c}$ backgrounds. Finally we present the construction of the specific signal control sample used in the fit procedure.

4.1 Signal simulation tuning

In this section we present the different corrections applied to the MC signal simulation. They are done at two levels.

The first tuning corresponds to the correction of the simulated differential decay distribution of signal events because of a problem in the generator and also to use a different model for the decay distribution.

The second tuning corresponds to corrections defined from measurements of the distributions of variables, entering in Fisher discriminants. These corrections are obtained with $D^+ \to K^-\pi^+\pi^+$ events. In the fitting procedure, explained in Section 6, to control the background rate, we use the shape of the distribution of the F_{cc} variable for signal and background. It is therefore a requirement for this analysis to control the shape of the distributions of individual variables entering into the definition of F_{cc}.

$D^+ \to K^-\pi^+\pi^+$ events are used also to compare the resolution obtained in data and in simulation on the D^+ direction determination and on missing energy, by the algorithm used to reconstruct semileptonic decays.

4.1.1 Correction applied on generated charm semileptonic decays into a resonant state

The generic simulation of $e^+e^- \to c\bar{c}$ events in BaBar appears not to be correct in particular when a charm hadron decays semileptonically.
This is because the model (ISGW2) used to account for the q^2 dependence of hadronic form factors is rather different from actual measurements and also because, in $D \to P_1P_2e^+\nu_e$, where P_1 and P_2 are pseudo scalar mesons, the 5 kinematic variables are not generated according to the expected differential decay rate.
To cure the first problem, special samples of signal events have been generated assuming a pole mass behaviour of the hadronic form factors (SLPOLE model). This is done easily by activating the corresponding option in the generator. These events are used, in the following, to fit data. In anycase the difference between real and expected

differential decay rate distributions is not critical as we are going to measure the q^2 variation of the decay rate. At this level we would like to have simply a simulated distribution that does not differ much from data.

The second problem is due to the fact that the algorithm generates, in a first step and independently of the values of the four variables (q^2 and the three angles), the mass of the hadronic system by using for instance a Breit-Wigner distribution. This is not correct because Eq. (1.43) cannot be factorized in this way. Figure 4.1 presents this effect, and one clearly sees the disagreement over all the mass spectrum and over the q^2 distribution between the expected distribution (TOY) and what EvtGen provides by default. Moreover EvtGen only produces events within a mass range of $\pm 15\Gamma$ on each side of the pole mass. For masses below the K^{*0} pole this does not cause any problem but for higher masses all events are cut above $1.65\ GeV/c^2$.

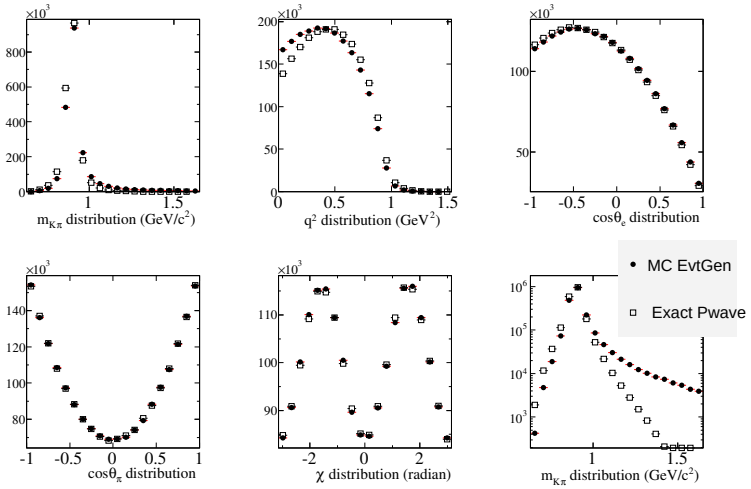

Figure 4.1: *Comparison between EvtGen (PHOTOS off) and correct distribution for a decay $D^+ \to \bar{K}^{*0} e^+ \nu_e$. Distributions are normalised to the same number of events.*

Also, since for a given mass value, EvtGen generates randomly sets of values for the other 4 variables in a loop until a given set is accepted, it happens that if the maximum number of iterations is somewhat limited, there will be less events in phase space regions with low probability, for instance high mass and low q^2. All these effects are acknowlegded in the following.

As the problem we want to cure is purely of generator origin, after having verified that one can reproduce it with a toy we have preferred to use results from large statistics toy simulations that reproduce the EvtGen algorithm so to define the corrections . With this large statistics we are then able to define more precisely the correction of the MC EvtGen signal simulation.

The following procedure is used: for each event the $K\pi$ mass value is generated using an accept-reject method where the PDF that corresponds to the mass distribution is independent of the other four variables and is given by:

$$PDF(m) \propto p^* \times \left| \frac{-m_{K^{*0}(892)} \Gamma_{K^{*0}}(892) F_1(m)}{m^2 - m^2_{K^*(892)} + i m_{K^*(892)} \Gamma_{K^*(892)}(m)} \right|^2 . \tag{4.1}$$

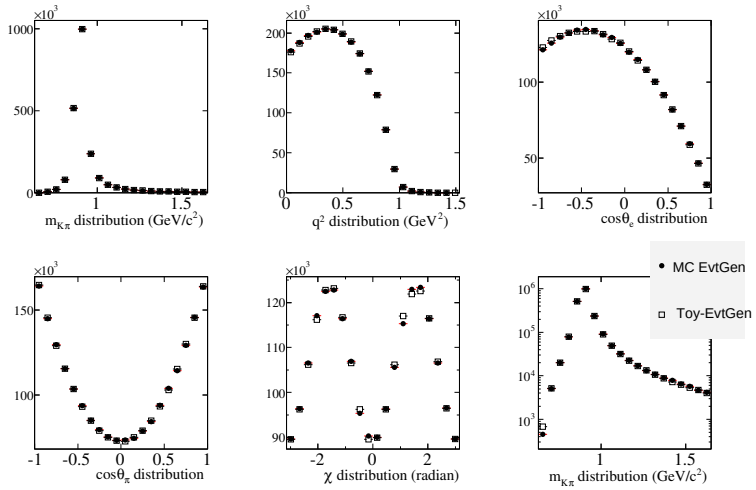

Figure 4.2: *Decay variables distributions. Comparison between events generated with the MC EvtGen (no Photos generator used) program using the SLPole $D^+ \to \bar{K}^{*0} e^+ \nu_e$ model and those obtained with a toy generator using a similar algorithm as EvtGen. The two samples are normalized to the same number of events.*

In this expression:

- m is the $K\pi$ mass;
- $m_{K^*(892)}$ is the $K^*(892)$ pole mass;
- $\Gamma^0_{K^*(892)}$ is the nominal width of the $K^*(892)$ for $m = m_{K^*(892)}$;
- $\Gamma_{K^*(892)}(m)$ is the mass dependent $K^*(892)$ width. $\Gamma_{K^*(892)}(m) = \Gamma_{K^{0*}(892)} \frac{p^*}{p_0^*} \frac{m_{K^*(892)}}{m} F_1^2(m)$;
- $F_1(m) = \frac{p^*}{p_0^*} \frac{B(p^*)}{B(p_0^*)}$ where B is the Blatt-Weisskopf damping factor: $B = 1/\sqrt{1 + r_{BW}^2 p^{*2}}$.

The values of the parameters entering in these expressions are the same as those used in EvtGen.

Once a mass value is accepted, random combinations of the other variables are produced and are accepted/rejected using a PDF which is proportional to the $D^+ \to \overline{K^{*0}}(892) e^+ \nu_e$ differential decay rate ($d^4\Gamma/dq^2 d\cos\theta_e d\cos\theta_\pi d\chi$), at fixed value of the $K\pi$ mass, given in Eq. 1.47.

In Figures 4.2 and 4.3 are compared projections of the differential decay rate distribution over the 5 kinematic variables. They are obtained from the SLPOLE generator in EvtGen, without calling PHOTOS, and from an independent simulation "'a la EvtGen". They agree within 1%. For this comparison, values of the parameters which determine the form factors as $r_2,\ r_V,\ m_A$ and m_V are the same in the two programs.

In Figures 4.4-4.5 are compared distributions obtained with the toy program "à la EvtGen" and the exact result expected for a P-wave.

To correct for the observed difference, the ratio between the projected mass distributions, normalized to the same number of entries, is used. It is parameterized as an exponential of a 7th order polynomial, and fitted over the full mass range. This ratio is used as a $K\pi$ mass dependent weight attached to each event generated "à la EvtGen".

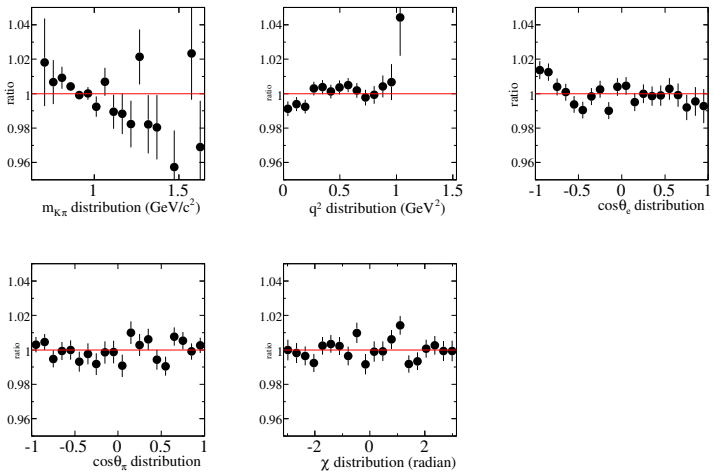

Figure 4.3: *Ratio between the Toy and the MC distributions given in Figure 4.2.*

To evaluate if there are remaining differences between the exact and corrected differential decay rates for a P-wave, we have compared binned distributions obtained with the two models. The two samples are normalized to the same number of events and we have plotted the difference between bin contents divided by the corresponding uncertainty:

$$x = \frac{N(exact) - N(EvtGen - like\ corrected)}{\sqrt{N(exact) + N(EvtGen - like\ corrected)}} \tag{4.2}$$

The distribution of the x variable measured in each of the 2800 bins used in the measurement of the semileptonic differential decay rate (see Section 6) is given in Figure 4.8. In this comparison 10 million of signal events have been generated (40 times the data). This distribution is fitted using a Gaussian whose average value (-0.001 ± 0.019) and standard deviation (0.997 ± 0.014) are compatible with 0 and 1 respectively. This demonstrates that the applied correction to events generated with the EvtGen-like problem does not introduce any bias.

Of interest for the signal sample used in the data fit, is the region centered on the K^*_{892} pole mass value. Comparison between the distributions of the differential decay rate projected over the five kinematic variables is displayed in Figures 4.9 and 4.10, after corrections.

4.1.2 Correction of $c\bar{c}$ MC signal events for variables used in F_{cc} and F_{bb}

The decay $D^+ \to K^-\pi^+\pi^+$ is used to tune the simulation for the D^+ production caracteristics. Distributions of all variables, entering in the definition of Fisher discriminants, obtained in data and in the simulation are compared.

We have analyzed three events samples: simulated events from the continuum $e^+e^- \to c\overline{c}$, on-peak and off-peak data. These samples are normalized to the number of signal events measured with on-peak data when the

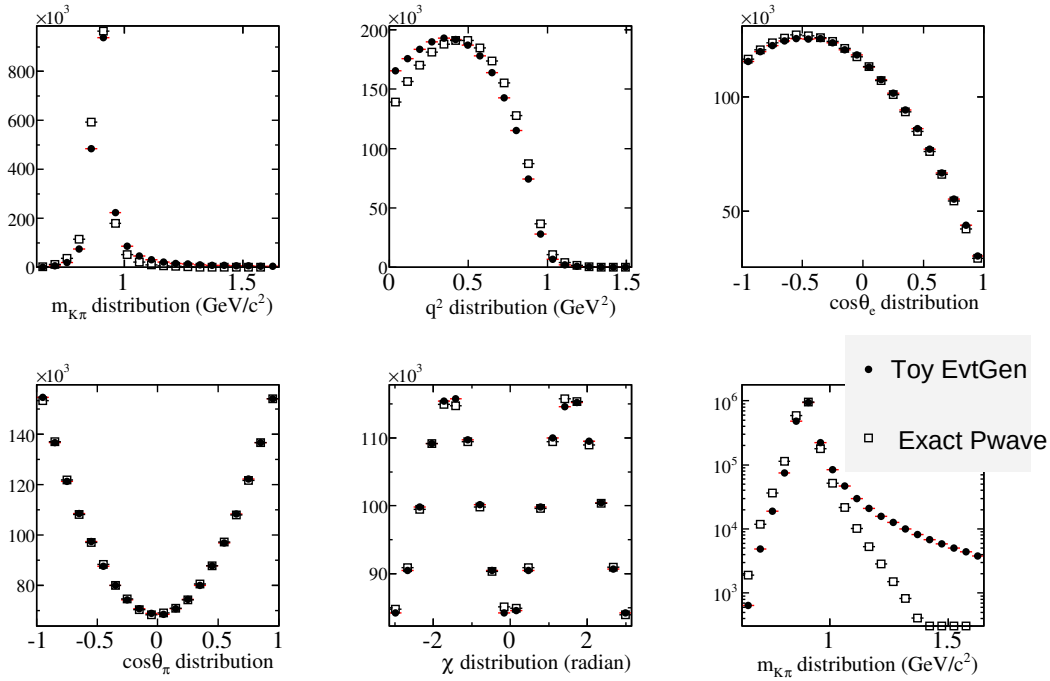

Figure 4.4: *Comparison between projected distributions over the 5 kinematic variables obtained with toy simulations, where one reproduces the EvtGen algorithm and the other reproduces correctly the P-wave. Distributions are normalized to the same number of events.*

D^+ is expected to originate from continuum. Such candidates are selected by requiring that the fraction of the beam momentum taken by the D^+ (x_D) exceeds 0.48 to eliminate D^+ cascading from B mesons. The off-peak data sample is used for events having $x_D < 0.48$.

Numbers of signal events analyzed using Run4 statistics are given in Table 4.1.

sample	D^+ signal
$x_D > 0.48$	
MC $e^+e^- \to c\bar{c}$	1174009 ± 1295
Data on-peak	957385 ± 1262
Data off-peak	225803 ± 602
$x_D < 0.48$	
Data off-peak	58754 ± 482

Table 4.1: *Number of reconstructed $D^+ \to K^-\pi^+\pi^+$ decays used to measure corrections on variables used in Fisher discriminants.*

$D^+ \to K^-\pi^+\pi^+$ event selection

Kaon and pion candidates are taken from the same lists of particles as used for the semileptonic decay channel. It is requested that the three tracks form a vertex with a loose cut of 10^{-7} on the χ^2 probability. The three

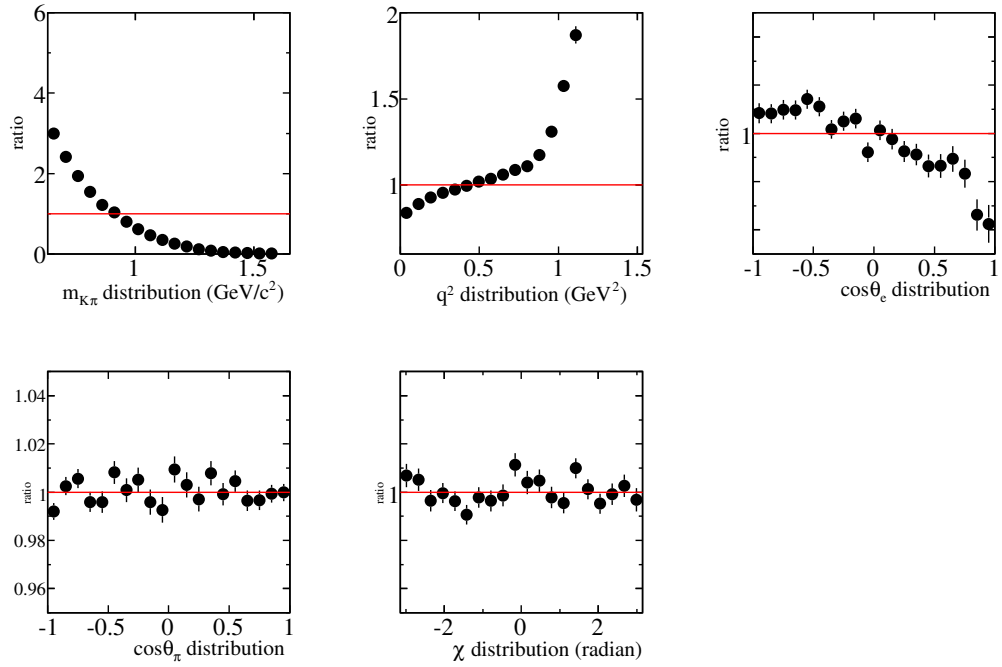

Figure 4.5: *Ratio between exact and EvtGen projected distributions over the 5 kinematic variables as given in Figure 4.4.*

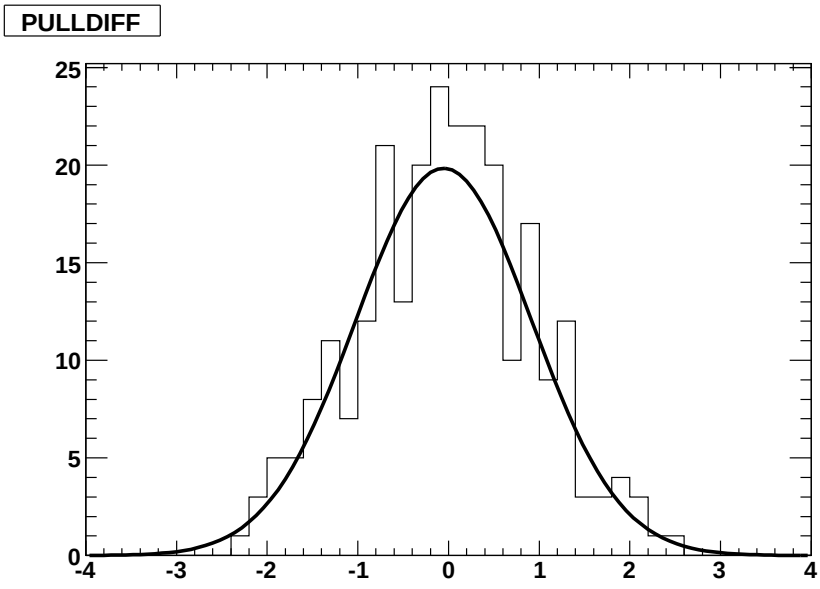

Figure 4.6: $\frac{N_{MCEvtGen}-N_{TOYEvtGen}}{uncertainty}$ *per bin coming from a* 20×20 *2D plot over* $m_{K\pi}, q^2$ *variables. Mean is* -0.05 ± 0.06 *and sigma is* 0.97 ± 0.06

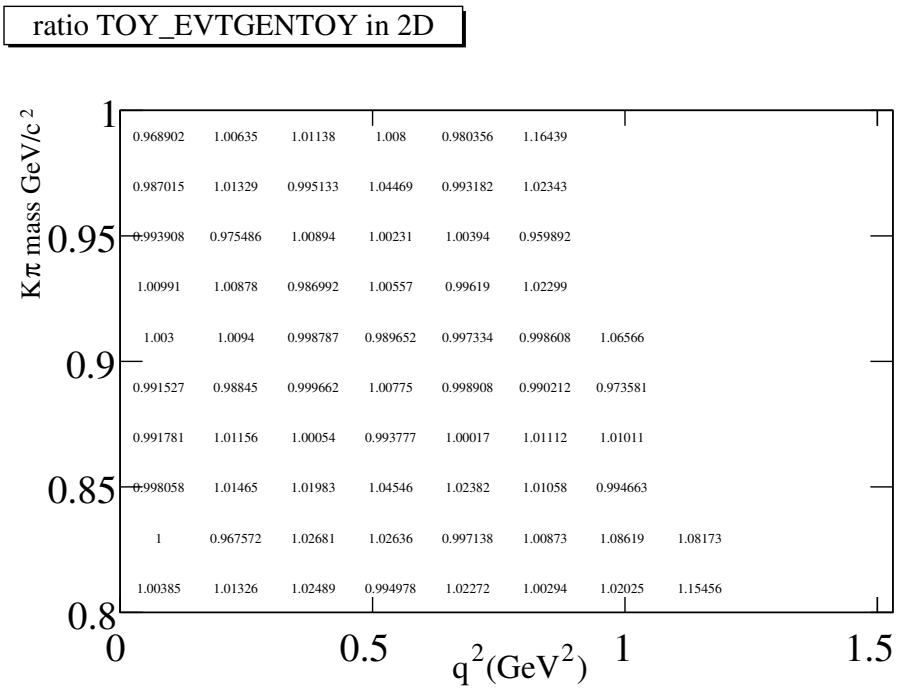

Figure 4.7: *Ratio between Toy EvtGen distribution and MC EvtGen distribution in* 10×10 *2D plot over* $m_{K\pi}, q^2$ *variables.*

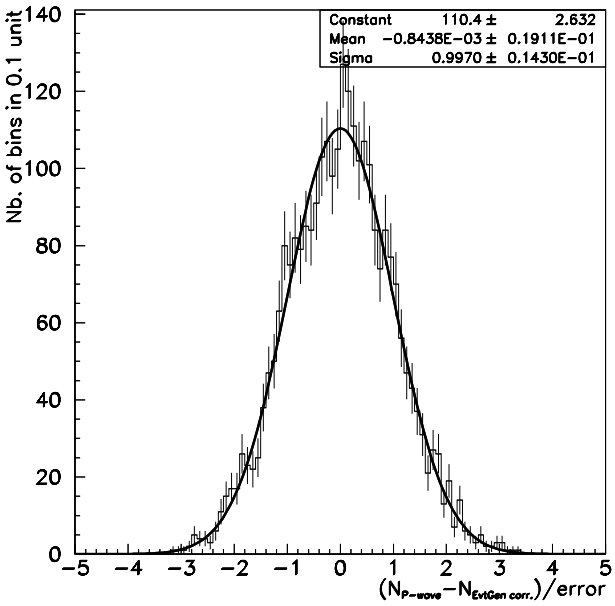

Figure 4.8: *Distribution of the values of the* x *variable (Equation 4.2) measured in each of the 2800 bins used in the fit of the semileptonic differential decay rate. It shows that the correction applied to P-wave events generated with EvtGen does not introduce any bias.*

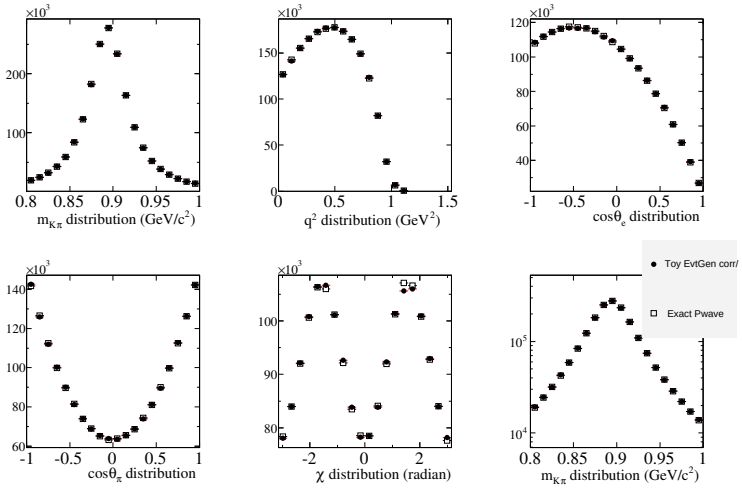

Figure 4.9: *Comparison between corrected EvtGen like and exact P-wave distributions of the differential decay rate projected over the different dynamical variables. The considered $K\pi$ mass interval corresponds to the one used for this category of simulated events in the fit to data.*

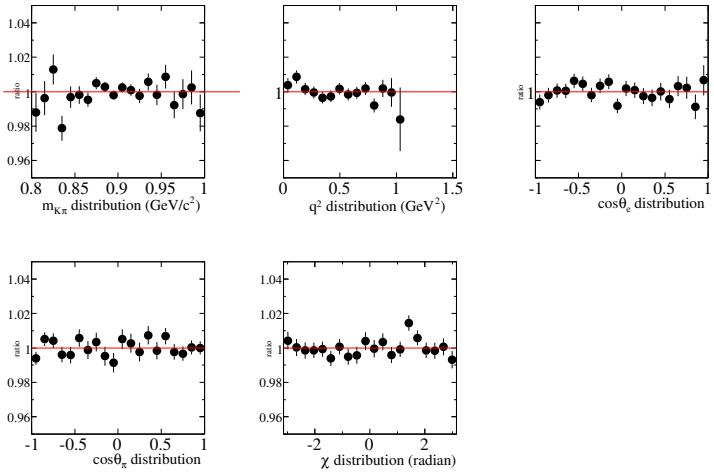

Figure 4.10: *Ratio between exact and corrected EvtGen like distributions for each of the dynamical variables.*

tracks are selected in the same event hemisphere as defined using the direction of the thrust axis. A candidate is kept if it has a positive decay distance relative to the position of the event primary vertex. Other selection cuts, as used for the semileptonic channel, are applied: $\cos\theta_{thrust} < 0.7$ and less than 3 GeV of missing energy in the hemisphere opposite to the candidate. The $K\pi\pi$ mass distribution is shown in Figure 4.11 for the three analyzed event samples: simulated $e^+e^- \rightarrow c\overline{c}$ continuum, on-peak and off-peak data. From these spectra we define signal and sidebands mass intervals corresponding respectively to $m_{K\pi\pi} \in [1.849,\ 1.889]$ GeV/c^2 and $m_{K\pi\pi} \in [1.798,\ 1.838] \cup [1.900,\ 1.940]$ GeV/c^2

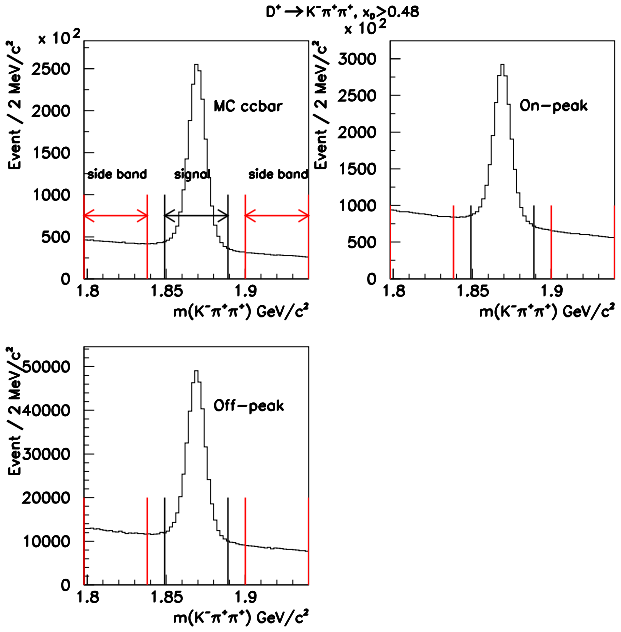

Figure 4.11: *$K^-\pi^+\pi^+$ mass distributions for candidates with $x_D > 0.48$ used to measure corrections applied on the simulation.*

All distributions given in the following of this section are obtained by subtracting half the content of the corresponding distribution from sidebands to the distribution of events from the signal region.

Measurement of corrections used for signal events

We compute a weight which depends on the different variables entering in the definition of Fisher discriminants such that, when this weight is applied on simulated events, corresponding projected distributions over the different variables are similar as those obtained in data. Weights are obtained iteratively.

As the energy spectrum of selected D^+ mesons, which correspond to a reconstructed semileptonic decay signal, is different from the corresponding spectrum of reconstructed $K^-\pi^+\pi^+$ decays, the measured energy spectrum of $D^+ \rightarrow K^-\pi^+\pi^+$ in simulated and in data events is weighted such that it becomes similar to the corresponding spectrum for the reconstructed semileptonic signal.

Comparison between distributions of individual variables entering in the definition of the Fisher discrim-

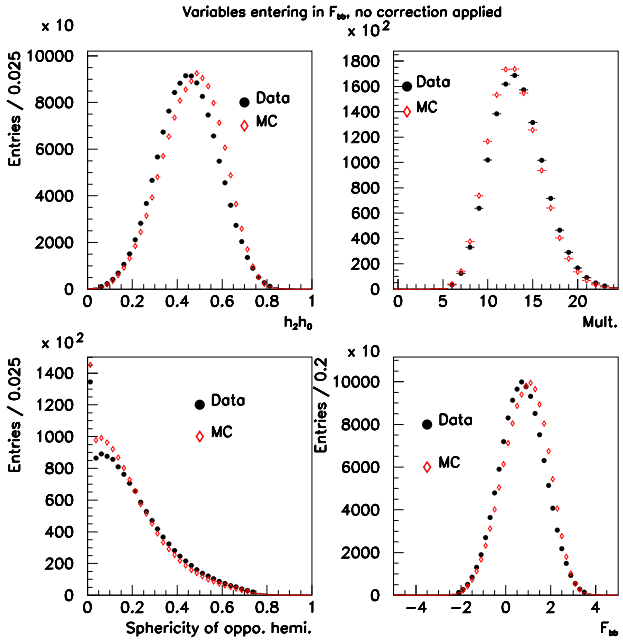

Figure 4.12: *Comparison between data and MC for $D^+ \to K^-\pi^+\pi^+$ for distributions of variables entering in F_{bb} when no correction is applied.*

inants, obtained for data and simulation, are done before and after applying corrections. Distributions of the values of the two discriminant variables obtained before and after applying corrections are also given.

Variables entering in F_{bb} Before applying corrections, distributions of the variables entering in F_{bb}, namely h_2h_0, the total particle multiplicity and the sphericity measured in the hemisphere opposite to the candidate, obtained using data and simulation, are compared in Fig 4.12. The relative variations of the difference - (data-MC)/MC - between distributions measured with the two samples are given in Figure 4.13. Corresponding distributions for the values of the discriminant F_{bb} are also displayed in these figures.

Similar comparisons obtained after applying corrections are given in Figure 4.14 and 4.15. Differences, which attain 20-30% before correction, remain at a level below 5% on individual variables and the agreement is almost perfect for the distributions of the values of F_{bb}.

Variables entering in F_{cc} Variables entering in F_{cc} are : *specmass, plead, Pchi2, Pchi2kepi, pd01, chi2Dflight* and *rRatio*.
Before applying corrections, distributions of x_D, $specmass$, $plead$ and of the cosine of the angle between the leading spectator track and the D candidate, obtained using data and simulation, are compared in Fig 4.16.
The relative variations of the difference - (data-MC)/MC - between distributions measured with the two samples are given in Figure 4.17. Distributions for the other variables entering in F_{cc} ($Pchi2kepi$, $rRatio$, $chi2Dflight$) and for F_{cc} itself are given in Figure 4.18 and 4.19.

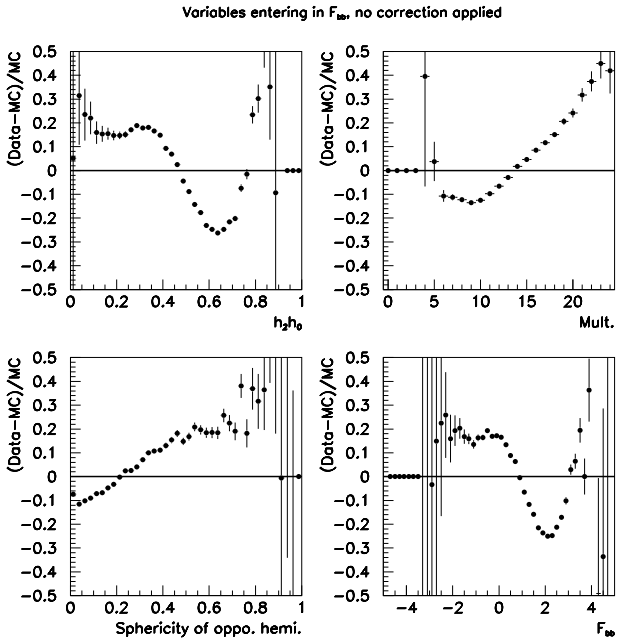

Figure 4.13: *Relative difference - (Data-MC)/MC - for $D^+ \to K^-\pi^+\pi^+$ measured with distributions of variables entering in F_{bb} when no correction is applied.*

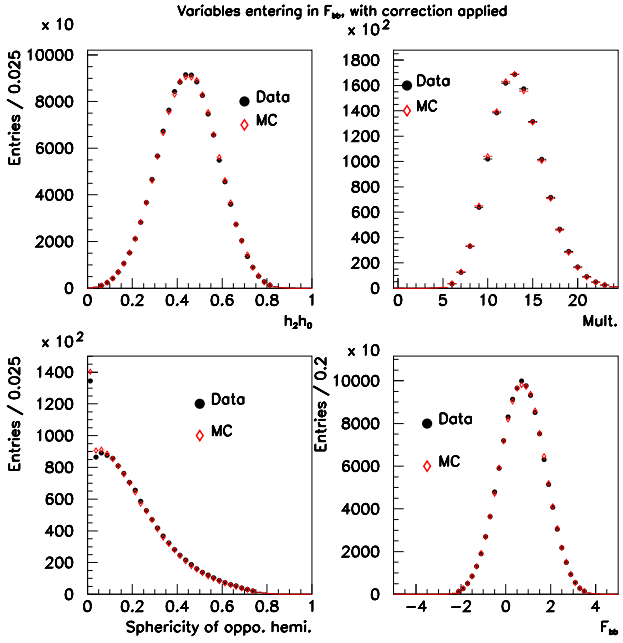

Figure 4.14: *Comparison between data and MC using the $D^+ \to K^-\pi^+\pi^+$ control sample for variables entering in F_{bb}, after corrections applied.*

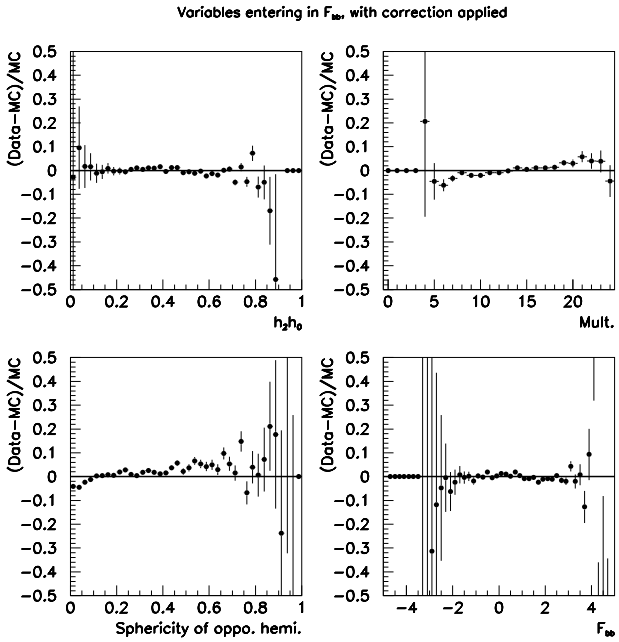

Figure 4.15: *Ratio between data and MC using the $D^+ \to K^-\pi^+\pi^+$ control sample for variables entering in F_{bb}, after corrections applied.*

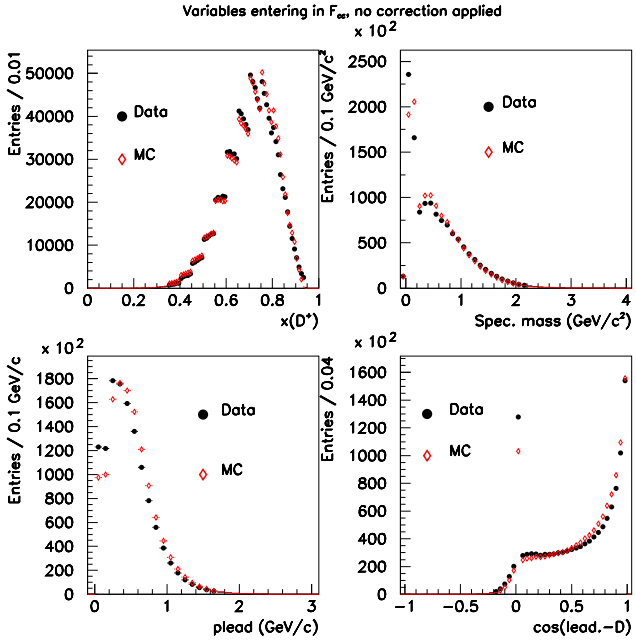

Figure 4.16: *Comparison between data and MC in $D^+ \to K^-\pi^+\pi^+$ for variables entering in F_{cc} when no corrections are applied.*

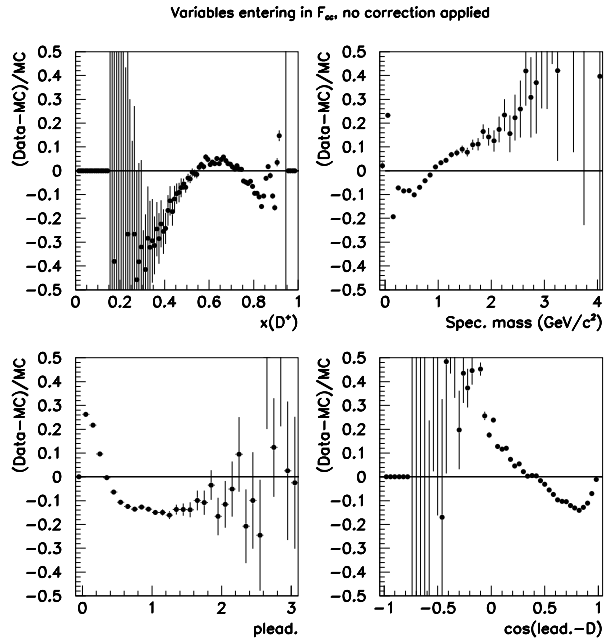

Figure 4.17: *Ratio between data and MC in $D^+ \to K^-\pi^+\pi^+$ for variables entering in F_{cc} when no corrections are applied.*

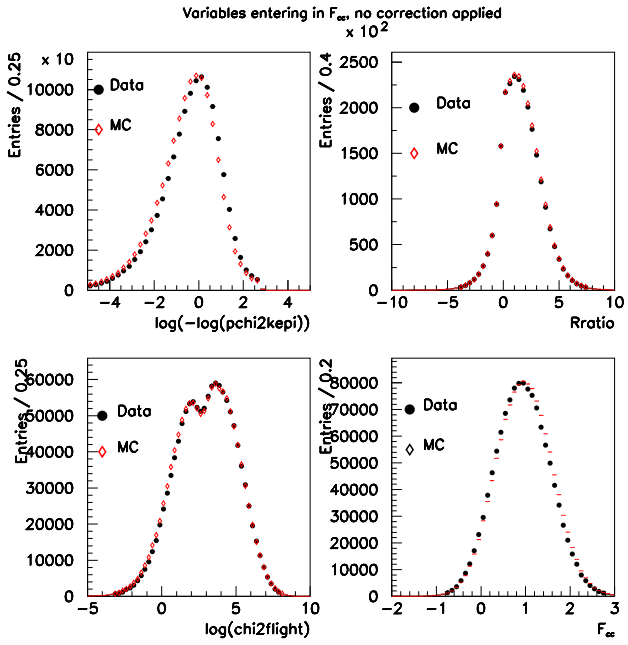

Figure 4.18: *Comparison between data and MC in $D^+ \to K^-\pi^+\pi^+$ for variables entering in F_{cc} when no corrections are applied.*

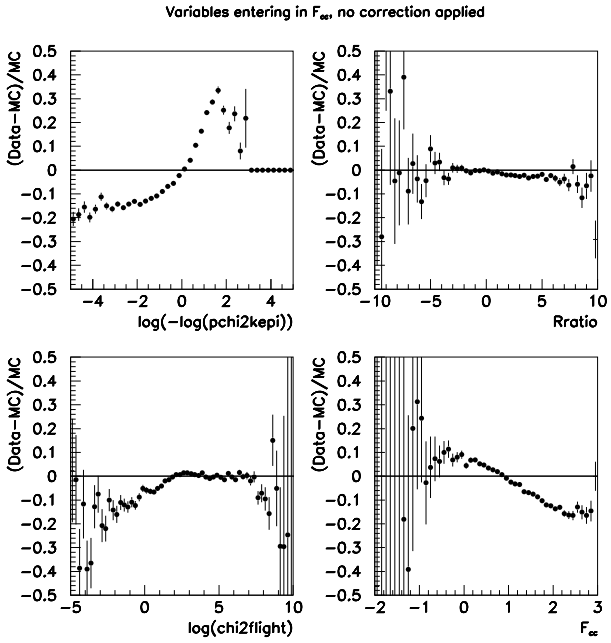

Figure 4.19: *Ratio between data and MC in $D^+ \to K^-\pi^+\pi^+$ for variables entering in F_{cc} when no corrections are applied.*

Similar comparisons obtained after applying corrections are given in Figure 4.20 -4.23. Differences, which attain 20-30$\%$ before correction, remain at a level of the order of 5$\%$, or below.

The structure observed in Fig 4.16 and 4.18 top-left is due to the fact that$K^-\pi^+\pi^+$ events have been weighted versus the value of the D momentum so that their distribution becomes similar to the distribution of accepted $K^-\pi^+e^+\nu_e$ decays. These weights are constants within intervals of the D momentum and induce the observed structure. These weights are applied on data and simulated events for the determination of tuning corrections.

In Section 7.2.1 are evaluated effects of these corrections on the values of fitted parameters. To determine the fraction of these corrections which is used in the evaluation of corresponding systematic uncertainties we have redone a determination of the corrections without requiring that the energy spectrum of the D^+ reconstructed in $K^-\pi^+\pi^+$ is similar as in the semileptonic channel. Differences measured on fitted parameters obtained using these two sets of corrections are taken as systematic uncertainties.

Cross-check of the corrections using matched Monte Carlo signal events

We have presented the method used for correcting the distributions of variables used in F_{cc} and F_{bb} for MC signal events. As explained above, distributions of these variables are obtained by subtracting those created with sideband events from distributions corresponding to events selected in the D^+ signal region. The signal and sidebands regions correspond to $40\ MeV/c^2$ intervals centered respectively on 1.869, 1.818 and $1.92\ GeV/c^2$.

The mass resolution on signal events is $\sim\ 6\ MeV/c^2$ but, because of track scattering at large angles and radiative events there are typically $6-7\%$ of signal events which are reconstructed outside the signal mass

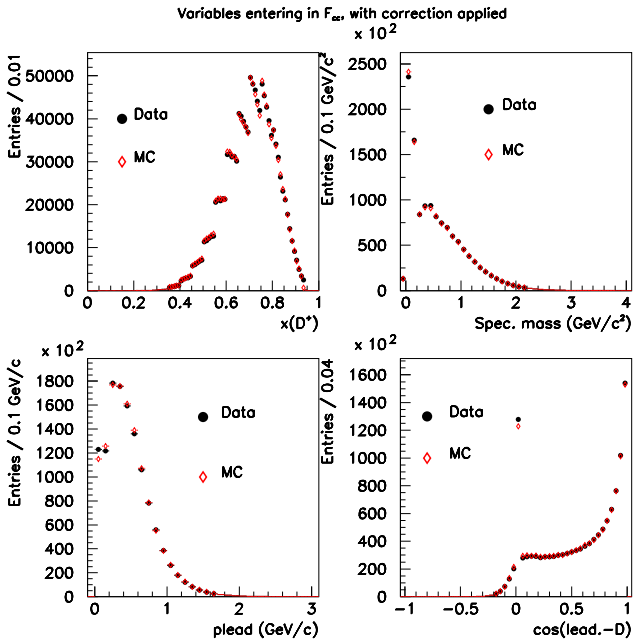

Figure 4.20: *Comparison between data and MC in $D^+ \to K^-\pi^+\pi^+$ for variables entering F_{cc} after applying corrections.*

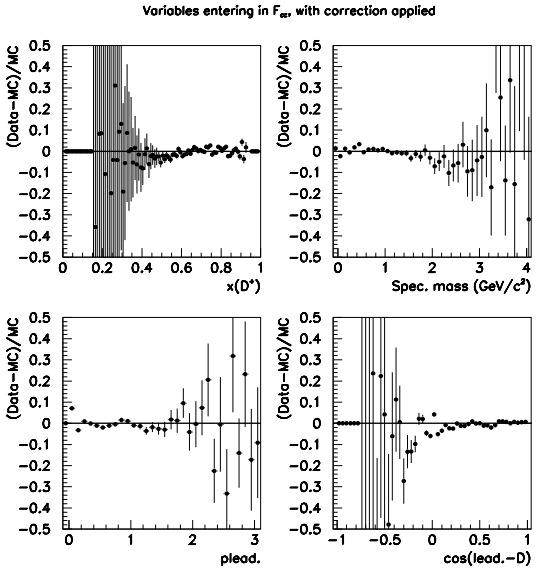

Figure 4.21: *Comparison between data and MC in $D^+ \to K^-\pi^+\pi^+$ for variables entering in F_{cc} after corrections applied.*

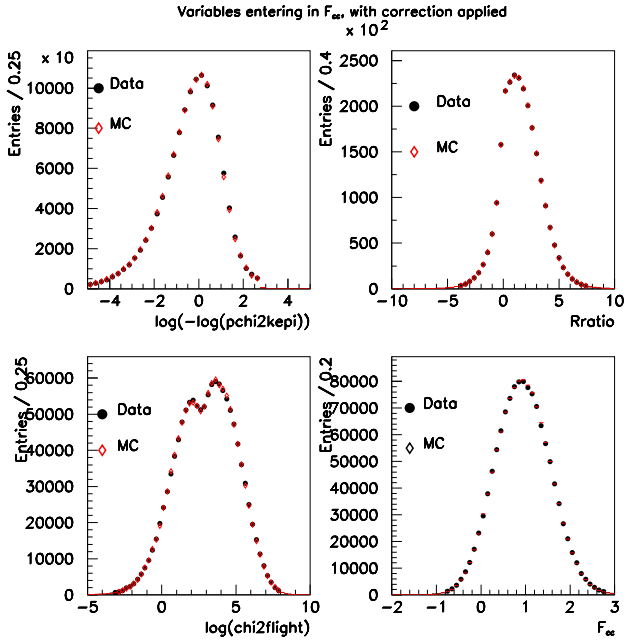

Figure 4.22: *Comparison between data and MC for variables entering in F_{cc} after corrections applied.*

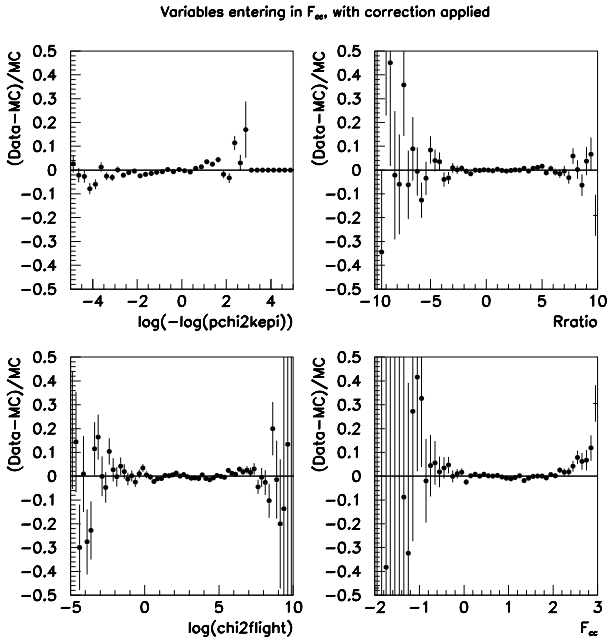

Figure 4.23: *Comparison between data and MC for variables entering in F_{cc} after corrections applied.*

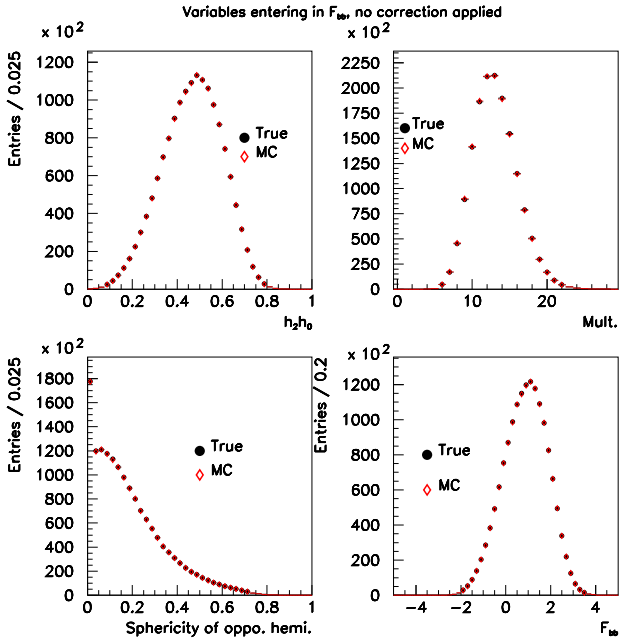

Figure 4.24: *Check of sideband subtraction using simulated events. Comparison between the distributions of the variables entering in F_{bb}. Red points are obtained using sideband subtraction whereas black points are for true signal events.*

window.

The distribution of a given variable can be different from the one expected for true signal events because:

- the estimated background level from sidebands differs from the true number of background events in the signal region. This happens if the combinatorial background level does not depend linearly on the mass.
- background events in sidebands originate from mechanisms that are different from those contributing in the signal region;
- the variable which is considered depends on the $K^-\pi^+\pi^+$ mass value.

Using the generic $c\bar{c}$ simulation we have compared the distributions of the different variables entering in F_{bb} obtained after sideband subtraction with the corresponding distributions from truth- matched events. There is a 2.2% excess of truth matched probably because, as we have explained, there is a small fraction of signal inside the sidebands. In anycase we are interested, in these studies, in the control of the shape of the distributions. Comparison is shown in Figures 4.24 and 4.25 after rescaling by 1.022.

Similar comparisons are shown in Figures 4.26-4.29 for variables used in the other discriminant variable (F_{cc}).

From these distributions one can conclude that the sideband subtraction allows to extract the distributions we need for the tuning procedure.

It can be noted also that, even if there were some discrepancies between the estimated and the exact distributions, as the same procedure is used on data, most of the discrepancy will be cancelled when taking the ratio between data and MC.

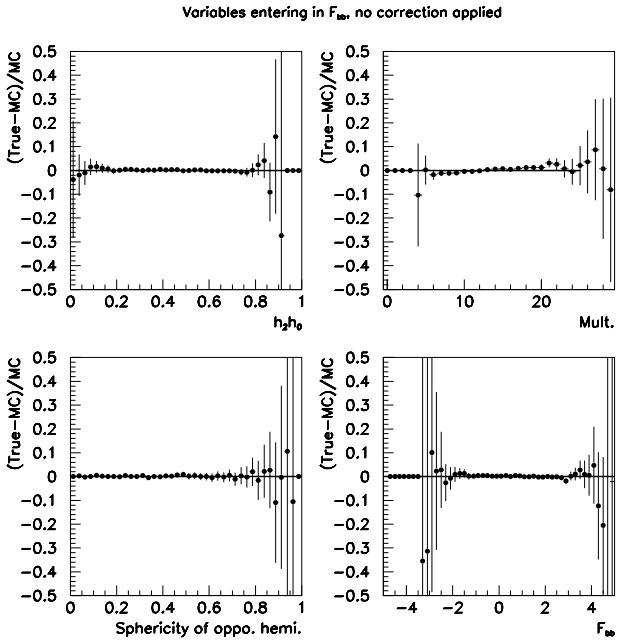

Figure 4.25: *Check of sideband subtraction using simulated events. Relative difference between distributions for true signal events (in simulation) and those obtained after sideband subtraction.*

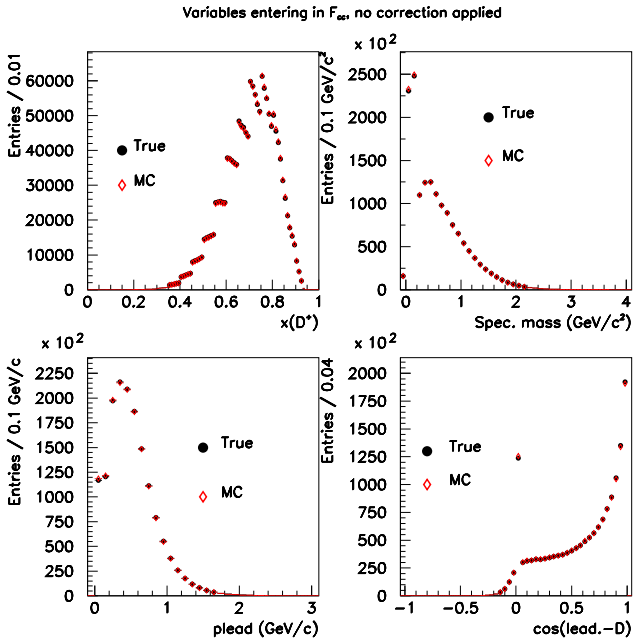

Figure 4.26: *Check of sideband subtraction using simulated events. Comparison between distributions of some of the variables entering in F_{cc}. Red points are obtained using sideband subtraction whereas black points are for true signal events.*

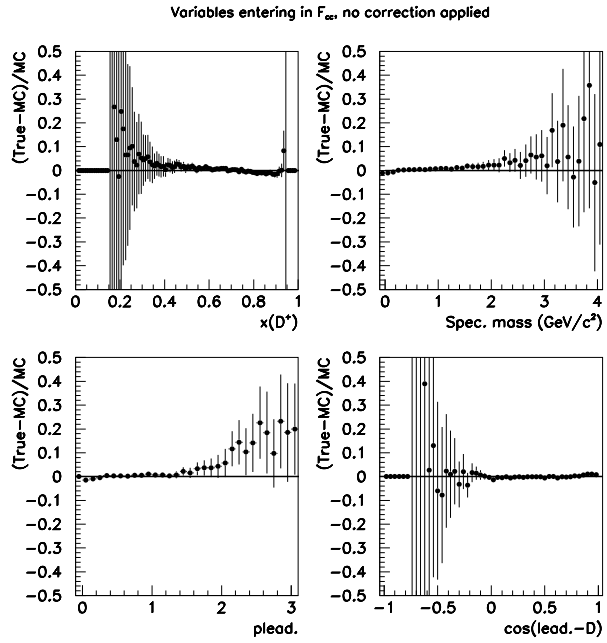

Figure 4.27: *Check of sideband subtraction using simulated events. Relative difference between distributions for true signal events and those obtained after sideband subtraction..*

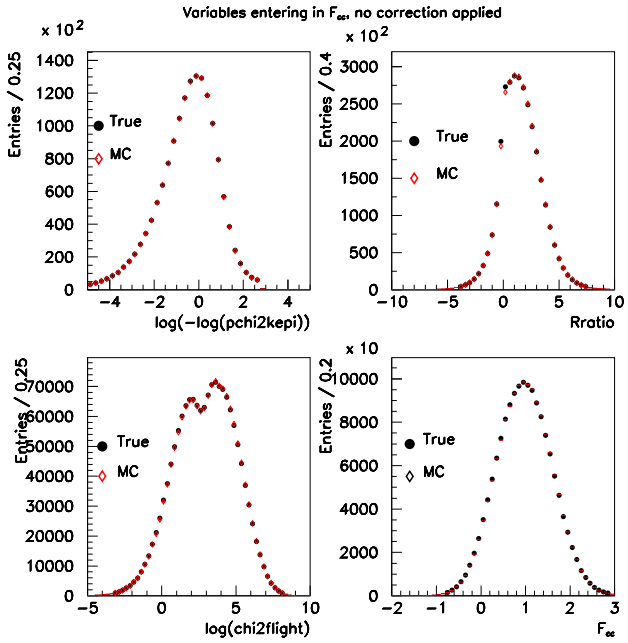

Figure 4.28: *Check of sideband subtraction using simulated events. Comparison between the distributions of the other variables entering in F_{cc}. Red points are obtained using sideband subtraction whereas black points are for true signal events.*

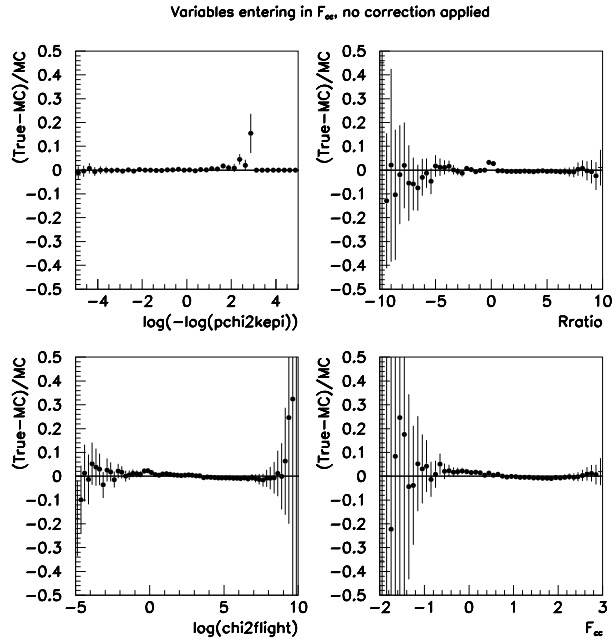

Figure 4.29: *Check of sideband subtraction using simulated events. Relative difference between distributions for true signal events and those obtained after sideband subtraction..*

4.1.3 Control of the D^+ direction and missing energy determination in simulated events.

With a fully reconstructed $D^+ \to K^-\pi^+\pi^+$ its direction is accurately measured and one can therefore compare the values of the two angles defining its direction, with those obtained when using all particles present in the event, but those attributed to the decay signal candidate. This last procedure is used to have an estimate of the D direction for the decay $D^+ \to K^-\pi^+e^+\nu$.

This event sample allows also to compare the missing energy measured in the D^+ hemisphere and in the opposite hemisphere for data and simulated events.

In this study, differences between data and simulation on the $c \to D^+$ fragmentation characteristics (see section 4.1.2) are corrected. Global cuts similar to those applied for the $D^+ \to K^-\pi^+e^+\nu$ analysis are used such that the topology of $D^+ \to K^-\pi^+\pi^+$ selected events is as close as possible to the one of semileptonic events.

Comparisons between measured values of the angles of the D^+ direction obtained with the two methods, in data and in the simulation, are displayed in Figure 4.30-top. The relative difference between these distributions is given in Figure 4.31. One can note that there is a 10% excess of data events in the tails of the distributions.

Corresponding distributions for the missing energy measured in the signal hemisphere ($E^{same}_{miss.}$) are given in Figures 4.30 and 4.31 bottom-left. In data and simulation these distributions have an offset of about $100 MeV/c^2$ which corresponds to energy escaping detection even in absence of neutrinos. To evaluate the neutrino energy, in D^+ semileptonic decays this bias is corrected.

The difference between the exact and estimated values of the two angles and missing energy is measured also versus the value of the missing energy in the opposite event hemisphere ($E^{opp.}_{miss.}$). In each slice of $E^{opp.}_{miss.}$ a

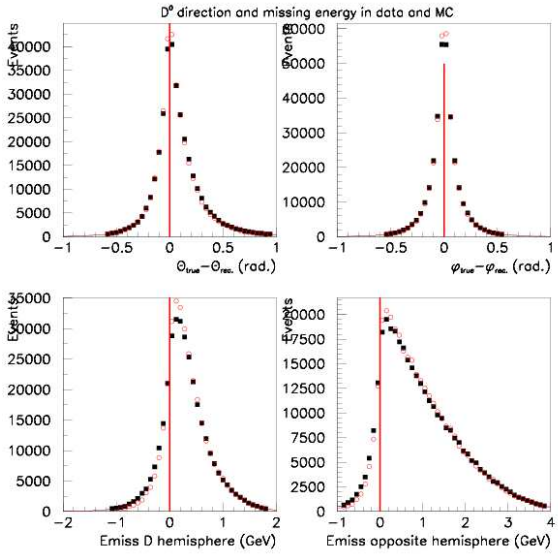

Figure 4.30: *Resolution distributions on θ, ϕ, $E_{miss.}^{same}$ and distribution of $E_{miss.}^{opp.}$ measured in data and in simulation before corrections.*

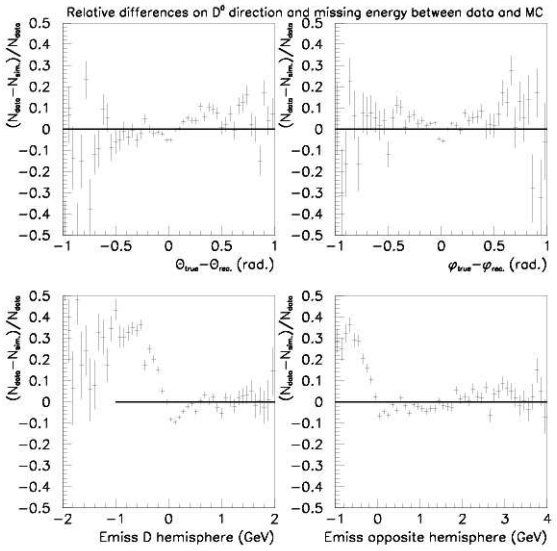

Figure 4.31: *Relative difference between resolution distributions measured in data and in simulation, without applying corrections.*

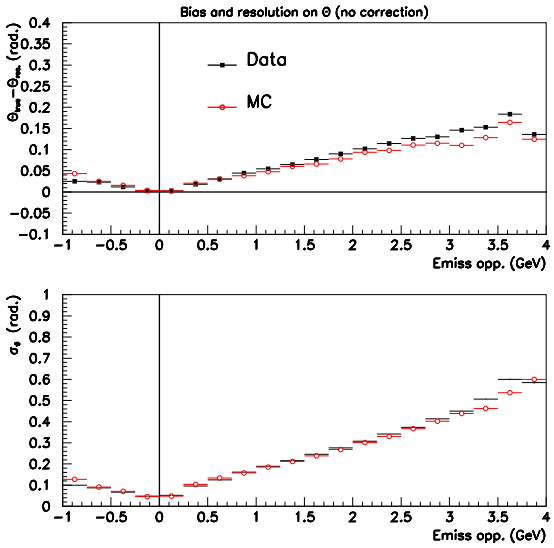

Figure 4.32: *Bias and uncertainty on the estimated value for θ versus the missing energy measured in the event opposite hemisphere; no correction is applied.*

Gaussian distribution is fitted and corresponding values of the average and standard deviation are plotted in Figures 4.32-4.34 versus $E^{opp.}_{miss.}$.

As expected the resolution decreases with $E^{opp.}_{miss.}$. One observes also that estimated values of θ and $E^{same}_{miss.}$ are biased and that the bias depends on $E^{opp.}_{miss.}$. This comes presumably from the fact that missing energy in the opposite hemisphere gives a tilt in the estimated polar angle and degrades the overall energy balance. These biases and standard deviation are parameterized versus $E^{opp.}_{miss.}$. Biases have been corrected and estimated reconstruction accuracies are used in the D^+ mass constrained fit (see Section 3.1.3).

No bias is observed on the azimuth estimate as there is the same chance, in a given event, that missed particles give an higher or a lower value of this angle estimate.

The agreement between distributions measured in data and in the simulation is rather good. We note, in Figure 4.35, that fitted uncertainties are slightly higher in data than in the simulation. From these measurements we have defined a smearing which is applied on simulated events estimates of θ, ϕ and $E^{same}_{miss.}$.

After having corrected for biases (in data and MC) and applied a smearing on simulated events (only), distributions given in Figures 4.36 and 4.37 are obtained.

Distributions of biases and errors on the three parameters - θ, ϕ, $E^{same}_{miss.}$ - versus $E^{opp.}_{miss.}$ are given in Figures 4.38-4.40.

Some differences remain on these distributions between data and simulation but their effect is very small on final measurements obtained in the present analysis. Before applying corrections we find that the resolution is slightly better in MC than in data. After applying corrections the situation is reversed. When evaluating systematic uncertainties we have used the total deviation on fitted parameters obtained when applying or not the corrections.

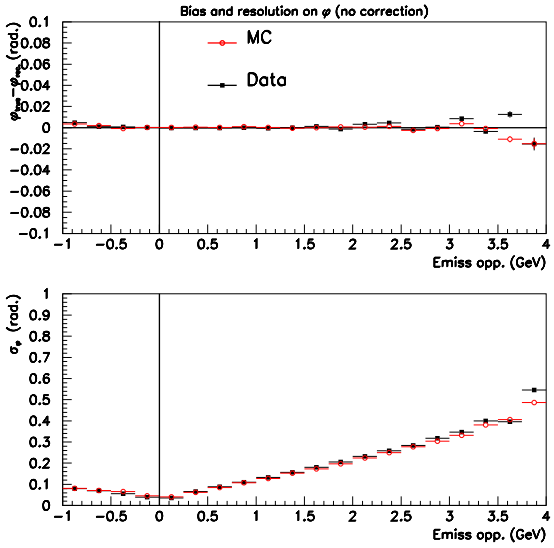

Figure 4.33: *Bias and uncertainty on the estimated value for ϕ versus the missing energy measured in the event opposite hemisphere; no correction is applied.*

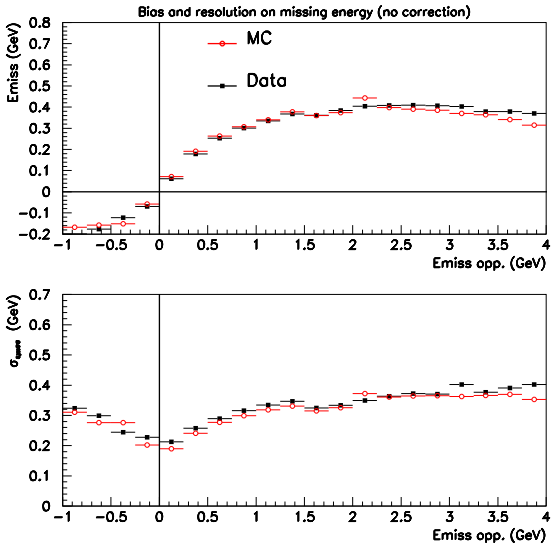

Figure 4.34: *Bias and uncertainty on the estimated value for the missing energy in the signal event hemisphere versus the missing energy measured in the opposite hemisphere; no correction is applied.*

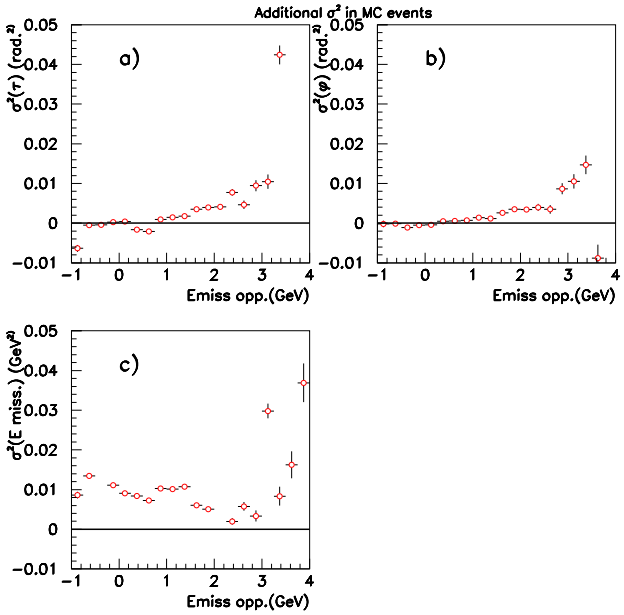

Figure 4.35: *Difference between standard deviation squared fitted on data and on simulated events for the three parameters entering the mass constrained fit. Only events with a missing energy lower than 3 GeV are used.*

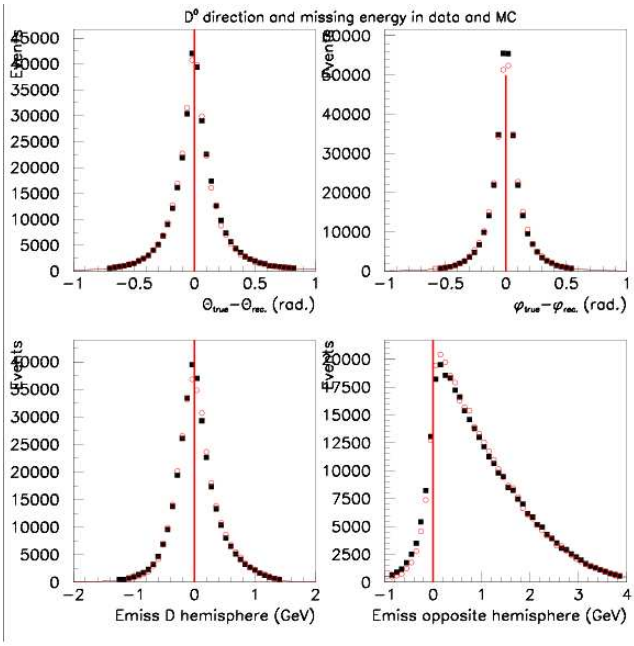

Figure 4.36: *Resolution distributions on θ, ϕ, $E^{same}_{miss.}$ and distribution of $E^{opp.}_{miss.}$ measured in data and in simulation after applying corrections.*

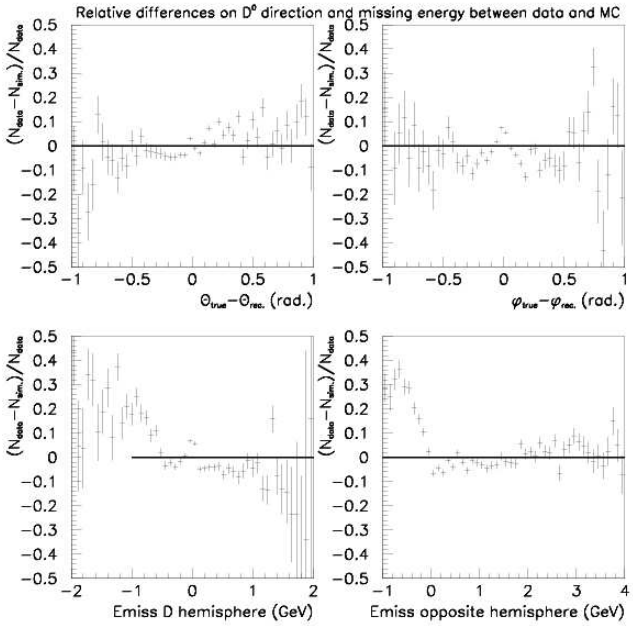

Figure 4.37: *Relative difference between resolution distributions measured in data and in simulation, after applying corrections.*

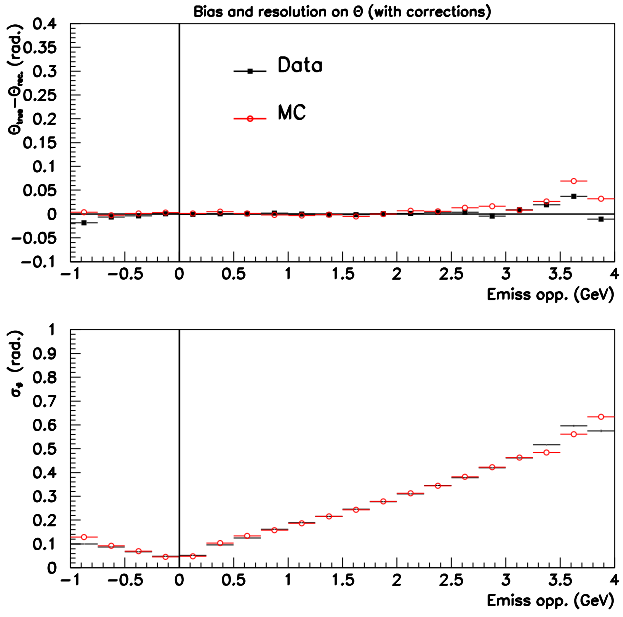

Figure 4.38: *Bias and error on the estimated value for θ versus the missing energy measured in the event opposite hemisphere; after correction.*

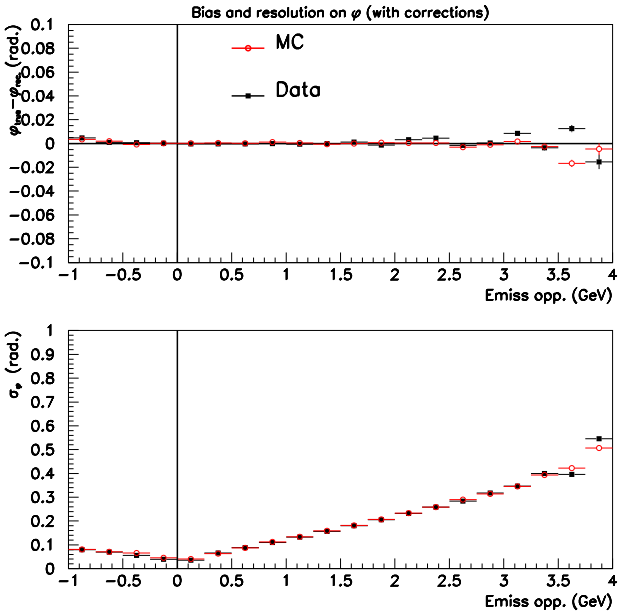

Figure 4.39: *Bias and error on the estimated value for ϕ versus the missing energy measured in the event opposite hemisphere; after correction.*

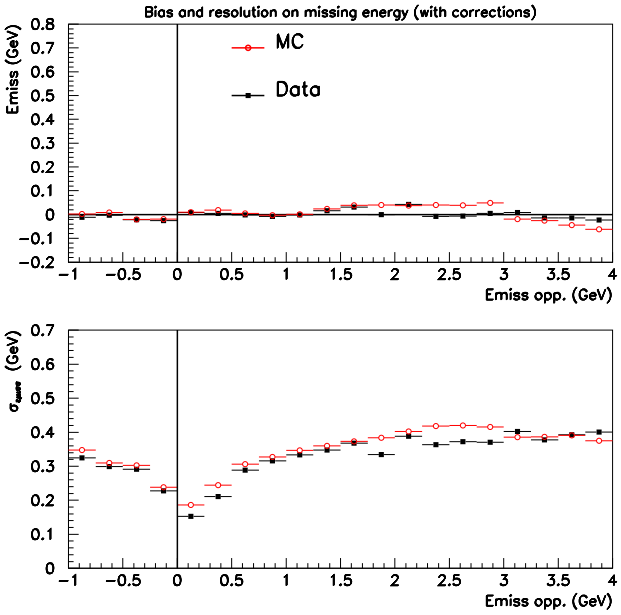

Figure 4.40: *Bias and error on the estimated value for the missing energy in the signal event hemisphere versus the missing energy measured in the opposite hemisphere; after correction.*

We have not considered the difference existing on the missing energy in the opposite hemisphere as it is small and as this quantity is used only in the parameterization of the corrections.

4.2 $B\bar{B}$ simulation tuning

The background remaining from $\Upsilon(4S)$ decays is evaluated using a sample of simulated events normalized to the analyzed integrated luminosity in data. This is done by considering that charged and neutral B mesons are produced with the same cross section equal to 0.525 nb.

To verify that the rate and production characteristics of these events are similar as in data, distributions of different variables are compared with those obtained by subtracting Offpeak from Onpeak data events, isolating in this way the contribution from B events alone. The analyzed Onpeak and Offpeak integrated luminosities correspond to the statistics of Run1 to 5 and amount respectively to $347.5\ fb^{-1}$ and $34\ fb^{-1}$. The number of events in data and Monte Carlo as well as the ratio data/MC are presented in Table 4.2 for 3 cuts of the F_{cc} discriminant variable. $F_{cc} > 0.5$ is the nominal cut on this variable whereas the two other values are used to verify the stability of the analysis.
In the following we analyze events where the particle candidates have the correct charge combination ($K^-\pi^+e^+$), referred as Right-Sign (RS) events, as well as ($K^-\pi^-e^+$) events, referred as Wrong-Sign (WS) events.

Cut value	Data	MC	ratio
>0.4	2673 ± 220	1712 ± 7	1.56 ± 0.13
>0.5	2015 ± 200	1202 ± 6	1.68 ± 0.17
>0.7	1070 ± 161	571 ± 4	1.88 ± 0.28

Table 4.2: *Values of the ratio between $B\bar{B}$ events in data (On-Off)Peak and in MC for different cuts on F_{cc} measured in RS events and corresponding to Runs 1-5. Samples are normalized to the same integrated luminosity.*

Distributions of the values of the F_{bb} and F_{cc} variables are presented in Figures 4.41 and 4.42, with the nominal cut $F_{cc} > 0.5$ applied. In Figure 4.43 we present the ratio Data/MC for the 5 dynamical variables obtained in the same conditions. Corresponding distributions obtained with the other cuts are presented in the Appendix.

The F_{bb} variable's main input comes from the h_2h_0 distribution, which shows an important discrepancy between data and MC for high values of this variable. The F_{cc} Monte Carlo shape is compatible with the shape in data. We have big uncertainties in the plots of the ratio between distributions, these are caused by the low statistics of OffPeak data.

We correct the $B\bar{B}$ background estimate by renormalizing the rate of events according to the values of Table 4.2 and evaluate the corresponding systematic uncertainties for now by varying this renormalization according to quoted uncertainties.
The same study is done with events with the charge conjugation ($K^-\pi^-e^+$), used in the next section for control of charm background. We present in Table 4.3 the number of events in data and Monte Carlo, as well as their

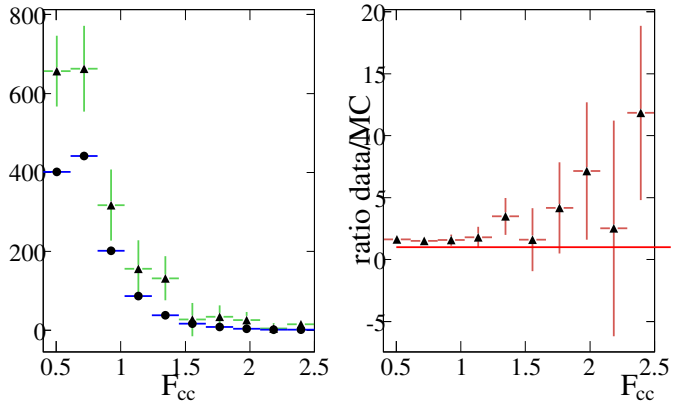

Figure 4.41: *Left: Distributions of the F_{cc} variable for $B\bar{B}$ events satisfying nominal cuts and corresponding to Runs 1-5. In $\triangle$ (OnPeak-OffPeak) data, (•) $B\bar{B}$. Right: ratio* $\frac{(OnPeak-OffPeak)data}{B\bar{B}}$

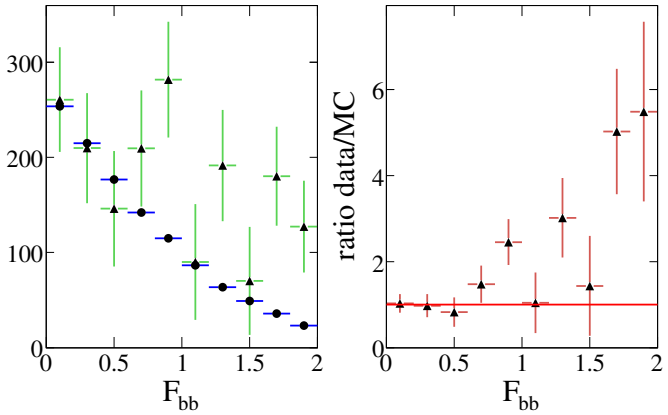

Figure 4.42: *Left: Distributions of the F_{bb} variable for $B\bar{B}$ events corresponding to Runs 1-5. In $\triangle$ (OnPeak-OffPeak) data, (•) $B\bar{B}$. Right: ratio* $\frac{(OnPeak-OffPeak)data}{B\bar{B}}$.

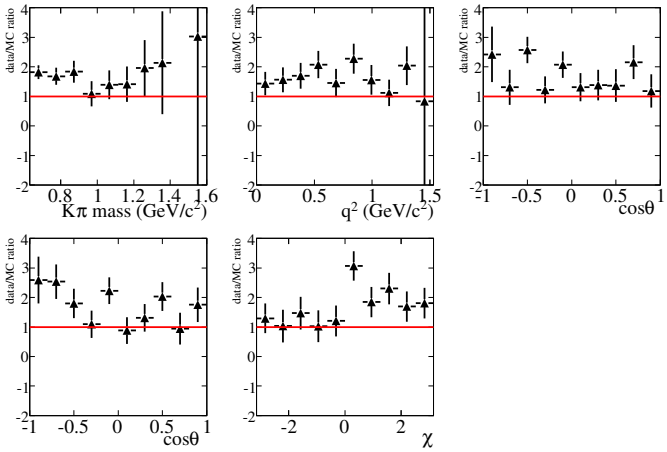

Figure 4.43: *Ratios data/MC for $B\bar{B}$ events versus $m_{K\pi}$, q^2, $cos\theta_e$, $\cos\theta_\pi$ and χ for nominal cuts and using Runs 1-5.*

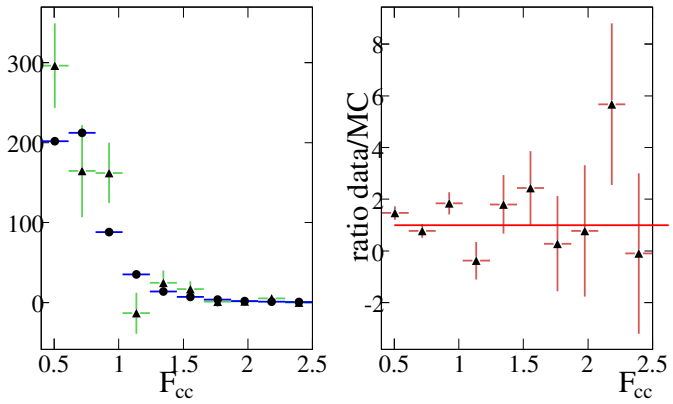

Figure 4.44: *Left: Distributions of the F_{cc} variable for WS $B\bar{B}$ events satisfying nominal cuts and corresponding to Runs 1-5. In $\triangle$ (OnPeak-OffPeak) data, (•) $B\bar{B}$. Right: ratio $\frac{(OnPeak-OffPeak)data}{B\bar{B}}$.*

ratio for the 3 cuts on F_{cc} previously discussed.

Cut value	Data	MC	ratio
>0.4	1032 ± 110	832 ± 5	1.24 ± 0.13
>0.5	665 ± 93	568 ± 4	1.17 ± 0.16
>0.7	250 ± 64	254 ± 3	0.98 ± 0.25

Table 4.3: *Values of the ratio between $B\bar{B}$ events in data (On-Off)Peak and in MC for different cuts on F_{cc} measured in WS events and corresponding to Runs 1-5. Samples are normalized to the same integrated luminosity.*

For WS events we apply a global scaling of the $B\bar{B}$ background estimate according to the results in Table 4.3.

4.3 $c\bar{c}$ background simulation tuning

As the main source of background originates from track combinations in which some particles come from a charm meson decay and others from hadronization it is necessary to verify if the fragmentation of a charm quark into a charm meson is similar in data and in the simulation and also if the production characteristics of charged particles accompanying the charm meson are similar.

In this purpose, we compare distributions between data and MC for event shape variables that enter in the Fisher discriminant F_{bb}. We also measure the production characteristics of charged pions and kaons, produced during the fragmentation of the charm quark, as they correspond to a large fraction of the background in the present analysis. We have done these measurements separately for D^{*+}, D^0 (vetoing D^0 from D^{*+} decays) and for D^+.

Wrong-sign (WS) events of the type $K^-\pi^-e^+$ are used to verify that corrections applied to the simulation are working because origins of these events are quite similar as those of the background contributing to RS events.

Finally we evaluate uncertainties associated with the control of the charm background.

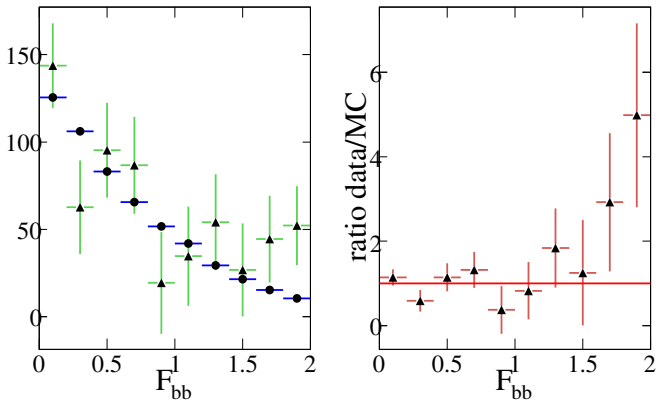

Figure 4.45: *Left: Distributions of the F_{bb} variable for WS $B\bar{B}$ events satisfying nominal cuts and corresponding to Runs 1-5. In $\triangle$ (OnPeak-OffPeak) data, (•) $B\bar{B}$. Right: ratio* $\frac{(OnPeak-OffPeak)data}{B\bar{B}}$.

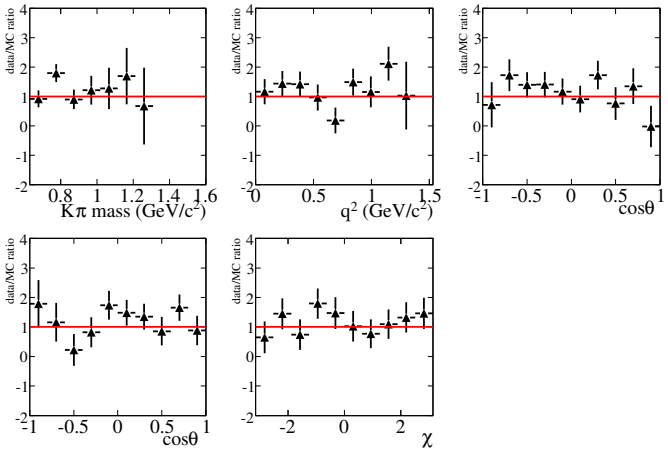

Figure 4.46: *Values of the ratio between $B\bar{B}$ events in data (On-Off)Peak and in MC for different cuts on F_{bb} measured in WS events and corresponding to Runs 1-5. Samples are normalized to the same integrated luminosity.*

4.3.1 Studies of particle production accompanying c-hadrons in $c\bar{c} \to DX$

Corresponding measurements and corrections applied to the simulation are explained in Appendix A, B and C.

4.3.2 Correction of D semileptonic decay form factors

By default, D semileptonic decays are generated in EvtGen using the ISGW2 decay model. As this model does not reproduce present measurements (this was shown for instance in the BaBar analysis of $D^{*+} \to D^0\pi^+, D^0 \to K^-e^+\nu_e$) [41], events have been reweighted such that they correspond to hadronic form factors behaving according to the simple pole ansatz.
For decay processes of the type $D \to Pe\nu$ the weight is equal to the square of the ratio between the corresponding hadronic form factors, multiplied by a constant such that the total decay branching fraction remains unchanged after the transformation. For all Cabibbo favoured decays we use a pole mass value equal to $1.884\ \mathrm{GeV/c^2}$ (which corresponds to the BaBar measurement for the decay channel $D^0 \to K^-e^+\nu_e$) whereas for Cabibbo suppressed decays we use $1.9\ GeV/c^2$ [34].

For decay processes of the type $D \to Ve\nu,\ (V \to P_1P_2)$, where P and V are respectively pseudo-scalar and vector mesons, corrections depend on $q^2, \cos\theta_e \text{ and } \cos\theta_\pi$. They are evaluated iteratively using projections of the differential decay rate versus these three variables as obtained in EvtGen and in a toy simulation which contains the espected distribution. The parameterisation is defined using the decay $D^+ \to K^-\pi^+e^+\nu_e$ and the following values of the parameters are used.

$$r_V = 1.6,\ r_2 = 0.8,\ m_V = 2.1\ \mathrm{GeV/c^2} \text{ and } \mathrm{m_A} = 2.5\ \mathrm{GeV/c^2}. \tag{4.3}$$

In Figure 4.47 are compared distributions generated in EvtGen for the channel $D^+ \to \overline{K^{*0}}e^+\nu_e$ and those expected when S and P-waves contribute. Several effects have

to be corrected (in addition to the intrinsic problem identified in EvtGen, see Section 4.1.1).

In the $K\pi$ final state there are also, in EvtGen, two components present in addition to the K^* (see Figure 4.48):

- phase space at the 7.4% level, relative to K^*(892);
- K_2^* at the 3.4% level in the $K^-\pi^+$ final state.

In data there is no evidence for these components but we measure a 5% rate for an S-wave which interferes with the K^*(892). The corrections we apply thus eliminate the phase space and K_2^* components and they create and S-wave component of characteristics similar to data. After corrections distributions are compared in Figure 4.49 with expectations from the exact decay rate expression.

It can be noted that these corrections do not provide a good agreement between expectations and simulation for the mass of the hadronic system. We have considered that corrections on the lepton variables were more important as background events contain most of the time a lepton from charm. In addition, corrections for the mass distribution would require a detailed study for several hadronic final states.

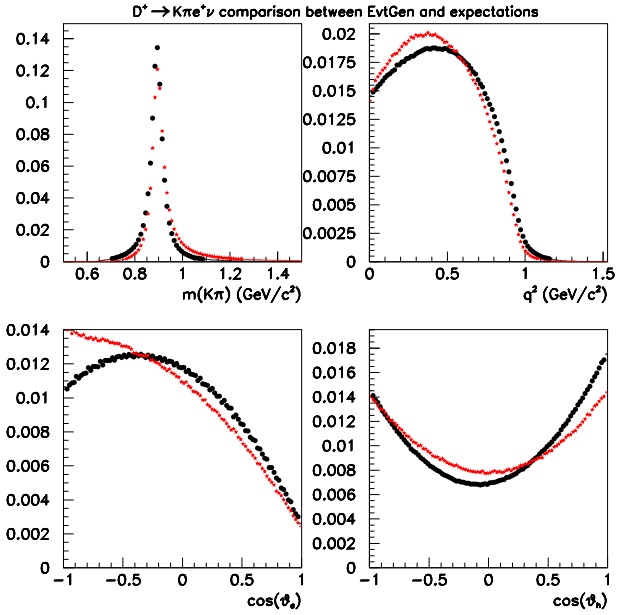

Figure 4.47: *Comparison between normalized distributions obtained for the channel $D^+ \to K^-\pi^+e^+\nu_e$ for events produced with EvtGen and those expected. The K^* component is only considered in EvtGen whereas the S-wave is included in the expected "exact" distribution.*

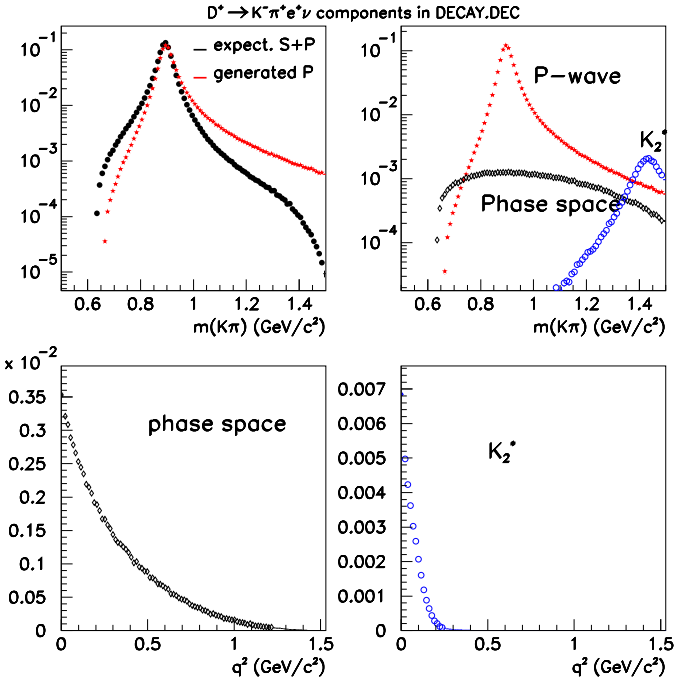

Figure 4.48: *Top right: The P-wave, phase space and K_2^* components generated in EvtGen. Bottom plots indicate the q^2 distributions for the phase space and K_2^* components.*

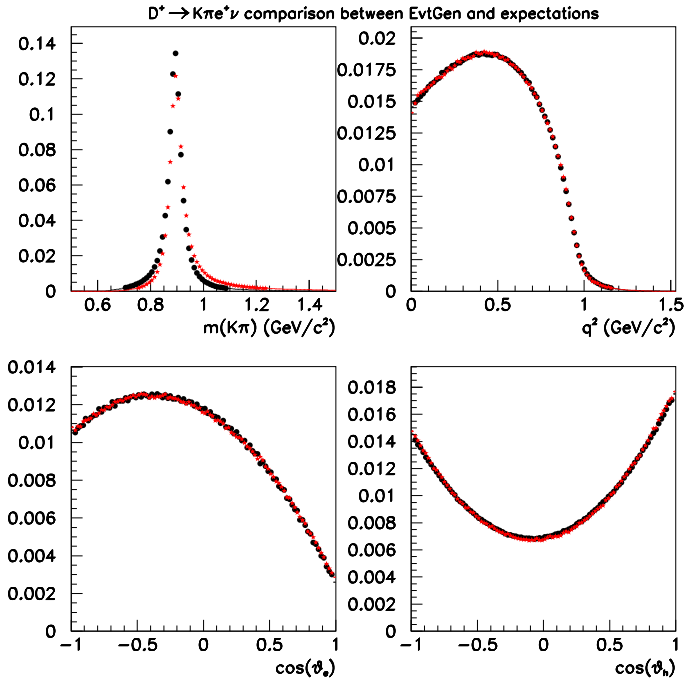

Figure 4.49: *Same comparison as in Figure 4.47 after corrections applied on events generated with EvtGen.*

It has been verified also if charm semileptonic decay branching fractions used in EvtGen are similar with recent measurements quoted in [13].

Decay	PDG BR[13]	EvtGen BR
$D^0 \to \pi^- e^+ \nu_e$	$(2.83 \pm 0.17) \times 10^{-3}$	3.4×10^{-3}
$D^0 \to K^- e^+ \nu_e$	$(3.58\% \pm 0.06)\%$	3.5%
$D^0 \to \overline{K^{*-}} e^+ \nu_e$	$(2.18 \pm 0.16)\%$	2.25%
$D^0 \to \rho^- e^+ \nu_e$	$(1.9 \pm 0.4) \times 10^{-3}$	2.2×10^{-3}
$D^+ \to \overline{K^{*0}} e^+ \nu_e$	$(5.49\% \pm 0.31)\%$	5.54%

Table 4.4: *Branching ratios for the most important semileptonic decays contributing to charm background.*

As all branching fractions agree within uncertainties (apart for $D \to \pi e^+ \nu_e$, which is then rescaled) only the shapes of charm semileptonic decay distributions are corrected.

We take 10% of the effect from these corrections as remaining systematic uncertainties.

4.3.3 Analysis of Wrong-Sign events

Among the different charge combinations, which correspond to wrong sign (WS) events, $K^- \pi^- e^+$ are used as contributing production and decay mechanisms to this final state are rather similar as those contributing to RS background events. This is illustrated in Figure 4.50 and Table 4.5 where the various charm meson decay

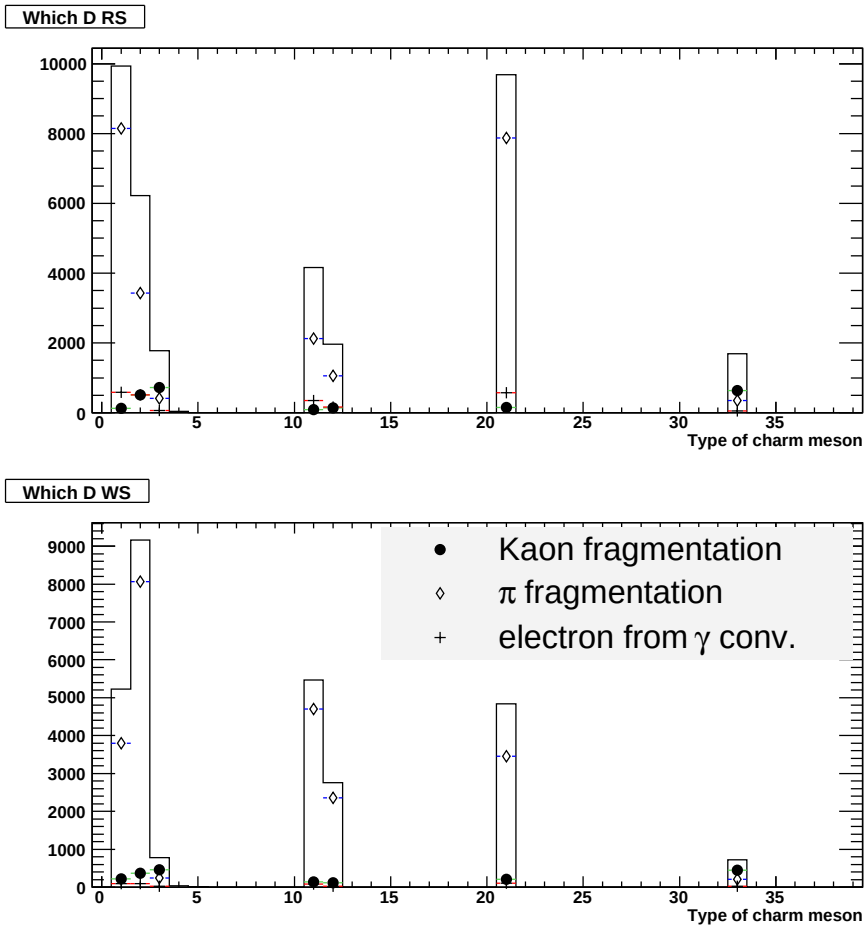

Figure 4.50: *Sources of charm background and contributions of events with a fragmentation pion, kaon or electron from conversion. Identification codes used for the different charm mesons are:1,2,3 respectively for D^0, D^+, and D_s not cascading from a D^{*+}. 11 and 12 respectively for a D^0 and D^+ cascading from a D^{*+}. 21 for a D^0 cascading from a D^{*0}. 33 for a D_s from a D_s^*.*

contributions are evaluated for RS and WS events according to the simulation.

channel	RS	WS
D^0	27.2%	16.9%
D^+	16.8%	29.7%
D_s	4.5%	2.8%
$D^{*+} \to D^0$	12.9%	20.6%
$D^{*+} \to D^+$	5.4%	9.7%
$D^{*0} \to D^0$	28.6%	17.3%
$D_s^* \to D_s$	4.5%	2.9%

Table 4.5: *Fractions for each type of charm mesons in RS and WS background events, after all analysis cuts.*

The number of events in Wrong-sign distributions for Runs123, Run4, Run5 data and Monte Carlo are presented in Table 4.6 before and after applying the latter corrections.

run	data	$c\bar{c}MC$	B^+B^-MC	B^0B^0MC	uds MC	total MC
123 before corr/	26850 ± 164	28650 ± 112	861 ± 15	698 ± 14	1098 ± 30	31307 ± 118
123 after corr/	-	24519 ± 106	1007 ± 18	817 ± 17	1098 ± 30	27441 ± 113
4 before corr/	22683 ± 151	24270 ± 142	715 ± 15	579 ± 14	920 ± 30	26484 ± 147
4 after corr/	-	20801 ± 132	837 ± 18	678 ± 19	920 ± 30	23236 ± 138
5 before corr/	28393 ± 168	30670 ± 139	888 ± 17	729 ± 16	1194 ± 32	33481 ± 145
5 after corr/	-	26217 ± 129	1040 ± 20	853 ± 19	1194 ± 32	29304 ± 136

Table 4.6: *Number of Wrong Sign candidates for different runs in data and Monte Carlo. For the latter, numbers are given before corrections and after corrections on tuning and on hadronic form factors ($c\bar{c}$) and on renormalization ($B\bar{B}$). Values for Run123, Run4 and Run5 are on lines 1,3 and 5 respectively.*

Distributions of the 5 kinematic variables measured in data and simulation are compared, before and after applying corrections on $\Upsilon(4S)$ and continuum $c\bar{c}$ simulated events, in Figure 4.51 and Figure 4.53 respectively. The distributions of the Fisher discriminants and of the variation of background $cos\theta_\pi$ asymmetry with the hadronic mass, before and after these corrections are applied, are presented in Figures 4.52 and 4.54.

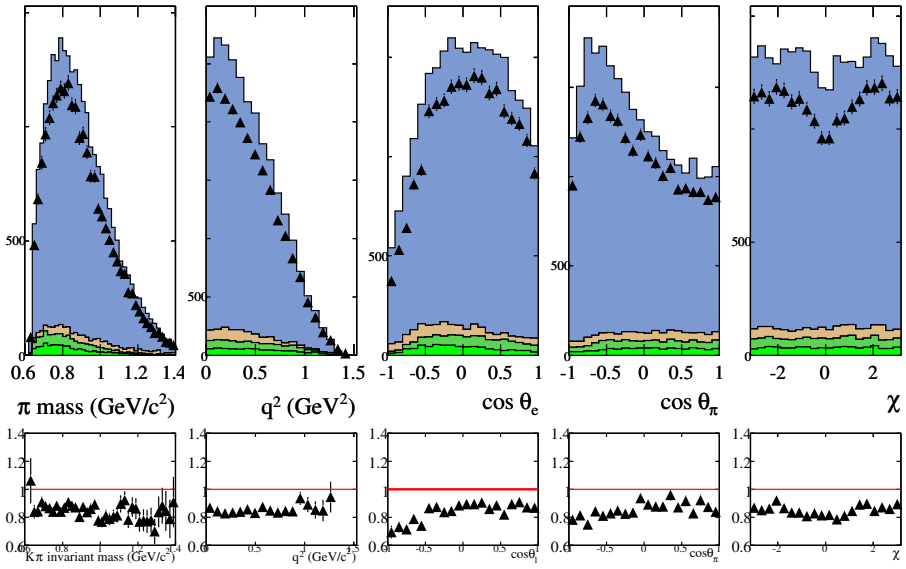

Figure 4.51: *Run4 distributions of the 5 dynamical variables for WS events in data and MC before any corrections are applied. ($\triangle$) data , MC in stacking order : $B^0\bar{B}^0$, B^+B^-, uds and $c\bar{c}$. Lower row: ratio data/MC for upper row plots.*

The remaining rate difference between data and Monte Carlo is taken into account by renormalizing the charm background. The ratio between remaining data events and the estimated (and corrected) charm background is 0.98 ± 0.01.

It can be seen that a good agreement exists in the discriminant variables distributions between data and Monte Carlo after the corrections in Figure 4.54 as well as for most dynamical variables in Figure 4.53. One can observe

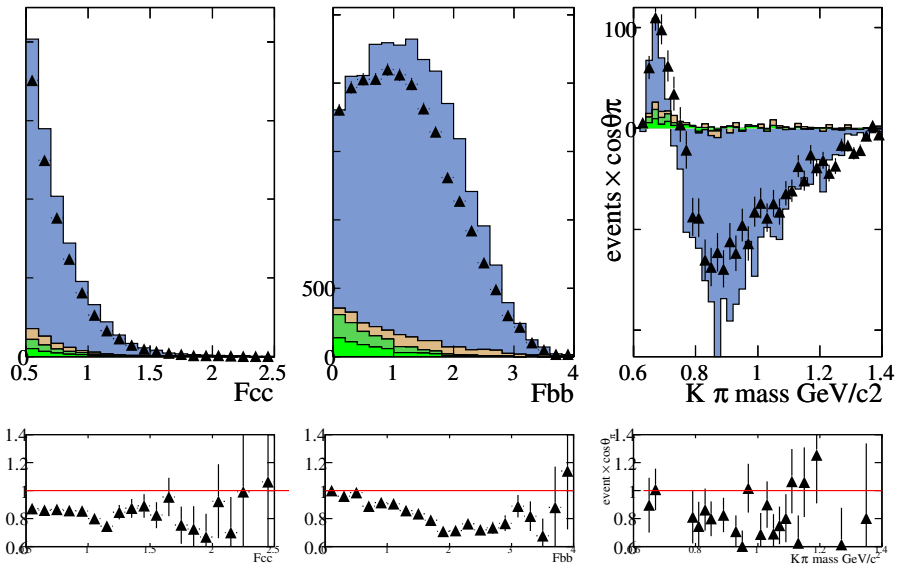

Figure 4.52: *Run 4 distribution for WS data and MC for the Fisher discriminants and asymmetry variation with mass before corrections on charm decays. (△) data , MC in stacking order : $B^0\bar{B}^0, B^+B^-, uds$ and $c\bar{c}$. Lower row: ratio data/MC for upper row plots.*

however that some discrepancy remains in the q^2 distribution.
An additional correction is applied over the charm simulation events in order to harmonize the shape of the Monte Carlo charm contribution in q^2 with the data shape. The ratio data/MC versus q^2 is fitted using a linear expression: $\frac{data}{MC} = (1.028 \pm 0.016) - (0.118 \pm 0.028)q^2$ and a weight is applied on simulated events. The final distributions for WS events are given in 4.55 and 4.56. In general the studied variables show that the MC reproduces correctly the data distributions and remaining discrepancies are of lower order.

Similar evaluations have been done for BaBar runs 1,2,3 and 5. The obervations about the behaviour of the dynamical variables and of the Fisher discriminants are similar to those made for run4. The corresponding figures from 13.20 to 13.31 can be found in the Appendix section.

To strengthen the case of using WS events to control RS $c\bar{c}$ background we present if Figure 4.57 the distribution for q^2 and $\cos\theta_l$ for WS and RS charm background after all cuts.
Their similarity illustrates the reliability of the study of WS events.
The observed difference in the WS events q^2 distribution has been parameterized and this correction has been applied on RS background events. Half of the variation measured on fitted parameters is used as corresponding systematic uncertainty.

4.3.4 Summary of the corrections applied on the Monte Carlo charm background

We apply the following corrections to the estimated charm background:

- tuning corrections for fragmentation properties and for Fisher discriminant variables;

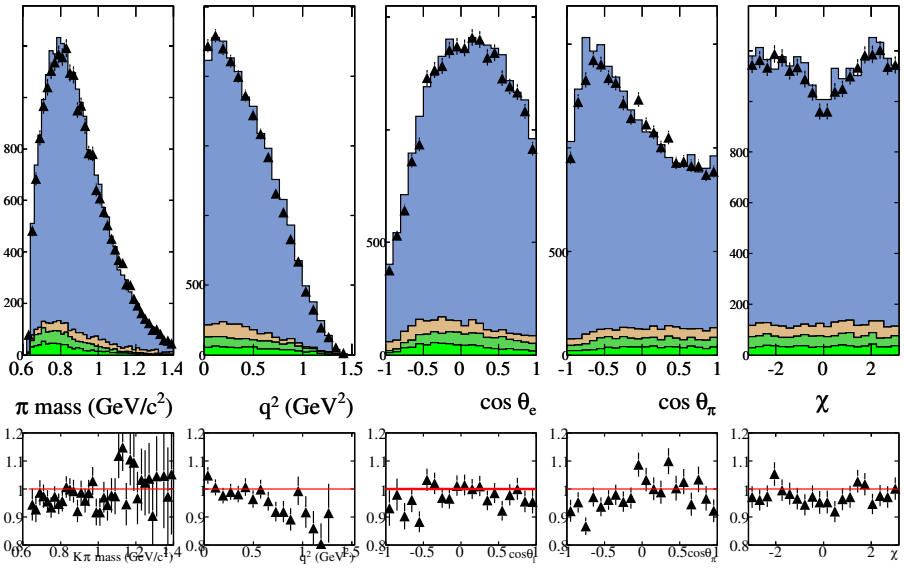

Figure 4.53: *Run 4 distributions of the 5 dynamical variables for WS events in data and MC after tuning and form factor corrections. (△) data , MC in stacking order : $B^0\bar{B}^0, B^+B^-, uds, c\bar{c}$. Lower row: ratio data/MC for upper row plots.*

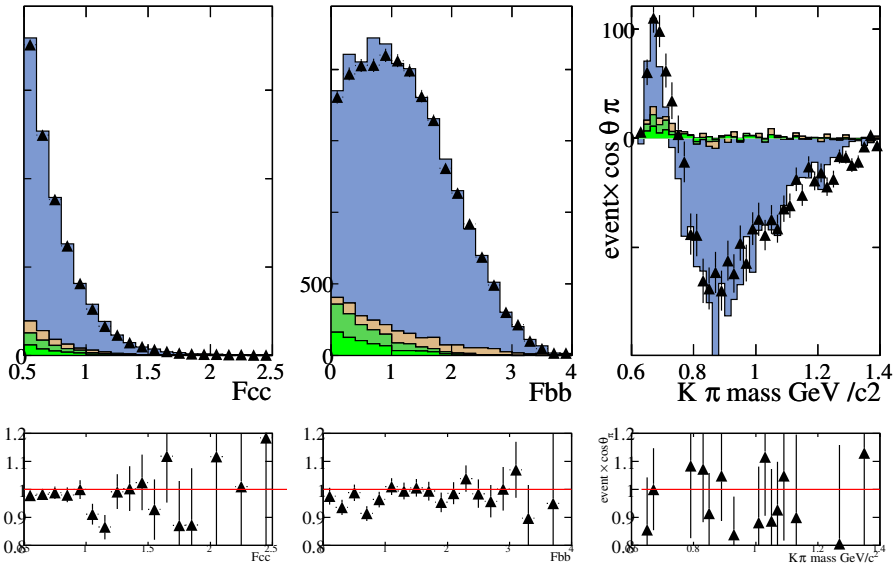

Figure 4.54: *Run4 distribution for WS data and MC for the Fisher discriminants and asymmetry variation with mass after tuning corrections and form factor corrections on charm decays. (△) data , MC in stacking order : $B^0\bar{B}^0, B^+B^-, uds, c\bar{c}$. Lower row: ratio data/MC for upper row plots.*

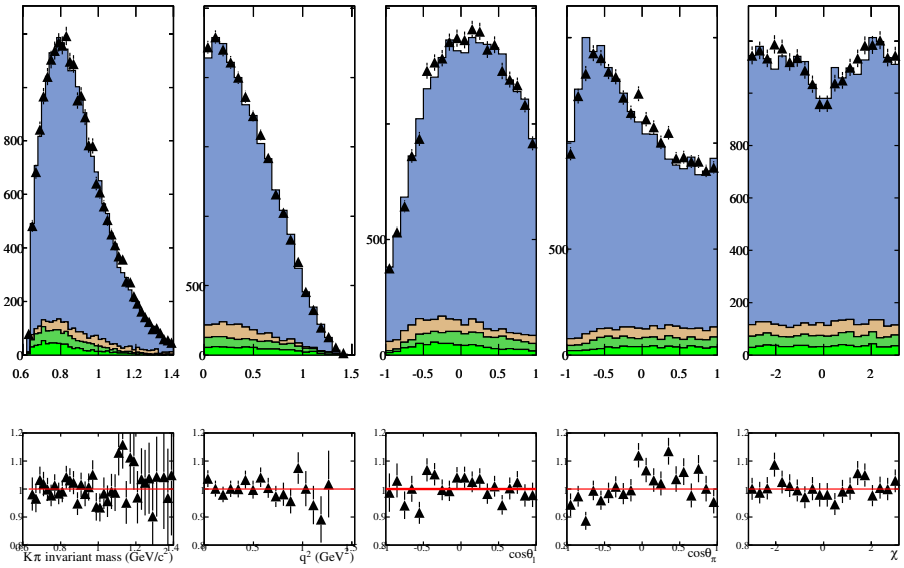

Figure 4.55: *Run4 distributions of the 5 dynamical variables for WS events in data and MC after tuning, form factor corrections, renormalisation of the charm contribution and after applying a correction versus q^2. ($\triangle$) data , MC in stacking order : $B^0\bar{B}^0, B^+B^-, uds, c\bar{c}$. Lower row: ratio data/MC for upper row plots.*

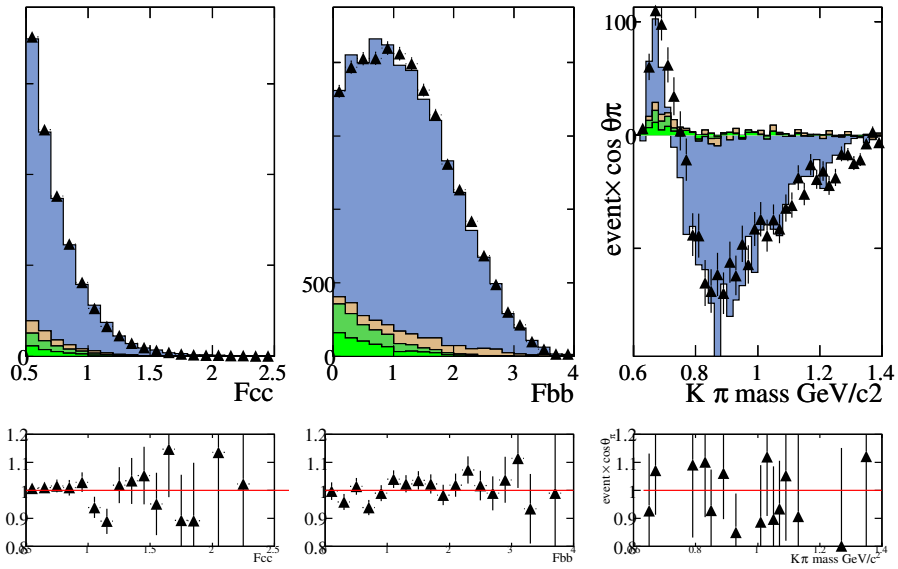

Figure 4.56: *Distribution for WS data and MC for the Fisher discriminants and asymmetry variation with mass after tuning, form factor corrections on charm decays, renormalization of the charm contribution and after applying a correction versus q^2. ($\triangle$) data , MC in stacking order : $B^0\bar{B}^0, B^+B^-, uds, c\bar{c}$. Lower row: ratio data/MC for upper row plots.*

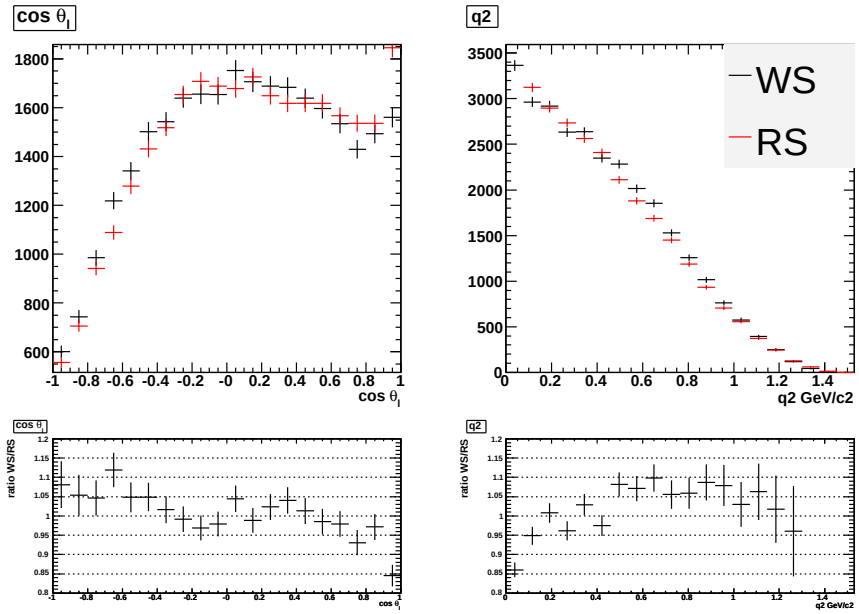

Figure 4.57: *Upper plot: comparison between RS and WS charm background q^2 and $\cos\theta_l$ distributions. The RS sample is normalized to WS. Lower plot: ratio between these distributions.*

- correction for semileptonic decay models;

- renormalization of the rate and correction of the q^2 shape;

The uncertainties associated to each of these effects are calculated for systematic errors purposes in the appropriate section.

4.4 Construction of a specific dataset for signal

The desired signal distribution has both S and P-wave components. A priori one can transform a sample of events generated according to a P-wave by applying a weight, on each event, equal to the ratio between the S+P and the P-wave decay rates:

$$W_{SP/P} = \frac{\frac{d^5\Gamma_{S+P}}{dm^2 dq^2 d\cos(\theta_K) d\cos(\theta_e) d\chi}}{\frac{d^5\Gamma_P}{dm^2 dq^2 d\cos(\theta_K) d\cos(\theta_e) d\chi}} \tag{4.4}$$

However, since there are only few events in the P-wave distribution, for $K\pi$ mass values away from the $K^*(892)$ pole, large weights are obtained in these regions. Therefore the signal distribution is constructed by

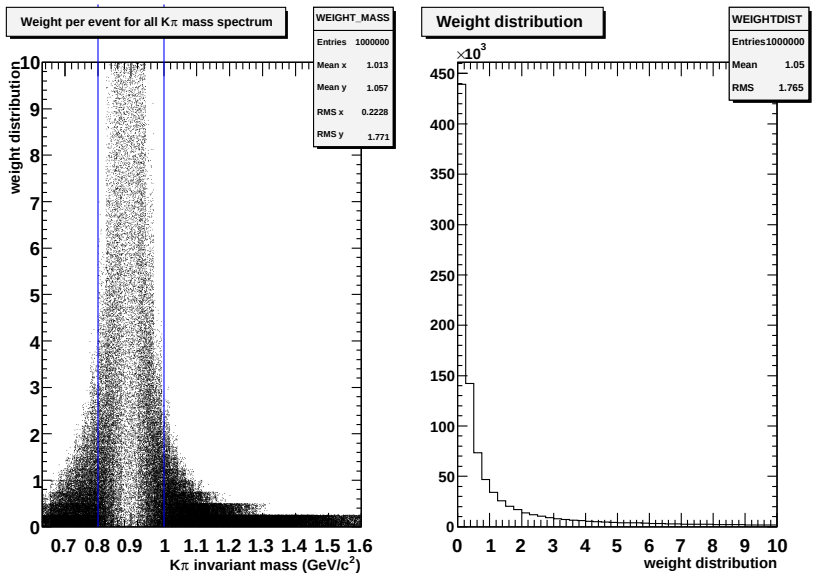

Figure 4.58: *Left:distribution of weights, versus the $K\pi$ mass, that transform an initial PHSP to an S+P-wave distribution. These events are used, in the following, for values of $m_{K\pi}$ external to the interval defined by the two lines. Right: weight distribution.*

using as input a uniform phase space (PHSP) distribution for low and high $K\pi$ mass values and a corrected SLPOLE distribution (see Section 4.1.1) around the $K^{*0}(892)$ pole, in the interval [0.8, 1.0] GeV/c^2.

The uniform phase space distribution corresponds to the following differential decay rate:

$$\frac{d^5\Gamma}{dm^2 dq^2 d\cos(\theta_K) d\cos(\theta_e) d\chi} = \frac{p^* \times p_{K\pi}}{2m} \times cste. \tag{4.5}$$

This distribution is flat in $\cos\theta_\pi, \cos\theta_e$ and χ. There is a large number of events at low masses and a considerable number of events at masses higher than 1 GeV/c^2.

To obtain a distribution corresponding to the differential decay rate for an S+P-wave, these events are weighted according to:

$$W_{SP/PHSP} = \frac{d^5\Gamma_{S+P}}{d^5\Gamma_{PHSP}} \tag{4.6}$$

Figures 4.58 and 4.59 show respectively the weight distribution versus the $K\pi$ mass for events used to produce the composite S+P MC distribution starting by either a PHSP or a P-wave SLPOLE sample. From these distributions we have decided to use the SLPOLE P-wave distribution for $m_{K\pi} \in [0.8, 1.0] GeV/c^2$ and the PHSP simulation outside this region. In this way individual weights do not exceed ≈ 2.

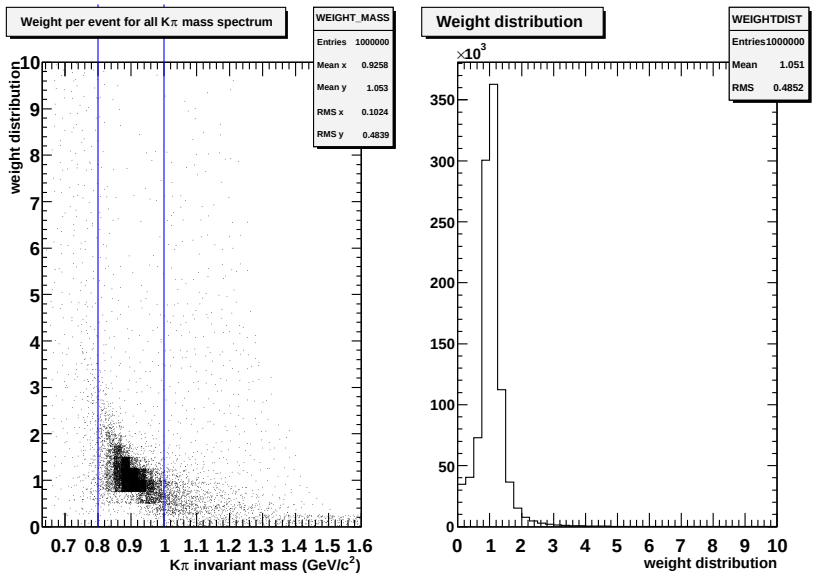

Figure 4.59: *distribution of weights, versus the $K\pi$ mass, that transform an initial P-wave SLPOLE to an S+P-wave distribution. These events are used, in the following, for values of $m_{K\pi}$ situated inside the interval defined by the two lines. Right: weight distribution.*

A variable, α, is defined to provide the relative normalization between the two event samples. Events from the PHSP sample are multiplied by α and the resulting combination of transformed PHSP and SLPOLE events is distributed according to the differential decay rate $d^5\Gamma_{S+P}(\vec{\lambda_0})$, where $\vec{\lambda_0}$ corresponds to a given set of values for the different parameters. The variable α is defined as follows:

$$\frac{\sum_{m_{K\pi}\in[0.8,\ 1.0]} d^5\Gamma_{S+P}(\vec{\lambda_0})}{\sum_{m_{K\pi}\leq 0.8,\ \geq 1.0} d^5\Gamma_{S+P}(\vec{\lambda_0})} = \frac{\sum_i^{N_{SLP}^{pole}} \frac{W_i^{S+P}(\vec{\lambda_0})}{W_i^{P}(\vec{\lambda_0})} \times W_i^{EvtGen}}{\alpha \sum_i^{N_{PHSP}^{tails}} \frac{W_i^{S+P}(\vec{\lambda_0})}{W_i^{PHSP}}} \tag{4.7}$$

where the fraction in the left member of this equality corresponds to the ratio between integrated decay rates for and S+P-wave over the mass interval corresponding to the $K^*(892)$ pole region and to the complementary region, respectively.

W_i^{EvtGen} is the correction applied to the SLPole generated mass distribution to correct for the error in the EvtGen algorithm.

To construct the simulated sample for signal events which corresponds to a S+P-wave, with parameter values given by $\vec{\lambda_0}$, the weight applied to each simulated event, i, is then:

- for events generated with SLPOLE using a P-wave and with a mass in the interval $[0.8,\ 1.0]\ \mathrm{GeV/c^2}$:

$$\frac{W_i^{S+P}(\vec{\lambda_0})}{W_i^{P}(\vec{\lambda_0})} \times W_i^{EvtGen}; \tag{4.8}$$

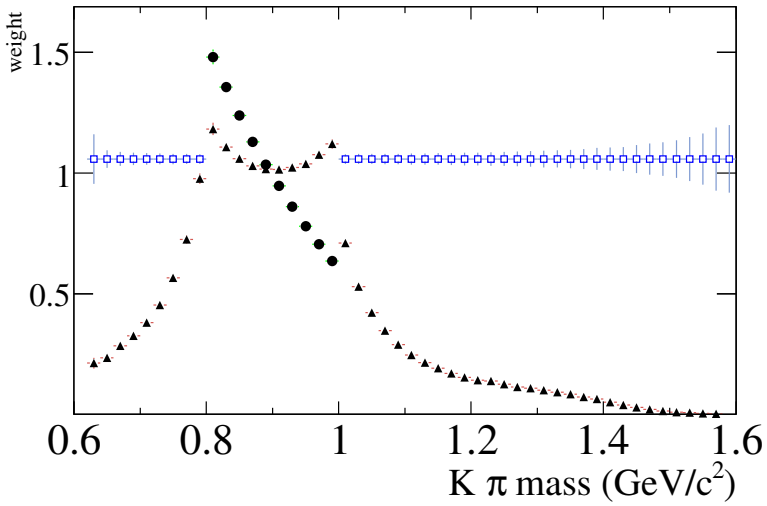

Figure 4.60: *Average weights versus the $K\pi$ mass needed so that the transformed and combined PHSP and SLPole input samples distributions become equivalent to a S+P wave distribution. In □ the value of α for the PHSP sample. In • the value of the correction due to EvtGen mass distribution for the SLPole sample. In △ the value of the ponderation of each of the samples into an S+P-wave distribution.*

- for events generated uniformly over the phase-space (PHSP) and with a mass in the interval ≤ 0.8 or ≥ 1.0 GeV/c^2:

$$\alpha \frac{W_i^{S+P}(\vec{\lambda_0})}{W_i^{PHSP}}. \tag{4.9}$$

The average weight for the signal sample is given in Figure 4.60 versus the $K\pi$ mass.

Figures 4.61 and 4.62 compare projections over the 5 kinematic variables of the obtained dataset with an exact S+P-wave distribution. A similar comparison is done in 2D -$(q^2,\ m_{K\pi})$ and $(q^2,\ \cos\theta_e)$- in Figure 4.63.

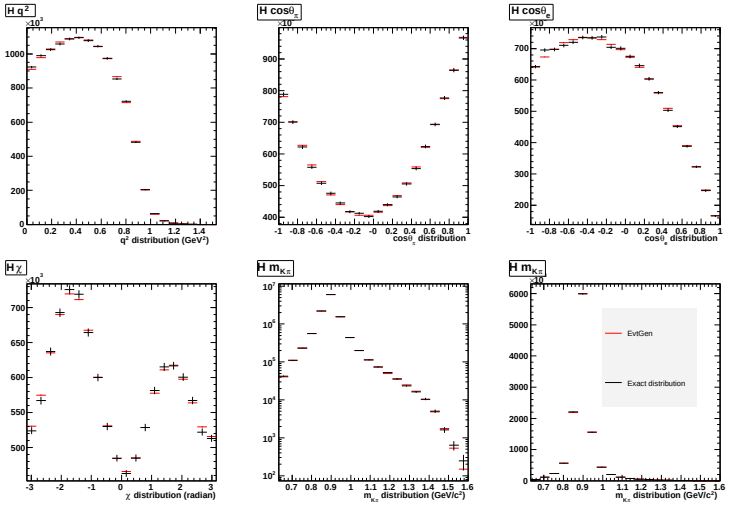

Figure 4.61: *Projections versus the 5 kinematic variables of the exact S+P and of the constructed distributions using a P-wave SLPole and a PHSP in different $m_{K\pi}$ intervals.*

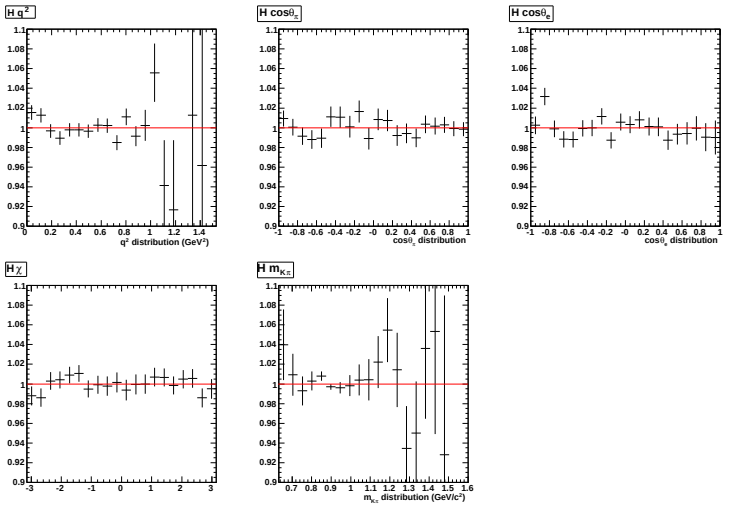

Figure 4.62: *Ratio between the exact and the constructed distributions for an S+P-wave.*

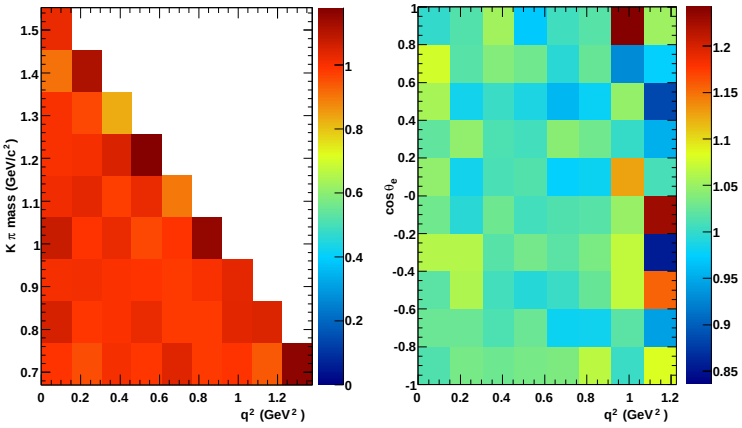

Figure 4.63: *Ratio between the exact and the constructed distribution. Left: Agreement over* q^2 *and* $m_{K\pi}$ *ranges. Right: Agreement over* q^2 *and* $\cos\theta_e$ *range*

Chapter 5

Smoothing of the background component

In this section we present the smoothing of the reference background distribution used in the analysis.
First we define the binning used for the analysis. We make a 5-dimensional fit in the following variables: $\chi, cos\theta_e, cos\theta_\pi, q^2, m_{K\pi}$. We use 5 equally sized bins in χ, 4 equally sized bins in $cos\theta_e$, 5 equally sized bin in $cos\theta_\pi$, 4 bins in q^2 and 7 bins in $m_{K\pi}$. We define in table 5.1 the boundaries for each bin for the two last variables. They have been chosen to select similar numbers of signal events in each bin.

variable	bounds for bins
$q^2\ (GeV^2)$	$0.\ ;\ 0.22185\ ;\ 0.4284\ ;\ 0.6426\ ;\ 1.53$
$m_{K\pi}\ (GeV/c^2)$	$0.63\ ;\ 0.84534\ ;\ 0.87444\ ;\ 0.88899\ ;\ 0.90063\ ;\ 0.91518\ ;\ 0.9501\ ;\ 1.6$

Table 5.1: *Bins size for q^2 and $m_{K\pi}$ variables.*

Since our fit approach does not include statistical fluctuations of the estimated number of events in each bin, effects of these fluctuations have to be evaluated. For signal we have generated dedicated samples which correspond to about 5 times the data statistics.

Unfortunately, to estimate the background, which comes mainly from continuum $e^+e^- \rightarrow c\bar{c}$ events, the available statistics of simulated events, in Run4, is similar to data. We have roughly 25k background events distributed over 2800 bins and the distribution is not uniform as shown in Figure 5.1.

Important biases appear in the determination of the fit parameters if we use simply, as estimates for background in each bin, the actual values obtained from the MC. This effect is measured with pull distributions in section 6. To reduce these biases, we perform a smoothing of the background distribution.

This smoothing is based on the article of [64]. The basic idea is to spread the contribution of each event in each of the dimensions according to a Gaussian distribution. This is a smoothing procedure where correlations between the variables are neglected. One must also take into account boundary effects and in our case this is done by reflecting the dataset about each of the boundaries.

Contributions of the different events, i (=1 to n), at a given point, with phase space coordinates $\vec{x}$, in d-

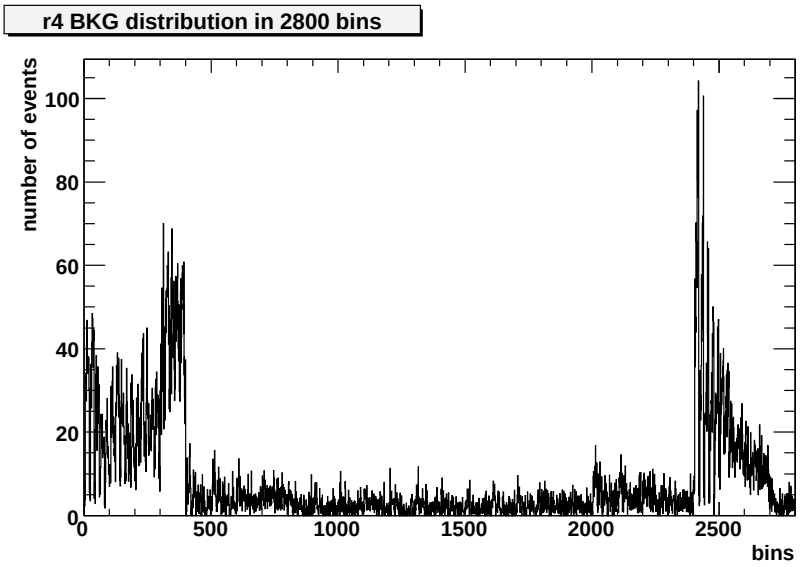

Figure 5.1: *Distribution of background events in each bin. The bin number is obtained from the expression:* $I_\chi + 5 \times I_{\cos\theta_l} + 20 \times I_{\cos\theta_\pi} + 100 \times I_{q^2} + 400 \times I_{m_{K\pi}}$ *where* I_X *is the bin number in the* X *coordinate.*

dimensions, is given by the following expression:

$$\hat{f}_0(\vec{x}) = (\frac{1}{n}) \sum_{i=1}^{n} \left[\prod_{j=1}^{d} \frac{1}{h_j} K(\frac{x_j - t_{ij}}{h_j}) \right] \tag{5.1}$$

with:

$$K(x_j) = \frac{e^{\frac{-x^2}{2}}}{\sqrt{2\pi}} \tag{5.2}$$

h_j is the smoothing parameter used for the j coordinate. The h_j parameters are given by the expression:

$$h_j = (\frac{4}{d+2})^{1/(d+4)} \sigma_j n^{-1/(d+4)} \tag{5.3}$$

Values for σ_j are defined by us and depend on the considered dimension.
This way of smoothing an initial distribution is known as the fixed kernel method. To evaluate the contribution of each event in a given bin it remains to integrate expression (5.1) over each bin domain.

Distributions of events, for all pairs of two variables, are shown in Figures 5.2-5.7. One can observe that there is no visible correlation between $\cos\theta_l$ and χ. The value of this correlation is -0.003. We can also observe that χ is essentially uncorrelated with all other variables, on the other hand $\cos\theta_l$ is correlated with the remaining variables. The adopted solution is to smooth independently χ and $\cos\theta_l$ for each bin in ($m(K\pi)$, q^2 and $\cos\theta_\pi$.)

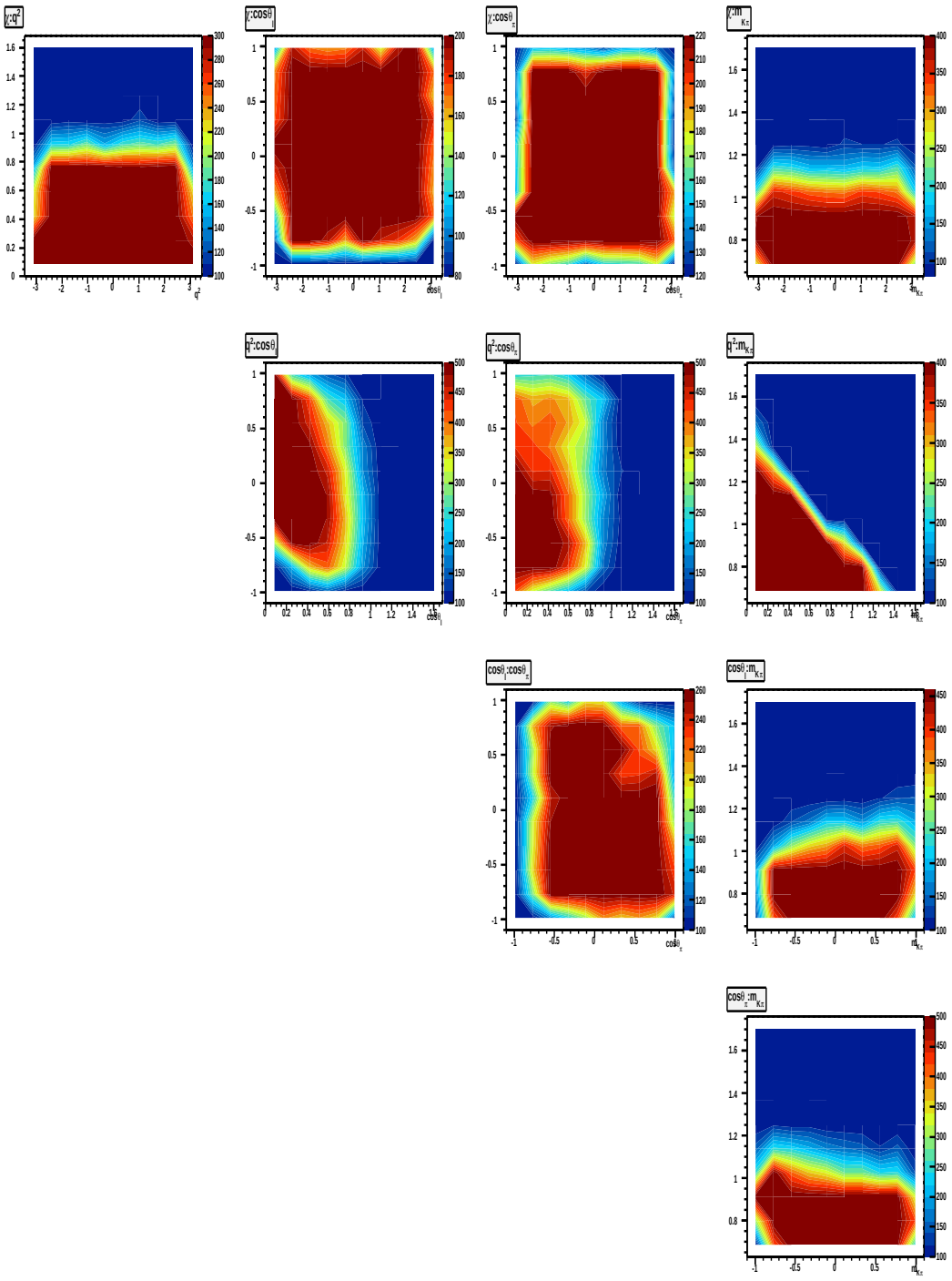

Figure 5.2: *Distributions of simulated background events in Run4 for all 2-D projections. This is just a way of showing possible correlations in phase space.* $\chi, q^2, cos\theta_e, cos\theta_\pi$ *are on the vertical axis of distributions in lines 1 to 4, respectively.* $q^2, cos\theta_e, cos\theta_\pi, m_{K\pi}$ *are on the horizontal axis of columns 1 to 4 respectively.*

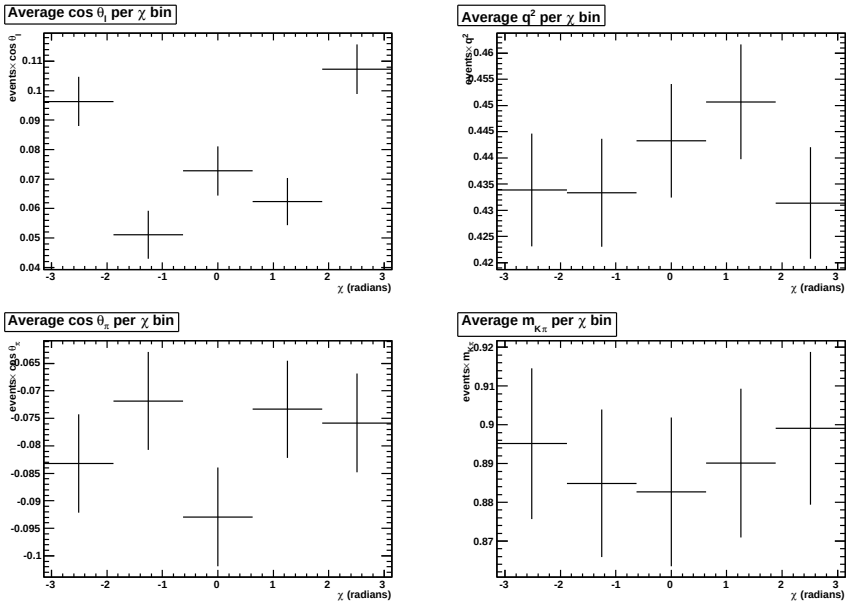

Figure 5.3: *Variation of the averages of decay variables in each bin of* χ.

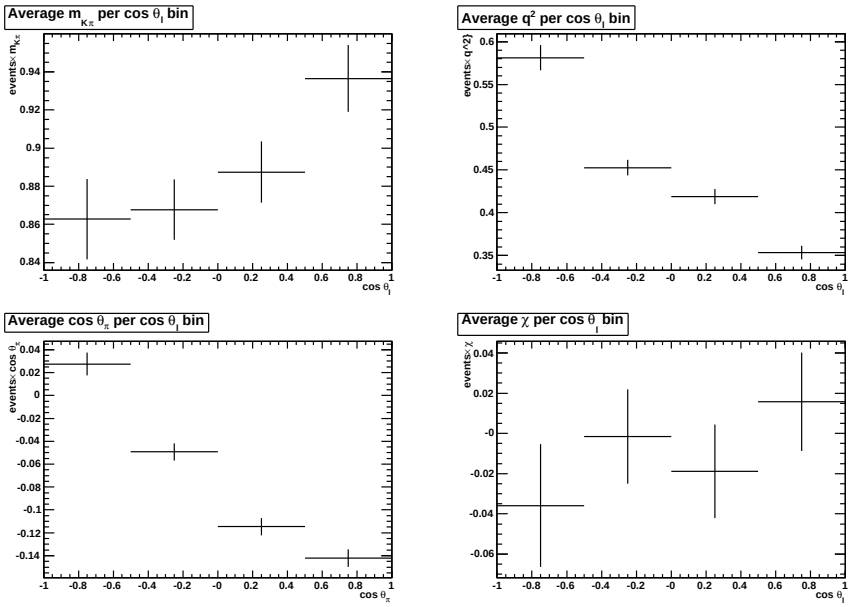

Figure 5.4: *Variation of the averages of decay variables in each bin of* $\cos\theta_l$.

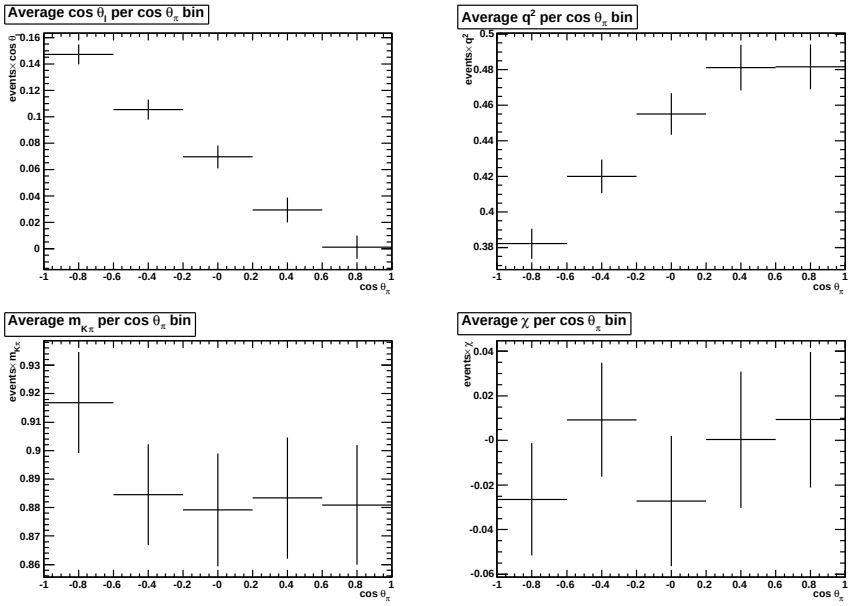

Figure 5.5: *Variation of the averages of decay variables in each bin of* $\cos\theta_\pi$.

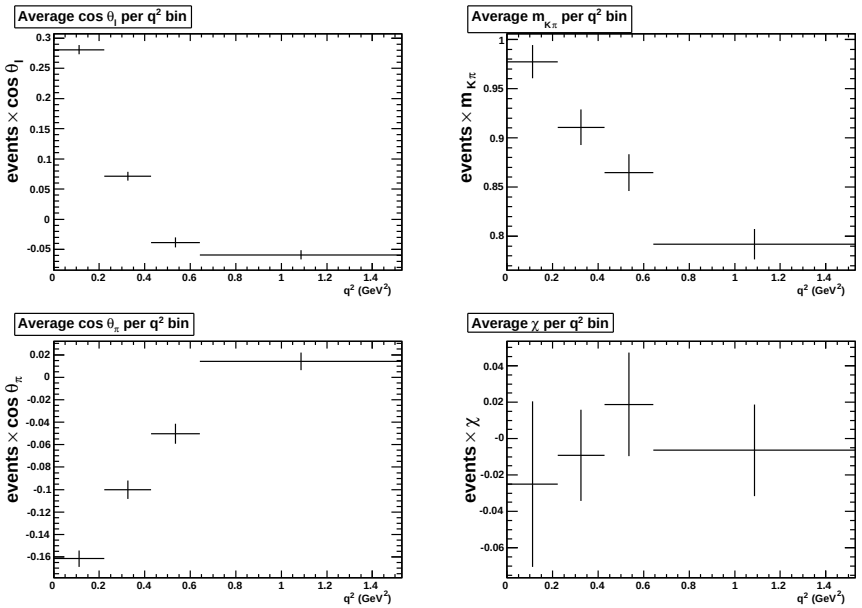

Figure 5.6: *Variation of the averages of decay variables in each bin of* q^2.

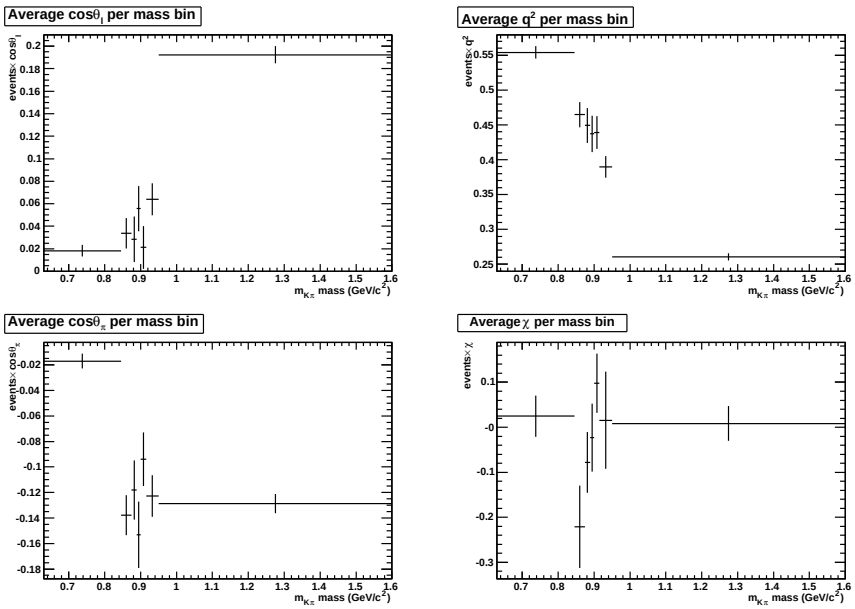

Figure 5.7: *Variation of the averages of decay variables in each bin of* $m_{K\pi}$.

5.1 Improvement in the background estimate

To evaluate quantitatively the effect of smoothing over a given distribution we use distributions generated with a toy program.

We construct two similar background distributions which reproduce approximately the shape of the BaBar MC background in each of the 5 dimensions. The phase space limitation is the only source of correlation between variables (it correlates q^2 and $m_{K\pi}$). One of these distributions has 20k events (which is similar to the background statistics available in Run4) while the other contains 2M events, that we normalize to 20k.

Our purpose is to compare both the low statistics and the corresponding smoothed distributions, with the high statistics sample. This is presented in Figure 5.8 where we plot the difference measured in each bin between the number of events estimated with the large statistics sample and the low statistics one, smoothed or not, divided by its error. This error is taken as the square root of the number of events obtained with the large statistics sample (properly normalized).

The quantity $\frac{N_i - N_{BigBKG}}{\sigma_{BigBKG}}$, where i stands for either the smoothed distribution or the low statistics sample, is thus plotted for each bin.

We observe that on the upper plot, the mean is -0.01 ± 0.02 and the sigma 0.88 ± 0.01. On the lower plot the mean is 0.01 ± 0.01 and the sigma is 0.45 ± 0.01.

We compare the effect of the smoothing procedure to that of having a background control sample of higher statistics, in fits to toy samples: We have made pull distributions for toys with 70k (S+P wave) signal events and with no or 32k background events, and where the signal control sample has 315k events. These distributions have been obtained with 500 toy experiments. The following situations have been considered:

- no background exists. We fit the S+P wave parameters and the signal rate;

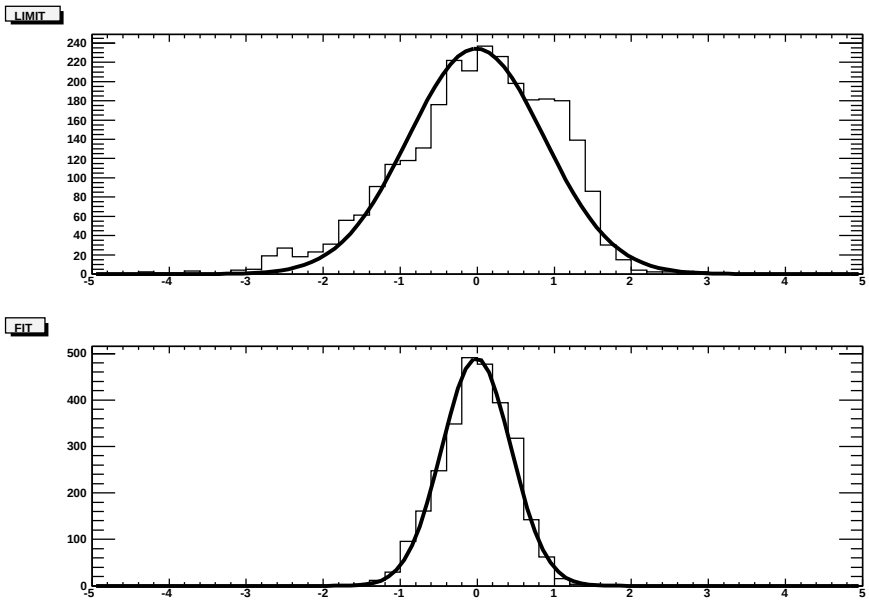

Figure 5.8: *Upper plot: Difference between large and low statistics bkg divided by uncertainty of the former. Lower plot: Relative difference between large and the smoothed bkg divided by uncertainty of the former.*

- the background control sample is not smoothed. The background rate is fixed to the expected value (32k). We fit the S+P wave parameters and the signal rate. The background control sample has 1.1 times the background data sample statistics;

- similar as above but now the background control sample has 4.4 times the background data statistics;

- the background control sample is smoothed. The background rate is fixed to the expected value (32k). We fit the S+P wave parameters and the signal rate. Th background control sample has 1.1 times the events of background in the data sample;

We observe (Table 5.2) that:

- having 4.5 times the signal statistics in the control sample (first column) we get an average deviation of 1.1. (Using for the control sample 10 times the data gives pull distributions with a $\sigma \approx 1.0$).

- the addition of background (second column) increases the average deviation and creates biases in most of the parameters if the background control sample has similar statistics as the background in the data sample;

variable	no bkg	1.1 $\times$ stats, no Smoothing	4.4$\times$ stats, no Smoothing	1.1 $\times$ stats, Smoothing
$\Gamma^0(K^{*0})$	(0.07,1.14)	(-0.68,1.15)	(0.05,1.11)	(0.10,1.16)
$m(K^{*0})$	(0.09,1.15)	(0.01,1.19)	(0.06,1.16)	(0.03,1.20)
r_{BW}	(0.12,1.09)	(0.10,1.23)	(0.15,1.10)	(0.12,1.21)
λ_A	(0.23,1.12)	(-0.28,1.11)	(0.24,1.11)	(0.19,1.14)
r_V	(-0.20,1.12)	(0.49,1.11)	(-0.21, 1.09)	(-0.17,1.11)
r_2	(0.11,1.08)	(-0.44,1.17)	(0.13,1.10)	(0.07,1.15)
r_S	(-0.12,1.11)	(0.01,1.29)	(-0.13,1.14)	(-0.11,1.23)
a_S	(0.13,1.11)	(-0.03,1.26)	(0.08, 1.11)	(0.03,1.18)
Ns	(-0.04,0.98)	(-1.28,0.98)	(-0.02,0.97)	(0.02,0.97)

Table 5.2: *Pull results to study the effect of background smoothing for toys data samples with similar statistics as in Run4. For each fitted parameter we give the bias and normalized standard deviation (bias, sigma). We consider 4 situations. 1st) signal only. 2nd) not smoothing the background control sample. The background control sample has 1.1 times the events of the background data sample. 3rd) not smoothing the background control sample. The background control sample has 4.4 times the events of the background data sample. 4th) smoothing the background control sample. The background control sample has 1.1 times the events of the background data sample.*

- having a background control sample with 4.4 times the statistics of the background data sample (third column) reduces greatly the biases and some of the pull standard deviations;

- smoothing a background control sample that has similar statistics as the background data sample (fourth column) reduces significantly biases but does not reduce really the pull standard deviations.

We conclude that the smoothing procedure has an effect which is not completely equivalent in having more background events in the control sample than in the data sample: biases are reduced but fluctuations essentially remain.

Chapter 6

Fitting procedure

Here we explain our procedure for extracting signal parameters as well as signal and background rates from the BaBar data samples.
This procedure is reasonably complex and requires validation. The validation of the fit program is obtained using distributions generated with a toy program that emulates the behaviour of BaBar data and of the Monte Carlo BaBar simulation. Several hundred of independently created distributions are fitted and pull distributions are constructed for fitted parameters. Possible bias and standard deviation values that differ respectively from 0 and unity, coming from these pulls, are included as systematic uncertainties for the analysis. Statistics used for the toy data, signal control and background samples are similar with those existing for Run4 data. Therefore the MC limited statistics effect in the fit precision is included in these tests. The signal control sample corresponds to events containing only signal and are used in the fit to measure the signal component. Number of events in this sample is usually between to 4.5 and 5 times the real signal statistics.
A crosscheck of the fit procedure is made using the Monte Carlo BaBar simulation. Here we do two tests. The first is to construct a data sample of Monte Carlo signal, and fit this data sample with the remaining available Monte Carlo. These samples have all the selection cuts used in the analysis. With this test we check if the detector acceptance and resolution affect the fit outcome.
The second test is to see if we can fit different signal distributions using the same Fisher distributions. For this, we create 3 S+P "data samples" with a background component. Each of these signal distributions have different values for r_V and r_2. We perform the fit for each of these distributions using the same F_{cc} discriminant pdf. The rate of background in this test is similar to the one we find in our analysis.

6.1 Likelihood distribution

The fit minimizes $(-2\log)$ of a likelihood expression. This expression is composed of two parts, the first being a binned likelihood. Here, the data and control samples are distributed in bins over 5 dimensions ($q^2, \cos\theta_\pi$, $\cos\theta_e, \chi, m_{K\pi}$). In each bin the measured number of events is compared with expectations from the simulation according to Poisson statistics.
We have divided the variation range of the variables χ and $\cos\theta_\pi$ in 5 equally sized bins whereas for the variables q^2 and $m_{K\pi}$ we use 4, and 7 bins respectively. For these two last variables we use bins of different size so that

each one contains approximately the same amount of signal events. The $\cos\theta_e$ variable is distributed over 4 bins of equal size. In total there are 2800 bins.
The second part of the expression consists of an unbinned likelihood expression. Here we use the values of the discriminant variable F_{cc} of the data sample to determine the fraction of background events.

The likelihood expression is given in Equation (6.1).

$$\mathcal{L} = \prod_{i=0}^{Nbins} P(n^i_{data}|n^i_{MC}) \times \prod_{j=1}^{Ndata\ evts} (\frac{N_S}{N_S+N_B} \times pdf^S_j + \frac{N_B}{N_S+N_B} \times pdf^B_j) \tag{6.1}$$

Here i ranges from 0 to 2799. n^i_{data} is the number of data events in bin *i*, n^i_{MC} is the sum of the MC estimates for background and signal events in the same bin. The expression for this quantity is:

$$n^i_{MC} = \frac{N_S}{W^{tot}_{fit}(\vec{\lambda_0},\vec{\lambda})} \times \sum_{j=0}^{N^{bin\ i}_{events}} \frac{W_j(\vec{\lambda})}{W_j(\vec{\lambda_0})} C_j + \frac{N_B}{W^{tot}_{BKG}} \times W^i_{BKG}$$

$$W^{tot}(\vec{\lambda_0},\vec{\lambda}) = \sum_{j=0}^{N^{all\ bins}_{events}} \frac{W_j(\vec{\lambda})}{W_j(\vec{\lambda_0})} C_j$$

$\vec{\lambda},\ \vec{\lambda_0}$ correspond, respectively, to the set of fitted parameters and to the set of parameters used to produce simulated events. $W_j(\vec{\lambda})$ is the value of the expression for the decay rate (see Eq. 1.43) for event *j* using the set of parameters $(\vec{\lambda})$, $W_j(\vec{\lambda_0})$ is the value for the same expression and for the same event using $(\vec{\lambda_0})$. In these ponderations we use the generated values of the kinematic variables.
C_j is the correction weight applied to each signal event from tuning. This last weight is unchanged during the fit.
W^i_{BKG} is the estimated number of background events in bin i and W^{tot}_{BKG} is the estimated total number of background events.

N_S and N_B are the expected total number of signal and background events in the data sample. The estimated background in each bin is obtained after smoothing over the variables χ and $\cos\theta_e$.

The functions $pdf^{S,B}$ are the pdf of the F_{cc} distributions for signal and background respectively, defined using the Monte Carlo samples.

The fitted parameters for a signal composed of the $K^{*0}(892)$ and a S-wave parameterised with the LASS model are listed below:

- $m(K^{*0}_{892})$, the mass of the vector meson K^{*0}_{892};
- $\Gamma^0(K^{*0}_{892})$, the width of the vector meson K^{*0}_{892};
- r_{BW}, the Blatt-Weisskopf damping factor;

- m_A the pole mass used in axial vector and scalar form factors;
- r_2, the ratio $\frac{|A_2(0)|}{|A_1(0)|}$;
- r_V, the ratio $\frac{|V(0)|}{|A_1(0)|}$;
- r_S, a parameter which characterizes the strength of the S-wave;
- a_S, the scattering length entering in the LASS parameterization;
- N_S and N_B, respectively signal and background event numbers.

For the S-wave parameterization we use the value $b_S = 1.76\ (GeV/c)^{-1}$ [19] as measured by LASS and the parameters of the $K_0^*(1430)$ given in [13], $M(K_0^*(1430)) = 1.435\ GeV/c^2$, $\Gamma^0(K_0^*(1430)) = 0.279\ GeV/c^2$.

6.2 Fit validation

6.2.1 Analysis of pull distributions

We have produced pull distributions of fitted parameters to validate the fitting method. We analyse the impact of several of the implementations/corrections applied to simulated events. These controls are done step by step adding in turn a new feature given in the list which follows such that the final test is representative of a fit done on data.
Each experiment of the toy signal sample has 50k events on average, distributed according to a Poisson law. The signal control sample contains for most cases 225k events, in agreement with the statistics available when fitting data. The background distribution in each experiment contains 20k events and the same statistics is used in the control sample. All numbers of events are distributed according to the Poisson law.

Pull distributions for fitted parameters are obtained in the following conditions:

- the fitting program having the same structure for toy and real experiments is run on a P-wave and on an S+P-wave decay models where the control sample has 10 times or 4.5 times the statistics of the data sample;
- we include background having similar projected distributions over the kinematic variables as in data but without most of the correlations between each variable;
- we smooth the background distribution as explained in a previous section;
- we use the Fisher information to evaluate the rate of signal and background;
- we use reweighted phase space and P-wave distributions to simulate an S+P-wave distribution;
- we apply the correction to P-wave events produced with EvtGen using the SLPOLE model.

For each experiment, a different control sample is also generated. For each study, the average value and standard deviation of the pull distribution of fitted parameters are listed in Tables 6.2 and 6.3. Below are commented results obtained in these different conditions.

Check of the fitting program We fit a P-wave distribution using also a P-wave for the control sample. This last distribution is obtained using the same values for the parameters and corresponds to approximately 10 and 4.5 times the statistics of the experiment. The same binning is used for the five kinematic variables as in data.

Fitted parameters are the resonance mass and width together with the form factor ratios (at $q^2 = 0$) and the axial pole mass. Results are presented in lines (A) and (A2) of Tables 6.2 and 6.3. Pull distributions are presented in Figures 13.32 and 13.33. All distributions are well fitted with Gaussians. Average values of these distributions are ≤ 0.1 and their standard deviation is close to 1 σ for the larger control sample, otherwise the standard deviation is closer to 1.1σ.

We have also tested the addition of an S-wave to the model. Again we use the same model and parameter values for the "$data$" and for the control and we use two control samples, one with 10 times and the other with 4.5 times the data samples statistics. Additionnal parameters are fitted: the relative amplitude of the S-wave to the P-wave, the scattering length term of the S-wave and the barrier factor for the P-wave. Corresponding pull distributions are given in Figures 13.34 and 13.35. Results are presented in lines (B) and (B2) of Tables 6.2 and 6.3.

parameters	control	fake data
$m_{K^{*0}(892)}\ (MeV/c^2)$	896	896
$\Gamma^0_{K^{*0}(892)}\ (MeV/c^2)$	50.3	50.3
$r_{BW}\ (GeV/c)^{-1}$	3.0	3.0
r_2	0.78	0.78
r_V	1.82	1.82
$m_A(GeV/c^2)$	2.5	2.5
$m_V(GeV/c^2)$	2.1	2.1
r_S	0.3	0.3
$a\ (GeV^{-1})$	2.0	2.0
$b\ (GeV^{-1})$	3.3	3.3
$m_{K^*_0(1430)}\ (MeV/c^2)$	1412	1412
$\Gamma^0_{K^*_0(1430)}\ (MeV/c^2)$	294	294
$m_S(GeV/c^2)$	2.5	2.5

Table 6.1: *Values of the parameters used in the fits.*

Fit results including background The background component is added in the fake data distribution and in the control sample. Both have similar statistics, as it happens in our analysis. The fit is done first, without fitting the bakground rate and without smoothing the background distribution. The distributions are shown in Figure 13.36. The introduction of background biases several of the parameters and increases the standard deviation from 1 to 1.2. This shows the need for a control of its fluctuations.

We next perform a smoothing to the background distribution as explained in a previous chapter. Corresponding pull distributions are presented in Figure 13.37. The smoothing of the background greatly reduce the

biases.

We then fit the background rate using the distribution of the values of the F_{cc} Fisher discriminant. Corresponding results are presented in Figure 13.38.

The S+P signal distribution is obtained from reweighted phase space and P-wave distributions We reproduce the implementation of the composed control dataset used in the fit of real data. We use a P-wave in the $K^{*0}(892)$ region ($m_{K\pi} \in [0.8, 1.0]$ GeV/c^2) while for the rest of the mass range we take a phase space distribution. Each event belonging to these distributions is reweighted such that the final distribution corresponds to an S+P-wave. The expressions that correspond to this step are the following:

$$W_{SP/P} = \frac{\frac{d^5\Gamma_{S+P}}{dm^2 dq^2 d\cos(\theta_K) d\cos(\theta_e) d\chi}}{\frac{d^5\Gamma_P}{dm^2 dq^2 d\cos(\theta_K) d\cos(\theta_e) d\chi}} \tag{6.2}$$

$$W_{SP/PHSP} = \frac{d^5\Gamma_{S+P}}{d^5\Gamma_{PHSP}} \tag{6.3}$$

In this case the phase space distribution is given by :

$$\frac{d^5\Gamma_{PHSP}}{dm_{K\pi} dq^2 d\cos\theta_l d\cos_{\theta_\pi} d\chi} = p_{K\pi} p^* \tag{6.4}$$

and the decay rate for the P-wave and S+P-wave is given in Wise[38].

The weighted P-wave and phase-space samples are normalized such that they correspond to the integrated decay rate of the S+P-wave, over their respective mass intervals. This is done by multiplying the weighted phase space sample by the factor α:

$$\alpha = \frac{\sum_{i=0}^{Nslp\ events} \frac{d^5\Gamma_{S+P}}{d^5\Gamma_P}}{\sum_{j=0}^{Nphsp\ events} \frac{d^5\Gamma_{S+P}}{d^5\Gamma_{PHSP}}} \times \frac{\%\ tail\ events\ in\ the\ S+P\ distribution}{\%\ pole\ events\ in\ the\ S+P\ distribution} \tag{6.5}$$

Here $Nslp$ stands for the number of events of the P-wave sample in the pole region, $Nphsp$ stands for the number of events of the phase space distribution outside of the pole region. Number of events appearing in the expression for α are evaluated at the generation level, before applying any selection or reconstruction procedure.

Correction of generated events in EvtGen with the SLPOLE model To quantify the effects of the imperfect corrections applied to the EvtGen generated P-wave distribution we have examined pull distributions of the fitted parameters obtained in this way. Results are presented in Figure 13.40.

Summary of the validation tests Biases on some of the fitted parameters are varying from 0.1 to 0.3 sigma. The standard deviation of the pulls is of the order of 1.2. This increase comes from the fact that statistical fluctuations on estimates, in each bin, for the signal and background number of events are not included in the likelihood. As observed with pull distributions, the main effect comes from the background estimate as the statistics of corresponding simulated events is only similar to data.

This effect is included as a systematic uncertainty equal to:

$$\sqrt{1.2^2 - 1} \times \sigma_{stat} = 0.7 \times \sigma_{stat}$$

6.2.2 Fit results on full simulation

We make an additional test of the fit procedure using the full MC simulation for signal only.

Test of the fit of the S $\&$ P-wave parameters

We perform a fit to a Monte Carlo sample made up of a SLPole $D^+ \rightarrow \bar{K^{*0}}(892)e^+\nu_e$ where the distribution of events in mass has been filtered to correct the EvtGen mass generation bug. This sample is composed of events with a hadronic mass between [0.8;1.0] GeV/c^2. This "data" sample is fitted using another set of SLPole sample (5 times more statistics), which has been reweighted to correct the EvtGen mass distribution bug. These distributions are created from the full sample of SLPole used to fit BaBar data from runs1-5. They have therefore been subjected to the acceptance of the detector, as well as the selection cuts applied as in a true data fit.
Fitted values of the parameters are compared with their true values in Table 6.4.

Results do not indicate a problem.

Check of the independence of the signal pdf to different values for r_2 $\&$ r_V

We want to test if we can fit different possible signal distributions using the same signal pdf for F_{cc}. The signal F_{cc} pdf is obtained using a MC distribution generated with r_2=0.78 and r_V=1.82.
Full Monte Carlo signal distributions are created for different values for r_2 and r_V:(r_2=0.6,r_V=1.82), (r_2=0.9,r_V=1.82), (r_2=0.78,r_V=1.4) and (r_2=0.78,r_V=2.0).
The background distribution for "'$data$"' and "'$control$"' are the same. We find that the fitted parameters are in agreement with their nominal values within quoted uncertainties. Results are given in Table 6.5. This test allows us to believe that the signal pdf found with our initial parameterisation for the S+P-wave can be used to fit real data.

PULL	$m_{K^*(892)}$	$\Gamma_{K^*(892)}$	r_{BW}	r_2	r_V	m_A
A)Pwave	$(0.1, 1.03)$	$(0.1, 1.02)$	$(-)$	$(-0.08, 0.99)$	$(0.08, 1.01)$	$(-0.06, 0.95)$
$A2$)Pwave	$(0.04, 1.08)$	$(0.09, 1.11)$	$(-)$	$(-0.06, 1.11)$	$(0.05, 1.09)$	$(0.0, 1.03)$
B)SPwave	$(0.1, 1.01)$	$(0.1, 0.99)$	$(-0.09, 1.06)$	$(-0.12, 1.04)$	$(0.11, 1.05)$	$(-0.14, 1.01)$
$B2$)SPwave	$(0.08, 1.18)$	$(0.09, 1.09)$	$(0.11, 1.08)$	$(0.17, 1.11)$	$(-0.21, 1.09)$	$(0.19, 1.16)$
$C) = (B2)$ with background (fixed)	$(0.20, 1.21)$	$(-0.82, 1.26)$	$(-0.08, 1.27)$	$(-1.08, 1.14)$	$(1.52, 1.20)$	$(-0.78, 1.00)$
$D) = (B2)$ with background fixed and smoothed in MC	$(0.13, 1.15)$	$(-0.14, 1.26)$	$(0.11, 1.23)$	$(-0.21, 1.12)$	$(0.34, 1.05)$	$(0.00, 1.04)$
$E) = (D)$ with Fit to BKG using Fcc	$(0.12, 1.20)$	$(0.10, 1.11)$	$(0.07, 1.06)$	$(-0.15, 1.22)$	$(0.25, 1.00)$	$(-0.04, 1.06)$
$F) = (E)$ with composed Signal sample	$(0.19, 1.10)$	$(0.12, 1.13)$	$(-0.08, 1.19)$	$(-0.28, 1.20)$	$(0.33, 1.08)$	$(-0.20, 1.16)$
$G) = (F)$ with corrected EvtGen-like Signal sample	$(-0.56, 1.14)$	$(-0.23, 1.14)$	$(0.30, 1.19)$	$(-0.31, 1, 20)$	$(0.35, 1.12)$	$(-0.20, 1.13)$

Table 6.2: *Results from pull distributions for P-wave fitted parameters. In lines A and B the signal control sample has 10 times the statistics of each experiment whereas for other cases this statistics is only 4.5 times higher (as available when fitting data).*

PULL	r_S	a_S	N_S	N_B
A)Pwave	$(-)$	$(-)$	$(-)$	$(-)$
$A2$)Pwave	$(-)$	$(-)$	$(-)$	$(-)$
B)SPwave	$(-0.01, 1.01)$	$(0.02, 1.04)$	$(-)$	$(-)$
$B2$)SPwave	$(-0.12, 1.11)$	$(0.11, 1.10)$	$-0.00, 0.99$	$(-)$
$C) = (B2)$ with background (fixed)	$(0.23, 1.29)$	$(-0.25, 1.29)$	$(-2.05, 1.08)$	$(-)$
$D) = (B2)$ with background fixed and smoothed in MC	$(0.01, 1.18)$	$(-0.20, 1.15)$	$(-0.22, 1.09)$	$(-)$
$E) = (D)$ with Fit to BKG using Fcc	$(-0.02, 1.20)$	$(-0.19, 1.11)$	$(-0.21, 1.04)$	$(0.21, 1.14)$
$F) = (E)$ with composed Signal sample	$(-0.01, 1.19)$	$(-0.32, 1.05)$	$(0.08, 1.05)$	$(0.01, 1.20)$
$G) = (F)$ with corrected EvtGen-like Signal sample	$(-0.19, 1.24)$	$(-0.09, 1.21)$	$(0.19, 1.05)$	$(-0.19, 1.21)$

Table 6.3: *Result from pull distributions for S-wave fitted parameters and number of events.In lines A and B the signal control sample has 10 times the statistics of each experiment whereas for other cases this statistics is only 4.5 times higher (as available when fitting data).*

variable	Result	True value	$\frac{\delta}{\sigma}$
$\Gamma^0(K^*)$ (GeV/c^2)	0.05029 ± 0.00023	0.0505	0.91
$m(K^*)$ (GeV/c^2)	0.89616 ± 0.00009	0.8961	0.66
m_A (GeV/c^2)	2.47 ± 0.08	2.5	0.374
m_V (GeV/c^2)	2.10 ± 0.17	2.1	0.02
$r_{BW}(GeV/c)^{-1}$	3.26 ± 0.18	3.0	1.44
r_V	1.824 ± 0.037	1.82	-0.11
r_2	0.770 ± 0.020	0.78	0.5
Ns	162833 ± 403	162833	0.

Table 6.4: *Fit results on the full event simulation for Runs1-5*

parameter	(r_2=0.6,r_V=1.82)	(r_2=0.9,r_V=1.82)	(r_2=0.78,r_V=1.4)	(r_2=0.78,r_V=2.0)
r_2	0.57 ± 0.04	0.88 ± 0.04	0.76 ± 0.04	0.76 ± 0.04
r_V	1.81 ± 0.04	1.80 ± 0.04	1.39 ± 0.03	1.99 ± 0.04
m_A (2.5)(GeV/c^2)	2.36 ± 0.13	2.37 ± 0.13	2.39 ± 0.13	2.38 ± 0.13
$\mathrm{m}(K^{*0}(892))$ (0.896) (GeV/c^2)	0.8959 ± 0.0002	0.8959 ± 0.0002	0.8959 ± 0.0002	0.8959 ± 0.0002
$\Gamma^0(K^{*0}(892))$ (0.0503) (GeV/c^2)	0.0507 ± 0.0005	0.0505 ± 0.0005	0.0506 ± 0.0004	0.0508 ± 0.0005
$r_{BW}(GeV/c)^{-1}$ (3.0)	2.68 ± 0.20	2.71 ± 0.22	2.66 ± 0.21	2.72 ± 0.21
r_S (0.3)	0.296 ± 0.010	0.296 ± 0.010	0.297 ± 0.010	0.295 ± 0.010
a_S (2.0) $(GeV/c)^{-1}$	2.19 ± 0.16	2.19 ± 0.16	2.18 ± 0.17	2.20 ± 0.16

Table 6.5: *Fit results for complete MC distributions with different input values of r_2 and r_V while using the same signal pdf. All other parameters are left unchanged from their values given in the left column.*

Chapter 7

Extraction of S and P-wave parameters from the BaBar dataset

We present results of a fit to the BaBar dataset of Runs1-5 which corresponds to an integrated luminosity of $347\ fb^{-1}$. This fit is done in the hypothesis of having a signal comprising only S and P-wave components and assuming the LASS parameterization for the S-wave phase (δ_S) and taking an amplitude proportional to $\frac{m}{p^*} sin\delta_S$. The Monte Carlo signal and background samples are corrected as explained in previous sections. We compare as well results found by fitting the entire dataset with those obtained by fitting Runs123, Run4 and Run5 independently.

The functions $pdf^{S,B}$ used for data fitting are of the following form:

$$pdf^S = c_2 \times e^{\frac{-(x-c_0)^2}{2c_1^2}} + c_5 \times e^{\frac{-(x-c_3)^2}{2c_4^2}}; \tag{7.1}$$

$$pdf^B = \exp(\sum_{i=0}^{4} d_i x^i); \tag{7.2}$$

The parameters are presented in Table 7.1. They have been determined by fitting the MC signal and background control samples F_{cc} binned distributions. These MC distributions are presented in Figure 7.1.

signal parameter	**value**		**bkg parameter**	**value**
c_0	-0.492 ± 0.016		d_0	10.8 ± 0.01
c_1	0.8959 ± 0.0046		d_1	-1.465 ± 0.031
c_2	66410 ± 1556		d_2	-1.736 ± 0.029
c_3	0.5508 ± 0.0059		d_3	0.4039 ± 0.0206
c_4	0.5706 ± 0.0028		d_4	-0.007 ± 0.006
c_5	41820 ± 652			

Table 7.1: *Signal and background parameters used for Fcc pdf's for fit to Runs 1-5. The amplitude coefficients (c_2, c_5 for signal and d_0 for background, are not normalized. During the fitting procedure these distributions are normalized to 1.*

The χ^2 of the fits are: 60.93 with 54 degrees of freedom for the signal and 62.1 with 55 degrees of freedom for the background.

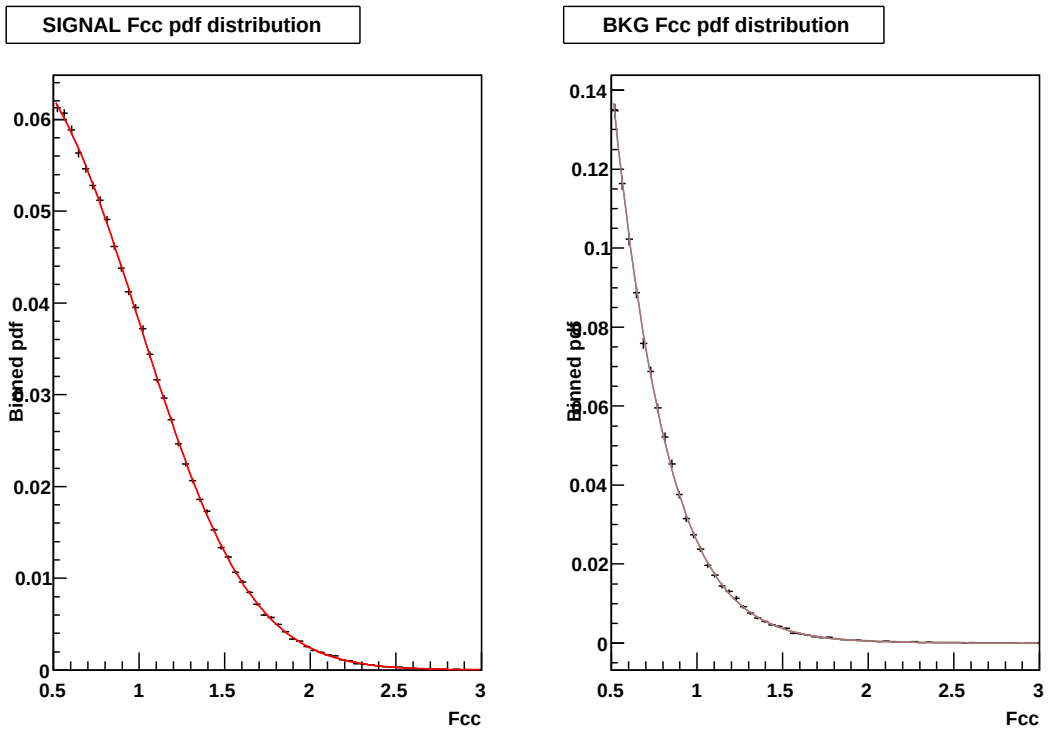

Figure 7.1: *F_{cc} distribution for signal and background Monte Carlo samples. From these distribution we extract the pdfs used in the unbinned part of the fit.*

7.1 Results

Values of fitted parameters are given in Table 7.2. Projected distributions over the five kinematic variables are displayed in Figure 7.2. Comparing data and the fitted distribution, some significant differences are observed at small q^2, large $m(K\pi)$ and between the negative and positive χ angle distributions. The first two effects are correlated as an excess of events at large mass gives also an excess at small q^2 because of the limited phase-space available. These differences can result from an incomplete description of the signal or of the set of corrections applied to simulated events.

The correlation matrix for parameters listed in the same order as in Table 7.2 is presented in Table 7.3.

We have performed a cross-check for these results by fitting individually Runs1-3, Run4 and Run5, to have 3 independent fits with similar statistics. We show in Figure 7.3 the comparison between all results. There is generally a good agreement between runs for all variables.

We compare in Figure 7.4 the fit results for other variables, namely the F_{cc} distribution, the variation of the average value of $\cos\theta_\pi$ versus the $K\pi$ mass, the D reconstructed momentum and the lepton momentum in the D center of mass system.

The contribution of each bin to the overall χ^2 of the fit and the distribution of the difference, χ_{bin}, between measured and expected number on events in each bin, divided by the corresponding uncertainty are displayed in Figure 7.5. We define the $\pm\sqrt{\chi^2}$ in each bin i as:

$$\chi_i = \frac{n_i^{data} - n_i^{estimated}}{\sqrt{n_i^{estimated} + \sigma_i^2(bkg) + \sigma_i^2(signal)}} \tag{7.3}$$

variable	Result
$\Gamma^0(K^*)(GeV/c^2)$	0.04594 ± 0.00023
$m(K^*)(GeV/c^2)$	0.8944 ± 0.0001
$m_A(GeV/c^2)$	$2.70^{+0.11}_{-0.10}$
r_V	1.480 ± 0.016
r_2	0.825 ± 0.020
r_S	0.2437 ± 0.0045
$a_S(GeV/c)^{-1}$	2.76 ± 0.10
$r_{BW}(GeV/c)^{-1}$	3.75 ± 0.149
N_S	244603 ± 669
N_B	106622 ± 566

Table 7.2: *Fit results on BaBar Run1-5 data assuming a signal composed of S and P-waves, where the S-wave phase δ_S is parameterized using the LASS model and assuming that its amplitude is proportional to $\frac{m}{p^*} sin\delta_S$.*

-	Γ^0	m	m_A	r_V	r_2	r_S	a_S	r_{BW}	N_S	N_B
Γ^0	1.000	0.144	0.051	-0.090	0.033	-0.024	0.132	0.029	0.314	-0.378
m	0.144	1.000	-0.060	-0.041	-0.052	0.055	0.128	0.145	0.059	-0.060
m_A	0.051	-0.060	1.000	-0.550	0.845	-0.411	-0.066	0.519	0.101	-0.116
r_V	-0.090	0.041	-0.550	1.000	-0.529	0.227	0.014	-0.343	-0.127	0.129
r_2	0.033	-0.052	0.845	-0.529	1.000	-0.353	-0.077	0.485	0.131	-0.148
r_S	-0.024	0.128	-0.411	0.227	-0.353	1.000	0.654	-0.210	0.132	-0.157
a_S	0.132	0.145	-0.066	-0.014	-0.077	0.654	1.000	0.095	0.067	-0.077
r_{BW}	0.029	0.036	0.519	-0.343	0.485	-0.210	0.095	1.000	0.135	-0.187
N_S	0.314	0.059	0.101	-0.127	0.131	0.132	0.067	0.135	1.000	-0.548
N_B	-0.378	-0.060	-0.116	0.129	-0.148	-0.157	-0.077	-0.187	-0.548	1.000

Table 7.3: *Statistical correlation matrix for fit of S+P-waves signal, with S-wave phase δ_S is parameterized using the LASS model and assuming that its amplitude is proportional to $\frac{m}{p^*} sin\delta_S$.*

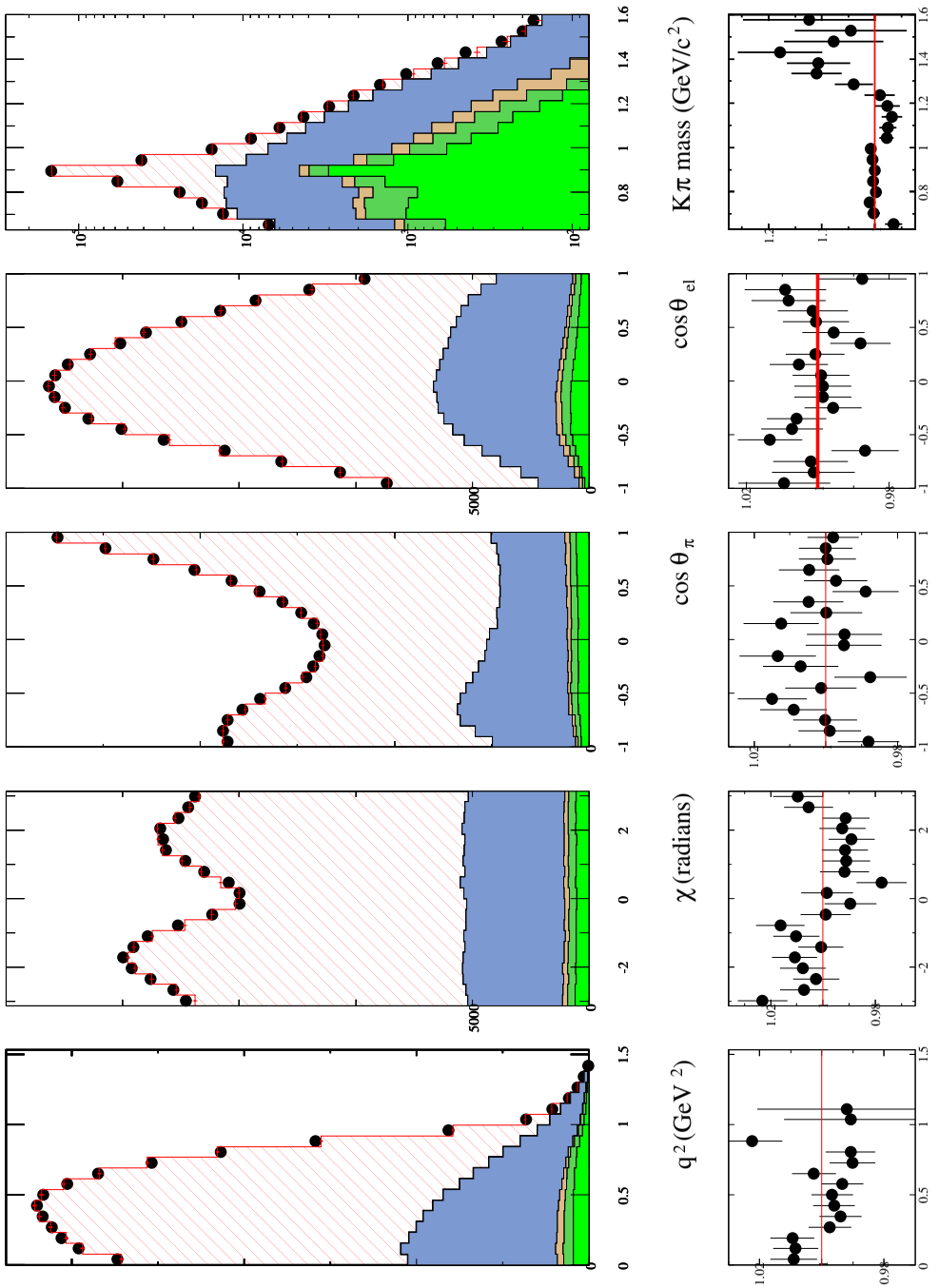

Figure 7.2: *Projections of data and of the fitted MC distribution over each of the 5 kinematic variables. Color code: red(signal),blue(charm bkg), light brown(uds bkg), dark green(B^+B^- bkg), light green($B^0\bar{B}^0$).*

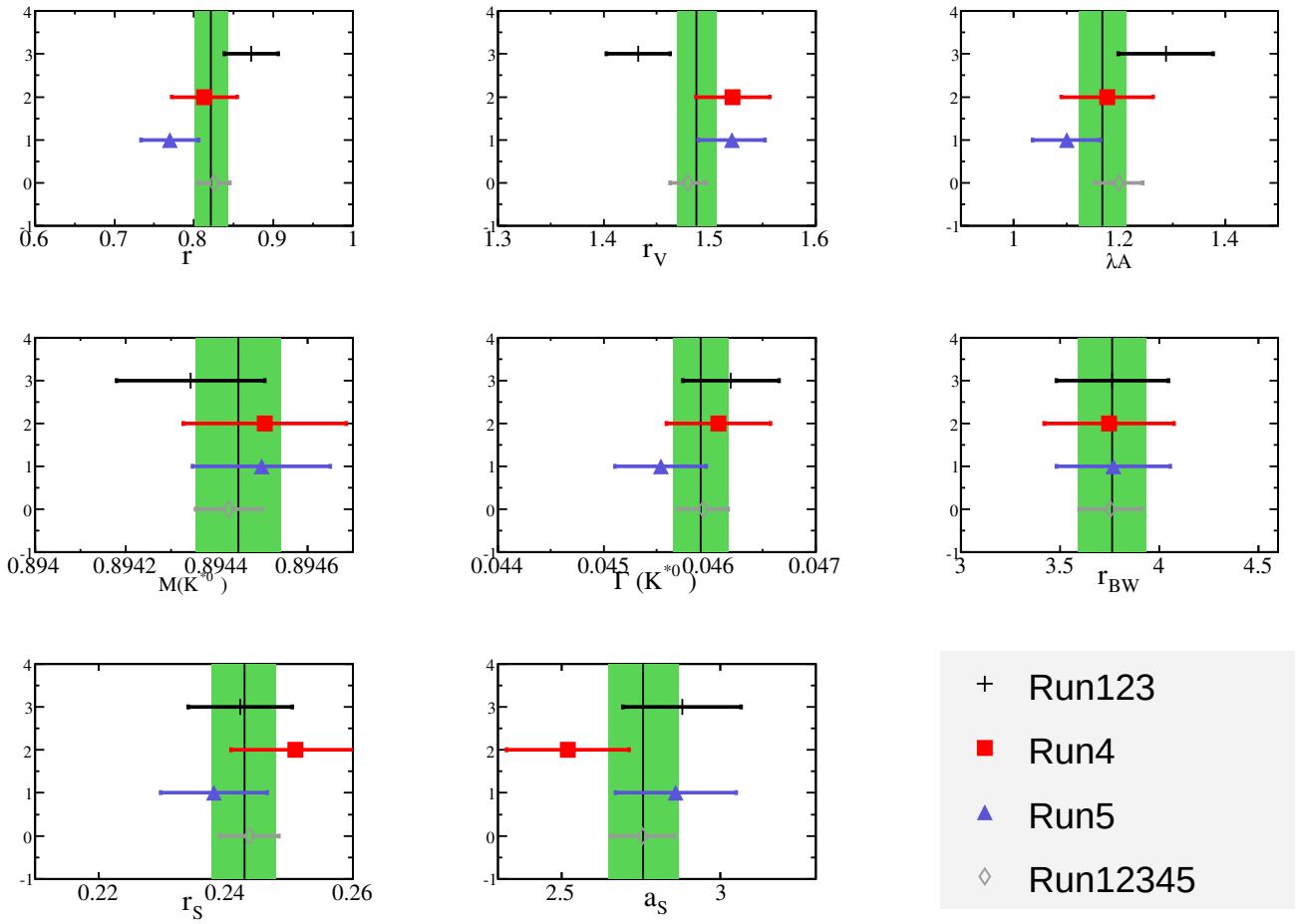

Figure 7.3: *Comparison between sets of Runs and the entire analyzed dataset for fitted parameters. The black vertical line for each parameter represents the weighted average of the 3 Runs, the colored box represents the ±1 sigma uncertainty for this value. In the first row right plot, λ_A goes for the parameter ($m_A = 1.266 + \lambda_A^2$), which is what we actually fit.*

In this expression we take into account the uncertainties in the evaluation of the background level and weighting procedure $\sigma_i^2(bkg) = \sum_{j=1}^{Nbkg_i} w_j^2$, where w_j is the weight for the event j in bin i and $\sigma_i^2(signal) = N_S^2 \sum_{j=1}^{Nsig_i} w_j^2 / W^{tot^2}$.

The total χ^2 value is 2938 and the number of degrees of freedom is 2790. This corresponds to a probability of 2.5%. This small probability can result from the presence of few bins having large contributions or from an overall deviation from the normal law in each bin. The distribution of χ_{bin}, given in Figure 7.5-right is fitted with a Gaussian. The obtained parameters of this fit are: $< \chi_{bin} >= -0.06 \pm 0.02$ and $\sigma_{\chi_{bin}} = 1.007 \pm 0.014$.
The bias comes from the fact that Gaussian distributions are assumed for the number of events in each bin whereas the corresponding statistics originates from the Poisson law which is asymmetric.
We reproduce this bias when determining the total χ^2 as well as the χ distribution from the result of one of the fits to a toy distribution analyzed in Section 6.2.1 (case (D) in Tables 6.2 and 6.3). We find in this case a bias of -0.063 ± 0.018.

We have also fitted individually Runs1-3, Run4 and Run5, which provide three independent results using similar statistics. Results are summarized in Table 7.4 and presented in figures 7.6, 7.7 and 7.8.

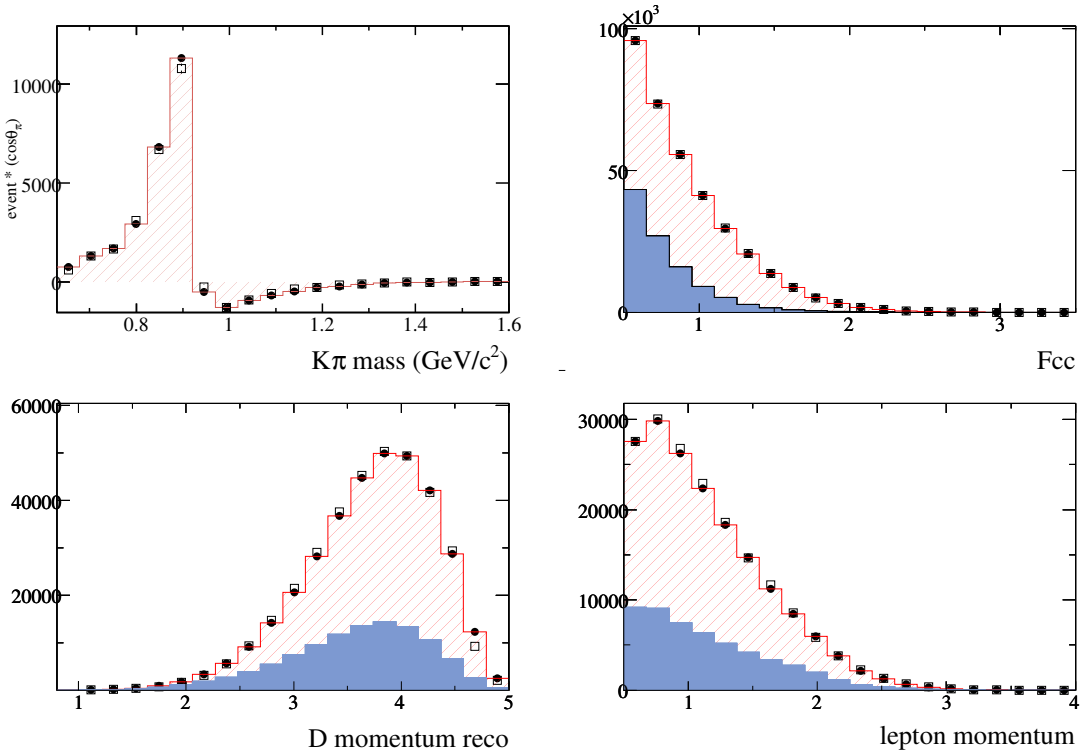

Figure 7.4: *fit results for the variation of the average value of* $\cos\theta_\pi$ *with the* $K\pi$ *mass (upper left),* F_{cc} *distribution (upper right), reconstructed D momentum (lower left) and lepton momentum in the D center of mass system (lower right). Empty squares are the data.*

Values of $\sigma_{\chi_{bin}}$ are compatible with unity for individual Runs.
Fit probabilities are reasonable. Individual results and the global average are compared in Figure 7.3. In addition to statistical uncertainties, quoted error bars include effects from the limited statistics of simulated events.

Run	$< \chi_{bin} >$	$\sigma_{\chi_{bin}}$	Probability
123	-0.059 ± 0.019	0.973 ± 0.014	49.2%
4	-0.056 ± 0.018	0.935 ± 0.013	99.9%
5	-0.056 ± 0.019	0.988 ± 0.015	38.6%
12345	-0.055 ± 0.019	1.007 ± 0.014	2.5%

Table 7.4: *Average values for* χ_{bin} *and dispersion per Run.*

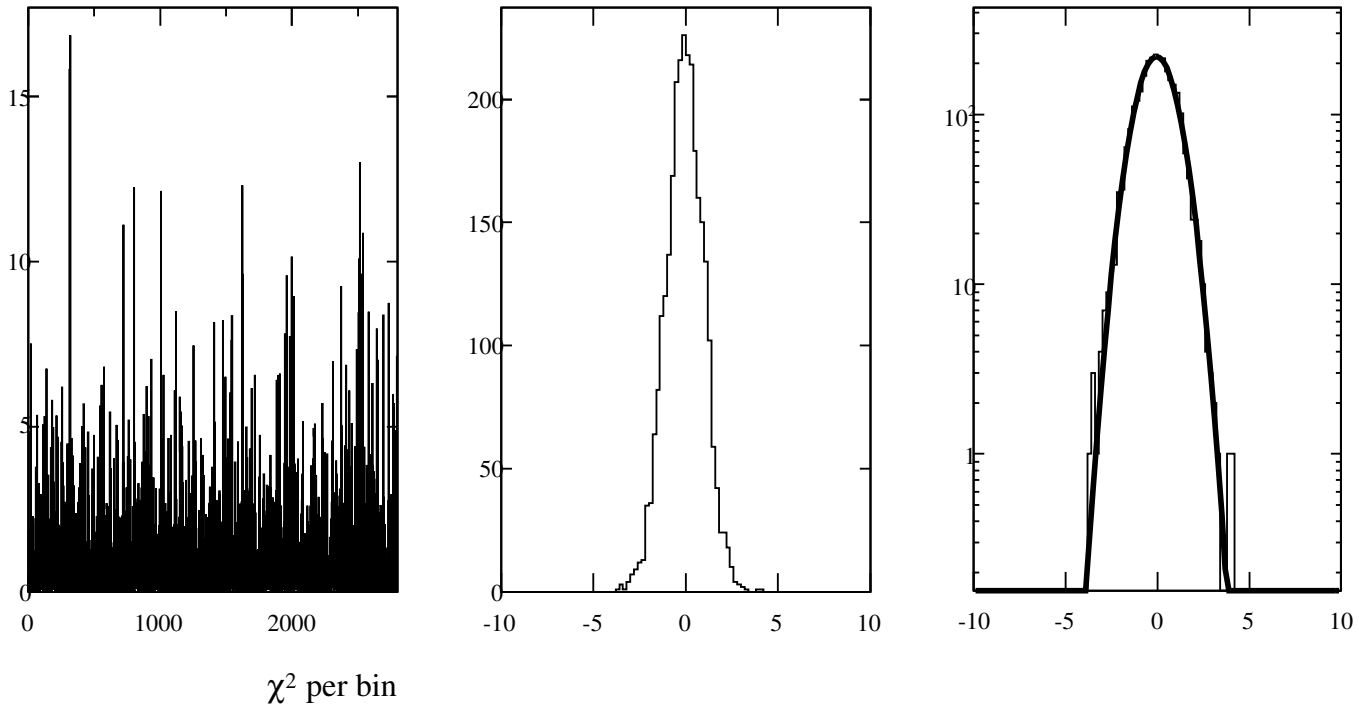

Figure 7.5: *Left plot: χ^2 distribution for each bin of fit to Runs1-5. Center and Right plots: Pull distribution for all bins.*

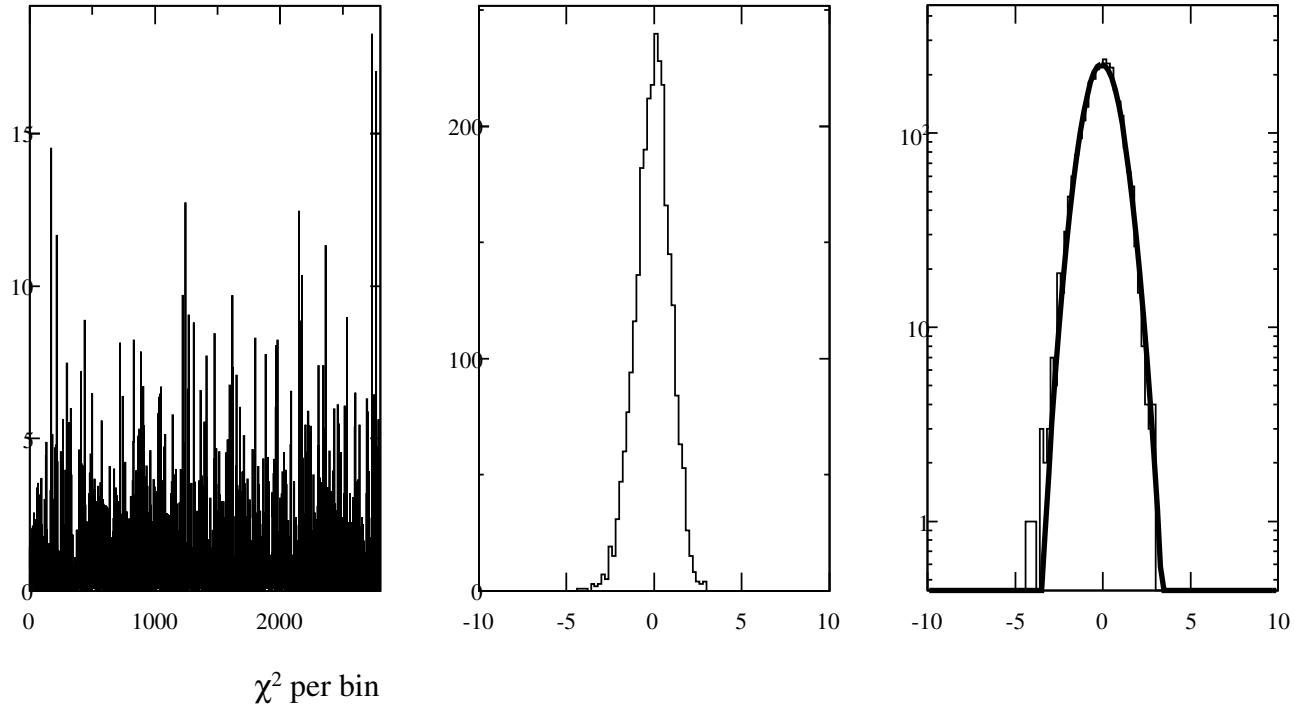

Figure 7.6: *Left plot: χ^2 distribution for each bin fo fit to Runs1-3. Center and Right plots: Pull distribution for all bins.*

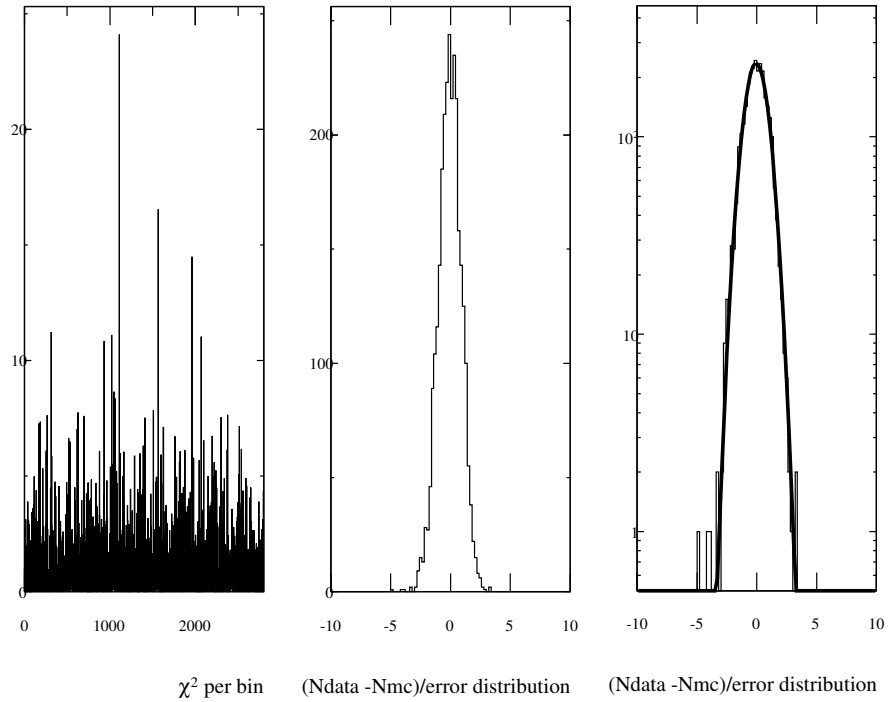

Figure 7.7: *Left plot: χ^2 distribution for each bin fo fit to Run4. Center and Right plots: Pull distribution for all bins.*

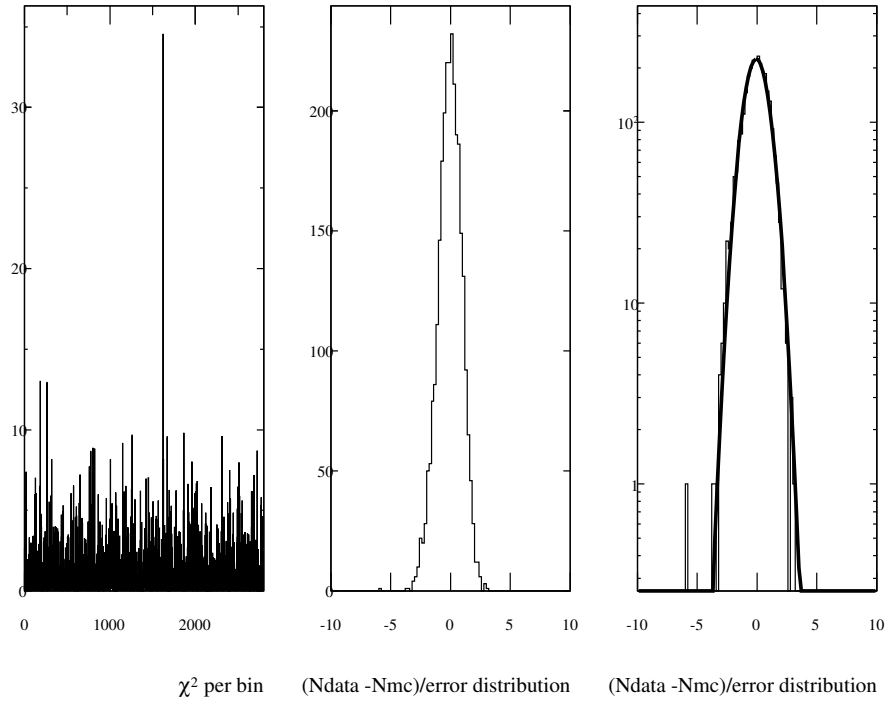

Figure 7.8: *Left plot: χ^2 distribution for each bin fo fit to Run5. Center and Right plots: Pull distribution for all bins.*

7.2 Systematic uncertainties

The systematic uncertainty on each fitted parameter (x) is defined as the difference between fit results in nominal conditions ($x[0]$) and those obtained, ($x[i]$), after changing a variable or a condition (i) by an amount which corresponds to an estimate of the uncertainty in the determination of this quantity:

$$\delta[x] = x[0] - x[i]; \tag{7.4}$$

The total effect of corrections over either signal or background simulation are also presented. For signal simulation these include : corrections on fragmentation properties, corrections on the estimate of the D direction and momentum as well as uncertainties related to the limited knowledge of radiative events. For the overall background we evaluate the systematic associated with the smoothing procedure. For the charm background we analyse the effect of corrections on particle production associated with D^0, D^+ and D^{*+}, the remaining discrepancies between data and MC measured with WS events as well as corrections on form factors for semileptonic decays.
For $B\bar{B}$ events we analyse the impact on the differences between data and simulation as well as corrections on form factors for semileptonic decays of charmed mesons.
The uncertainty associated to the PID is also considered. We also quantify the effect of the limited statistics used to evaluate the background level, taking advantage of the tests made with toy generators in previous sections.
Some of the aforementioned corrections affect directly the F_{cc} distribution for signal or background. Therefore the pdf for signal (or background) used in each of the fits for any systematic uncertainty is updated for the corresponding distribution.

7.2.1 Systematic uncertainties related to signal production and decay

The production mechanism of D^+ mesons used in the simulation has been corrected to agree with corresponding measurements in data. Total effects of these corrections and an evaluation of remaining uncertainties are presented.
An evaluation of systematic uncertainties attached to the simulation of radiative events in $D^+ \to K^-\pi^+e^+\nu(\gamma)$ is also given.
For each systematic uncertainty we also present the distortion of the corresponding F_{cc} distribution as compared to the nominal distribution.

Systematic uncertainties associated to the correction of Fisher input variables

The signal control sample is corrected as explained in Section 4, where we use a hadronic control sample to define a weight, for each event. This is done taking into account that the D momentum distribution is not the same in the hadronic and in the semileptonic case.
In a first step, results of the nominal fit are compared with those obtained when no correction is applied. This is shown in line (A) of Table 7.5.
It was seen in Section 4 that remaining differences between data and simulation on projected distributions of the different variables entering in the definition of Fisher discriminants F_{bb} and F_{cc} are very small. But there could be differences through correlations between the different variables entering in the weight definition. Therefore the systematic uncertainty we associate to these corrections is obtained by defining new event's weights without taking into account that the momentum distribution of reconstructed D's is different in hadronic and in semileptonic samples. Results are presented in line (I) of Table 7.6. We take 100% of the variations as systematic uncertainties.

Systematic uncertainties associated with the estimates of the D direction

In Section 4.1.3 it is observed that estimates of the D^+ direction and energy are more accurate in the simulation than in data. Smearing parameters were measured to have a better agreement between the two samples. Effects on fitted parameters observed after removing these smearing corrections are presented in line (IV) of Table 7.6. We take 100% of the difference to the results of the nominal fit as systematic uncertainty.

Uncertainties from the simulation of radiative events

The rate of radiative events is changed in order to evaluate the corresponding variation on fitted parameters. Most of radiative events correspond to radiation from the charged lepton, although a non negligible part comes from radiation of the $K^{*0}(892)$.
In $D \to Pe\nu_e$, by comparing two generators (PHOTOS and KLOR), the CLEO-c collaboration has used a variation of 16% to evaluate corresponding systematic uncertainties [66]. We have increased the fraction of radiative events (simulated by PHOTOS) by 30% (keeping constant the total number of events) and obtained the corresponding variations on fitted parameters given in Table 7.6 row (II). We take 100% of the variations as systematic uncertainties.

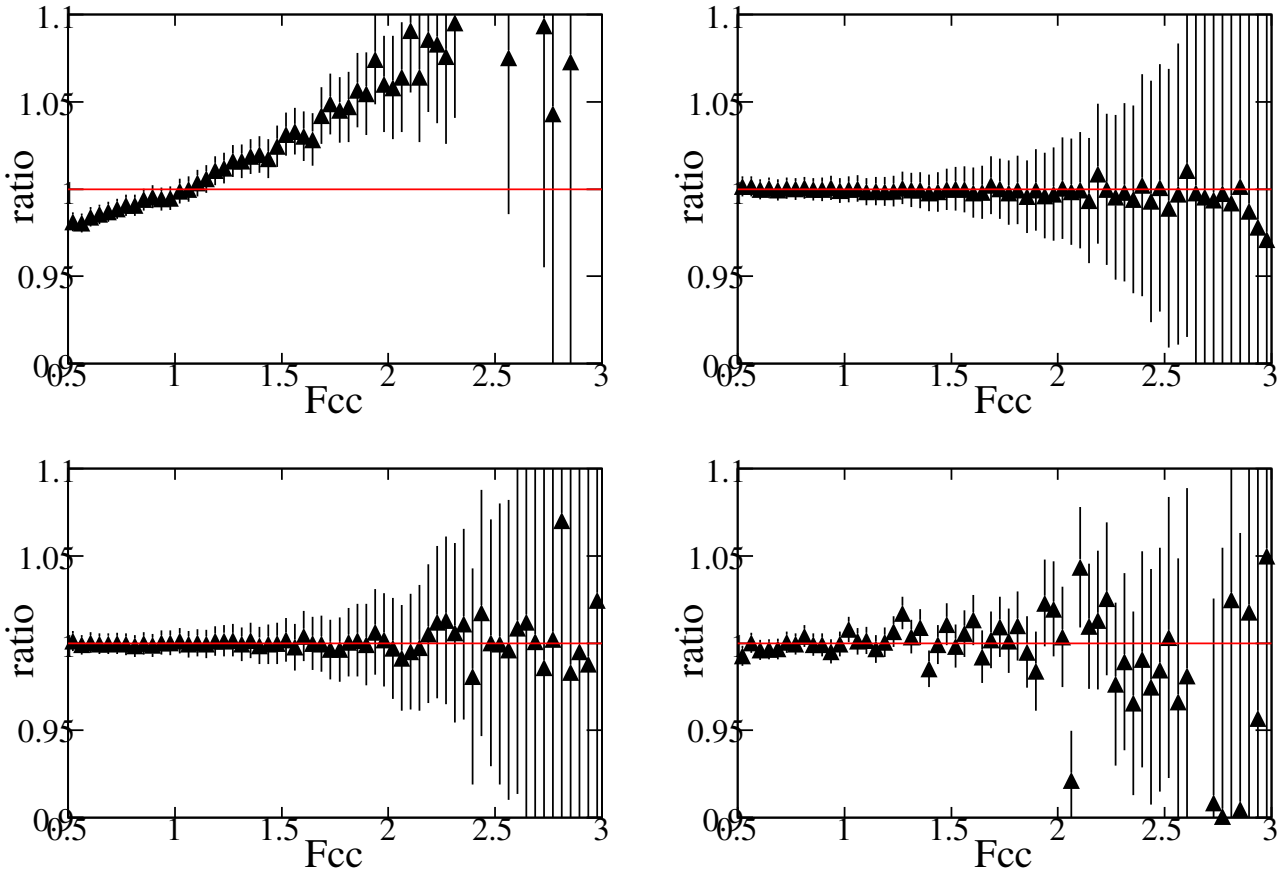

Figure 7.9: *These plots represent the distortion induced by different systematic uncertainties on the pdf. for the F_{cc} variable measured with signal events. Upper left plot: Case for no corrections on variables entering the F_{bb}, F_{cc} variables. Upper right plot: Case for increase of the fraction of radiative events. Down left plot: Case for no tweaking for electron candidates. Down right plot: Case for no smearing over the corrections on the D^+ direction*

7.2.2 Uncertainties related to corrections applied on background

Beauty and charm components of background have been tuned using control samples. Corrections applied on both components involve also renormalization of the corresponding background level. The charm background is tuned to correct the fragmentation model for $c \to D$ mesons and for accompanying charged pions and kaons. Corrections of semileptonic decay rate and decay model are also applied.
For each correction we present also the distortion of the corresponding F_{cc} distribution as compared to the nominal distribution.

$B\bar{B}$ background correction

The remaining $B\bar{B}$ background events, expected from simulation, have been rescaled by 1.7 ± 0.2 (see Section 4.2). The effects induced on the Fcc pdf for background and on fitted parameters, by a variation of -0.2 of the scaling factor are given in Table 7.6 row (V). The systematic uncertainties are small as expected, since the $B\bar{B}$ contribution to the background is fairly small.

Fragmentation, rate and form factor corrections on $c\bar{c}$ background

We present the total variations on the fit results induced when not applying corrections on the charm Monte Carlo background in row (B) of Table 7.5. In the following we decouple each contribution to these corrections and evaluate the variation for each associated parameter.

- *fragmentation associated systematic uncertainties:* The corrections related to particle production accompanying c-hadrons ($D^0,\ D^{*+} \to D^0\pi^+$ and D^+) are given in Appendix. Corrections measured for the D_s^+ fragmentation distribution, in the $D_s^+ \to K^+K^-e^+\nu_e$ analysis, are also applied on simulated events. For non-strange D-mesons, these corrections concern discrepancies on the momentum and angle distributions of charged pions and kaons as well as those measured on more global variables (as h_2h_0). These discrepancies are at worse of the order of 30%. After correction with weights as function of these variables, remaining discrepancies are 5 times smaller.
  We present in row (VIII) of Table 7.6 the shift in the results as compared to the nominal fit, when switching off this correction. We take as systematic for our analysis 20% of the difference between the nominal results and those found without these corrections.

- *rate and shape of charm background:* We found, using WS events, that there is a variation in the ratio data/MC versus q^2. The RS events charm MC background has been reweighted versus q^2 using the same procedure. The validation of this correction depends on how much the assumption that WS events behave similarly as RS events is correct. We present the effect of not applying this correction in Table 7.5 and of only not applying the correction on the q^2 shape. It is this last correction that gives some differences in the values of the parameters. We present in Row (V) of Table 7.6 the variation of the fit results by not applying the correction on the q^2 shape. We evaluate the corresponding systematic to 50% of the effect found by not applying this correction.

- *form factor correction systematics:* The form factor corrections include those on decays into pseudo-scalar and vector mesons, generated by EvtGen using the ISGW2 model, into a more correct SLPole model. The biggest contribution to charm background comes from a D^0 decaying into $Ke\nu_e$ associated with a fragmentation pion. In this channel the only variable is the pole mass of the form factor. This parameter is measured with high precision. The systematic uncertainty associated to the control of hadronic form factors will be evaluated by applying these corrections but changing the value of the pole mass for the form factor of the

decay $D^0 \to K^- e^+ \nu_e$ from $1.884\ GeV/c^2$ to $1.784\ GeV/c^2$ while preserving the same rate of this kind of events. In row (VI) of Table 7.6 we present the effect that corresponds to not making any correction of the form factor models. For the time being we take 10% of this value.

7.2.3 Fitting procedure

Fluctuations on MC number of events estimates in each bin are not included in the likelihood, therefore one quantifies this effect using fits to toy distributions.
Pull distributions (Section 5.1) of fitted parameters, obtained in similar conditions as in Run4, have a standard deviation of 1.2. This increase is attributed to the limited MC statistics used for the signal (4.5 times the data) and, mainly, from the available statistics used to evaluate the background from $e^+e^- \to c\overline{c}$ continuum events. We have included this effect as a systematic uncertainty corresponding to 0.7 times the quoted statistical uncertainty of the fit.

Background Smoothing

The MC background distribution that enters in the fit to data is smoothed to reduce corresponding fluctuations effects. The method of smoothing has been presented in Section 5 and we only remind that there are two free parameters that we optimize for the smoothing procedure, one related to the smoothing in the $\cos\theta_e$ variable and the other for the χ variable.
The evaluation of the associated systematic uncertainty is performed by varying these free parameters under reasonable limits and refitting data. The limit values were determined by shifting the parameter value until the agreement between the smoothed distribution and an initial background distribution starts to degrade. We find that the degradation is only observed for the parameter that smooths χ. The corresponding systematic uncertainties are very small and are neglected.
For consistency we present as well the shift from nominal results if no smoothing is applied. This last result is given in Table 7.5, row (D).

7.2.4 Particle identification efficiencies

We evaluate the effect of not correcting for remaining differences between data and MC on particle identification by switching off the tweaking for electron candidates in the signal MC sample. Results are given in Table 7.6.

7.2.5 Uncertainties associated to parameters kept constant in the fit

Our signal model has 4 fixed parameters, the vector pole mass m_V, the effective range term b_S of the non resonant component of the S-wave, as well as the mass and width of the S-wave component $K_0^*(1430)$. The pole mass is basically uncorrelated with the other fixed parameters and the corresponding systematic uncertainty can be defined independently from them. This is done by varying the pole mass by $\pm 0.1\ GeV/c^2$.
It is however less trivial to define the systematics associated with the S-wave parameters, as they are correlated: the effect of the b_S term is accentuated with increasing the $K\pi$ break-up momentum, therefore at higher $K\pi$ masses, overlapping with the effect of the phase variation of the $K_0^*(1430)$. This is given in Figure 7.11, where for the same value of a_S we have drawn three curves, obtained for different values of the other parameters under discussion, that reproduce a similar phase variation versus the $K\pi$ mass. The dotted line corresponds to the values we take in our fit, while the others correspond to values of the parameters that differ from the nominal value by one sigma.
We do not associate any systematic uncertainty to the modelisation of the S-wave precisely since we assume this

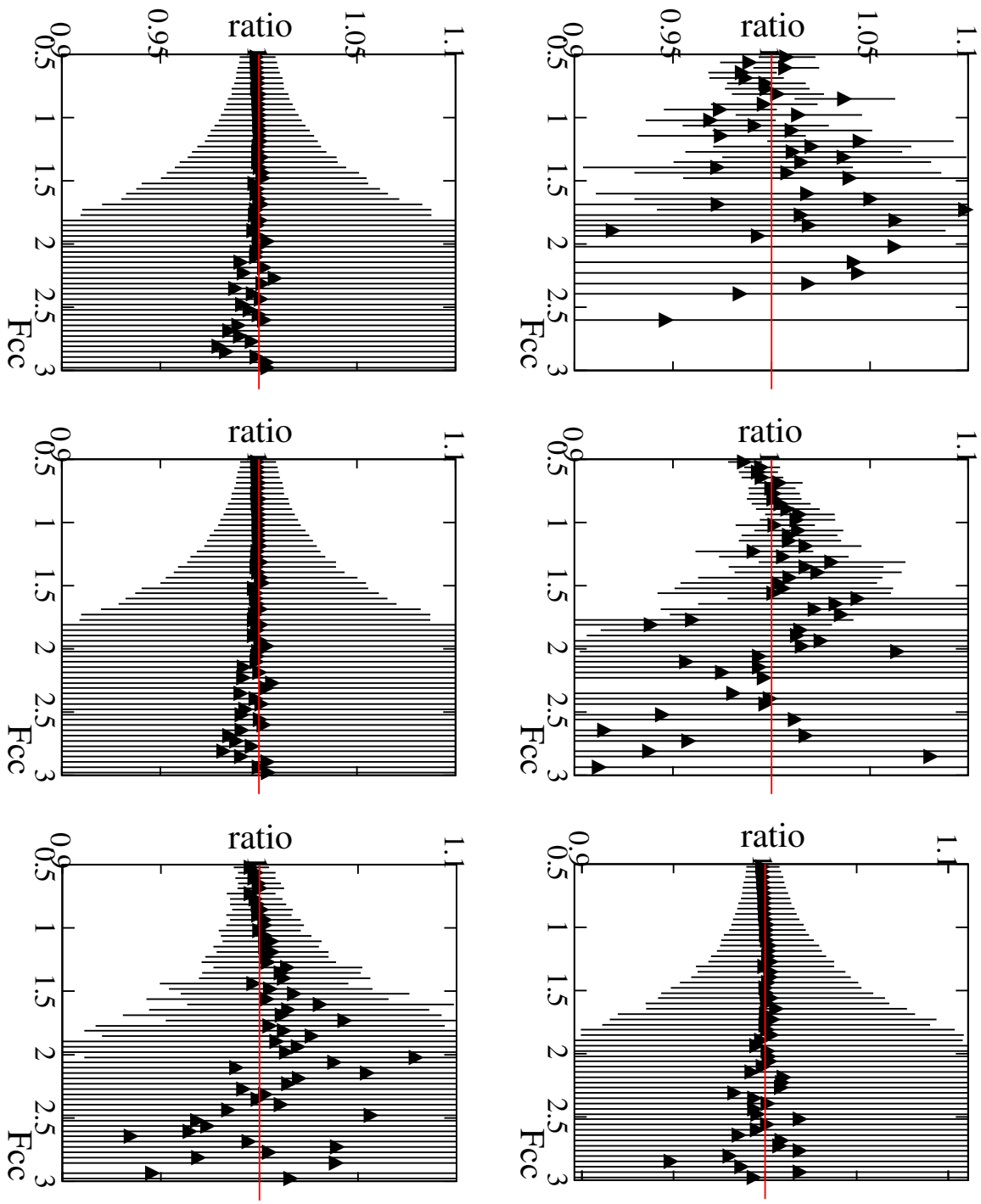

Figure 7.10: *These plots represent the distortion of the BKG PDF for each systematic as compared to the pdf for the nominal fit. Upper left plot: no tuning on fragmentation pions is applied, Upper center plot: no tuning on fragmentation pions nor corrections on semileptonic decays models are applied, Upper right plot: $B\bar{B}$ normalization lowered by 0.2, Lower left plot: corrections on charm background coming from WS control sample studies are not applied, Lower center plot: no corrections of the charm background q^2 shape defined by WS control sample is applied, Lower right plot: no corrections on semileptonic decay models are applied.*

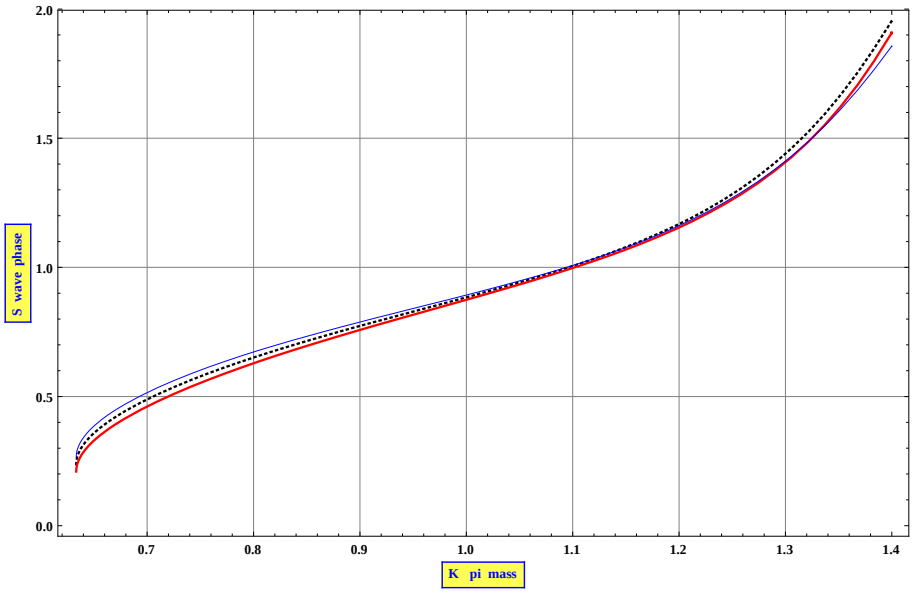

Figure 7.11: *Variation of the phase of the S-wave using the LASS parameterisation for the same generic value of the parameter a_S and using 3 sets of values for $b_S, m(K_0^*(1430)), \Gamma^0(K_0^*(1430))$. Dotted line: $b_S = 1.76\ (GeV/c)^{-1}, m = 1.435\ (GeV/c^2), \Gamma^0 = 0.279\ (GeV/c^2)$,Red line: $b_S = 1.\ (GeV/c)^{-1}, m = 1.45\ (GeV/c^2), \Gamma^0 = 0.248\ (GeV/c^2)$,blue line:$b_S = 2.38, m = 1.4466\ (GeV/c^2), \Gamma^0 = 0.3165\ (GeV/c^2)$*

model with the LASS values for the parameters in question.
To verify if the values of LASS parameters are consistent with data we have performed a less model dependent fit of the S-wave phase, which is the subject of the following section.

variation	$\Delta m_{K^{*0}(892)}$	$\Delta\Gamma^0_{K^{*0}(892)}$	Δr_{BW}	Δm_A	Δr_V	Δr_2	Δr_S	Δa_S	ΔN_S	ΔN_B
signal										
(A)no Fcc,Fbb tuning	-0.30	2.09	1.50	-3.66	0.53	0.35	1.0	-1.56	2.8	-3.26
BKG										
(B)no (tuning,f.f.) corr/	-1.21	-0.72	-8.7	3.4	0.32	2.1	1.11	-4.5	-2.9	3.3
(C)no corr/ from WS	0.53	0.89	1.96	-1.98	1.12	-0.57	-1.0	0.42	0.21	-0.25
(D)no smoothing	0.06	-0.035	-0.34	-0.63	0.19	-0.36	-0.69	0.4	-0.77	0.9

Table 7.5: *Total variations of fitted parameters expressed as $\frac{x[0]-x[i]}{\sigma_{stat}}$ for extreme cases in which some of the corrections on MC or of fit procedure are not applied.*

7.2.6 Summary on systematic uncertainties

Systematic uncertainties associated to each analyzed effect are given in Table 7.7. They have been obtained with Runs1-5.

variation	$\Delta m_{K^{*0}(892)}$	$\Delta\Gamma^0_{K^{*0}(892)}$	Δr_{BW}	Δm_A	Δr_V	Δr_2	Δr_S	Δa_S	ΔN_S	ΔN_B
signal										
(I)	-0.15	-0.17	0.15	-0.23	0.31	0.15	-0.1	0.14	-0.32	0.37
(II)	-0.43	0.11	-0.14	-0.13	0.35	0.1	-0.1	-0.12	-0.31	0.36
(III)	-0.26	-0.14	0.35	0.79	-0.74	0.55	-0.30	0.54	0.12	-0.14
(IV)	0.33	0.36	0.2	-0.14	0.06	-0.24	0.36	-0.38	0.52	-0.6
BKG										
B$\bar{B}$										
(V)	-0.09	0.07	-0.11	0.18	-0.05	-0.04	0.24	-0.37	-0.58	0.67
c$\bar{c}$										
(VI)	-0.86	-1.3	-2.56	3.0	0.55	1.75	0.09	-2.53	-2.1	2.44
(VII)	0.55	0.8	1.93	-2.0	0.98	-0.52	-0.93	0.46	0.27	-0.32
(VIII)	-0.3	0.6	-5.6	0.5	-0.31	0.3	1.11	-1.98	-0.45	0.52

Table 7.6: *Variations of the fitted parameters expressed as* $\frac{x[0]-x[i]}{\sigma_{stat}}$ *for the different effects evaluated:(I) Variation associated with the tuning of the signal control sample, (II) The fraction of radiative events increased by* 30% *for the signal control sample, (III) no electron tweaking for MCsignal events,(IV) no smearing for* $\theta_D, \phi_D, E_{miss}$ *for MCsignal, (V)* $B\bar{B}$ *bkg rate lowered by* 30%*,(VI) no correction on generated semileptonic models (VII) no correction of the* q^2 *shape for the charm background based on the WS control sample (VIII) no correction of events associated with fragmentation pions.*

variation	$\Delta m_{K^{*0}(892)}$	$\Delta\Gamma^0_{K^{*0}(892)}$	Δr_{BW}	Δm_A	Δr_V	Δr_2	Δr_S	Δa_S	ΔN_S	ΔN_B
signal										
(I)	-0.15	-0.17	0.15	-0.23	0.31	0.15	-0.1	0.14	-0.32	0.37
(II)	-0.43	0.11	-0.14	-0.13	0.35	0.1	-0.1	-0.12	-0.31	0.36
(III)	-0.26	-0.14	0.35	0.79	-0.74	0.55	-0.30	0.54	0.12	-0.14
(IV)	0.33	0.36	0.2	-0.14	0.06	-0.24	0.36	-0.38	0.52	-0.6
BKG										
B$\bar{B}$										
(V)	-0.09	0.07	-0.11	0.18	-0.05	-0.04	0.24	-0.37	-0.58	0.67
c$\bar{c}$										
(VI)	-0.086	-.13	-0.256	0.3	0.055	0.175	0.009	-0.253	-0.21	0.244
(VII)	0.28	0.4	0.97	-1.0	0.5	-0.26	-0.47	0.23	0.14	-0.16
(VIII)	-0.06	0.12	-1.12	0.1	-0.06	0.06	0.22	-0.4	-0.1	0.1
Fit program										
(IX)	0.06	-0.035	-0.34	-0.63	0.19	-0.36	-0.69	0.4	-0.77	0.9
(X)	0.7	0.7	0.7	0.7	0.7	0.7	0.7	0.7	0.7	0.7
small(XI)	0.00	0.00	0.05	0.07	1.15	0.08	-0.02	0.00	0.01	0.01
TOTAL										
σ_{syst}	0.98	0.93	1.76	1.65	1.69	1.05	1.23	1.23	1.41	1.58

Table 7.7: *Systematic uncertainties for all effects analysed expressed as* $\frac{x[0]-x[i]}{\sigma_{stat}}$*:(I) systematic uncertainty associated with the tuning of the signal control sample, (II) proportion of radiative events increased by* 30% *for the signal control sample, (III) no electron tweaking for MCsignal events,(IV) no smearing for* $\theta_D, \phi_D, E_{miss}$ *for MCsignal, (V)* $B\bar{B}$ *bkg rate lowered by* 30%*,(VI)* 10% *of the effect of no correction on the generated semileptonic models (VII)* 50% *of the effect of no correction of the* q^2 *shape for charm bkg based on the WS control sample, (VIII)* 20% *of the effect of no correction of events associated with fragmentation pions, (IX) no smoothing effect, (X) effects from limited stats,(XI) variation of -100* MeV/c^2 *of the vector-pole mass.*

Chapter 8

Measurement of the variation of the S-wave phase δ_S with the K π mass.

In this section we remind the fit method and present results obtained for a fit where we assume that the S-wave amplitude is proportional to $|\sin\delta_S|$ and δ_S is fitted in several intervals of the $K\pi$ mass, independently.

8.1 Fitting procedure

Instead of assuming a parameterization of the $K\pi$ S-wave in terms of the sum of a background term and the $K_0^*(1430)$, we fit the phase of the S-wave in different $K\pi$ mass intervals, assuming that the phase remains constant within each interval. We assume also, as in the previous measurement, that:

$$A_S^{1/2} = r_S \frac{m}{p^*} |\sin\delta_S^{1/2}| e^{i\delta_S^{1/2}} \tag{8.1}$$

In order to speed up the fit, we have fixed the form factor parameters (r_2, r_V, m_A). This is reasonable since these parameters are only slightly correlated with the S-wave. Also the signal and background number of events are fixed to the values of the previous fit. The data sample, Monte Carlo signal and background control samples are the same as before.

8.2 Results

Values of the fitted parameters are given in Tables 8.1 and 8.2. The S-wave phase variation is given in Figure 8.1. It is clear from the trend of the S-wave that a $K_0^*(1430)$ is observed for the first time in this channel (see Table 1.8 where FOCUS places a limit on this contribution).

variable	Result
$\Gamma^0(K^{*0})(GeV/c^2)$	0.04569 ± 0.00018
$m(K^{*0})(GeV/c^2)$	0.8944 ± 0.0001
$r_{BW}(GeV/c)^{-1}$	4.162 ± 0.155
r_S	0.2509 ± 0.0049

Table 8.1: *Fit results on BaBar Run1-5 data assuming a signal composed of S and P-waves, where the S-wave phase is fitted in 20 bins in $m_{K\pi}$. The S-wave expression follows $\frac{m}{p^*}|\sin\delta_S|e^{i\delta_S}$.*

The correlation matrix is given in Table 13.7 in the Appendix.

	$m_{K\pi} GeV/c^2$	$\Delta m_{K\pi} GeV/c^2$	$\delta_S^{1/2}$ radian	$\delta_S^{1/2}$ degree
δ_1	0.659068	0.029068	0.1512 ± 0.0167	8.66 ± 0.96
δ_2	0.6992795	0.0111435	0.4402 ± 0.0313	25.22 ± 1.79
δ_3	0.7178365	0.0074135	0.4509 ± 0.0409	25.84 ± 2.35
δ_4	0.741125	0.015875	0.5186 ± 0.0337	29.71 ± 1.93
δ_5	0.7765	0.0195	0.4866 ± 0.0292	27.88 ± 1.67
δ_6	0.807	0.011	0.6773 ± 0.0430	38.81 ± 2.47
δ_7	0.825	0.007	0.6772 ± 0.0519	38.80 ± 2.93
δ_8	0.846	0.014	0.6455 ± 0.0327	36.98 ± 1.87
δ_9	0.867	0.007	0.7471 ± 0.0468	42.81 ± 2.68
δ_{10}	0.879	0.005	0.6951 ± 0.0478	39.83 ± 2.74
δ_{11}	0.888	0.004	0.7513 ± 0.0559	43.04 ± 3.21
δ_{12}	0.896	0.004	0.8135 ± 0.0584	46.61 ± 3.35
δ_{13}	0.9045	0.0045	0.7024 ± 0.0631	40.25 ± 3.61
δ_{14}	0.9145	0.0055	0.9331 ± 0.0506	53.46 ± 2.90
δ_{15}	0.93	0.01	0.8902 ± 0.0398	51.00 ± 2.28
δ_{16}	0.975	0.035	0.9605 ± 0.0262	55.00 ± 1.50
δ_{17}	1.0465	0.0365	0.9802 ± 0.0379	56.16 ± 2.17
δ_{18}	1.124875	0.041875	1.2139 ± 0.0576	69.55 ± 3.30
δ_{19}	1.20574	0.03899	1.2947 ± 0.0828	74.18 ± 4.74
δ_{20}	1.422365	0.177635	1.7927 ± 0.0963	102.72 ± 5.52

Table 8.2: *Fit results on BaBar Run1-5 data assuming a signal composed of S and P-waves, where the S-wave phase is fitted in 20 bins in $m_{K\pi}$. The S-wave expression follows $\frac{m}{p^*} \sin \delta_S e^{i\delta_S}$. The second column gives the center of the bin in mass, the third column gives the half-width of the bin. The last two columns give the value and the statistical uncertainty of the phase expressed in radians and degrees respectively.*

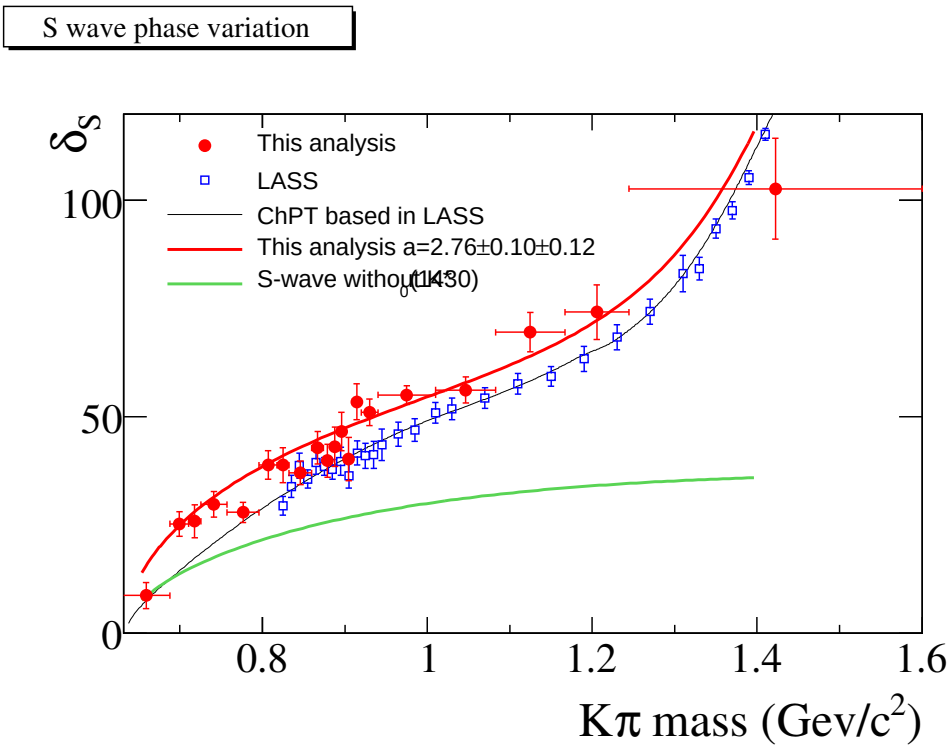

Figure 8.1: *Measurement of the variation of the S-wave phase . Analysis of BABAR data is done assuming that* $A^{1/2} = r_S|sin\delta^{1/2}|e^{1\delta^{1/2}}$. *The BaBar curve is the result of the fit explained in Section 6 which uses the parameterisation of the S-wave in terms of a background component and the* $K_0^*(1430)$. *In this fit only* r_S *and the scattering length* a_S *are free parameters. Points with error bars are the result of a fit where the phase* $\delta_S^{1/2}$ *is fitted in each corresponding* $K\pi$ *mass interval (error bars contain statistical and systematic uncertainties). This fit shows the increase at large mass values over expectations from the background term. This increase is expected from the contribution of the* $K_0^*(1430)$. *BaBar results are compared with measurements from LASS and with a fit based on ChPT using the latter.*

8.3 Systematic uncertainties

We have performed several studies with toy distributions where we fit the "data" S-wave phase in several $K\pi$ mass intervals, the S-wave relative strength (r_S) as well as the $K^{*0}(892)$ parameters. Results are given in Table 8.3 and pull distributions are shown in Figures: 13.41 and 13.42 in the Appendix. We average the standard deviation found for the phases (=1.3σ_{stat}) and include this effect in the systematic uncertainty.

These values are determined from fits of toy experiments done in the following conditions:

- the signal control sample is a S+P wave distribution with 4.5 times the statistics of the fitted signal;
- the background control sample has slightly more statistics than the background in the fitted sample;
- the "data" sample has a signal component (S+P wave) with 70k events on average, and a background component with 32k events on average;
- the background control sample is smoothed;
- the form factor parameters as well as the signal and background rates are fixed in the fit to the generated values;

parameter	$(bias, \sigma)$		parameter	$(bias, \sigma)$
$\Gamma(K^{*0}(892))$	(0.14,1.21)		$M(K^{*0}(892))$	(0.00,1.23)
r_{BW}	(-0.21,1.22)		r_S	(-0.36,1.27)
δ_1	(2.50,1.14)		δ_2	(0.21,1.25)
δ_3	(0.18,1.39)		δ_4	(0.24,1.28)
δ_5	(0.27,1.30)		δ_6	(0.18,1.23)
δ_7	(0.17,1.26)		δ_8	(0.16,1.23)
δ_9	(0.12,1.15)		δ_{10}	(0.12,1.12)
δ_{11}	(0.01,1.17)		δ_{12}	(0.17,1.22)
δ_{13}	(0.16,1.31)		δ_{14}	(0.02,1.36)
δ_{15}	(0.05,1.32)		δ_{16}	(0.13,1.32)
δ_{17}	(-0.05,1.34)		δ_{18}	(0.08,1.38)
δ_{19}	(0.05,1.28)		δ_{20}	(1.62,1.38)

Table 8.3: *Biases and standard deviations results for fits using 500 toy distributions where the S-wave phase is measured in 20 bins in mass. In this fit the amplitude for the S-wave is similar to the elastic scattering expression.*

- for each event, the phase space term $\frac{m}{p*}$ in the decay rate is determined by using the value of the hadronic mass of the event;

The first and the last bin have a significant bias. We can reduce the bias of the first bin if we use, for each event, the value of the hadronic mass (m) at the center of the mass bin where the event is situated. The bias in the last bin can come from the fact that the bin is wide and the phase variation inside this bin is large.

We have considered the same sources of systematic uncertainties as in the previous fit method. Results are summarized in Tables 8.4 and 8.5.

variation	$\Delta M_{K^{*0}(892)}$	$\Delta\Gamma_{K^{*0}(892)}$	Δr_{BW}	Δr_S
(I)	-0.14	-0.22	-0.0	-0.33
(II)	-0.54	0.13	0.07	-0.04
(III)	-0.34	-0.03	0.48	-0.31
(IV)	0.20	0.17	0.12	0.43
BKG				
B$\bar{B}$				
(V)	-0.09	0.15	-0.03	0.22
c$\bar{c}$				
(VI)	-0.06	-0.01	-0.08	0.03
(VII)	0.25	0.09	0.50	-0.41
(VIII)	-0.08	0.20	-0.83	0.28
Fit program				
(IX)	0.34	-0.08	0.23	-0.65
(X)	0.83	0.84	0.86	0.91
TOTAL				
σ_{syst}	1.17	0.94	1.41	1.39

Table 8.4: *Systematic uncertainties on K^{*0} parameters and on the S-wave contribution expressed in terms of $\frac{x[0]-x[i]}{\sigma_{stat}}$. (I) systematic uncertainty associated with the tuning of the signal control sample, (II) fraction of radiative events increased by 30% in the signal control sample, (III) no electron tweaking for MCsignal events,(IV) no smearing for $\theta_D, \phi_D, E_{miss}$ for MCsignal, (V) $B\bar{B}$ bkg rate lowered by 30%,(VI) no correction on the generated semileptonic models (VII) no correction of the q^2 shape for charm bkg based on the WS control sample (VIII) no correction of events associated with fragmentation pions, (VIII) no correction of events associated with fragmentation pions, (IX) no smoothing effect, (X) effects from limited MC stats.*

var/	$\Delta\delta_1$	$\Delta\delta_2$	$\Delta\delta_3$	$\Delta\delta_4$	$\Delta\delta_5$	$\Delta\delta_6$	$\Delta\delta_7$	$\Delta\delta_8$	$\Delta\delta_9$	$\Delta\delta_{10}$	$\Delta\delta_{11}$	$\Delta\delta_{12}$	$\Delta\delta_{13}$	$\Delta\delta_{14}$	$\Delta\delta_{15}$	$\Delta\delta_{16}$	$\Delta\delta_{17}$	$\Delta\delta_{18}$	$\Delta\delta_{19}$	$\Delta\delta_{20}$
signal																				
(I)	-0.16	-0.02	0.04	-0.01	0.03	0.07	0.06	0.12	0.15	0.10	0.05	0.07	0.04	0.08	0.09	0.03	-0.04	0.02	-0.02	0.05
(II)	-0.28	-0.17	-0.17	-0.19	-0.06	-0.05	-0.01	0.04	-0.15	0.04	-0.02	0.02	0.06	0.14	0.00	-0.01	-0.19	-0.12	-0.09	0.03
(III)	-0.09	0.01	-0.01	-0.03	0.00	0.00	0.10	0.22	0.13	0.26	0.32	0.12	0.35	0.23	0.27	0.30	0.02	0.16	0.05	0.03
(IV)	-0.14	-0.36	-0.85	-0.62	-0.24	-0.28	0.40	-0.17	-0.12	0.21	-0.18	0.08	0.26	-0.45	0.20	-0.13	0.28	0.01	-0.29	-0.40
BKG																				
B$\bar{B}$																				
(V)	-0.44	-0.31	-0.16	-0.21	-0.08	-0.05	-0.08	-0.18	-0.15	-0.10	-0.07	-0.07	-0.07	-0.09	-0.13	-0.30	-0.26	-0.24	-0.16	-0.09
c$\bar{c}$																				
(VI)	-0.31	-0.21	-0.13	-0.22	-0.19	-0.09	-0.06	-0.12	-0.06	-0.06	-0.04	-0.04	-0.04	-0.05	-0.08	-0.20	-0.23	-0.18	-0.07	-0.24
(VII)	0.49	0.39	0.25	0.32	0.18	0.10	0.08	0.17	0.18	0.16	0.13	0.10	0.06	0.07	0.09	0.21	0.13	0.09	0.02	0.22
(VIII)	-0.34	-0.32	-0.18	-0.30	-0.35	-0.19	-0.01	-0.05	-0.11	-0.09	-0.08	-0.03	-0.02	-0.04	-0.08	-0.16	-0.06	-0.11	-0.19	-0.20
(IX)	-1.16	-0.59	-0.83	-0.49	-0.25	-0.14	0.29	0.36	0.26	0.36	0.20	0.12	0.09	0.10	0.18	0.07	0.24	0.01	0.06	0.07
(X)	2.63	0.86	0.85	0.86	0.87	0.85	0.85	0.85	0.84	0.84	0.83	0.85	0.85	0.83	0.83	0.84	0.83	0.83	0.83	1.82
TOTAL																				
σ_{syst}	3.01	1.22	1.26	1.17	1.01	0.89	0.92	1.06	0.98	0.98	0.99	0.88	0.96	1.02	0.92	1.01	0.97	0.93	0.88	1.87

Table 8.5: *Systematic uncertainties for all effects analysed expressed as* $\frac{x[0]-x[i]}{\sigma_{stat}}$*:(I) systematic uncertainty associated with the tuning of the signal control sample, (II) proportion of radiative events increased by* 30% *for the signal control sample, (III) no electron tweaking for MCsignal events,(IV) no smearing for* $\theta_D, \phi_D, E_{miss}$ *for MCsignal, (V)* $B\bar{B}$ *bkg rate lowered by* 30%*,(VI)* 10% *of the effect of no correction on the generated semileptonic models (VII)* 50% *of the effect of no correction of the* q^2 *shape for charm bkg based on the WS control sample, (VIII)* 20% *of the effect of no correction of events associated with fragmentation pions, (IX) no smoothing effect, (X) effects from limited stats*

Chapter 9

Measurement of the S-wave amplitude and of the variation of the S-wave phase $\delta_S^{1/2}$ with the K π mass

In this section we remind the fit method and present results obtained for a fit where we do not assume that the S-wave amplitude behaves as $\frac{m}{p^*}|\sin\delta|$ and we also fit the value of the S-wave phase in several bins of the $K\pi$ mass.

9.1 Fitting procedure

We fit the phase variation of the S-wave in two ways: as in section 8.3, the value of the S-wave phase is fitted in several $K\pi$ mass intervals, assuming that it remains constant within each interval, or we use the parameterisation from LASS and fit some of the parameters.
We parameterize the amplitude of the S-wave using a polynomial dependence versus a variable x which is defined in the same way as in Ke_4 decays. This dependence is used from threshold up to the $K_0^*(1430)$ mass pole. Above this value we use the dependence given by the $K_0^*(1430)$ Breit-Wigner mass distribution. Previous experiments (LASS, $K^-\pi^+\pi^+$ Dalitz analyses) have observed a sharp decrease of the S-wave amplitude in this region.

$$A_S^j = r_S P(m) \exp i\delta_j,\ m(K\pi) < m_{K_0^*(1430)}; \tag{9.1}$$

$$A_S^j = r_S P(m_{K^{*0}(1430)}) \sqrt{\frac{(m_{K_0^*(1430)}\Gamma_{K_0^*(1430)})^2}{(m^2_{K_0^*(1430)} - m^2)^2 + (m_{K_0^*(1430)}\Gamma_{K_0^*(1430)})^2}} \exp i\delta_j,\ m(K\pi) > m_{K_0^*(1430)}. \tag{9.2}$$

where $P(m) = 1 + r_S^{(1)} \times x + r_S^{(2)} \times x^2 + ...$ and $x = \sqrt{(\frac{m(K\pi)}{m_K+m_\pi})^2 - 1}$. The coefficients $r_S^{(i)}$ have no dimension. We have tried a linear and a quadratic dependence for $P(m)$. Uncertainties on fitted parameters show that a linear dependence is enough.

In order to speed up the fit when the phase is measured in several $K\pi$ mass intervals, we have fixed the K^{*0} Breit-Wigner parameters (mass, width, barrier factor) and the form factor parameters (r_2, r_V, m_A) to the values found in the fit of Section 9.2.1. Also for this fit the total signal and background number of events are fixed to the values of the previous fit. The data sample, Monte Carlo signal and background control samples are the same as before.

9.2 Results

9.2.1 Results using the LASS parameterisation for the S-wave phase

variable	Result
$\Gamma^0(K_0^*)(GeV/c^2)$	0.04579 ± 0.00023
$m(K_0^*)(GeV/c^2)$	0.8945 ± 0.0001
$m_A(GeV/c^2)$	$2.68^{+0.11}_{-0.10}$
r_V	1.480 ± 0.016
r_2	0.824 ± 0.020
r_S	0.477 ± 0.025
$r_S^{(1)}$	0.15 ± 0.06
$a_S(GeV/c)^{-1}$	1.78 ± 0.15
$r_{BW}(GeV/c)^{-1}$	4.20 ± 0.23
N_S	244619 ± 697
N_B	106602 ± 567
$b_S(GeV/c)^{-1}$	-1.93 ± 0.69

Table 9.1: *The S-wave amplitude is defined in Equation 9.2. The phase is parameterized using LASS expression given in Equation 1.34; The signal is the sum of S+P-wave components.*

The correlation matrix is given in Table 9.2.

-	Γ^0	m	m_A	r_V	r_2	r_S	$r_S^{(1)}$	a_S	r_{BW}	N_S	N_B	b_S
Γ^0	1.00	0.09	0.05	-0.07	0.02	-0.15	0.10	-0.04	0.02	0.29	-0.34	0.09
m	0.09	1.00	-0.22	0.11	-0.22	-0.15	0.15	0.12	0.22	0.01	0.02	-0.09
m_A	0.05	-0.22	1.00	-0.55	0.86	-0.09	-0.04	-0.04	0.25	0.09	-0.09	0.03
r_V	-0.07	0.11	-0.55	1.00	-0.53	0.08	0.01	-0.01	-0.15	-0.12	0.08	-0.00
r_2	0.02	-0.22	0.86	-0.53	1.00	-0.08	-0.03	-0.04	0.26	0.09	-0.10	0.03
r_S	-0.15	-0.15	-0.09	0.08	-0.08	1.00	-0.97	-0.07	-0.69	-0.44	0.40	0.06
$r_S^{(1)}$	0.10	0.15	-0.04	0.01	-0.03	-0.97	1.00	0.04	0.65	0.44	-0.41	-0.03
a_S	-0.04	0.12	-0.04	-0.01	-0.04	-0.07	0.04	1.00	-0.02	-0.09	0.05	-0.96
r_{BW}	0.02	0.22	0.25	-0.15	0.26	-0.69	0.65	-0.02	1.00	0.44	-0.31	-0.02
N_S	0.29	0.01	0.09	-0.12	0.09	-0.44	0.44	-0.09	0.44	1.00	-0.52	0.10
N_B	-0.34	0.02	-0.09	0.08	-0.10	0.40	-0.41	0.05	-0.31	-0.52	1.00	-0.08
b_S	0.09	-0.09	0.03	-0.00	0.03	0.06	-0.03	-0.96	-0.02	0.10	-0.08	1.00

Table 9.2: *Statistical correlation matrix for fit of S+P-wave signal, with the S-wave phase δ_S parameterized using the expression in Equation 1.34.*

Projections over the 5 kinematic variables for data and fit results are displayed in Figure 9.1:

The total χ^2 of this fit is 2935 for 2788 degrees of freedom. This corresponds to a probability of 2.6 $\%$
The chi2 distribution is shown in Figure 9.2.

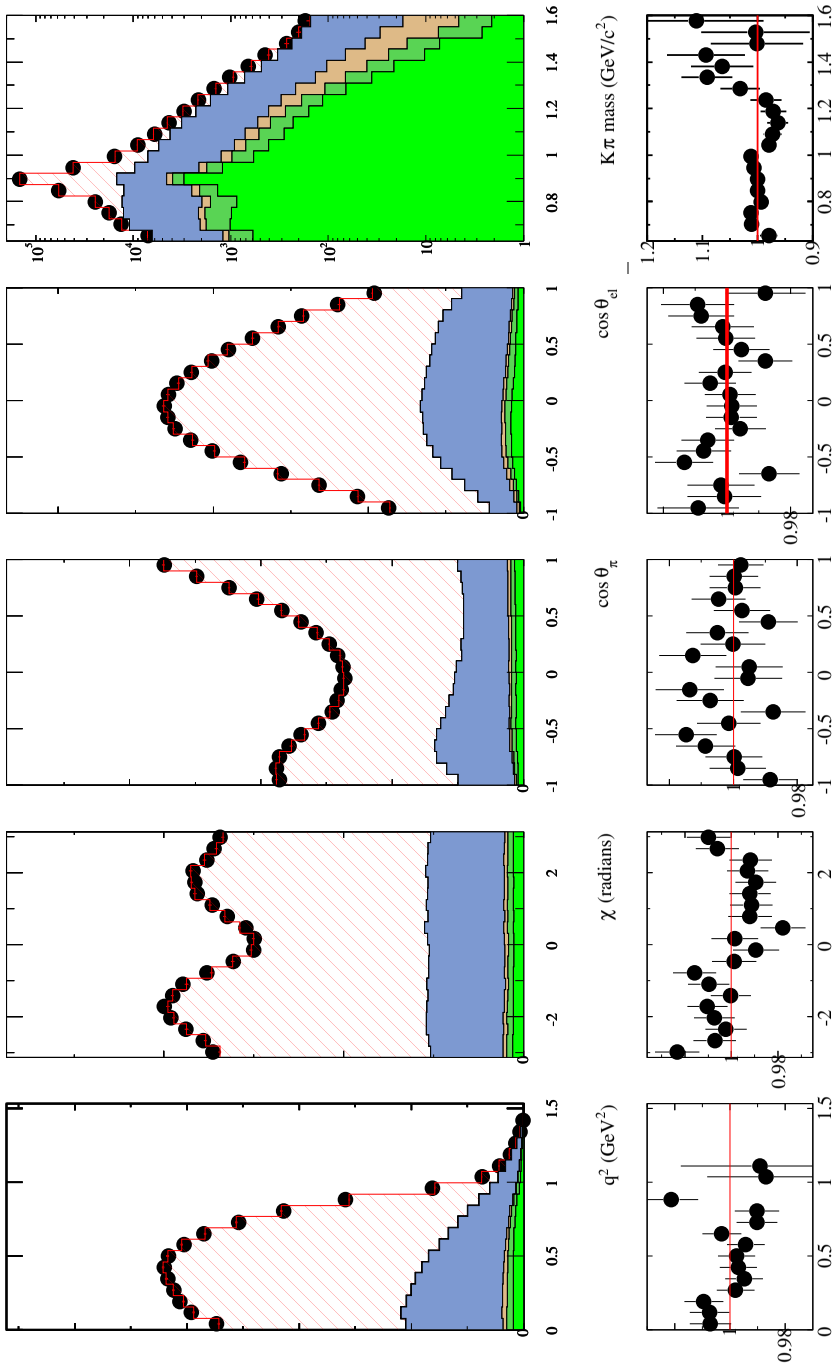

Figure 9.1: *Projections of data and of the fitted MC distribution over each of the 5 kinematic variables. Color code: red(signal),blue(charm bkg), light brown(uds bkg), dark green(B^+B^- bkg), light green($B^0\bar{B}^0$).*

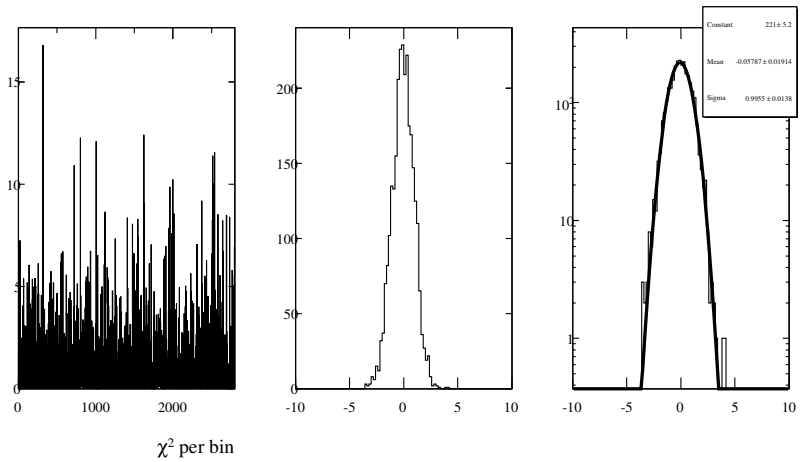

Figure 9.2: *Left plot: distribution of the χ^2 value in each bin. The fit is done using the LASS parameterisation for the S-wave phase. Center and Right plots: pull distribution for all bins.*

9.2.2 Fit of the $K\pi$ S-wave in several $K\pi$ mass intervals

As explained, in this fit the parameters which define the q^2 variation of the hadronic form factors ($r_2,\ r_V$ and m_A) are fixed. Total numbers of signal and background events are fixed also. Values of the fitted parameters are given in Table 9.3. The S-wave phase variation and amplitude are given in Figure 9.3 [1]. In this Figure the measured phase and amplitude are compared with the previous determination (Section 9.2.1) when the phase variation is parameterized using the LASS expression. We find that they are in agreement within uncertainties.
We compare also in Figure 9.4 the phase and amplitude for the fit of the phase in several bins to the phase found by the LASS collaboration and to our fit assuming the S-wave amplitude to be given as $\frac{m}{p*}\sin\delta_S$ (Section 7.1). We find good agreement between both determinations of the S-wave amplitude.

variable	**Result**		
r_S	0.505 ± 0.031		
$r_S^{(1)}$	0.076 ± 0.061		
δ (degrees)		$m_{K\pi}\ GeV/c^2$	$\Delta m_{K\pi}\ GeV/c^2$
δ_1	79.96 ± 11.12	0.659068	0.029068
δ_2	19.40 ± 9.42	0.706693	0.018557
δ_3	30.42 ± 4.34	0.760625	0.035375
δ_4	31.48 ± 2.62	0.828	0.032
δ_5	37.00 ± 2.90	0.88	0.02
δ_6	51.02 ± 2.57	0.955	0.055
δ_7	57.33 ± 1.16	1.0465	0.0365
δ_8	76.96 ± 3.43	1.124875	0.041875
δ_9	75.67 ± 5.63	1.20574	0.03899
δ_{10}	116.42 ± 9.25	1.422365	0.177635

Table 9.3: *Fit of the S-wave amplitude and phase; the signal is the sum S+P-wave components.*

The correlation matrix is given in Table 9.4.

[1]Note: In this plot the evaluated systematic uncertainties are included in the error bars

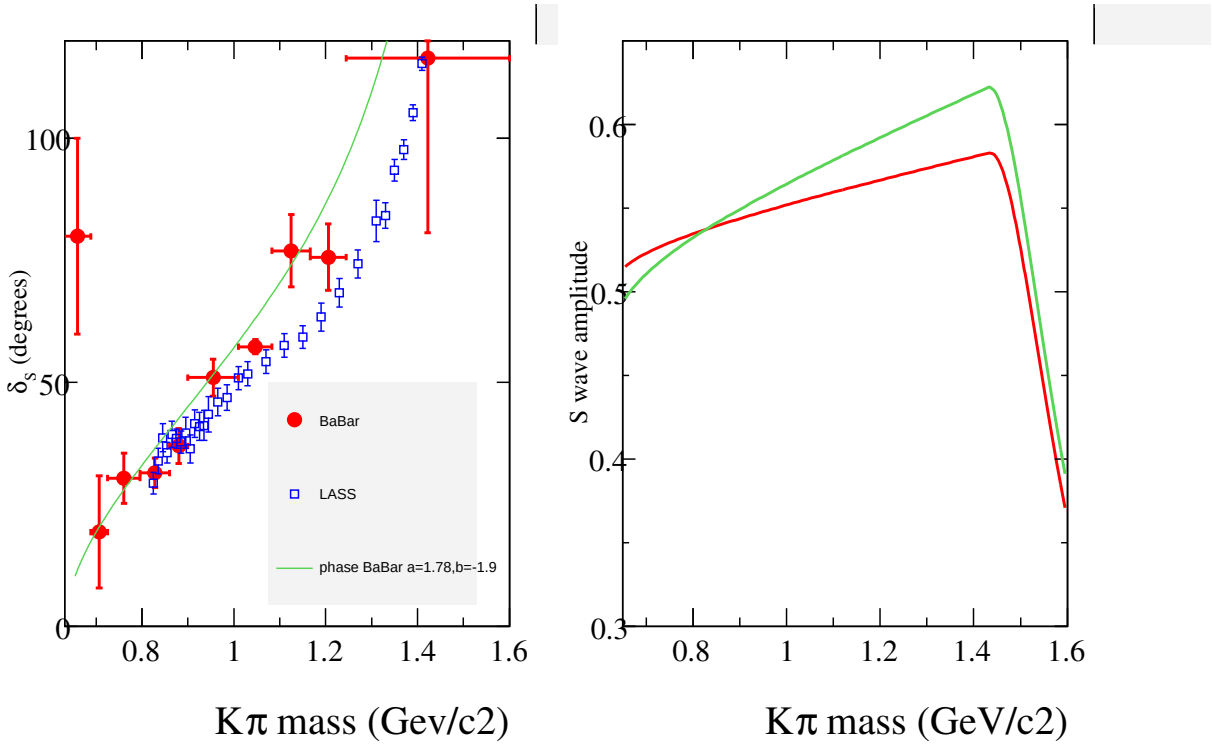

Figure 9.3: *Left plot: (red points) this analysis giving the S-wave phase variation using Equation 9.2 versus $m_{K\pi}$. The variation of the S-wave amplitude (A_S) versus m is also fitted using Equation 9.2, (green line): result from section 9.2.1 in which we use the LASS parameterization for δ and fit the scattering length and effective range parameters (a_S, b_S). (blue points) measurements from LASS corrected for $\delta^{3/2}$; Right plot: (red line) fitted S-wave amplitude in fit of S-wave phase in several mass bins, (green line) amplitude found in fit of Section 9.2.1.*

	r_S	r_S^1	δ_1	δ_2	δ_3	δ_4	δ_5	δ_6	δ_7	δ_8	δ_9	δ_{10}
r_S	1.00	-0.98	-0.36	0.29	0.40	0.21	-0.16	-0.03	-0.00	0.10	0.12	0.23
r_S^1	-0.98	1.00	0.35	-0.28	-0.37	-0.18	0.12	0.03	0.01	-0.11	-0.14	-0.25
δ_1	-0.36	0.35	1.00	-0.08	-0.15	-0.08	0.07	0.01	0.00	-0.03	-0.04	-0.08
δ_2	0.29	-0.28	-0.08	1.00	0.09	0.07	-0.06	-0.01	0.00	0.02	0.03	0.060
δ_3	0.40	-0.37	-0.15	0.09	1.00	0.07	-0.09	-0.01	0.00	0.03	0.04	0.08
δ_4	0.21	-0.18	-0.08	0.07	0.07	1.00	-0.10	-0.00	0.00	0.01	0.01	0.03
δ_5	-0.16	0.12	0.07	-0.06	-0.09	-0.10	1.00	-0.09	-0.00	0.00	-0.00	-0.01
δ_6	-0.03	0.03	0.01	-0.01	-0.01	-0.00	-0.09	1.00	-0.03	-0.00	-0.00	-0.01
δ_7	-0.00	0.01	0.00	0.00	0.00	0.00	-0.00	-0.03	1.00	-0.05	-0.00	-0.00
δ_8	0.01	-0.11	-0.03	0.02	0.03	0.01	0.00	-0.00	-0.05	1.00	-0.03	0.04
δ_9	0.12	-0.14	-0.04	0.03	0.04	0.01	-0.00	-0.00	-0.00	-0.03	1.00	-0.00
δ_{10}	0.23	-0.25	-0.08	0.06	0.08	0.03	-0.01	-0.01	-0.00	0.04	-0.00	1.00

Table 9.4: *Statistical correlation matrix for the parameters listed in Table 9.3*

9.3 Systematic uncertainties

We have performed a similar study of the systematic uncertainties as those explained in previous sections. We present in Table 9.5 and 9.6 the systematic uncertainties.

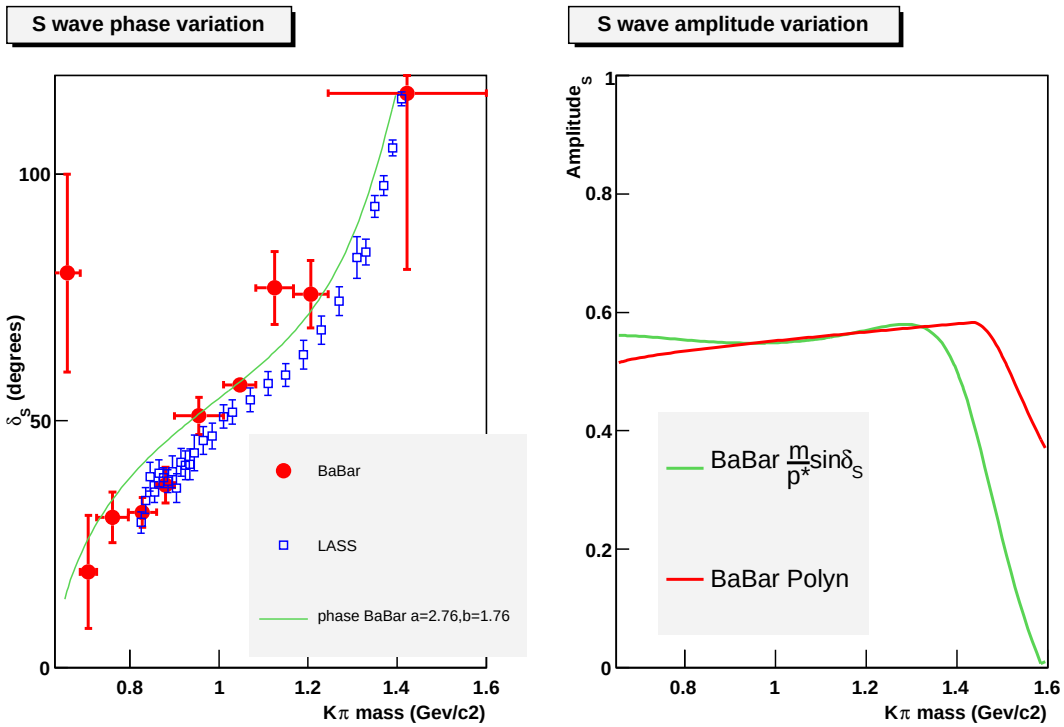

Figure 9.4: *Left plot: (red points) this analysis giving the S-wave phase variation using Equation 9.2 for the variation of the amplitude versus $m_{K\pi}$. (green line): result from section 7 in which we assume that $A_S(m) = \frac{m}{p^*}|\sin\delta|$ and use the LASS parameterization for δ. (blue points) measurements from LASS corrected for $\delta^{3/2}$; Right plot: (red line) fitted S-wave amplitude, (green line) amplitude found using results from section 7*

-	Γ	M	m_A	r_V	r_2	r_S	$r_S^{(1)}$	a_S	r_{BW}	N_S	N_B	b_S
TOTAL												
σ_{syst}	0.93	0.98	1.65	1.69	1.05	0.87	0.96	1.23	1.76	1.41	1.58	1.01

Table 9.5: *Systematic uncertainties on the S-wave contribution expressed in terms of $\frac{x[0]-x[i]}{\sigma_{stat}}$. These are the final results including all systematic uncertainties effects.*

variation	Δr_S	$\Delta r_S^{(1)}$	$\Delta\delta_1$	$\Delta\delta_2$	$\Delta\delta_3$	$\Delta\delta_4$	$\Delta\delta_5$	$\Delta\delta_6$	$\Delta\delta_7$	$\Delta\delta_8$	$\Delta\delta_9$	$\Delta\delta_{10}$
(I)	-0.05	-0.01	0.07	0.15	0.03	-0.06	0.13	0.09	0.04	0.05	0.03	-0.04
(II)	-0.06	0.03	0.06	0.10	-0.01	-0.02	-0.05	0.10	-0.24	-0.12	-0.08	-0.06
(III)	-0.26	0.44	-0.04	0.14	0.01	-0.04	0.18	0.62	0.02	-1.77	-0.11	-0.19
(IV)	-0.15	0.21	-0.06	-0.21	-0.04	-0.11	-0.29	-0.18	-0.07	-0.10	0.00	-0.13
BKG												
B$\bar{B}$												
(V)	-0.22	0.23	0.24	0.03	-0.06	0.05	-0.07	-0.31	-0.26	-0.21	-0.16	-0.10
c$\bar{c}$												
(VI)	-0.28	0.21	0.11	0.01	-0.00	-0.03	-0.01	-0.16	-0.21	-0.17	-0.11	-0.04
(VII)	0.29	-0.36	-0.27	0.10	0.21	0.04	0.11	0.11	0.15	0.19	0.14	0.23
(VIII)	-0.29	0.30	0.05	-0.07	-0.02	-0.03	-0.01	-0.09	-0.16	-0.24	-0.28	-0.44
Fit program												
(IX)	-0.11	-0.07	1.34	0.30	0.25	-0.01	0.33	0.10	0.14	0.05	0.12	-0.01
(X)	0.60	0.61	0.56	0.53	0.54	0.53	0.53	0.78	0.54	0.53	0.54	3.69
TOTAL												
σ_{syst}	0.87	0.96	1.50	0.69	0.64	0.55	0.74	1.09	0.73	1.91	0.68	3.73

Table 9.6: *Systematic uncertainties for all effects analysed expressed as* $\frac{x[0]-x[i]}{\sigma_{stat}}$*:(I) systematic uncertainty associated with tuning of signal control sample, (II) proportion of radiative events increased by* 30% *for signal control sample, (III) no electron tweaking for MCsignal events,(IV) no smearing for* $\theta_D, \phi_D, E_{miss}$ *for MCsignal, (V)* $B\bar{B}$ *bkg rate lowered by* 30%*,(VI)* 10% *of the effect of no correction on the generated semileptonic models (VII)* 50% *of the effect of no correction of the* q^2 *shape for charm bkg based on the WS control sample, (VIII)* 20% *of the effect of no correction of events associated with fragmentation pions, (IX) no moothing effect, (X) effects from limited stats*

Chapter 10

Searches for other contributions to the decay $D^+ \to K^-\pi^+e^+\nu_e$

10.1 P' wave contribution and S-wave "a la LASS"

For the P', we consider the possible contribution of the $K^{*0}(1410)$. It is parameterized using a similar Breit-Wigner expression to that of the $K^{*0}(892)$. The L=1 form factor components are in this case written as:

$$\begin{aligned} \mathcal{F}_{11} &= (BW + r_{P'}e^{i\delta_{P'}}BW')2\sqrt{2}qH_0 \\ \mathcal{F}_{21} &= (BW + r_{P'}e^{i\delta_{P'}}BW')2q\,(H_+ + H_-) \\ \mathcal{F}_{31} &= (BW + r_{P'}e^{i\delta_{P'}}BW')2q\,(H_+ - H_-) \end{aligned} \tag{10.1}$$

where BW stands for the Breit-Wigner of the $K^{*0}(892)$ and BW' for that of the $K^{*0}(1410)$. As the phase space region where this component contributes is scarcely populated (high $K\pi$ mass), one is considerably less sensitive to the structure of the resonance. Therefore we fix the Breit-Wigner parameters of this resonance and fit only its relative strength and phase, $r_{P'}$ and $\delta_{P'}$ respectively.

Results for a P' contribution using the S-wave parameterization given in Equation 1.40. Results are presented in Table 10.1 for a fit where the S-wave component is evaluated using the LASS parameterisation for the phase and assuming that the amplitude is proportional to $\frac{m}{p^*}|sin\delta|$. Results of the fit are compared to data in Figure 10.1. In this fit the $K^{*0}(892)$ Breit-Wigner parameters as well as the L=1 form factor parameters are fitted. The total rate of signal and background are also evaluated.

The correlation matrix for parameters listed in the same order as in Table 10.1 is given in Table 10.2:

Values of the L=1 form factor parameters are almost identical with those found in Section 7.1 and the signal and background rates are well compatible. On the other hand the P-wave Breit-Wigner parameters as well as the S-wave are significantly different from those found when the P′ is not included.

The contribution of each bin to the overall χ^2 of the fit and the distribution of the difference, χ_{bin}, between measured and expected number on events in each bin, divided by the corresponding uncertainty are displayed in Figure 10.2. The total χ^2 value is 2903 and the number of degrees of freedom is 2788. This corresponds to a probability of 6.2%.

Although we find different values for the S-wave parameters from those found in the section 7, the total fraction of S-wave is well compatible. Fractions for each component are given in Table 10.3 and compared with those obtained without a P′. The total fraction in the former is different from 1 because of inteference between the P and P′.

variable	Result S+P+P′	Result S+P
$\Gamma^0(K_0^*)(GeV/c^2)$	0.04635 ± 0.00027	0.04594 ± 0.00023
$m(K_0^*)(GeV/c^2)$	0.8950 ± 0.0002	0.8944 ± 0.0001
$m_A(GeV/c^2)$	$2.67^{+0.10}_{-0.10}$	$2.70^{+0.11}_{-0.10}$
r_V	1.485 ± 0.017	1.480 ± 0.016
r_2	0.822 ± 0.020	0.825 ± 0.020
r_S	0.2680 ± 0.0072	0.2437 ± 0.0045
$a_S(GeV/c)$	2.24 ± 0.11	2.76 ± 0.10
$r_{BW}(GeV/c)$	2.765 ± 0.368	3.75 ± 0.149
$r_{P'}$	0.065 ± 0.012	
$\delta_{P'}(deg.)$	18.5 ± 12.2	
N_S	244137 ± 690	244603 ± 669
N_B	107087 ± 606	106622 ± 566

Table 10.1: *Results for a S+P+P′ fit to Runs1-5 assuming the LASS parameterisation for the S-wave and comparison to results for a fit assuming S+P.*

-	Γ^0	m	m_A	r_V	r_2	r_S	a_S	r_{BW}	$r_{P'}$	$\delta_{P'}$	N_S	N_B
Γ^0	1.000	0.560	-0.051	0.043	-0.051	0.415	0.459	-0.516	0.530	-0.520	0.159	-0.088
m	0.560	1.000	-0.213	0.193	-0.183	0.648	0.608	-0.774	0.836	-0.768	-0.182	0.272
m_A	-0.051	-0.213	1.000	-0.561	0.855	-0.334	-0.121	0.260	-0.128	0.129	0.122	-0.133
r_V	0.043	0.193	-0.561	1.000	-0.529	0.259	0.100	-0.257	0.138	-0.182	-0.149	0.179
r_2	-0.051	-0.183	0.855	-0.529	1.000	-0.286	-0.113	0.238	-0.099	0.112	0.136	-0.158
r_S	0.415	0.648	-0.334	0.259	-0.286	1.000	0.841	-0.629	0.674	-0.559	-0.014	0.054
a_S	0.459	0.608	-0.121	0.100	-0.113	0.841	1.000	-0.514	0.692	-0.436	-0.047	0.072
r_{BW}	-0.516	-0.774	0.260	-0.257	0.238	-0.629	-0.514	1.000	-0.813	0.898	0.250	-0.372
$r_{P'}$	0.530	0.836	-0.128	0.138	-0.099	0.674	0.692	-0.813	1.000	-0.675	-0.184	0.255
$\delta_{P'}$	-0.520	-0.768	0.129	-0.182	0.112	-0.559	-0.436	0.898	-0.675	1.000	0.231	-0.365
N_S	0.159	-0.182	0.122	-0.149	0.136	-0.014	-0.047	0.250	-0.184	0.231	1.000	-0.588
N_B	-0.088	0.272	-0.133	0.179	-0.158	0.054	0.072	-0.372	0.255	-0.365	-0.588	1.000

Table 10.2: *Statistical correlation matrix for fit of S+P+P′ waves signal, with S-wave parameterized with LASS expression*

Component	fractions in S+P+P′	fractions in S+P
S-wave	5.82%	5.68%
P-wave	94.18%	94.32%
$K^{*0}(892)$	93.39%	94.32%
$K^*(1410)$	0.27%	0%

Table 10.3: *Fractions for different signal components in the hypotheses of having S+P+P′ or S+P. In the first case, the sum of the fractions for the two K^* does not correspond exactly to the P-wave fraction because of interference*

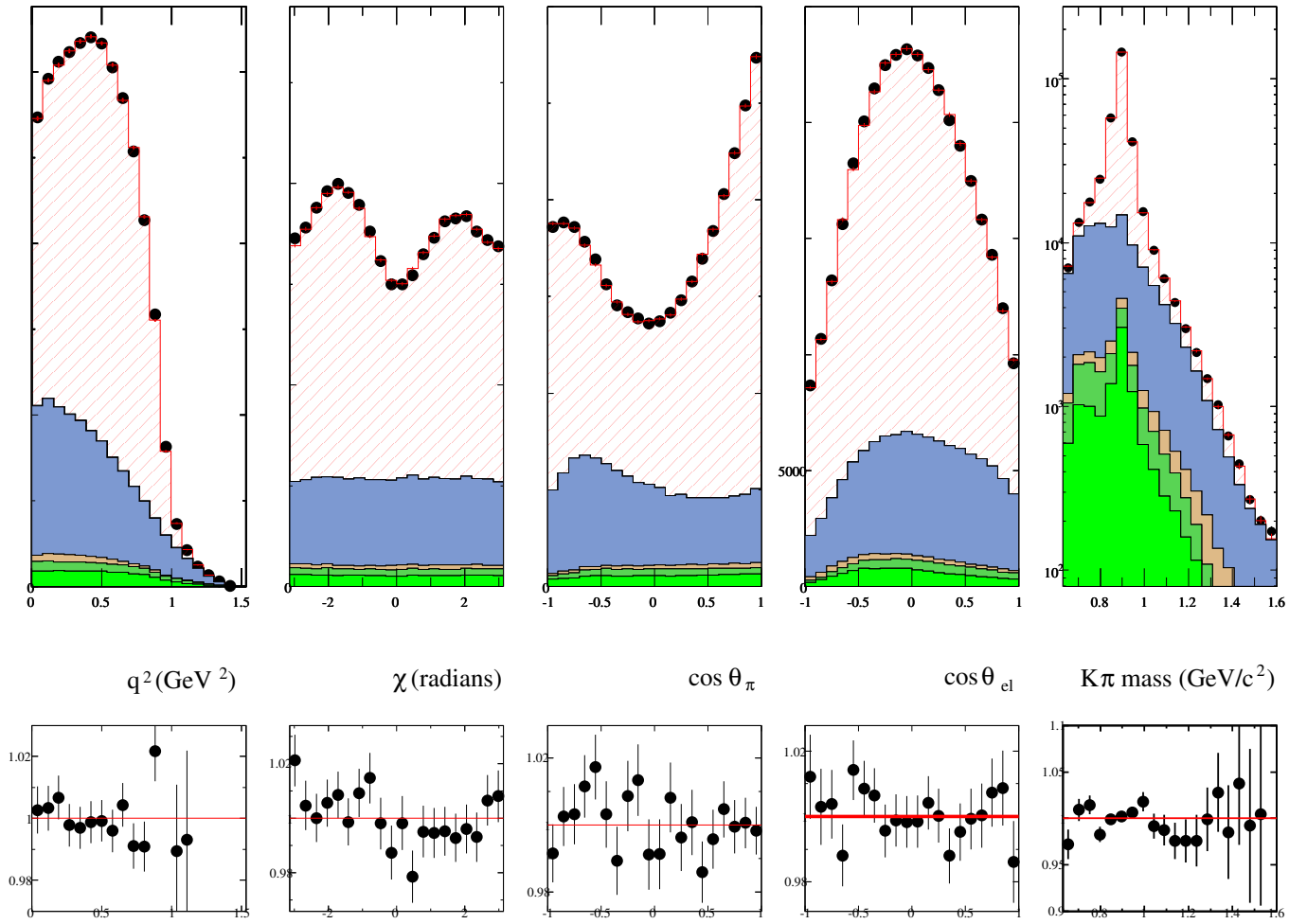

Figure 10.1: *Projections of data and of the fitted MC distribution over each of the 5 kinematic variables. Color code: red(signal),blue(charm bkg), light brown(uds bkg), dark green(B^+B^- bkg), light green($B^0\bar{B}^0$).*

We present in Figure 10.3 the distribution of the different signal components versus $m_{K\pi}$ and q^2.

Systematic uncertainties. Systematic uncertainties associated to each analyzed effect are presented in Table 10.4.They have been obtained with Runs1-5. We take as the effect of limited control statistics the same value found in the analog fit to a model having only S+P-waves components.

10.2 Fit of the P′ contribution and of the S-wave amplitude and phase

We have repeated the analysis explained in Section 9, adding a P′ component.
We have fixed for this fit all the parameters of the P-wave to the values determined in fit done in Section 10.1. The total number of signal and background events is also fixed. This as been done in order to accelerate the fit.

Results Values of fitted parameters are given in Table 10.5.

variation	$\Delta m_{K^{*0}(892)}$	$\Delta\Gamma^0_{K^{*0}(892)}$	Δr_{BW}	Δm_A	Δr_V	Δr_2	Δr_S	Δa_S	$\Delta r_{P'}$	$\Delta\delta_{P'}$	ΔN_S	ΔN_B
signal												
(I)	0.04	-0.03	-0.08	-0.25	0.32	0.14	-0.04	-0.09	0.06	-0.16	-0.34	0.40
(II)	-0.09	0.13	-0.16	-0.14	0.36	0.09	-0.02	-0.10	0.04	-0.16	-0.30	0.35
(III)	0.06	0.05	-0.09	0.73	-0.74	0.51	-0.12	0.30	0.14	-0.21	0.06	-0.07
(IV)	-0.14	0.03	0.42	-0.17	0.04	-0.24	0.14	-0.18	-0.25	0.41	0.67	-0.79
BKG												
B$\bar{B}$												
(V)	-0.32	0.02	0.28	0.24	-0.15	0.04	0.03	-0.11	-0.37	0.23	-0.07	0.08
c$\bar{c}$												
(VI)	0.04	-0.01	-0.16	0.30	0.06	0.18	0.09	-0.25	0.03	-0.12	-0.18	0.21
(VII)	-0.50	-0.05	0.89	-0.89	0.40	-0.22	-0.69	0.55	-0.69	0.61	0.43	-0.50
(VIII)	-0.06	0.13	0.05	0.13	-0.08	0.08	0.12	-0.21	-0.13	-0.07	0.02	-0.02
Fit program												
(IX)	-0.14	-0.15	0.05	-0.57	0.15	-0.34	-0.67	0.47	-0.20	0.14	-0.72	0.84
(X)	0.7	0.7	0.7	0.7	0.7	0.7	0.7	0.7	0.7	0.7	0.7	0.7
(XI)	0.00	0.00	0.05	0.07	1.15	0.08	-0.02	0.00	0.00	0.00	0.01	0.01
TOTAL												
σ_{syst}	0.95	0.74	1.29	1.51	1.67	1.02	1.21	1.13	1.13	1.12	1.38	1.55

Table 10.4: *Systematic uncertainties for all effects analysed expressed as* $\frac{x[0]-x[i]}{\sigma_{stat}}$*:(I) systematic uncertainty associated with tuning of signal control sample, (II) proportion of radiative events increased by* 30% *for signal control sample, (III) no electron tweaking for MCsignal events,(IV) no smearing for* $\theta_D, \phi_D, E_{miss}$ *for MCsignal, (V)* $B\bar{B}$ *bkg rate lowered by* 30%*,(VI)* 10% *of the effect of no correction on the generated semileptonic models (VII)* 50% *of the effect of no correction of the* q^2 *shape for charm bkg based on the WS control sample, (VIII)* 20% *of the effect of no correction of events associated with fragmentation pions, (IX) no smoothing effect, (X) effects from limited stats,(XI) variation of -100* MeV/c^2 *of the vector-pole mass.*

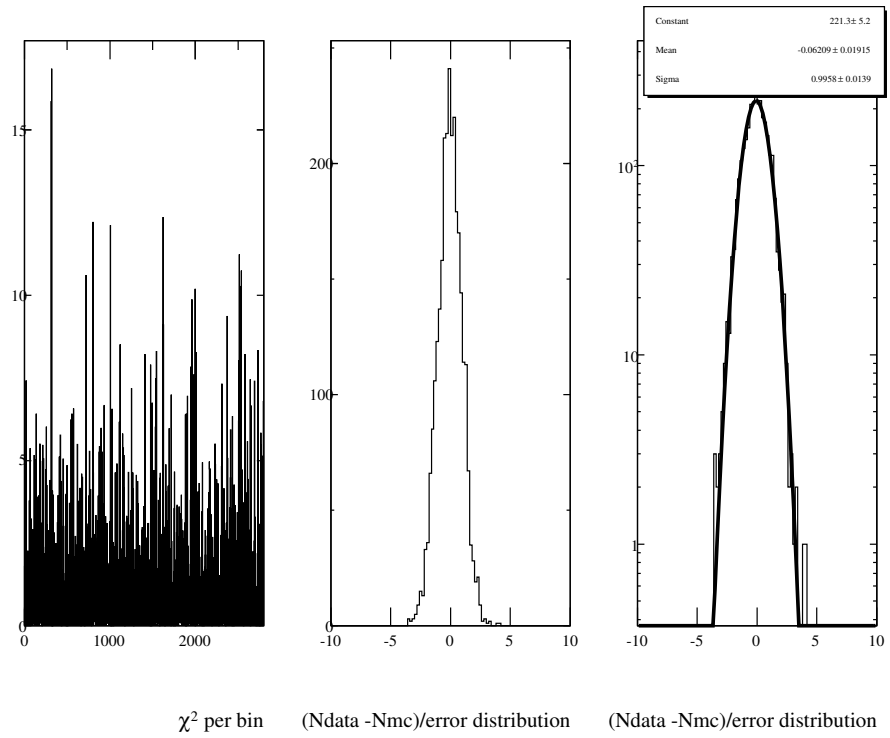

Figure 10.2: *Left plot: distribution of thee χ^2 value in each bin. The fit is done using the LASS parameterization for the S-wave phase. Center and Right plots: Pull distribution for all bins.*

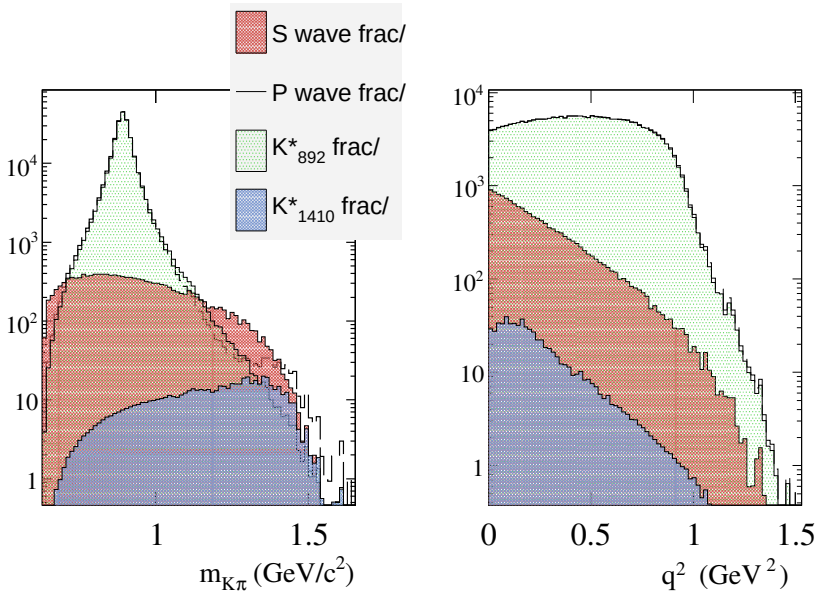

Figure 10.3: *Distributions of S,P and P′ signal components which corresponds to the results of the fit to BaBar data*

The statistical correlation matrix for parameters, listed in the same order as in Table 10.5, is given in Table 10.6.

variable	Result		
$r_{P'}$	0.057 ± 0.0076		
$\delta_{P'}$	0.085 ± 0.514		
r_S	0.489 ± 0.073		
$r_S^{(1)}$	0.138 ± 0.172		
		$m_{K\pi}\ GeV/c^2$	$\Delta m_{K\pi}\ GeV/c^2$
δ_1	77.69 ± 14.73	0.659068	0.029068
δ_2	17.88 ± 10.83	0.706693	0.018557
δ_3	29.45 ± 5.56	0.760625	0.035375
δ_4	31.05 ± 3.05	0.828	0.032
δ_5	34.55 ± 2.56	0.88	0.02
δ_6	48.53 ± 1.38	0.955	0.055
δ_7	54.15 ± 4.24	1.0465	0.0365
δ_8	70.19 ± 6.30	1.124875	0.041875
δ_9	59.59 ± 11.46	1.20574	0.03899
δ_{10}	68.18 ± 9.74	1.422365	0.177635

Table 10.5: *Fit results for a signal composed of S+P+P′ wave. The S-wave phase and amplitudes are fitted.*

The variation of the S-wave phase is given in Figure 10.4 and compared with LASS results and with the result found in section 10.1.

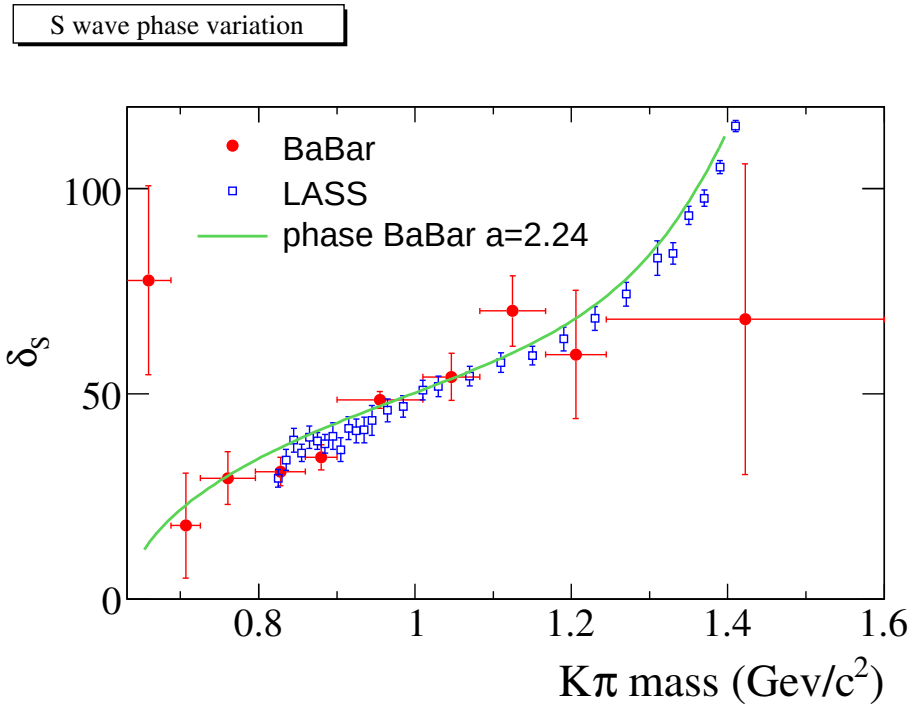

Figure 10.4: *S-wave phase variation which corresponds to a fit of BaBar data assuming a signal composed of S+P+P′(red) and where the S-wave phase and amplitudes are fitted (error bars include both statistical and systematical uncertainties), (blue) phase variation measured by LASS after corrections for $\delta^{3/2}$, (green) result found in section 10.1.*

-	$r_{P'}$	$\delta_{P'}$	r_S	$r_S^{(1)}$	δ_1	δ_2	δ_3	δ_4	δ_5	δ_6	δ_7	δ_8	δ_9	δ_{10}
$r_{P'}$	1.000	0.808	0.667	-0.680	-0.475	0.439	0.522	0.264	0.129	-0.494	-0.698	-0.727	-0.756	-0.568
$\delta_{P'}$	0.808	1.000	0.932	-0.944	-0.636	0.565	0.652	0.333	0.170	-0.601	-0.849	-0.840	-0.823	-0.384
r_S	0.667	0.932	1.000	-0.996	-0.673	0.586	0.689	0.370	0.113	-0.563	-0.787	-0.758	-0.727	-0.249
$r_S^{(1)}$	-0.680	-0.944	-0.996	1.000	0.669	-0.583	-0.680	-0.356	-0.135	0.571	0.798	0.767	0.737	0.254
δ_1	-0.475	-0.636	-0.673	0.669	1.000	-0.381	-0.469	-0.254	-0.074	0.385	0.538	0.522	0.504	0.189
δ_2	0.439	0.565	0.586	-0.583	-0.381	1.000	0.395	0.223	0.066	-0.342	-0.479	-0.468	-0.454	-0.185
δ_3	0.522	0.652	0.689	-0.680	-0.469	0.395	1.000	0.245	0.061	-0.396	-0.553	-0.542	-0.528	-0.223
δ_4	0.264	0.333	0.370	-0.356	-0.254	0.223	0.245	1.000	-0.032	-0.199	-0.282	-0.280	-0.271	-0.115
δ_5	0.129	0.170	0.113	-0.135	-0.074	0.066	0.061	-0.032	1.000	-0.169	-0.143	-0.138	-0.136	-0.061
δ_6	-0.494	-0.601	-0.563	0.571	0.385	-0.342	-0.396	-0.199	-0.169	1.000	0.499	0.506	0.496	0.234
δ_7	-0.698	-0.849	-0.787	0.798	0.538	-0.479	-0.553	-0.282	-0.143	0.499	1.000	0.701	0.702	0.335
δ_8	-0.727	-0.840	-0.758	0.767	0.522	-0.468	-0.542	-0.280	-0.138	0.506	0.701	1.000	0.694	0.370
δ_9	-0.756	-0.823	-0.727	0.737	0.504	-0.454	-0.528	-0.271	-0.136	0.496	0.702	0.694	1.000	0.379
δ_{10}	-0.568	-0.384	-0.249	0.254	0.189	-0.185	-0.223	-0.115	-0.061	0.234	0.335	0.370	0.379	1.000

Table 10.6: *Statistical correlation matrix for fit results for the parameters listed in Table 10.5*

Systematic uncertainties associated with the (quasi-model independent) S+P+P′ fit. We have performed a similar study of the systematic uncertainties as the ones from previous sections. We present in Table 10.7 the systematic uncertainties.

variation	$\Delta r_{P'}$	$\Delta\delta_{P'}$	Δr_S	$\Delta r_S^{(1)}$	$\Delta\delta_1$	$\Delta\delta_2$	$\Delta\delta_3$	$\Delta\delta_4$	$\Delta\delta_5$	$\Delta\delta_6$	$\Delta\delta_7$	$\Delta\delta_8$	$\Delta\delta_9$	$\Delta\delta_{10}$
(I)	-0.16	-0.04	-0.02	0.00	0.049	0.101	0.012	-0.051	0.109	0.143	0.107	0.136	0.111	0.102
(II)	-0.11	-0.09	-0,06	0,05	0,03	0,01	-0,01	-0,04	-0,07	0,13	-0,11	-0,02	0,01	-0,01
(III)	-0,02	-0,06	0,01	0,00	0,04	0,17	0,05	-0,07	0,27	0,56	0,13	0,16	0,05	-0,01
(IV)	0,21	0,13	0,00	0,01	-0,01	-0,15	0,00	-0,09	-0,26	-0,24	-0,18	-0,22	-0,13	-0,22
BKG														
B$\bar{B}$														
(V)	0,33	0,09	-0,06	0,05	0,23	0,06	0,00	0,07	-0,05	-0,38	-0,35	-0,36	-0,33	-0,28
c$\bar{c}$														
(VI)	0,18	0,25	-0,11	0,08	0,10	0,03	0,03	-0,01	0,00	-0,19	-0,25	-0,26	-0,23	-0,23
(VII)	-0,29	0,04	0,15	-0,17	-0,21	0,04	0,15	0,02	0,12	0,14	0,18	0,28	0,27	0,39
(VIII)	-0,13	-0,09	-0,17	0,16	0,01	-0,08	-0,04	-0,04	-0,04	-0,04	-0,04	-0,12	-0,16	-0,29
Fit program														
(IX)	-0,80	-0,27	-0,19	0,15	1,00	0,26	0,14	0,00	0,21	0,33	0,53	0,49	0,54	0,40
(X)	0.7	0.7	0.60	0.61	0.56	0.53	0.54	0.53	0.53	0.78	0.54	0.53	0.54	3.69
TOTAL														
σ_{syst}	1.19	0.81	0.68	0.68	1.20	0.63	0.58	0.54	0.66	1.12	0.91	0.93	0.93	3.76

Table 10.7: *Systematic uncertainties for all effects analysed expressed as* $\frac{x[0]-x[i]}{\sigma_{stat}}$*:(I) systematic uncertainty associated with tuning of signal control sample, (II) proportion of radiative events increased by* 30% *for signal control sample, (III) no electron tweaking for MCsignal events,(IV) no smearing for* $\theta_D, \phi_D, E_{miss}$ *for MCsignal, (V)* $B\bar{B}$ *bkg rate lowered by* 30%*,(VI)* 10% *of the effect of no correction on the generated semileptonic models (VII)* 50% *of the effect of no correction of the* q^2 *shape for charm bkg based on the WS control sample, (VIII)* 20% *of the effect of no correction of events associated with fragmentation pions, (IX) no smoothing effect, (X) effects from limited stats.*

Chapter 11

Decay rate measurement

We measure the production rate of $D^+ \to K^-\pi^+e^+\nu_e(\gamma)$ events relative to $D^+ \to K^-\pi^+\pi^+(\gamma)$ and we compare this value to the same ratio obtained with simulated events. In this way, several systematic uncertainties cancel. In this respect, it has been tried to use as much as possible the same criteria to select events in the two decay channels. For the normalisation, we have considered only the P-wave contribution in the semileptonic decay channel.

11.1 Principle of the measurement

To obtain the value for the $D^+ \to K^-\pi^+e^+\nu_e(\gamma)$ decay branching fraction we have measured the ratio, R_D, between this branching fraction and the one corresponding to the decay $D^+ \to K^-\pi^+\pi^+(\gamma)$ for which we can use the World average value [13]:

$$B(D^+ \to K^-\pi^+\pi^+)_{data} = (9.22 \pm 0.21)\%$$

$$R_D = \frac{B(D^+ \to K^-\pi^+e^+\nu_e)_{data}}{B(D^+ \to K^-\pi^+\pi^+)_{data}} = \frac{N(D^+ \to K^-\pi^+e^+\nu_e)_{data}}{N(D^+ \to K^-\pi^+\pi^+)_{data}} \times \frac{\mathcal{L}(K\pi\pi)_{data}}{\mathcal{L}(K\pi e\nu)_{data}} = \frac{N(D^+ \to K^-\pi^+e^+\nu_e)^{reco}_{data}/\epsilon(D^+ \to K^-\pi^+e^+\nu_e)_{data}}{N(D^+ \to K^-\pi^+\pi)^{reco}_{data}/\epsilon(D^+ \to K^-\pi^+\pi)_{data}} \times \frac{\mathcal{L}(K\pi\pi)_{data}}{\mathcal{L}(K\pi e\nu)_{data}} \tag{11.1}$$

which becomes:

$$R_D = \frac{N(D^+ \to K^-\pi^+e^+\nu_e)^{reco}_{data}}{N(D^+ \to K^-\pi^+\pi)^{reco}_{data}} \times \frac{\mathcal{L}(K\pi\pi)_{data}}{\mathcal{L}(K\pi e\nu)_{data}} \times \frac{\epsilon(D^+ \to K^-\pi^+e^+\nu_e)_{MC}}{\epsilon(D^+ \to K^-\pi^+e^+\nu_e)_{data}} \times \frac{\epsilon(D^+ \to K^-\pi^+\pi^+)_{data}}{\epsilon(D^+ \to K^-\pi^+\pi^+)_{MC}} \times \frac{\epsilon(D^+ \to K^-\pi^+\pi)_{MC}}{\epsilon(D^+ \to K^-\pi^+e^+\nu_e)_{MC}}$$

The first line, in this expression corresponds to the product of the ratio between the measured number of signal events in data for the semileptonic and hadronic channels with the ratio of the corresponding luminosities. This last component is:

$$\frac{\mathcal{L}(K\pi\pi)_{data}}{\mathcal{L}(K\pi e\nu)_{data}} = \frac{98.68 fb^{-1}}{100.47 fb^{-1}} \tag{11.2}$$

The second line corresponds to the efficiencies in data and in the simulation, for the two channels. In this double ratio most of the differences between data and simulation are expected to cancel.
As $\epsilon(D^+ \to K^-\pi^+e^+\nu_e)_{MC}$ is similar to $\epsilon(D^+ \to \bar{K}^{*0}e^+\nu_e)_{MC}$ one can safely substitute the former by the latter in the expression. In this case the last line can be rewritten as:

$$\frac{\epsilon(D^+ \to K^-\pi^+\pi^+)_{MC}}{\epsilon(D^+ \to \bar{K}^{*0}e^+\nu_e)_{MC}} = \frac{N(D^+ \to K^-\pi^+\pi^+)^{reco}_{MC}}{N(D^+ \to K^-\pi^+\pi^+)^{gen}_{MC}} \times \frac{N(D^+ \to \bar{K}^{*0}e^+\nu_e)^{gen}_{MC}}{N(D^+ \to \bar{K}^{*0}e^+\nu_e)^{reco}_{MC}} = \frac{N(D^+ \to K^-\pi^+\pi^+)^{reco}_{MC}}{N(D^+ \to \bar{K}^{*0}e^+\nu_e)^{reco}_{MC}} \times \frac{N(D^+ \to \bar{K}^{*0}e^+\nu_e)^{gen}_{MC}}{2N(c\bar{c})_{K\pi\pi}\mathcal{P}(c \to D^+)B(D^+ \to K^-\pi^+\pi^+)_{MC}} \tag{11.3}$$

where:

- $N(D^+ \to \bar{K}^{*0}e^+\nu_e)^{gen}_{MC}$ stands for the dedicated MC SLPole signal samples generated used to fit BaBar Run4 data $= 1.17 \times 10^7$
- $N(c\bar{c})_{K\pi\pi}$ stands for the number of $c\bar{c}$ pairs used for the hadronic MC studies $= 1.517 \times 10^8$
- $\mathcal{P}(c \to D^+)$ stands for the probability that a c quark hadronizes into a D^+ = 26%
- $B(D^+ \to K^-\pi^+\pi^+)_{MC}$ is the EvtGen branching fraction for the hadronic channel $= 0.0923$

11.2 Isolation of $D^+ \to K^-\pi^+\pi^+$ events

In the selection of $D^+ \to K^-\pi^+e^+\nu_e$ several criteria have been used which are applied also for the selection of $D^+ \to K^-\pi^+\pi^+$ decays, to minimize the effect of differences between the two channels.

- *Particle identification:* the same lists of kaon and pion particles are used for the two channels.
- *Global event's topology:* events have been analyzed in the same way, distributing reconstructed particles in two hemispheres defined from the thrust axis. We keep events if $|\cos\theta_{thrust}| < 0.7$ and if the missing energy in the opposite hemisphere is smaller than 3 GeV.
- *Fragmentation related variables:* for the two channels we require that there is at least one spectator particle in the signal candidate hemisphere. The mass of the opposite hemisphere has to exceed 0.5 $\mathrm{GeV/c^2}$, as requested by the skim.
- *Vertexing:* it is required that the 3-prong decay vertex of the D^+ is reconstructed (positive χ^2 probability). The decay distance of the candidate, relative to the interaction vertex is required also to be positive.
- *Fisher variables:* the same cuts on F_{bb} and F_{cc} are used for the two channels.

We have applied also to signal simulated events candidates the same weights which have been defined to obtain agreement between data and simulation for distributions of the D^+ energy and of all variables entering in the definition of Fisher discriminants.

11.2.1 Corrections applied to the decay model

The model used to simulate $D^+ \to K^-\pi^+\pi^+$ in EvtGen differs from present measurements. As a result, if the efficiency is not exactly constant over the Dalitz decay plane, the number of reconstructed events depends on the decay model.

We have corrected for this effect events simulated with EvtGen, using the results of CLEO-c [65] corresponding to their Model I2 and a Breit-Wigner mass distribution for the κ. The decay amplitude has an explicit Bose-symmetric form for pion permutation.

$$\mathcal{M}(s,t) = \mathcal{A}(s,t) + \mathcal{A}(t,s) + \mathcal{A}^{I=2}_{L=0}(u) + \mathcal{A}_{BK}. \tag{11.4}$$

In this equation, $s = m^2(K^-\pi^+_1)$, $t = m^2(K^-\pi^+_2)$, $u = m^2(\pi^+_1\pi^+_2) = m^2_D + m^2_K + 2m^2_\pi - s - t$. The third amplitude corresponds to an S-wave, $I = 2$, $\pi^+\pi^+$ component. The last term $\mathcal{A}_{BK}$ is a constant amplitude over the Dalitz plane,

Each $K^-\pi^+$ amplitude is defined using an isobar model, considering that the decay $D \to abc$ proceeds through intermediate two-body states : $D \to Rc$, $R \to ab$. In our example $a = K^-$ and $b, c = \pi^+$. The intermediate state (ab) comes from the decay of a resonance R of spin L. The mass dependence of the resonance amplitude is assumed to behave according to a Breit-Wigner distribution. As the D meson as spin 0, there is the same angular momentum, L, between the resonance and the particle c.

$$\mathcal{A}(s,t) = \sum_R a_R \exp i\phi_R \cdot \Omega_L(s,t) \cdot F^L_D(q) \cdot F^L_R(p^*) \cdot A_R(s). \tag{11.5}$$

Resonances with a maximum spin of 2 have been considered. a_R and ϕ_R are constant quantities over the Dalitz plane corresponding respectively to the modulus and phase of the contributing resonance amplitude. Their values are obtained from a fit to data and are given in Table 11.1, which is taken from [65].

$\Omega_L(s,t)$ represents the angular distribution and is obtained from the Zemach tensor formalism. If we denote by p^* the breakup momentum of R in its rest frame and by q the momentum of the third particle in that frame, then:

$$\Omega_0(s,t) = 1,\ \Omega_1(s,t) = -4\vec{p}^*\vec{q}, \tag{11.6}$$

$$\Omega_2(s,t) = \frac{16}{3}\left[3\left(\vec{p}^*\vec{q}\right)^2 - \left(p^*\right)^2 q^2\right], \tag{11.7}$$

$F^L_{D,R}$ are Blatt-Weisskopf factors to damp effects from the centrifugal force when the value of the relative momentum between the two objects becomes large as compared with the value reached when the resonance mass is equal to its pole value. $F^L_{D,R}$ depend on the variable $z = (r_{D,R}p)^2$. For the decay $D \to Rc$, $z = (r_D q)^2$ whereas for the decay $R \to ab$, $z = (r_R p^*)^2$. They use $r_D = 5\ GeV^{-1}$ and $r_R = 1.5\ GeV^{-1}$ for all resonances with a spin larger or equal to 1. For scalar states, Blatt-Weisskopf factors are taken to be equal to one whereas, for higher spins, the following expressions are used:

$$F^1_{D,R}(z) = \sqrt{\frac{1+z_V}{1+z}},\ F^2_{D,R}(z) = \sqrt{\frac{9+3z_V+z_V^2}{9+3z+z^2}}, \tag{11.8}$$

z_V corresponds to the value of the z variable when particles have their nominal mass.

The standard Breit-Wigner expression is used for the remaining part of the amplitude:

$$A_R(s) = \frac{1}{m^2_R - s - im_R\Gamma(s)} \tag{11.9}$$

where the mass dependent width has the usual form:

$$\Gamma(s) = \Gamma_R \frac{m_R}{\sqrt{s}} \left(\frac{p^*}{p_R^*}\right)^{2L+1} \left|F_R^L(p^*)\right|^2 . \tag{11.10}$$

Γ_R and p_R^* are respectively the total width of the resonance and the value of the breakup momentum when the resonance mass is equal to m_R. In the present fit done by CLEO most of values for the nominal mass and width of resonances are taken from [13] as given in Table 11.1.

The $I = 2,\ S = 0$ component is expressed as:

$$\mathcal{A}_{L=0}^{I=2}(u) = a_{\pi\pi} \exp i\phi_{\pi\pi} \mathcal{W}_S^{I=2} \tag{11.11}$$

where $a_{\pi\pi}$ and $\phi_{\pi\pi}$ are respectively an amplitude and a phase which are constant over the Dalitz plane. The remaining part of the amplitude is written:

$$\mathcal{W}_S^{I=2} = \frac{\eta_0(s) \exp 2i\phi_0(s) - 1}{2i}. \tag{11.12}$$

For the expression of $\phi_0(s)$ they use results from a fit to data on the $I = 2$ component of $\pi\pi$ scattering (see the publication from CLEO to get this parameterization). The inelasticity $\eta_0(s)$ is expected to be unity below the opening of the $\rho\rho$ threshold and is reduced, above. A simple model is used, and corresponding parameters are fitted on their data:

$$\begin{aligned} \eta_0(s) &= 1 && m \le m_{min} \\ &= 1 - \frac{\Delta\eta}{2}\left[1 - \cos\left(\pi \frac{m - m_{min}}{m_{max} - m_{min}}\right)\right] && m_{min} < m \le m_{max} \\ &= 1 - \Delta\eta && m > m_{max} \end{aligned} \tag{11.13}$$

Fitted values for these parameters using Model I2 are: $\Delta\eta = 1$, $m_{min} = (1265 \pm 8) MeV/c^2$, $m_{max} = (1529 \pm 31) MeV/c^2$ and $\Delta\eta$ is fixed to the value 1.

Finally a uniform phase space component is added:

$$\mathcal{A}_{BK} = a_{BK} \exp i\phi_{BK}. \tag{11.14}$$

As measurements are not sensitive to the overall phase of the decay amplitude, the phase of the $K^*(892)$ is taken to be zero. By convention, all amplitudes have been determined considering that the amplitude of the $K^*(892)$, in $\mathcal{A}(s,t)$ is equal to unity. Values of all parameters corresponding to Model I2 are collected in Table 11.1. It can be noted that a large fraction of the final state is described by the non-resonant or S-wave components.

With this model a toy simulation is created and the corresponding Dalitz distribution is compared with the one produced in EvtGen. They show some differences (Figure 11.1).

We also observe that the generated distribution in EvtGen is highly depopulated in a small region of the Dalitz plane (Figure 11.2-top). To obtain events distributed as in the CLEO-c measurement and to avoid applying large weights to events located in this region, the following region is excluded from the Dalitz plane (Figure 11.2-bottom):

$$m_{max}^2(K\pi) > 2.1\ \mathrm{GeV/c^2} \text{ and } \mathrm{m_{min}^2(K\pi)} \in [0.8,\ 1.0]\ \mathrm{GeV/c^2}. \tag{11.15}$$

The fraction of events contained in this excluded region amounts to: 0.01625 in the CLEO-like simulation and 0.01465 ± 0.00005 in EvtGen.

After having normalized the two distributions to the same number of entries a weight is defined and applied on generated EvtGen events such that they become similar to the CLEO-c measurement. This weight is obtained in 2D $m^2(K\pi)$ bins of 0.025×0.025 extension in GeV^2/c^4 unit (Figure 11.3). In this ratio the distribution from EvtGen for decays without radiated gamma(s) is used.

component	amplitude	phase (°)	mass MeV/c^2	width (MeV/c^2)	Fraction (%)
$\overline{K^{*0}}(892)\pi^+$	1	0	895.4 ± 0.2	44.5 ± 0.7	10.30 ± 0.48
$\overline{K^{*0}}(1680)\pi^+$	4.45 ± 0.23	43.3 ± 3.6	1717	322	0.476 ± 0.048
$\overline{K_2^{*0}}(1430)\pi^+$	0.866 ± 0.030	-17.4 ± 3.5	1432.4	109	0.248 ± 0.022
$\overline{K_0^{*0}}(1430)\pi^+$	3.97 ± 0.15	45.1 ± 0.9	1461.1 ± 1.0	177.9 ± 3.1	15.06 ± 1.30
$\overline{K_0^{*0}}(800)\pi^+)$	5.69 ± 0.17	-149.9 ± 1.2	888.0 ± 1.9	550.4 ± 11.8	17.0 ± 1.0
BK	17.1 ± 0.4	1.9 ± 1.7			38.0 ± 1.9
$I = 2,\ S = 0$	30.3 ± 2.7	86.3 ± 3.3			13.4 ± 2.3

Table 11.1: *Values of the parameters corresponding to the fit of Model I2 obtained by CLEO [65]. Values quoted without an uncertainty are fixed in this fit.*

11.2.2 Measured signals

The number of signal candidates is measured from the $K^-\pi^+\pi^+$ mass distribution and subtracting events situated in sidebands of the signal region. The signal region corresponds to the mass interval $[1.849,\ 1.889]$ whereas sidebands are defined in the intervals $[1.798,\ 1.838]$ and $[1.900,\ 1.940]$. The combinatorial background mass distribution does not show any structure in addition to the signal in the considered total mass range. The $K^-\pi^+\pi^+$ mass distributions measured in simulated continuum charm events and in data are given in Figure 11.4.

Using a Gaussian distribution for the signal and a linear variation for the background, the value of the reconstructed D^+ mass and its resolution are measured in data and in simulation (see Table 11.2).

Sample	Mass (MeV/c^2)	Standard deviation (MeV/c^2)
Run2 data	1869.15 ± 0.07	6.26 ± 0.05
Run2 MC	1869.59 ± 0.01	6.17 ± 0.04
Run4 data	1868.98 ± 0.04	6.29 ± 0.03
Run4 MC	1869.50 ± 0.03	5.98 ± 0.03

Table 11.2: *Central mass value and standard deviation for D^+ reconstructed mass distributions in different samples.*

The reconstruction efficiency over the Dalitz plot is given in Figure 11.5-top. Apart for statistical fluctuations, these distributions indicate that the analysis has a very uniform efficiency over the Dalitz plane.

Measured numbers of candidates in data and simulation and for different values of the cut on the discriminant F_{cc} variable are given in Table 11.3.

Sample	$F_{cc} > 0.4$		$F_{cc} > 0.5$		$F_{cc} > 0.7$	
	MC	Data	MC	Data	MC	Data
Run4	72205.5 ± 292.3	55360.9 ± 260.0	68467.6 ± 282.5	52595.2 ± 251.2	59258.6 ± 258.9	45626.5 ± 229.9

Table 11.3: *Number of $D^+ \to K^-\pi^+\pi^+$ signal events measured in data and in simulation for different values of the cut on F_{cc}. Simulated events have been weighted to correct for measured differences between data and simulation.*

11.2.3 Efficiency corrections

Possible differences between data and simulation on efficiencies of the cuts used only to isolate the $D^+ \to K^-\pi^+\pi^+$ decay channel have been evaluated.

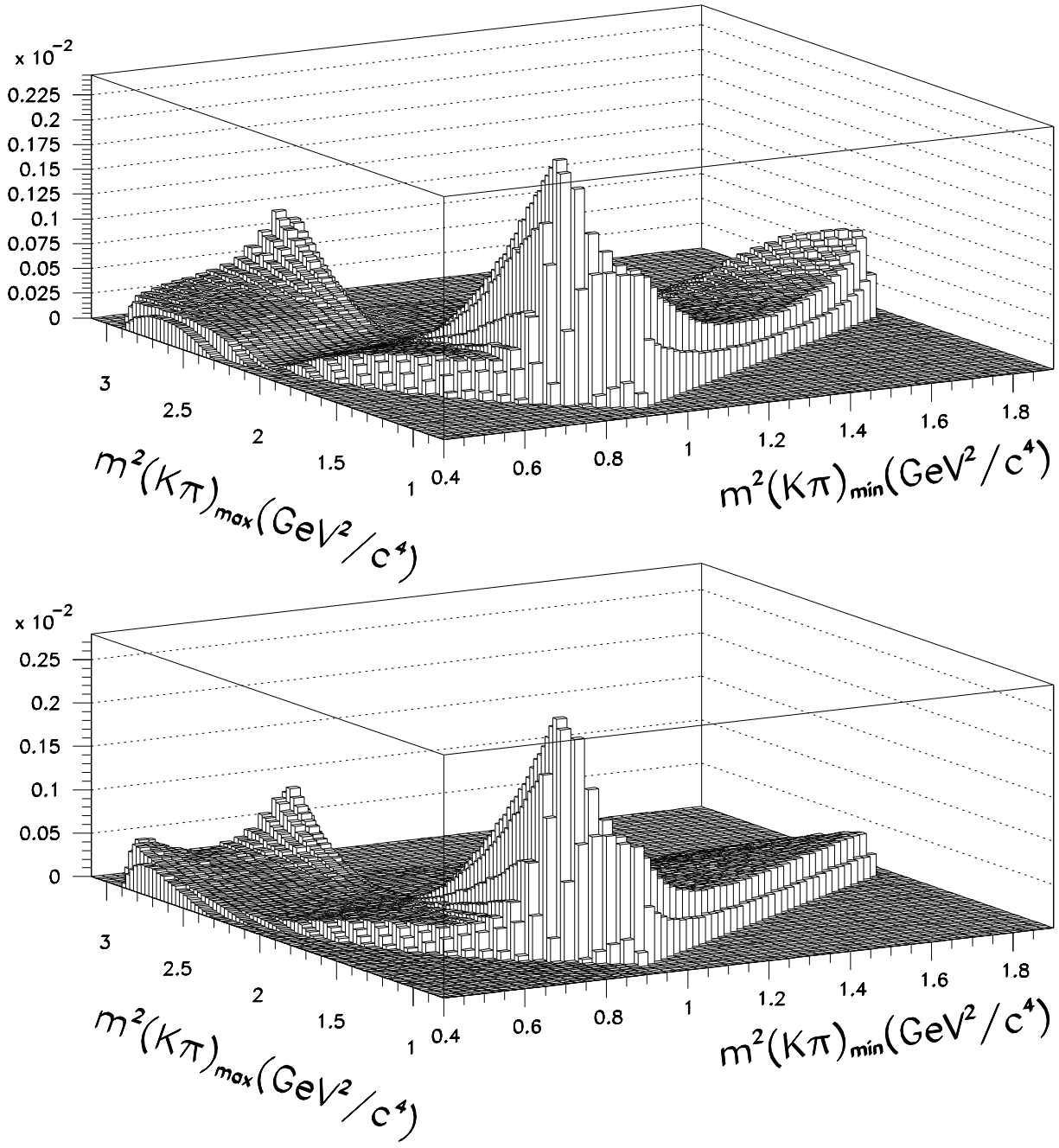

Figure 11.1: *Normalized Dalitz distributions for $D^+ \to K^-\pi^+\pi^+$ versus the minimum and the maximum values of the two $K^-\pi^+$ mass squared. The top plot distribution is obtained from Model I2 fitted on CLEO-c data. The bottom plot is obtained from EvtGen.*

- *Signal mass interval* The mass interval used to measure the signal is $40\ MeV/c^2$ and is centered on $1869\ MeV/c^2$. From the measured mass resolution (Table 11.2), close to $6\ MeV/c^2$, this interval corresponds to $\cong \pm 3\sigma$. Be-

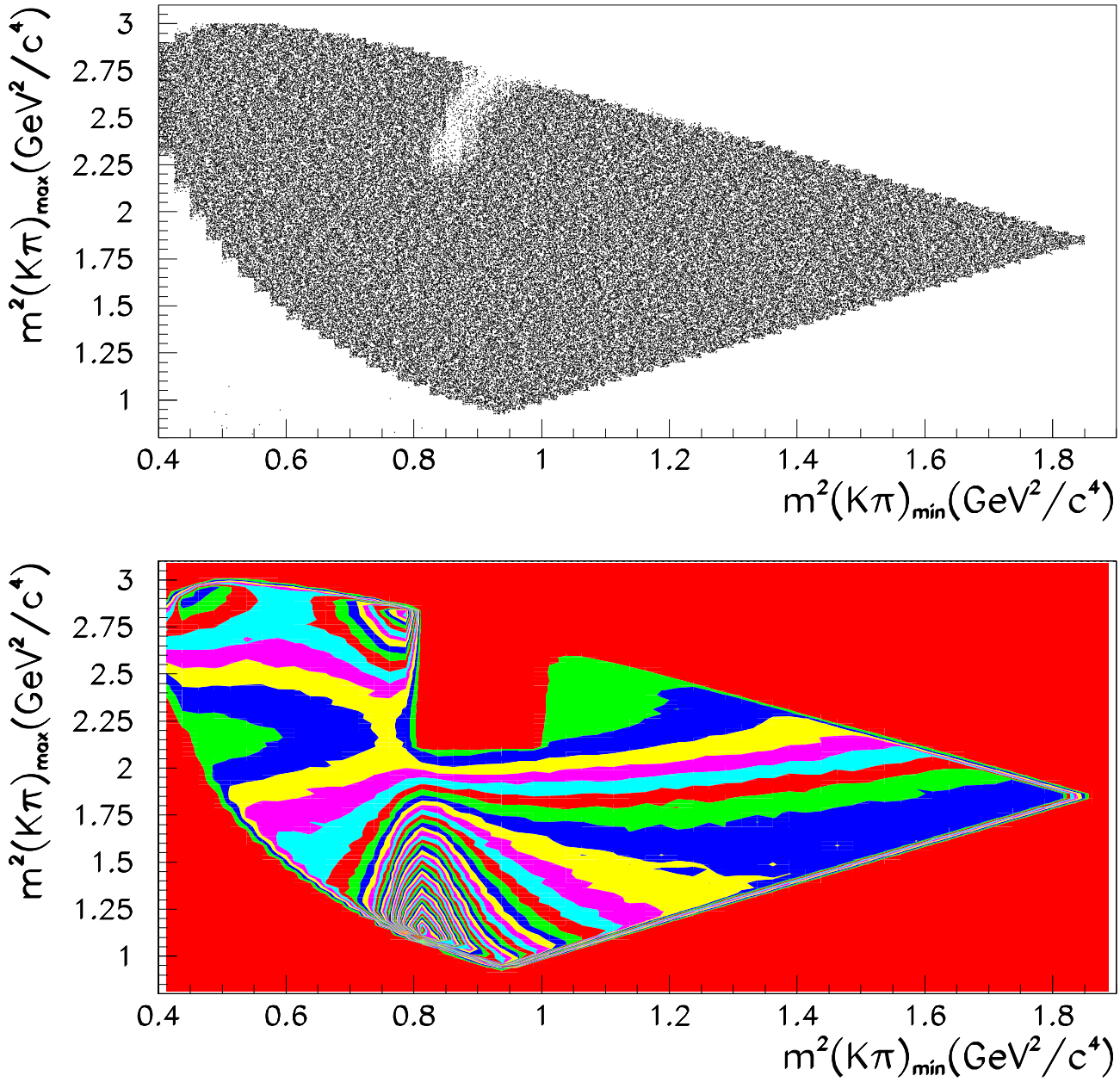

Figure 11.2: *Top: Dalitz plot distribution for $D^+ \to K^-\pi^+\pi^+$ obtained from EvtGen which displays a depopulated region. This distribution is obtained requiring that there are more than 200 events in each 0.025×0.025 $(GeV^2/c^4)^2$ bin. In total there are about 7M events. Bottom: the same Dalitz distribution after having excluded a domain around the depopulated region. There are 50 equidistant levels indicated.*

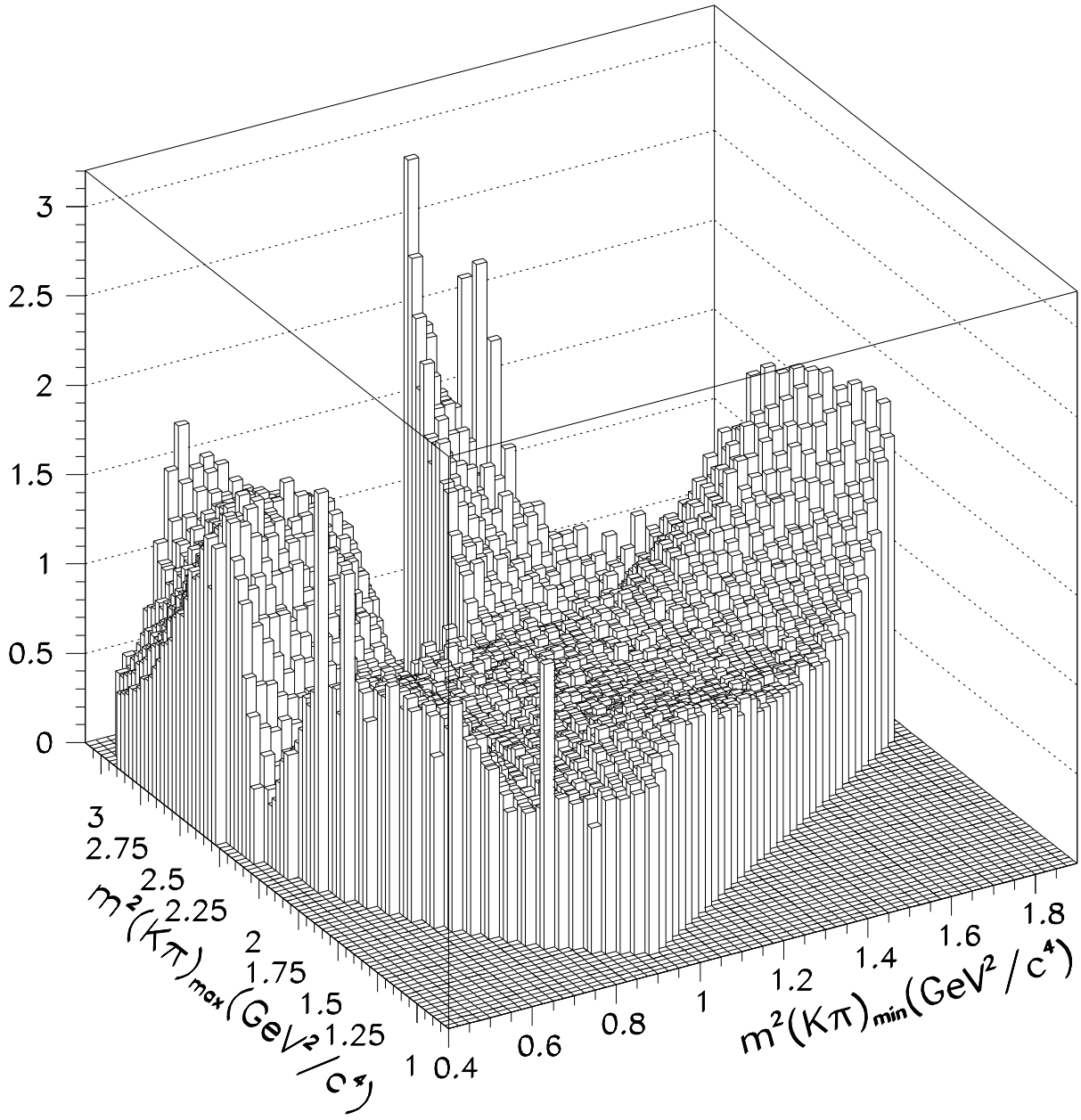

Figure 11.3: *Ratio between normalized distributions obtained with CLEO-c and EvtGen events.*

cause of photon radiation or non-Gaussian uncertainties, more events -than the few per mille expected from $\pm 3\sigma$- are expected to be in the tails of the mass distribution. In simulated events we measure that $(5.55 \pm 0.06)\%$ of signal events are outside the selected mass region.

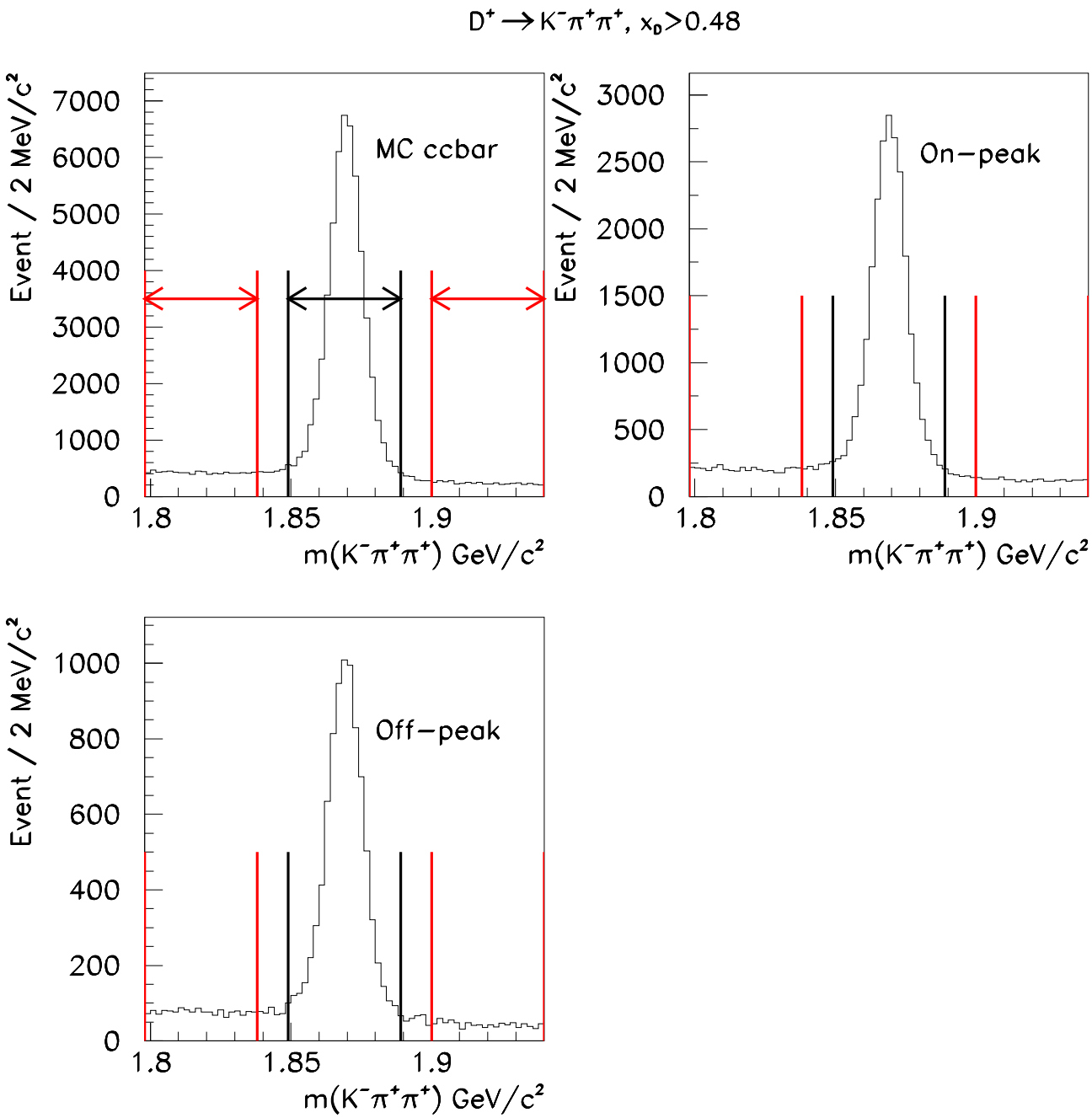

Figure 11.4: *$K^-\pi^+\pi^+$ mass distributions for $e^+e^- \to c\bar{c}$ (top-left), data on-peak (top-right) and data off-peak (lower-left). Events are selected with criteria similar as those applied on the D^+ semileptonic channel. The fraction of the beam momentum taken by the D^+ is requested to be higher than 0.48 to remove D^+ cascading from B mesons. Vertical lines indicate the mass intervals selected for the signal and sideband regions.*

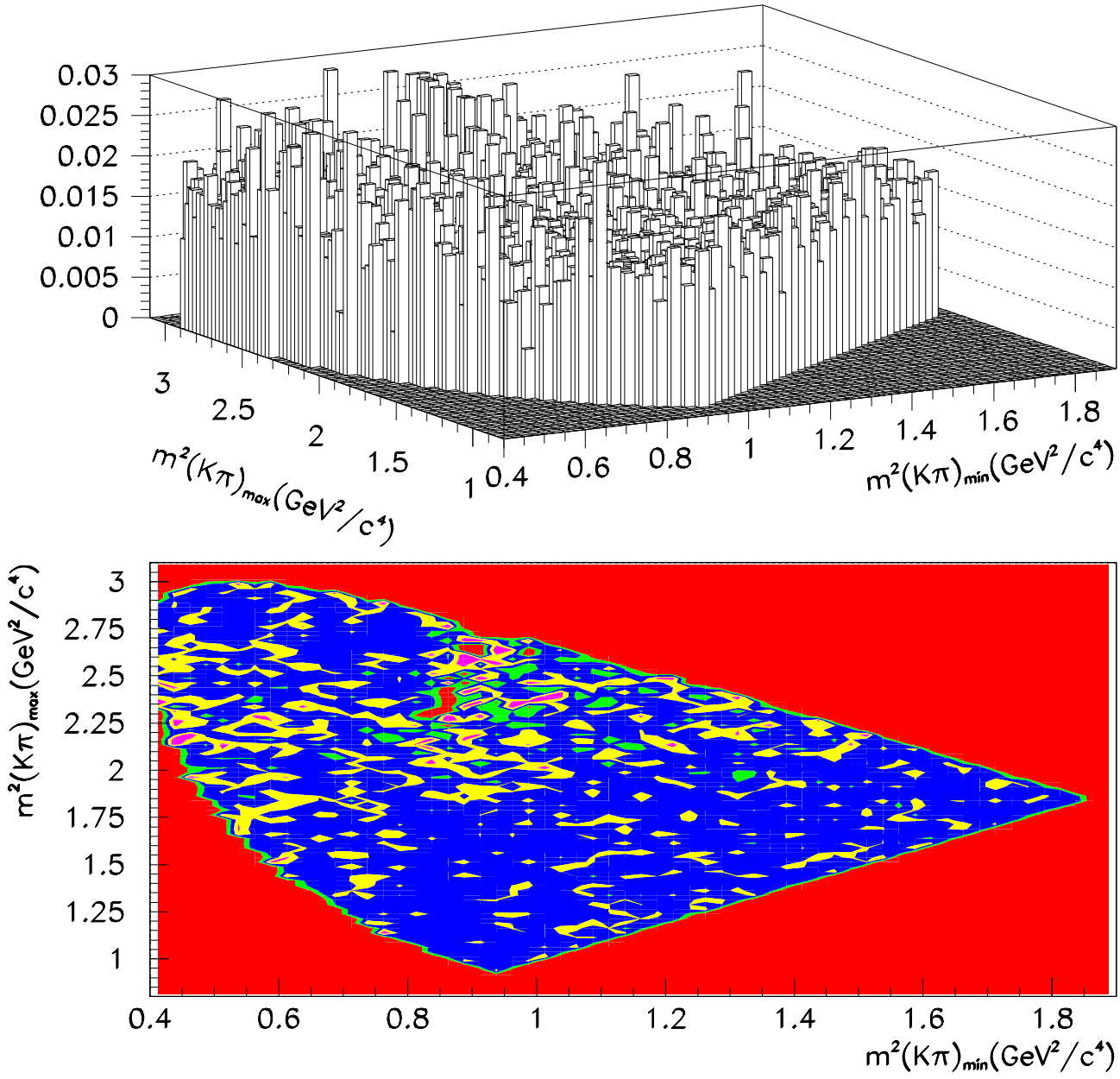

Figure 11.5: *Number of reconstructed signal events divided by the number of generated ones in each* 0.025×0.025 $(GeV^2/c^4)^2$ *bin of the Dalitz distribution for the decay* $D^+ \to K^-\pi^+\pi^+$. *Cuts used to isolate the* D^+ *semileptonic channel have been applied.*

- *Dalitz decay model* After having transformed the generated Evtgen distribution into the CLEO-like measurement we measure that the number of reconstructed D^+ signal varies by 1.0017 ± 0.0038 in Run2. This small variation comes from the uniform acceptance of the analysis which gives a small variation of the measured total decay rate versus the decay model.

- *pion track* As compared with the $K^-\pi^+e^+\nu_e$ final state, there is a π^+ in place of the e^+ in the reference channel. As there is no requirement on the PID for this pion we have considered that possible differences between data and simulation on tracking efficiency cancel when considereing the simultaneous reconstruction of the pion and the electron. What remains is the difference between data and simulation for the electron PID.

11.3 Isolation of $D^+ \to K^-\pi^+e^+\nu_e$ events

The event selection criteria are described in Section 3. Among them, are listed below those which are not common with the selection of the $D^+ \to K^-\pi^+\pi^+$ reference channel.

- the presence of a candidate electron;

- the condition that the mass constrained fit has converged and that the corresponding χ^2 probability is larger than 0.01.

11.3.1 Measured signals

Fitted numbers of signal events versus the value of the cut on the discriminant variable F_{cc} are given in Table 11.4.

Sample	$F_{cc} > 0.4$		$F_{cc} > 0.5$		$F_{cc} > 0.7$	
	MC	Data	MC	Data	MC	Data
Run4	381707	81322 ± 383	330969	70549 ± 363	237104	50989 ± 303

Table 11.4: *Number of $D^+ \to K^-\pi^+e^+\nu_e$ signal events measured in data and in simulation for different values of the cut on F_{cc}. Simulated events have been weighted to correct for measured differences between data and simulation.*

11.3.2 Efficiency corrections

Differences between data and simulation on the applied criteria which are different from those used to measure the $D^+ \to K^-\pi^+\pi^+$ signal are considered.

- *Electron selection:* We have evaluated the effects from electron identification by applying or not the tweaking procedure which was defined to obtain agreement between data and simulation for the electron signature. We use as remaining systematic 30% of this difference.

- *Mass constrained fit:* Differences between data and simulation on the fraction of events selected by the cut at 0.01 on the mass constrained fit probability have been measured in the $D^0 \to K^-e^+\nu_e$ analysis [41]. We use the same value for the actual decay channel: $\frac{\epsilon(D^0 \to K^-e^+\nu_e)_{MC}}{\epsilon(D^0 \to K^-e^+\nu_e)_{data}} = 1.0062 \pm 0.0006$.

11.4 Decay rate measurement

The measured relative decay rate is then:

$$R_D = \frac{B(D^+ \to K^-\pi^+e^+\nu_e)_{data}}{B(D^+ \to K^-\pi^+\pi^+)_{data}} = 0.4380 \pm 0.0036 \pm 0.0031 \pm 0.0029 \tag{11.16}$$

where the uncertainties are statistical, systematic and the last one corresponds to the variation of R_D with the different cuts on F_{cc}. In the following, we include this last uncertainty as a systematic.

Using the world average value for the branching fraction $D^+ \to K^-\pi^+\pi^+$, we find that:

$$B(D^+ \to K^-\pi^+e^+\nu_e) = (4.03 \pm 0.03 \pm 0.04 \pm 0.09) \times 10^{-2} \tag{11.17}$$

where the last quoted uncertainty comes from the accuracy on $B(D^+ \to K^-\pi^+\pi^+)$.

We have determined the fraction of S-wave from the value of r_S. We find that the S-wave fraction is $(5.68 \pm 0.21 \pm 0.24)\%$. Figure 11.6 presents distributions of the S and P-waves versus the $K\pi$ mass and q^2 that correspond to these results.

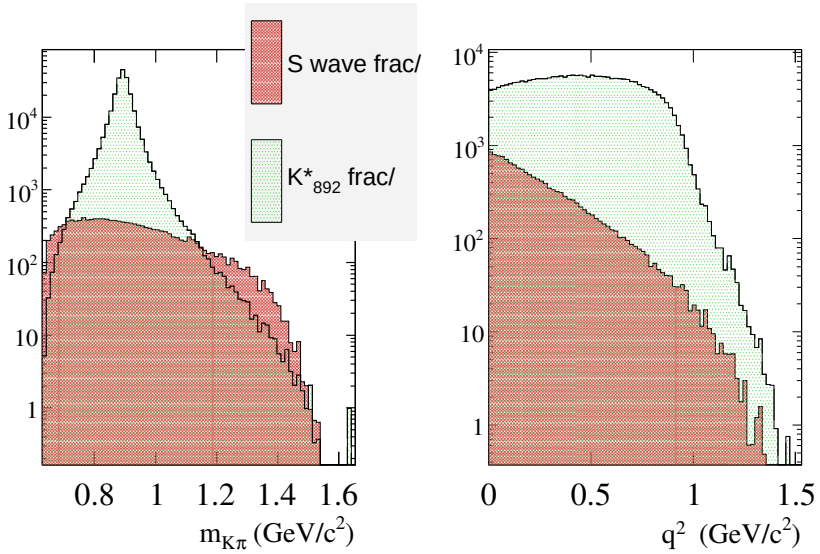

Figure 11.6: *Distributions of S and P-waves for this analysis which correspond to the results of the fit to BABAR data.*

The branching fraction for $D^+ \to \bar{K^{*0}}e^+\nu_e$ is defined by:

$$B(D^+ \to \bar{K^{*0}}e^+\nu_e) \times B(\bar{K^{*0}} \to K^-\pi^+) = B(D^+ \to K^-\pi^+e^+\nu_e) \times (1 - fraction_{Swave}) \tag{11.18}$$

therefore ,

$$B(D^+ \to \bar{K^{*0}}e^+\nu_e) \times B(\bar{K^{*0}} \to K^-\pi^+) = (3.81 \pm 0.03(stat) \pm 0.04(syst) \pm 0.09(ext.)) \times 10^{-2} \tag{11.19}$$

The last uncertainty corresponds to inputs external to our analysis.

11.5 Determination of the hadronic form factor A_1 at $q^2 = 0$

To have the corresponding value of $A_1(0)$ we integrate equation 1.43, restricted to the $\bar{K^{*0}}$ contribution, over $m_{K\pi}, q^2, cos\theta_e, cos\theta_\pi, \chi$. Integrating over the three angles, we obtain:

$$d\Gamma = \frac{G_F^2 \left|V_{cs}\right|^2}{(4\pi)^6 m_D^3} X\beta \frac{8\pi}{3} \left[\frac{1}{3}\left\{|\mathcal{F}_{11}|^2 + |\mathcal{F}_{21}|^2 + |\mathcal{F}_{31}|^2\right\}\right] dq^2 dm^2 \tag{11.20}$$

$$\tag{11.21}$$

The integration over the remaining variables gives:

$$\Gamma = \frac{\hbar B(D^+ \to K^-\pi^+e^+\nu_e)}{\tau_{D^+}} = \frac{G_F^2 \left|V_{cs}\right|^2}{(4\pi)^5 m_D^3} \frac{2}{3} |A_1(0)|^2 \mathcal{I} \tag{11.22}$$

with

$$\mathcal{I} = \frac{1}{|A_1(0)|^2} \int_0^{q^2 max} \int_{m_{K\pi}min}^{m_{K\pi}max} X\beta \left[\frac{1}{3}\left\{|\mathcal{F}_{11}|^2 + |\mathcal{F}_{21}|^2 + |\mathcal{F}_{31}|^2\right\}\right] dq^2 dm^2 \tag{11.23}$$

This value corresponds to:

$$A_1(0) = 0.6270 \pm 0.0027 \pm 0.0032 \pm 0.0076 \tag{11.24}$$

For this last evaluation we have used the values $\tau_{D^+} = (10.401 \pm 0.007) \times 10^{-13} s$ for the D^+ lifetime [14] and $V_{cs} = 0.9729 \pm 0.0003$. Corresponding uncertainties have been included in the last quoted error in Equation (11.24).

Chapter 12

Comparison with other experiments and with theoretical calculations

12.1 Comparison with other experiments

We have obtained precise results for several parameters that define the decay rate of the $D^+ \to K^-\pi^+e^+\nu_e$ using $347.5fb^{-1}$ of BaBar dataset. We compare results with those of previous experiments having the most precise measurements.

12.1.1 S-wave

We consider the results from FOCUS (Table 12.1) and observe that their value for the rate of the S-wave is compatible with ours and that we are around 4 times more accurate.
The same experiment gives a limit on the contribution from the $K_0^*(1430)$ at the 90% level while we find clearly an effect of this resonance in our fit to the phase variation in several mass intervals. We can quantify the non resonant and the $K_0^*(1430)$ contribution using the S-wave parameterization and results of chapter 7.1. In this model they amount to :
$fraction(NR) = (3.11 \pm 0.11 \pm 0.13)\%$ and $fraction(K_0^*(1430)) = (0.93 \pm 0.03 \pm 0.04)\%$, for a total S-wave fraction of $(5.68 \pm 0.21 \pm 0.24)\%$. The remaining contribution (1.64%) is attributed to a positive interference between these two components.

We have measured the scattering length term of the non resonant component of the S-wave using the LASS parameterization assuming several parameterizations for the S wave amplitude. We present our results and the one from LASS in Table 12.2.
We find the best agreement with LASS for the fit where we do not assume the amplitude of the S-wave to be similar with that in elastic scattering. The agreement is improved when including a P'.

Experience	S-wave fraction (%)
FOCUS	$5.30 \pm 0.74^{+0.99}_{-0.96}$
this analysis	$5.68 \pm 0.21 \pm 0.24$

Table 12.1: *Comparison of the fraction of the S-wave component in the semileptonic decay $D^+ \to K^-\pi^+l^+\nu_l$ measured for this analysis and most recent result.[26].*

Experiment	$a_S\ (GeV/c)^{-1}$
this analysis $(S+P\|A_S \propto \sin\delta)$	$2.76 \pm 0.10 \pm 0.11$
this analysis $(S+P\|A_S = polynome)$	$1.78 \pm 0.15 \pm 0.18$
this analysis $(S+P+P'\|A_S \propto \sin\delta)$	$2.24 \pm 0.11 \pm 0.12$
LASS	1.95 ± 0.09

Table 12.2: *Scattering length parameter results for our analysis and LASS. The first result is the outcome of the fit to a S+P signal scenario where the S-wave amplitude is proportional to* $\frac{m}{p*}|\sin\delta_S|$*. The second result is the outcome of the same signal scenario but with the S-wave amplitude parameterized with a polynomial expansion. The third result is a S+P+P' signal scenario where the S-wave amplitude is proportional to* $\frac{m}{p*}|\sin\delta_S|$*.*

We present the first direct measurements, in charm semileptonic decays, of the S-wave I=1/2 phase variation with the $K\pi$ mass without assuming a parameterization for this variation. Our results are presented in Figure 12.1 where they are compared with those from LASS. We provide complementary data, outside the reange covered by the LASS collaboration. We find agreement with LASS until 1 GeV for both of our fits and continue to have agreement at higher masses for the fit including a P' contribution.

12.1.2 The $K^{*0}(892)$ parameters

We consider the PDG value [14] as well as measurements that enter in this average but keeping only those which use the same definition for the Breit-Wigner and fit the value of the barrier factor. The comparison with our measurements of the mass and width of the resonance is given in Figure 12.2.

We have shifted the central value of the resonance mass by +0.5MeV/c^2 and increased its error by a similar value based on studies comparing reconstructed and simulated values of the $D^+ \to K^+\pi^+\pi^+$ signal in data and Monte Carlo where it has been found that the reconstructed mass of the D in data is shifted by around $-0.5MeV/c^2$ as compared to the value in the PDG. This new value and error for the mass of the K^{*0} are to be taken as reference for this analysis.
We are therefore compatible with the stated experiments and have a lower value than the PDG.
Our result for the width of the resonance has the best precision and is significantly lower than the PDG value and we are compatible with FOCUS. It must be mentioned that recent results for τ decays into $K_s\pi^-\nu_\tau$ have found a value for the width of the K^{*-} equal to $46.2 \pm 1.36\ MeV/c^2$ as compared to the $50.8 \pm 0.9\ MeV/c^2$ proposed by the PDG.
This indicates that the value for the $K^{*0}(892)$ width should be smaller than the PDG results.
We compare the value measured for the barrier factor with previous determinations from FOCUS and LASS in Table 12.3.

Experiment	$r_{BW}\ (GeV/c)^{-1}$
this analysis	$4.20 \pm 0.23 \pm 0.39$
FOCUS	$3.96 \pm 0.54^{+1.31}_{-0.90}$
LASS	3.4 ± 0.7

Table 12.3: *Barrier factor results for our analysis and other experiments.*

These results are in agreement and this analysis provides the most accurate measurement.

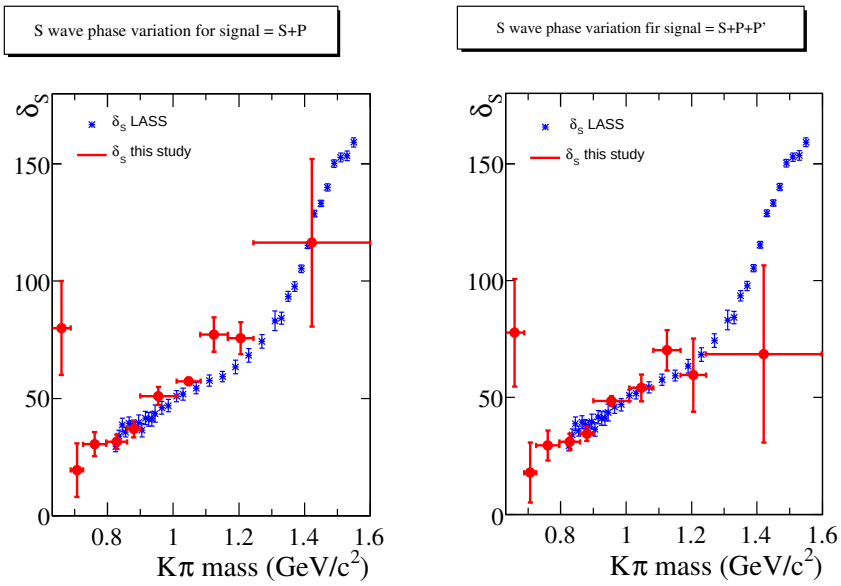

Figure 12.1: *Measured S-wave phase variation for our analysis and comparison with LASS. Our results on the left plot correspond to the S+P wave fit. The plot on the right corresponds to the S+P+P′ wave fit. In both of these fits the S-wave amplitude is parameterized with a polynomial expansion before the* $K^*(1430)$ *pole.*

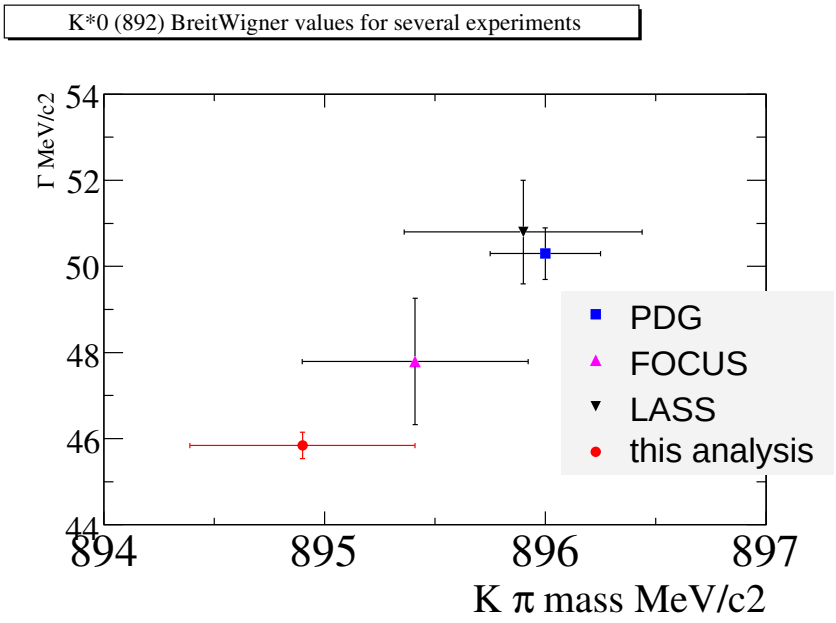

Figure 12.2: *Comparison of results for this analysis versus other results previously stated for the mass and width of the* $K^{*0}(892)$ *resonance*

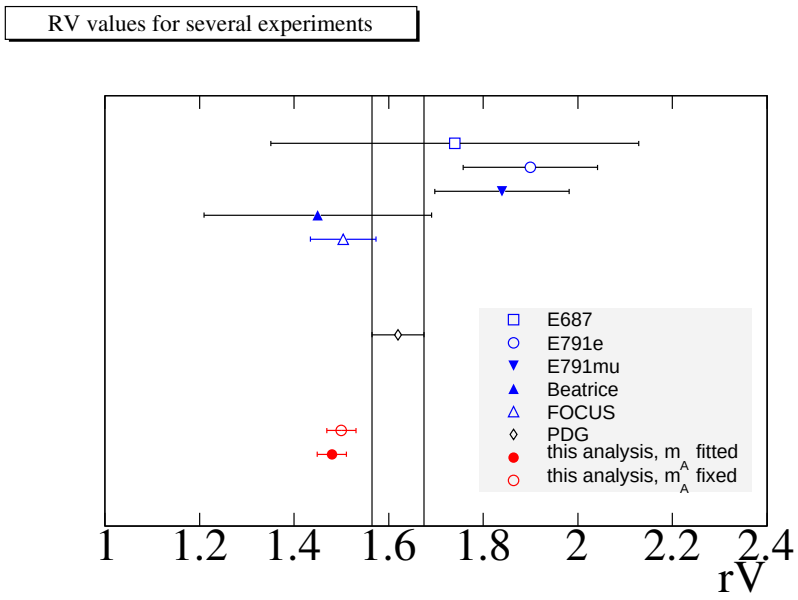

Figure 12.3: *Comparison of results for this analysis versus other results previously stated for the r_V form factor normalization factor*

12.1.3 The $D^+ \to \bar{K^*}^0 e^+ \nu_e$ hadronic form factors

We compare now our results for the form factor parameters to those of the main experiments included in the HFAG average and with the PDG/HFAG value.

Our results are quite compatible with most of the experiments (specially those more precise).
There is a however a clear difference with the PDG for r_V but this is due to the E791 results. We have the most precise results for this parameter.

We have a perfect agreement with the PDG/HFAG for r_2 and are twice more precise than this average.

All the experiments that enter in this comparison have used a value for the axial-vector pole mass equal to $2.5 GeV/c^2$. This analysis has provided for the first time in this channel a value for the axial-vector pole mass, using the simple pole model for the form factors and found it to be : $m_A = 2.68^{+0.11}_{-0.10}\ ^{+0.18}_{-0.16}\ GeV/c^2$ which is 1σ higher than the reference value for this mass.

For a direct comparison with FOCUS results, we have performed a fit fixing $m_A = 2.5\ GeV/c^2$, the same value FOCUS used.
The comparison with FOCUS follows in Table 12.4. This analysis is over 2.5 times more precise than FOCUS for r_V and over 5 times more precise for r_2.

12.1.4 P' wave

We have included a P' contribution in our fits and found out that this component is non-negligible, since it improves the signal rate at high mass (Figure 10.1). The S-wave phase variation is correlated with the P', and we find a different behaviour for it at high mass from the fit without a P' contribution. The S-wave rate is however

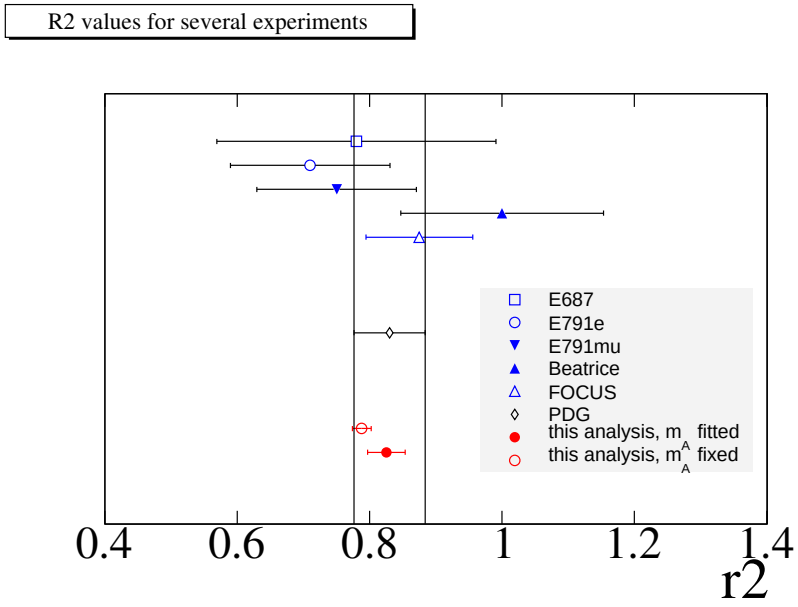

Figure 12.4: *Comparison of results for this analysis versus other results previously stated for the r_2 form factor normalization factor*

-	r_V	r_2
this analysis	$1.500 \pm 0.014 \pm 0.023$	$0.788 \pm 0.010 \pm 0.010$
FOCUS	$1.504 \pm 0.057 \pm 0.039$	$0.875 \pm 0.049 \pm 0.064$

Table 12.4: *Comparison of fitted r_V and r_2 with FOCUS for case where pole masses are fixed. We take as systematic uncertainty for our measurement the same relative proportion to the statistical uncertainty as when fitting m_A*

stable in the presence of the P'.
We present in Figure 12.5 the variation of the total P wave phase for the results of chapters 7 and 10.1, and compare them to the P wave phase variation found by the LASS collaboration.

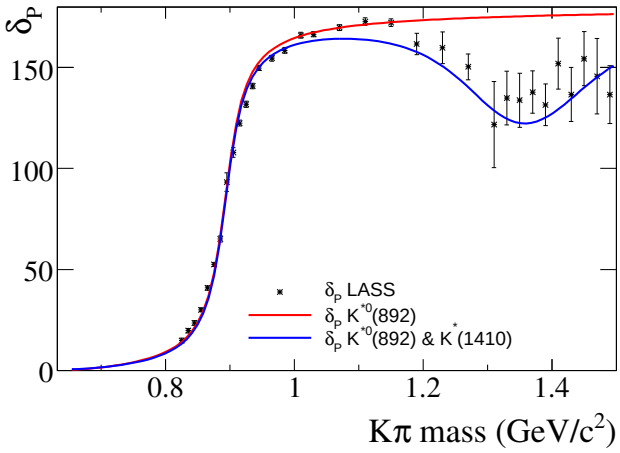

Figure 12.5: *Comparison between total P wave phase variation with $K\pi$ mass using central values results of chapters 7 and 10.2 vs the LASS results [15]*

We find that implementing the P' resonance we reproduce the high energy bump in the P wave phase found by LASS. Moreover comparing directly, versus the $K\pi$ mass (Figure 12.6), the measured difference between the phase of the two waves shows that results from the two experiments agree, as both are sensitive to the difference between the S and the P waves phases.

12.1.5 Branching Fractions

We compare our results, in Table 12.5, with the quoted values in the PDG [14] for the different decay modes.

Decay mode	This analysis	*PDG*	FOCUS
$D^+ \to K^{*0}e^+\nu_e, K^{*0} \to K^-\pi^+$	$(3.81 \pm 0.03 \pm 0.04 \pm 0.09)\%$	$(3.66 \pm 0.21)\%$	-
$D^+ \to K^-\pi^+e^+\nu_e$, S-wave	$(0.229 \pm 0.009 \pm 0.010 \pm 0.005)\%$	$< 0.7\%$ CL=90%	$(0.21 \pm 0.05)\%$

Table 12.5: *Branching fractions comparisons with other experimental results. The FOCUS result refers to the decay $D^+ \to K^-\pi^+\mu^+\nu_\mu$*

12.2 Comparison with theoretical calculations

12.2.1 Comparison between form factors results and Lattice QCD

We compare our results for the form factor dependence to LQCD calculations and to phenomenological models. In Figure 12.7 the results for r_2 and r_V are compared with those from Lattice [67], [68]. Both these lattice results are obtained in the quenched approximation, where sea quark effects are not taken into account.

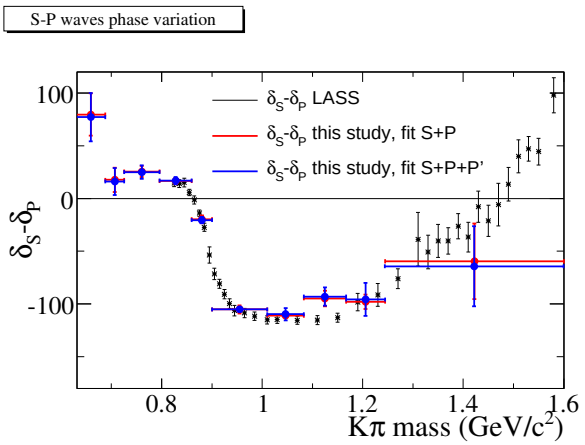

Figure 12.6: *Phase difference variation between the S and P waves in several bins of the $K\pi$ mass (red and blue points) as well as values determined by LASS [19]. The red points indicate the fit with the P wave made up of $K^{*0}(892)$ whereas for the blue points, the $K^*(1410)$ is included.*

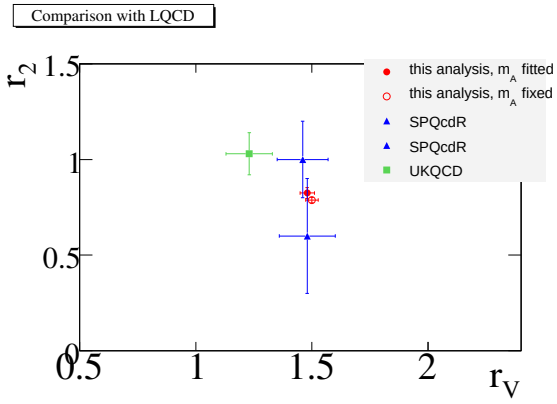

Figure 12.7: *Present results for r_2 and r_V compared with several LQCD calculations. These calculations are performed in the quenched approximation.The two SPQcdR results correspond to different values of the coupling.*

12.2.2 Comparison of form factors results with phenomenological models

We compare our results to predictions from the Fajfer-Kamenik ansatz [12]. In their model they predict $r_V = 1.60$, $r_2 = 0.5$. These predictions are not in agreement with our results, specially for r_2, which is much lower than the experimental result. This model gives as well $m_A = 2.44\ GeV/c^2$ and $A_1(0) = 0.62$. The pole mass is in marginal agreeement with our results while $A_1(0)$ is in good agreeement with our results.

Chapter 13

Conclusions

We have presented in this Thesis a detailed study of the decay $D^+ \to K^-\pi^+e^+\nu_e$ using 347.5 fb^{-1} of data registered with the *BABAR* detector. We have selected semileptonic continuum $c\bar{c}$ events and have used an untagged technique which allows to have a reasonable signal reconstruction efficiency, of around 3%. The background rejection strategy based on the use of enriched semileptonic samples and on Fisher discriminant variables gives a S/B ratio of 2.3, with over 240000 signal events. In the $K^{*0}(892)$ region, the ratio S/B is around 4.6.
We have done extensive MC correction and tuning studies that provide a more performant description of the true data behaviour.
The hadronic final state has been analyzed as being either a sum of S and P-waves or a sum of S, P and P'-waves. We have presented in both cases the variation of the S-wave phase and amplitude with the hadronic mass. This analysis provides for the first time a direct measurement of the $K\pi$ I=1/2 S-wave phase and amplitude. These measurements are done in several $K\pi$ mass intervals independently of an assumed model for the phase variation. These measurements agree with those from LASS and complement their results at lower values of the Kpi mass.
This demonstrate that measurements of the S-wave phase variation obtained in Dalitz distributions of D meson decays do not provide reliable values.
In the hypothesis of S+P-wave, we have measured the parameters that define the P-wave ($K^{*0}(892)$) resonance, its mass,width and barrier factor. The mass and barrier factor term are compatible with the world average and we provide the most precise value for the barrier factor. We find respectively $M(K^{*0}(892)) = 895.0\pm0.1\pm0.5\ MeV/c^2$ and $r_{BW} = 4.20 \pm 0.23 \pm 0.39\ (GeV/c)^{-1}$. For the $K^{*0}(892)$ width, we find $\Gamma(K^{*0}(892)) = 45.79 \pm 0.23 \pm 0.21$ MeV/c^2, which is smaller than the world average but is in agreement with most recent measurements, indicating that the true value of this width should be smaller than what is considered by the PDG.
We have performed the most precise measurement of the P-wave form factors $A_2(q^2)$,$V(q^2)$ relative to $A_1(q^2)$ at $q^2 = 0$ using the Single Pole model and have provided a first measurement of the axial-pole mass for this decay channel. We have measured as well $A_1(0)$. We obtain:
$r_V = 1.480 \pm 0.016 \pm 0.026$, $r_2 = 0.824 \pm 0.020 \pm 0.020$, $m_A = 2.68^{+0.11}_{-0.10} \pm 0.16\ GeV/c^2$ and $A_1(0) = 0.6270 \pm 0.0027 \pm 0.0032 \pm 0.0076$, where uncertainties are statistical and systematic respectively.
We determine $B(D^+ \to K^-\pi^+e^+\nu_e) = (4.03 \pm 0.03 \pm 0.04 \pm 0.09) \times 10^{-2}$. The S-wave relative contribution for this channel is equal to $(5.68 \pm 0.21 \pm 0.24)\%$, therefore we find the following branching ratios for the two partial waves:
$B(D^+ \to K^-\pi^+e^+\nu_e)_{S-wave} = (0.229 \pm 0.009 \pm 0.01 \pm 0.005)\%$ and $B(D^+ \to \bar{K^{*0}}e^+\nu_e) \times B(\bar{K^{*0}} \to K^-\pi^+) = (3.81 \pm 0.03(stat) \pm 0.04(syst) \pm 0.09(ext.))\%$. These measurements are compatible with those from previous experiments and we gain over a factor 3 in accuracy for the S-wave branching fraction.
We compare these results with those obtained in other experiments and with theoretical calculations. We find that our form factors results are in agreeement with some of the LQCD calculations, although much more precise. This will allow theorists to perfect their LQCD methods.

In the hypothesis of S+P+P'-wave, we have defined the P' resonance ($K^*(1410)$) using the PDG values for its mass, width and assumed a barrier factor equal to 3 GeV/c. We fit the P' relative strength ($r_{P'}$) to the P wave as well as its phase ($\delta_{P'}$). We find:
$r_{P'} = 0.065 \pm 0.012 \pm 0.014$ and $\delta_{P'}(degrees) = 18.5 \pm 12.2 \pm 13.6$, compatible with 0 degrees. The P' contribution to the branching fraction is found to be, in this hypothesis, equal to 0.27%.

These measurements, in the same manner as those obtained by the LASS collaboration, are sensitive to the difference between the phase of the S and P waves. Comparing the S-wave phase obtained by these two experiments can display differences which are due in fact to different P-wave parameterizations. Comparing directly, versus the Kpi mass, the measured difference between the phase of the two waves shows that results from the two experiments agree.

Appendix

A - Tuning of fragmentation and of particle production in events with a D^{*+}

Events with a D^{*+}

The D^0 is reconstructed in the $K^-\pi^+$ decay channel. It is required that the K is identified (KLHTight) whereas the pion is taken from the list of charged tracks not identified as electron, kaon or proton. The kaon and pion have to form a vertex with a χ^2 probability greater than 10^{-3}. The mass of the $K\pi$ system is selected between 1.837 and 1.893 $\mathrm{GeV/c^2}$ which corresponds typically to $\pm 4\sigma$ around the D^0 mass. D^{*+} candidates are obtained by adding to the two selected particles a charged pion of sign opposite to the kaon. The three tracks have to form a vertex with a χ^2 probability greater than 10^{-3}.

To eliminate D^{*+} from B meson decays we use the On-peak data sample if the candidate has a minimum momentum in the c.m. of the reaction such that $x_{D^*} = p^{D^*}_{c.m.}/E_{beam} > 0.48$. For lower momenta we use Off-peak events. Thus three data samples are analyzed: the generic MC, On- and Off-peak data. These samples are normalized to the number of reconstructed D^{*+} events for $x_{D^*} > 0.48$ in On-peak events. Weights, defined in the following are such that they do not change the initial normalization.

To measure the number of D^{*+} signal events we define two mass intervals in the $\delta_m = m(D^0\pi^+) - m(D^0)$ distribution. The signal region corresponds to $\delta_m \in [0.144,\ 0.147]\ \mathrm{GeV/c^2}$ wheras the background region is taken as $\delta_m \in [0.155,\ 0.170]\ \mathrm{GeV/c^2}$. The background subtracted distribution of a given variable is obtained in the following way. From the distribution of this variable obtained with events selected in the δ_m signal region we subtract the distribution obtained with events selected in the background region, properly rescaled. The scaling factor is equal to the ratio between the number of background events measured, on simulated $e^+e^- \to c\bar{c}$ events, in the signal and in the background regions in δ_m. The fraction of background in events selected in the signal region is typically 1% for $x_{D^*} > 0.48$ and 10% for $x_{D^*} < 0.48$.

Numbers of D^{*+} signal events analyzed in this study are given in Table 13.1 and δ_m distributions are given in Figure 13.1.

	$x_{D^*} > 0.48$	$x_{D^*} < 0.48$
MC (Run4)	109870	43273
On-peak (Run4)	286055	not used
Off-peak (Run1-5)	67330	23237

Table 13.1: *Numbers of D^{*+} signal events.*

To verify the agreement between real and simulated events, we have studied the distributions of the following variables:

- $x_{D^0} = p_{D^0}/E_{beam}$;
- $R_2 = h_2 h_0$;

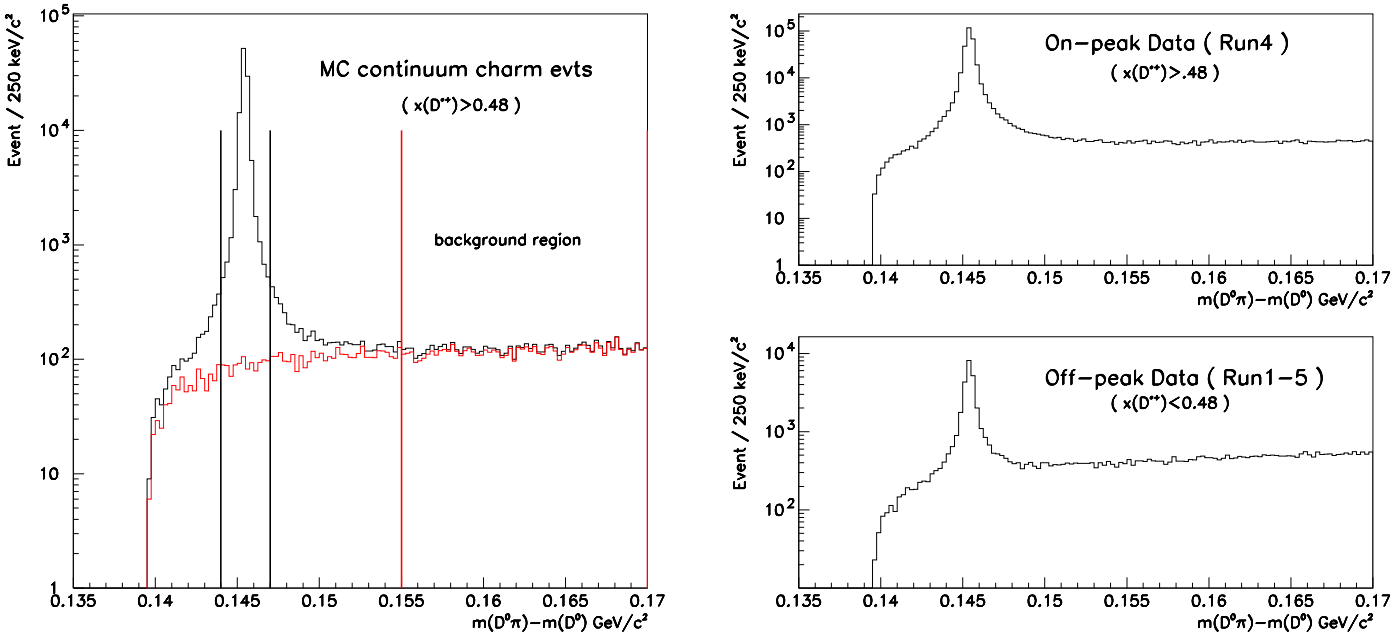

Figure 13.1: *Distributions of $\delta_m = m(D^0\pi^+) - m(D^0)$ for simulated events. The dotted histogram, on the left plot, corresponds to the combinatorial background. Intervals in δ_m which correspond respectively to signal and sideband regions are indicated. Plots on the right are obtained with data.*

- $mult.$: the total multiplicity of charged and neutral particles;
- n^{π}_{same} and $n^{\pi}_{opp.}$ the multiplicity of charged pions emitted in the same and in the opposite event hemisphere as the D^0. Hemispheres are defined using the reconstructed D^0 direction.

We have also measured, in the c.m. of the reaction, the momentum and angular distributions of emitted charged pions and kaons. The track angle is measured relatively to the direction of the D^0, if the particle is in the same hemisphere as the charm meson, or using the opposite direction if it is contained in the other hemisphere. Pions from the exclusively reconstructed D^{*+} are not included in the pion sample. As a result, particles in the same hemisphere as the D^0 are mainly produced by quark fragmentation whereas for those situated in the opposite hemisphere a large fraction comes from the decay of the other charm hadron. In each hemisphere we have also measured separately particles depending on their charge relative to the D^*. The variable $Q_{\pi/K} = q_{\pi/K} \cdot q_{D^*}$ which is the product between the electric charge of the particle and of the D^* is used in this purpose. Distributions of $x_{\pi/K}$ and $\cos\theta^{D^0}_{\pi/K}$ for particles emitted in each hemisphere are split according to this sign.

In place of using directly the momentum distribution of the particle we define[1]:

$$x_{\pi/K} = Q_{\pi/K} \log \frac{2 + \log_{10} p_{\pi/K}}{1 - x_{D^0}}, \; x_{D^0} = \frac{p_{D^0}}{E_{beam}} \tag{13.1}$$

to reduce the correlation between the momentum of the D^0 and of the particle when the latter comes from fragmentation.

[1]We use $2 + \log_{10} p_{\pi/K}$ instead of $\log_{10} p_{\pi/K}$ to avoid that $x_{\pi/K}$ changes sign for small values of $p_{\pi/K}$.

Expected origin of pion candidates

In Tables 13.2 and 13.3 we have compared the measured and expected numbers of pion candidates. Data and simulation have been normalized to the same number of reconstructed D^{*+} signal events for $x_{D^{*+}} > 0.48$.

Same hemisphere	$Q_\pi < 0$	$Q_\pi > 0$
Data (Run4)	331468	210500
MC (Run4)	341327	208919
fake π	31821	27604
π from strange (K^0,..)	16275	15630
π from fragmentation	270903	157582
π from charm	22027	8103

Table 13.2: *Pions produced in the same hemisphere as the D^{*+}.*

In the same hemisphere as the D^{*+} the difference between the average number of pions is rather small [2]: -3% and $+0.8\%$ respectively for opposite and same sign pions. About 77% of pion candidates come from quark fragmentation. There is also a good agreement between the total number of pions measured and expected in the

Opp. hemisphere	$Q_\pi < 0$	$Q_\pi > 0$
Data (Run4)	742077	454154
MC (Run4)	771355	470276
fake π	89673	73595
π from strange (K^0,..)	57091	58207
π from fragmentation	303812	199490
π from charm	320778	138985

Table 13.3: *Pions produced in the hemisphere opposite to the D^{*+}.*

hemisphere opposite to the D^{*+} (-3.8% and -3.4% for opposite and same sign respectively). The fraction of real pions from fragmentation is only 40% in this hemisphere.

Distributions before corrections

Before applying corrections, distributions of x_{D^0}, R_2, of the total particle multiplicity and of the pion multiplicity in the same and in the opposite hemisphere, measured in data and using the simulation, are compared in Figure 13.2. Differences in the shape of these distributions are observed.

In Figure 13.3 distributions of x_π and $\cos\theta_{\pi-D}$ are also compared. Whereas the total pion production rate is well reproduced by the simulation, as observed already, one measures differences in the energy and angular distributions of pions, especially when they are emitted in the same hemisphere as the D^0. In data, pions are less peaked in the direction of the D^0 than in the simulation. It is important to correct for these differences as a large fraction of background events from the $e^+e^- \to c\bar{c}$ continuum, in analyses of charm meson semileptonic decays, have a pion emitted from fragmentation. The values of the energy and angle of this pion, relative to the electron candidate determine the shape of the background spectrum versus the selected kinematic variables used in these analyses.

The difference in rate between pions with a positive or a negative charge relative to the D^{*+} illustrates charge correlations. Short distance correlations explain the excess of negative pions in the same hemisphere as the D^{*+}. Long distance correlations explain the excess of negative pions (from the anti-charm particle) in the opposite hemisphere.

[2] We measure the difference as (Data - MC)/MC.

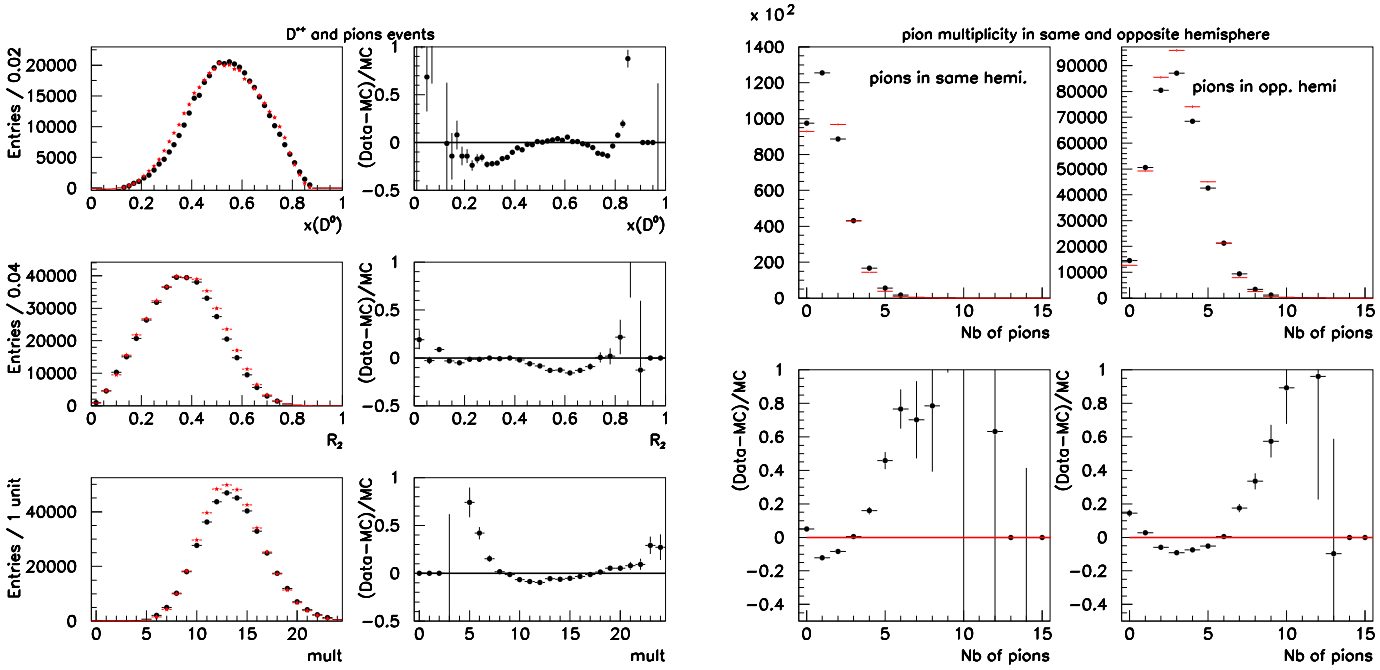

Figure 13.2: *Left: comparison between the distributions of x_{D^0}, R2 and of the total particle multiplicity obtained in data (black dots) and in the simulation (red) for events with a reconstructed D^{*+}. Right: charged pion multiplicity distributions measured in the same and in the opposite hemisphere as the D^{*+} are compared. No correction is applied to simulated events.*

Distributions after corrections

The sample of events used to define the corrections is restricted to satisfy several of the cuts used in the selection of $D^+ \to K^-\pi^+e^+\nu_e$ candidates namely:

- $R_2 > 0.2$;
- $\cos\theta_{thru.} < 0.70$;
- $F_{bb} > 0.$.

For each event the applied weight depends on global variables (x_{D^0}, R_2, $mult.$, n^{π}_{same}, $n^{\pi}_{opp,}$) and also on weights (wtr_j)evaluated for each pion and kaon emitted in the same hemisphere as the D^{*+}.

$$w = w(x_{D^0},\ R_2,\ mult.,n^{\pi}_{same},n^{\pi}_{opp,}) \prod_{j=1}^{n^{\pi/K}_{same}} wtr_j(x^j_{\pi},\ \cos\theta^j_{\pi-D}). \tag{13.2}$$

Distributions of the variables measured in data and in simulation, after corrections, are compared in Figure 13.4. In Figure 13.5 distributions of x_π and $\cos\theta_{\pi-D}$ are compared after applying corrections.

Differences which were at a level of 10-20% are now reduced to 5% or below.

B -Tuning of fragmentation and of particle production in events with a D^0

In this section we want to control particle production when a $c\bar{u} = D^0$ or D^{*0} charm meson is emitted. In this purpose we reconstruct a D^0 decaying into $K^-\pi^+$ and we veto D^0 cascading from a D^{*+} meson (as a D^{*+} corresponds to a bound $c\bar{d}$ state).

D^0 events with a veto against $D^{*+} \to D^0\pi^+$ decays.

The D^0 is reconstructed using the same procedure as explained in section 13. D^{*+} candidates are obtained by adding to the two selected particles a charged pion of sign opposite to the kaon. The three tracks have to form a vertex with a χ^2 probability higher than 10^{-3} and all candidates having a value of the mass difference $\delta_m = m(D^0\pi^+) - m(D^0)$ within the interval $\delta_m \in [0.143,\ 0.148]\mathrm{GeV/c^2}$ are eliminated.

To eliminate D^0 from B meson decays we use the On-peak data sample if the candidate has a minimum momentum in the c.m. of the reaction ($x_{D^0} = p^{D^0}_{c.m.}/E_{beam} > 0.48$). For lower momenta we use Off-peak events. Three data samples are thus used: the generic MC, On- and Off-peak data. These samples are normalized to the number of reconstructed D^0 events for $x_{D^0} > 0.48$ in On-peak events. To count D^0 signal events we define two mass regions in the $K\pi$ mass distribution. The signal region corresponds to $m_{K\pi} \in [1.837,\ 1.893]\mathrm{GeV/c^2}$ wheras events situated in the mass intervals $[1.774,\ 1.830] \cup [1.900,\ 1.956]\mathrm{GeV/c^2}$ are used to subtract the effect from the combinatorial background. The background subtracted distribution of a given variable is obtained in the following way. From the distribution of this variable obtained with events selected in the signal region we subtract the corresponding distribution obtained with events selected in the background region, weighted by 50% (as the sidebands are two times larger than the signal region). D^0 mass distributions are given in Figure 13.6, reconstructed D^{*+} mesons have been vetoed and no selection is applied on x_{D^0}.

Numbers of D^0 signal events analyzed in this study (after background subtraction) are given in Table 13.4.

We have studied the distributions of the same variables as in section A-2.

We have also measured, in the c.m. of the reaction, the momentum and angular distributions of the emitted charged pions. Conventions are similar as defined in Section 13.

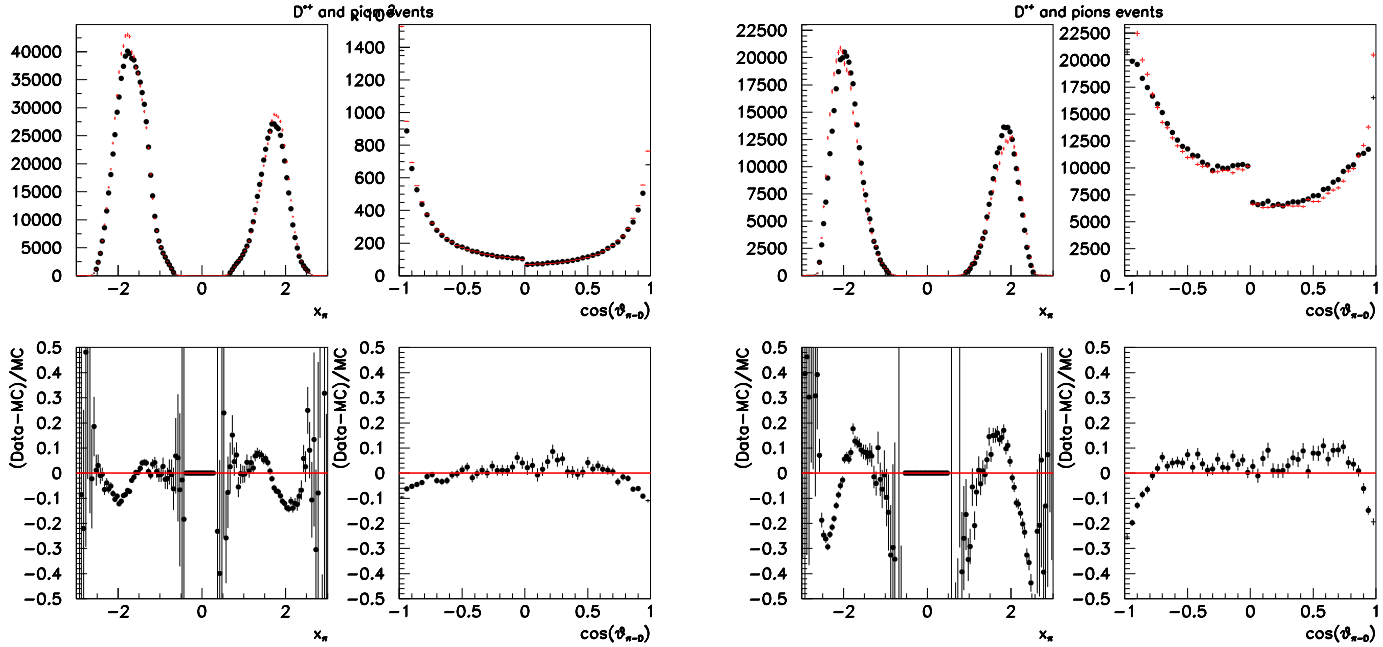

Figure 13.3: *Comparison between distributions of x_π and $\cos\theta_{\pi-D}$ measured in data and in the simulation for pions emitted in the opposite (tleft) or in the same (right) hemisphere as the reconstructed D^{*+}. No correction has been applied to simulated events.*

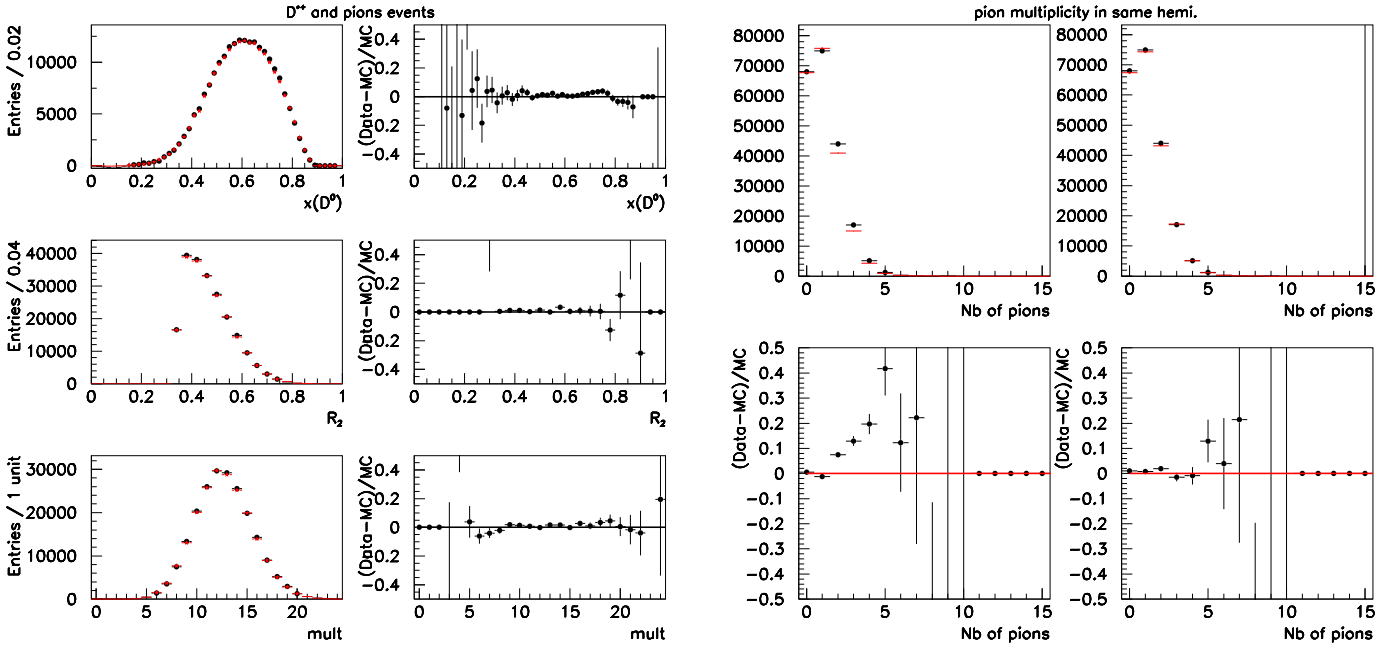

Figure 13.4: *Left: comparison between the distributions of x_{D^0}, R2 and of the total particle multiplicity obtained in data and in the simulation for events with a reconstructed D^{*+}. Right: charged pion multiplicity distributions measured in the same and in the opposite hemisphere as the D^{*+} are compared. Corrections have been applied to simulated events.*

	$x_{D^0} > 0.48$	$x_{D^0} < 0.48$
MC (Run4)	466298	
On-peak (Run4)	430429	not used
Off-peak (Run1-5)	293732	

Table 13.4: *Numbers of D^0 signal events.*

Expected origin of pion candidates

In tables 13.5 and 13.6 we have compared the measured and expected numbers of pion candidates. Data and simulation have been normalized to the same number of reconstructed D^0 signal events for $x_{D^0} > 0.48$.

Same hemisphere	$Q_\pi < 0$	$Q_\pi > 0$
Data (Run4)	478737	621379
MC (Run4)	462835	630228
fake π	71423	74044
π from strange (K^0,..)	27128	28607
π from fragmentation	312130	513653
π from charm	52154	13924

Table 13.5: *Pions produced in the same hemisphere as the D^0, a veto against D^{*+} is applied in the same hemisphere as the D^0.*

Opp. hemisphere	$Q_\pi < 0$	$Q_\pi > 0$
Data (Run4)	1171980	854124
MC (Run4)	1228510	880895

Table 13.6: *Pions produced in the hemisphere opposite to the D^0, a veto against D^{*+} is applied in the same hemsphere as the D^0.*

The overall pion multiplicity measured in data and in the simulation, in the same and in the opposite hemisphere, are in rather good agreement: differences being respectively of 0.6% and 3.9%.

As expected, in the same hemisphere as the D^0, real pions from fragmentation dominate ($\sim 75\%$).

Distributions before corrections

Distributions of x_{D^0}, R_2 and of the total particle multiplicity measured in data and using the simulation, before correction are compared in Figure 13.7. Differences in the shape of these distributions are observed.

In Figure 13.8 distributions of x_π and $\cos\theta_{\pi-D}$ are also compared. Whereas the total pion production rate is well reproduced by the simulation one measures differences in the energy and angular distributions of the pions, especially in the same hemisphere as the D^0. In data, pions are less peaked in the direction of the D^0 than in the simulation. If one compares the distributions measured for pions emitted in the same hemisphere as the D^0 with Figure 13.5 which is obtained for pions emitted with a D^{*+}, one can see that there is now an excess of positive particles accompanying the D^0 as expected from the hadronization of the spectator u-quark.

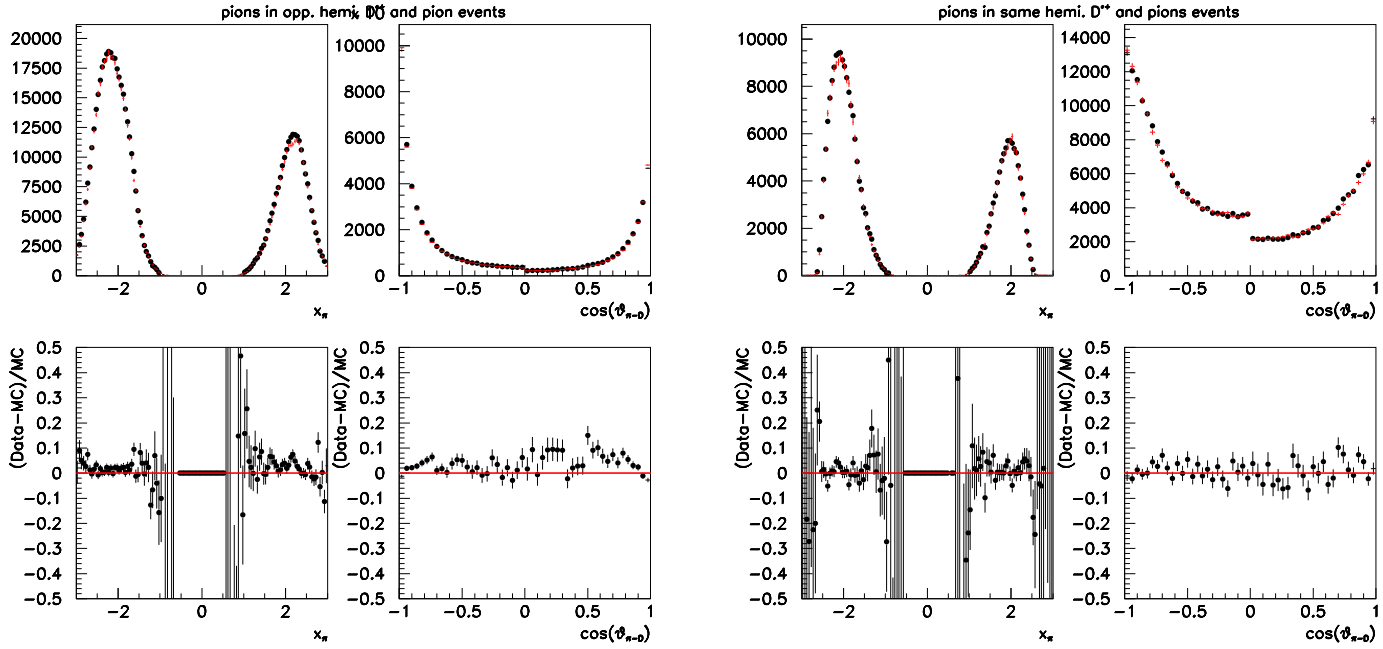

Figure 13.5: *Comparison between distributions of x_π and $\cos\theta_{\pi-D}$ measured in data and in the simulation for pions emitted in the opposite (top) or in the same (bottom) hemisphere as the reconstructed D^{*+}. Corrections have been applied to simulated events.*

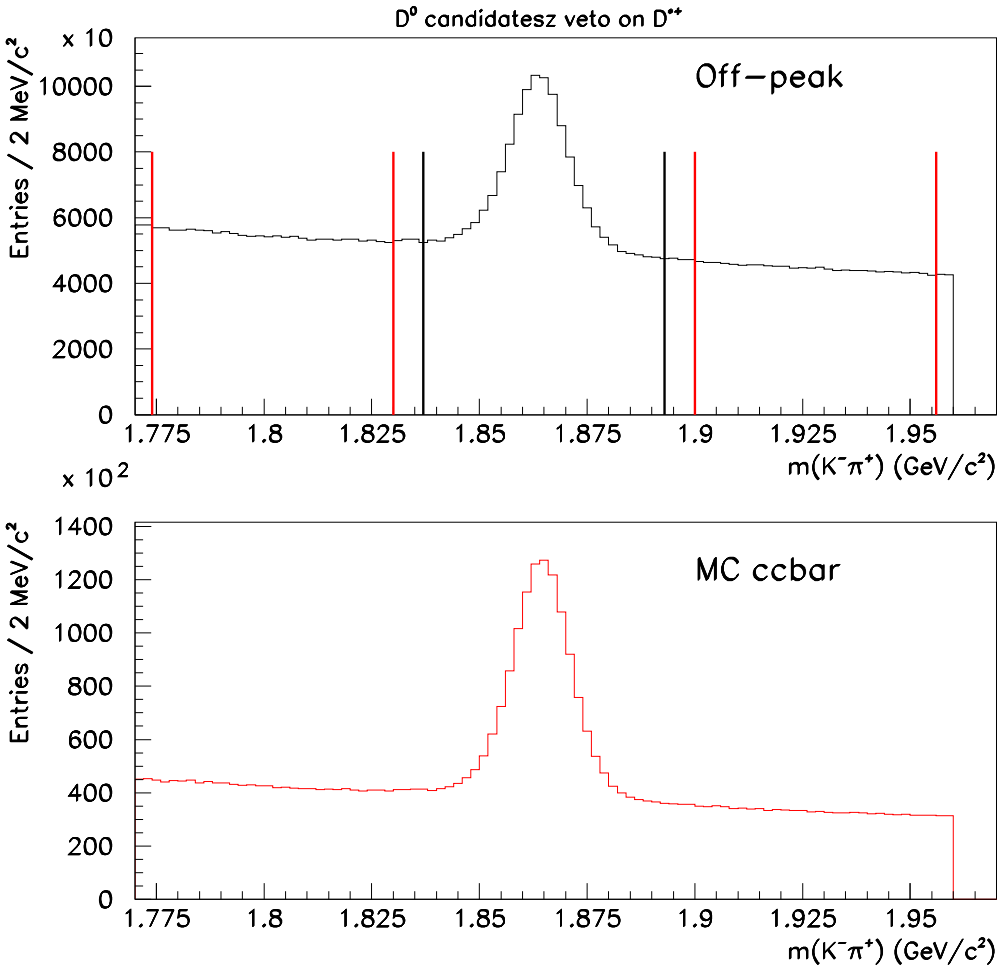

Figure 13.6: *$K\pi$ mass distributions obtained with generic $e^+e^- \to c\bar{c}$ simulated events (bottom) and with off-peak data (top). The mass intervals used to define the signal and sideband regions are indicated on the upper plot.*

Distributions after corrections

Distributions of x_{D^0}, R_2 and of the total particle multiplicity measured in data and using the simulation, after corrections, are compared in Figure 13.9. These corrections correspond to a weight applied on each event, which depends on 5 variables: $w(x_{D^0}, R_2, mult., n^{\pi}_{same}, n^{\pi}_{opp,})$.

We have also corrected the momentum and angular distributions of emitted pions, only in the same hemisphere as the D^0. This restriction comes from the fact that only pions emitted in this hemisphere are contributing to the background in other analyses and also because, in this hemisphere, we can have a direct control of the fragmentation process. In Figure 13.10 distributions of x_π and $\cos\theta_{\pi-D}$ are compared after applying corrections. These corrections correspond also to a weight which, in addition to the previous 5 variables, depends also on x_π and $\cos\theta_{\pi-D}$.

C - Tuning of fragmentation and of particle production in events with a D^+

The $c \to D^+$ fragmentation distribution and global event characteristics are measured in data and simulation.

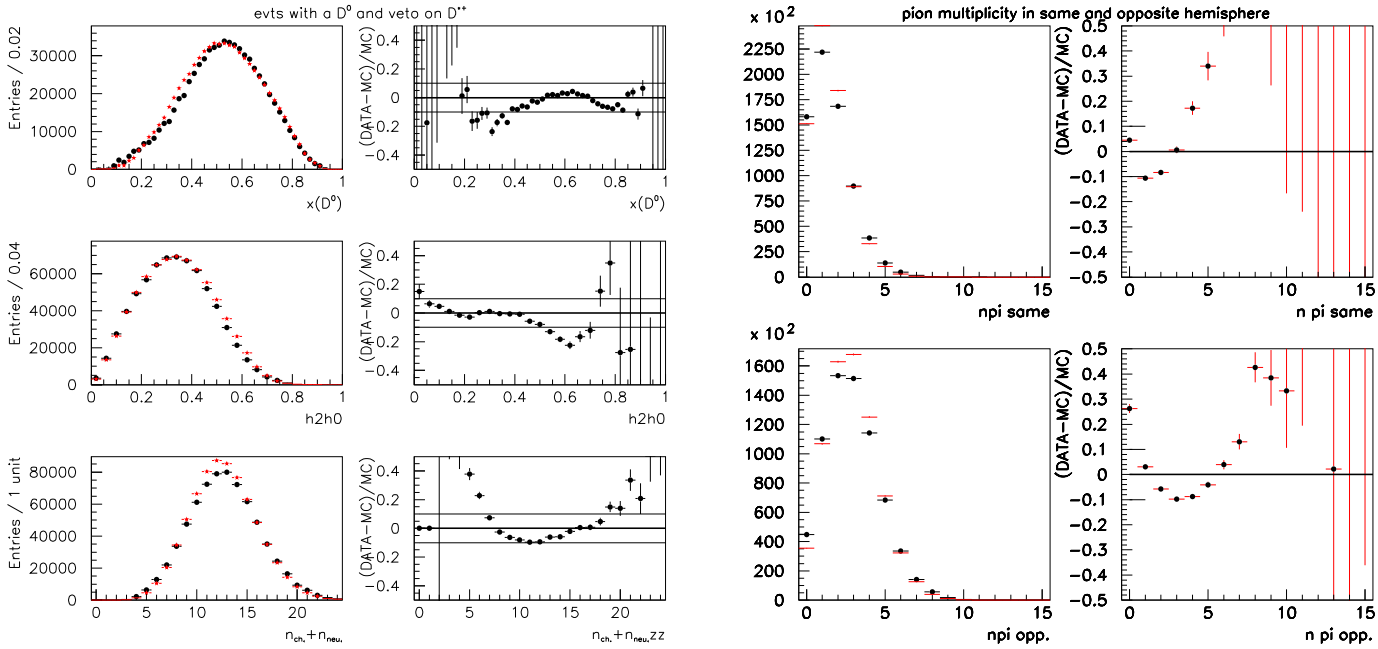

Figure 13.7: *Left: comparison between the distributions of x_{D^0}, R2 and of the total particle multiplicity obtained in data (black dots) and in the simulation for events with a reconstructed D^0. Right: charged pion multiplicity distributions measured in the same and in the opposite hemisphere as the D^0 are compared. No correction has been applied to simulated events.*

A weight is applied to simulated events to correct for measured differences as compared with data.

D^+ events.

The D^+ is reconstructed using its decay into $K^-\pi^+\pi^+$. The three tracks have to form a vertex with a χ^2 probability higher than 10^{-7} and a positive flight distance. Cuts on R_2, $\cos\theta_{thru.}$ and F_{bb} are similar as those applied to select the semileptonic channel.

To eliminate D^+ from B meson decays we use the On-peak data sample if the candidate has a minimum momentum in the c.m. of the reaction ($x_{D^+} = p^{D^+}_{c.m.}/E_{beam} > 0.48$). For lower momenta we use Off-peak events. Three data samples are thus used: the generic MC, On- and Off-peak data. These samples are normalized to the number of reconstructed D^+ events for $x_{D^+} > 0.48$ in On-peak events.

The mass distribution of these candidates, obtained with simulated charm events is given in Figure 13.11.

To count D^+ signal events we define two mass regions in the $K\pi\pi$ mass distribution. The signal region corresponds to $m_{K\pi\pi} \in [1.849,\ 1.889]\mathrm{GeV/c^2}$ wheras events situated in the mass intervals $[1.798,\ 1.838] \cup [1.900,\ 1.940]\mathrm{GeV/c^2}$ are used to subtract the effect from the combinatorial background.

The background subtracted distribution of a given variable is obtained in the following way. From the distribution of this variable obtained with events selected in the signal region we subtract the corresponding distribution obtained with events selected in the background region, weighted by 50% (as the sidebands are two times larger than the signal region).

We have studied the distributions of the same variables as in D^0 and D^{*+} tagged events. The determination of the weight is similar as in previous channels.

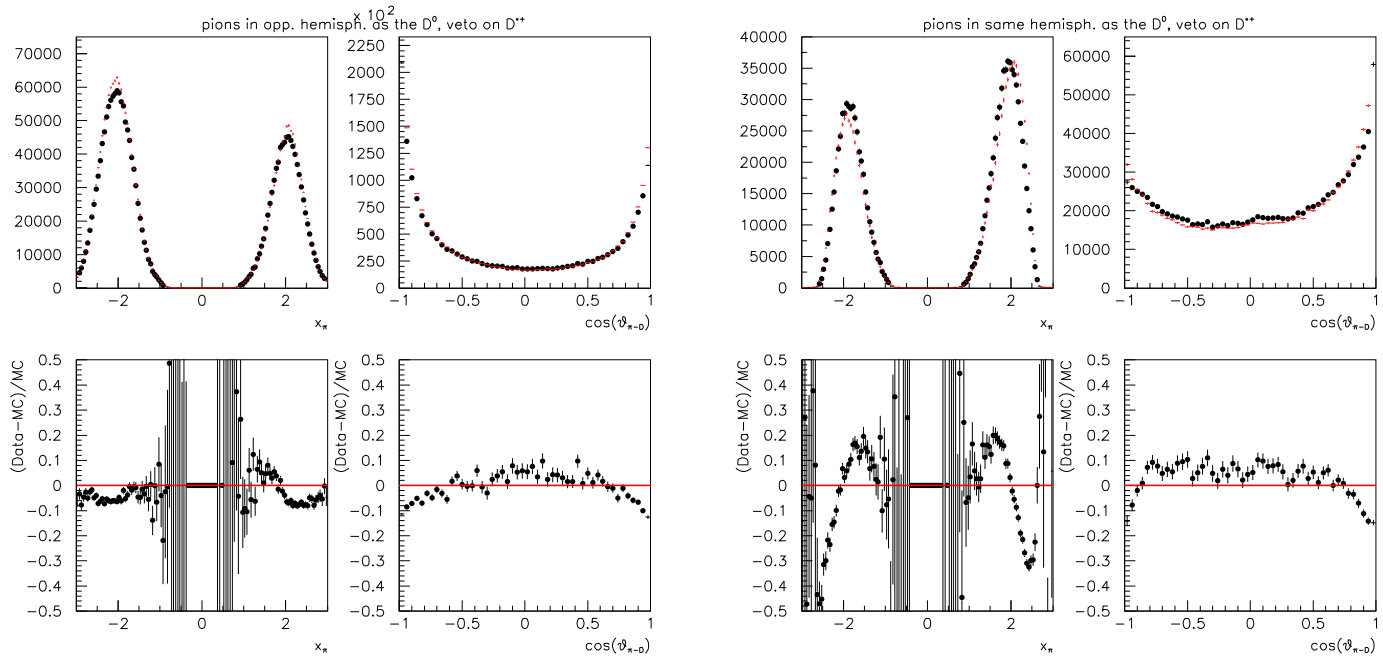

Figure 13.8: *Comparison between distributions of x_π and $\cos\theta_{\pi-D}$ measured in data and in the simulation for pions emitted in the opposite (top) or in the same (bottom) hemisphere as the reconstructed D^0. No correction has been applied to simulated events.*

Distributions after corrections

Distributions of x_{D^+}, R_2 and of the total particle multiplicity measured in data and using the simulation, after corrections, are compared in Figure 13.9. These corrections correspond to a weight applied on each event, which depends on 5 variables: $w(x_{D^+}, R_2, mult., n^\pi_{same}, n^\pi_{opp,})$.

We have also corrected the momentum and angular distributions of emitted pions, only in the same hemisphere as the D^+. This restriction comes from the fact that only pions emitted in this hemisphere are contributing to the background in other analyses and also because, in this hemisphere, we can have a direct control of the fragmentation process. In Figure 13.13 distributions of x_π and $\cos\theta_{\pi-D}$ are compared after applying corrections. These corrections correspond also to a weight which, in addition to the previous 5 variables, depends also on x_π and $\cos\theta_{\pi-D}$.

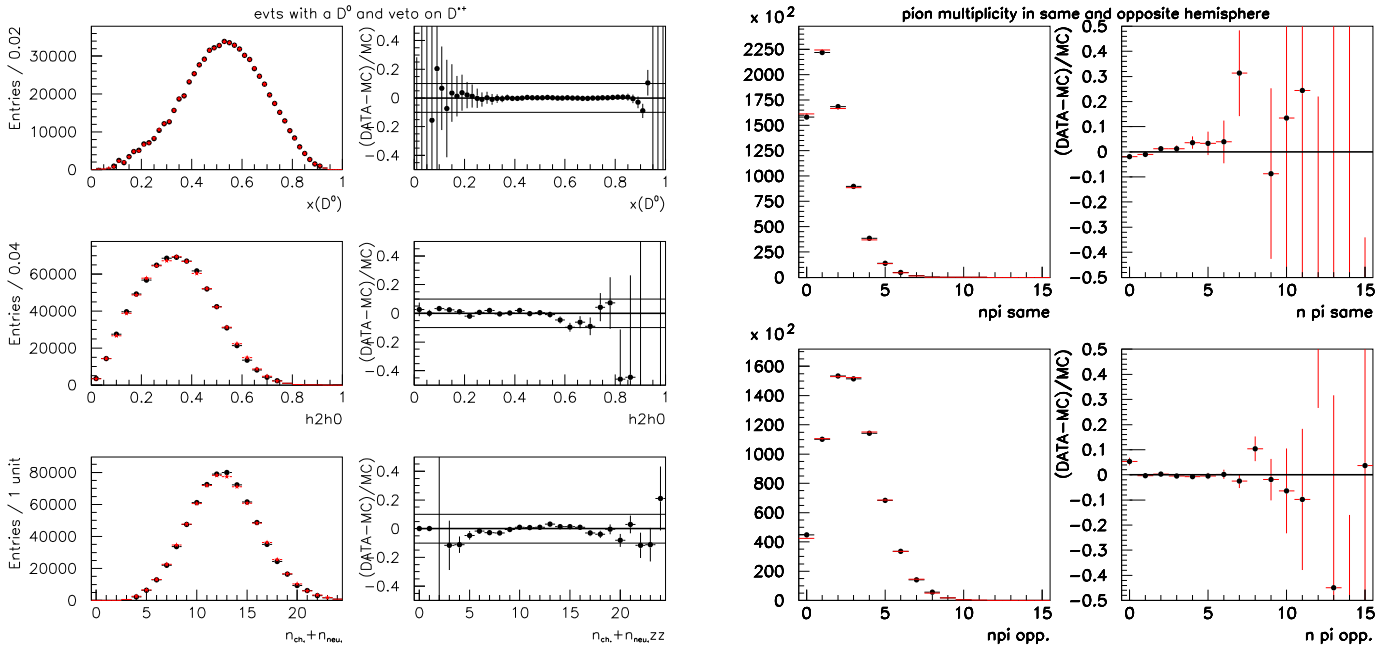

Figure 13.9: *Left: comparison between the distributions of x_{D^0}, R2 and of the total particle multiplicity obtained in data and in the simulation for events with a reconstructed D^0. Right: charged pion multiplicity distributions measured in the same and in the opposite hemisphere as the D^0 are compared. Corrections have been applied to simulated events.*

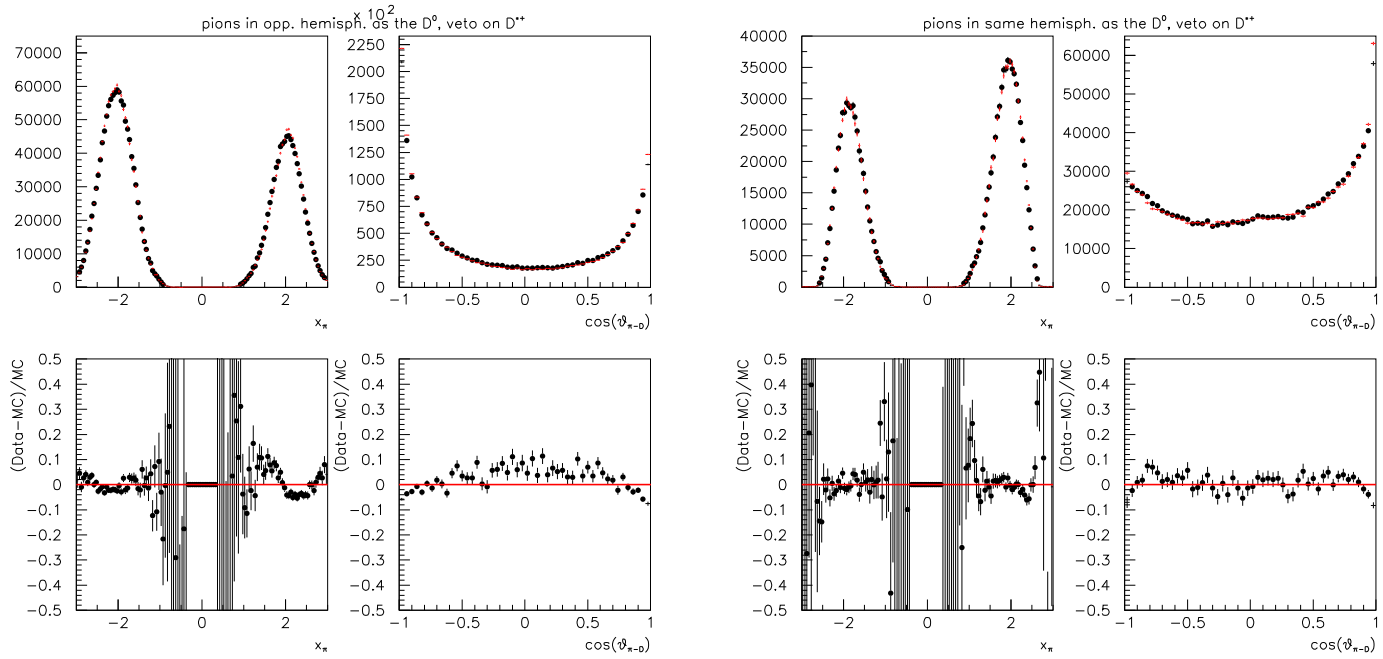

Figure 13.10: *Comparison between distributions of x_π and $\cos\theta_{\pi-D}$ measured in data and in the simulation for pions emitted in the opposite (top) or in the same (bottom) hemisphere as the reconstructed D^0. Corrections have been applied to simulated events.*

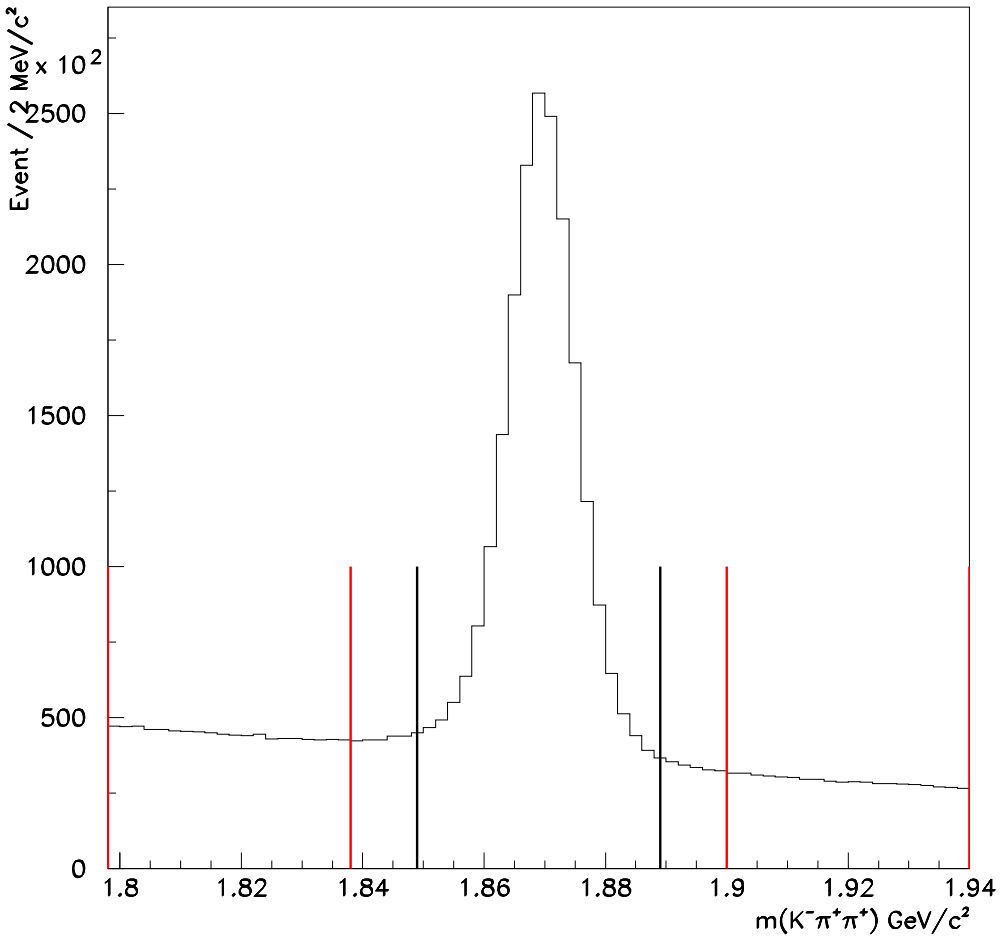

Figure 13.11: *$K^-\pi^+\pi^+$ mass distribution obtained with generic $e^+e^- \to c\bar{c}$ simulated events. Mass intervals used to define the signal and sideband regions are indicated.*

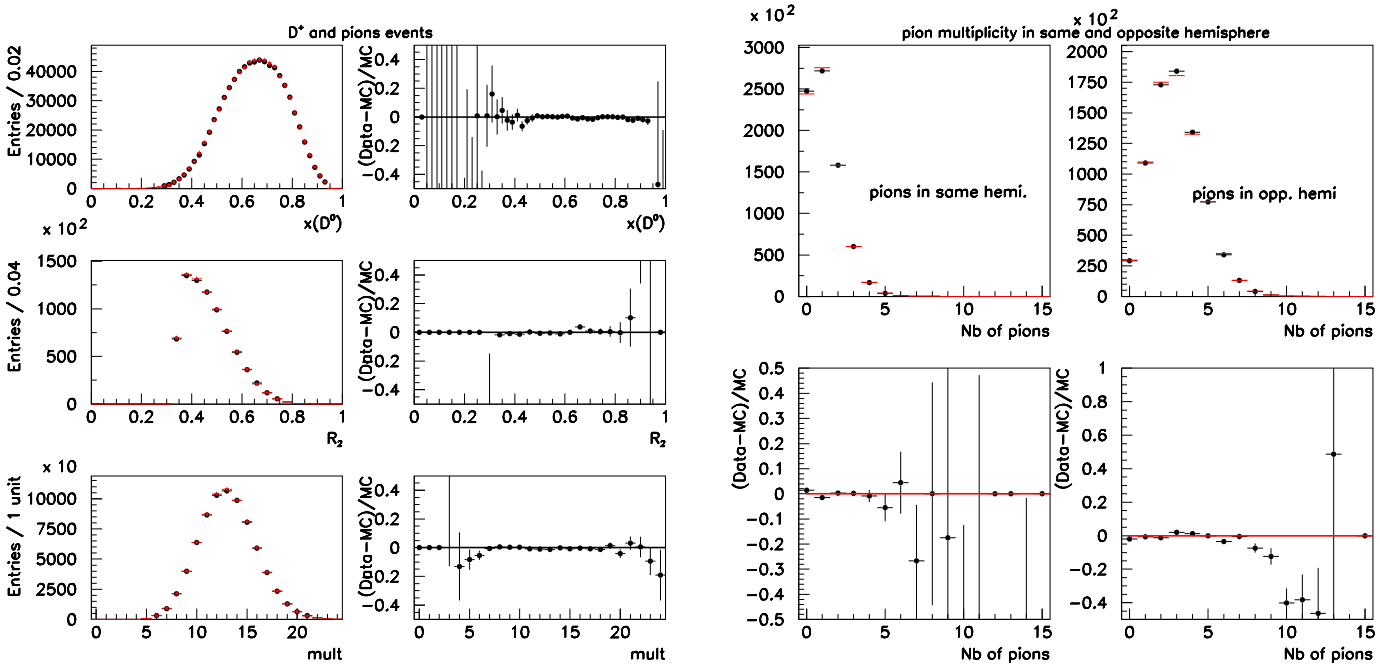

Figure 13.12: *Left: comparison between the distributions of x_{D^+}, R2 and of the total particle multiplicity obtained in data and in the simulation for events with a reconstructed D^+. Right: charged pion multiplicity distributions measured in the same and in the opposite hemisphere as the D^+ are compared. Corrections have been applied to simulated events.*

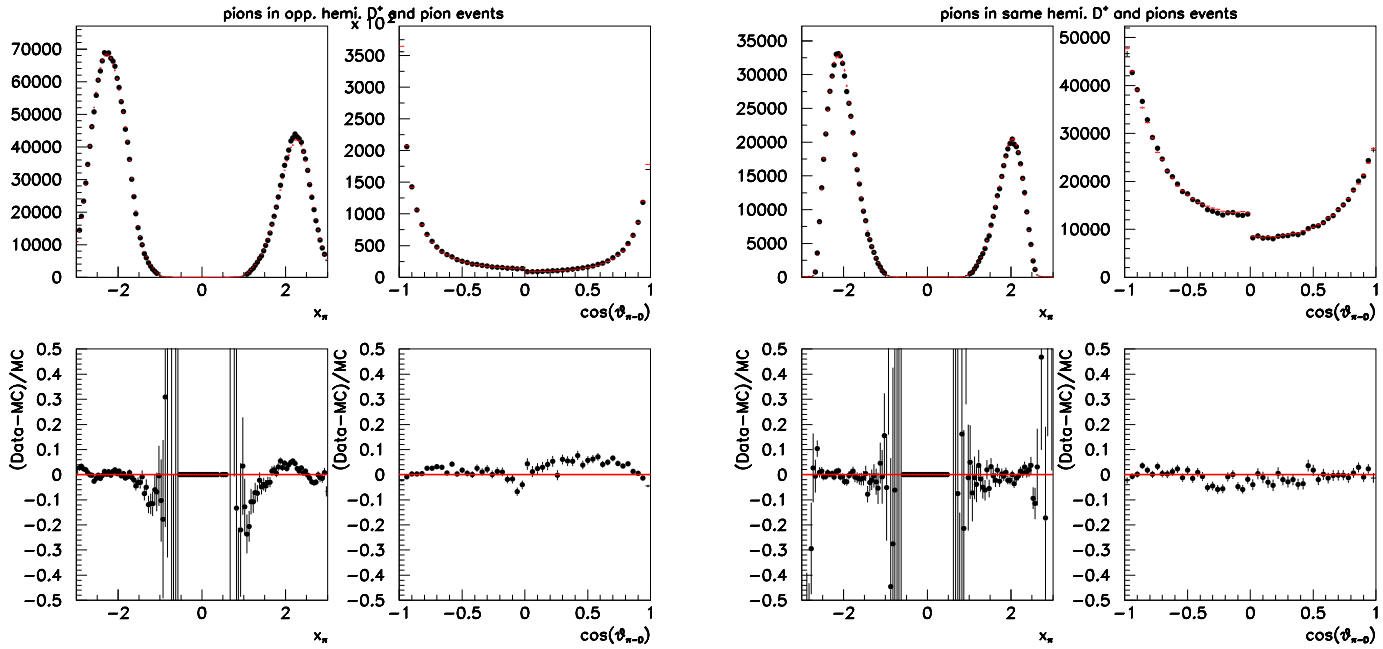

Figure 13.13: *Comparison between distributions of x_π and $\cos\theta_{\pi-D}$ measured in data and in the simulation for pions emitted in the opposite (top) or in the same (bottom) hemisphere as the reconstructed D^+. Corrections have been applied to simulated events.*

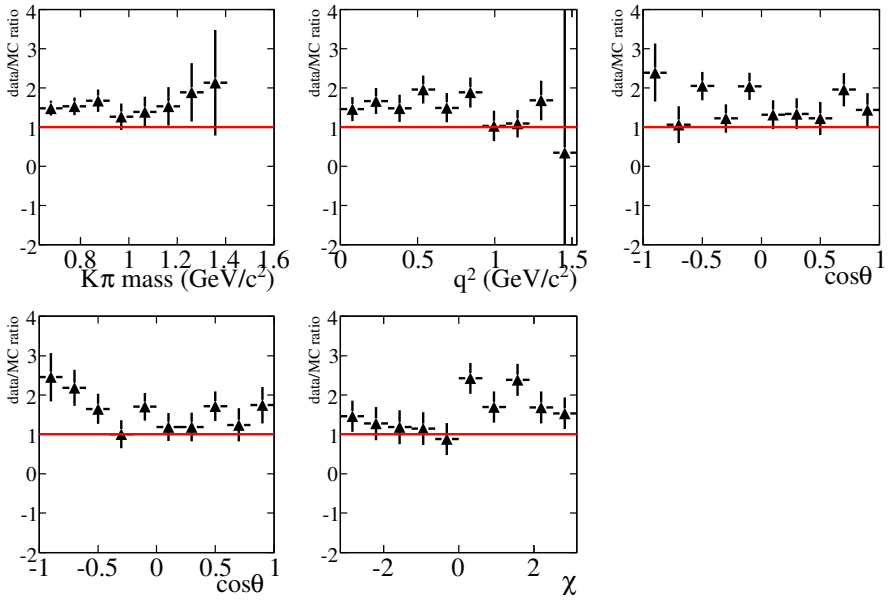

Figure 13.14: Ratio data/MC for $cos\theta_\pi, m_{K\pi}, q^2$ and $cos\theta_e$ with $F_{cc} > 0.4$

D - Behaviour of $B\bar{B}$ simulation for different cuts in F_{cc}

In this section we present the behaviour of Data OnPeak-OffPeak for data and simulation for other cuts in the F_{cc} variable.

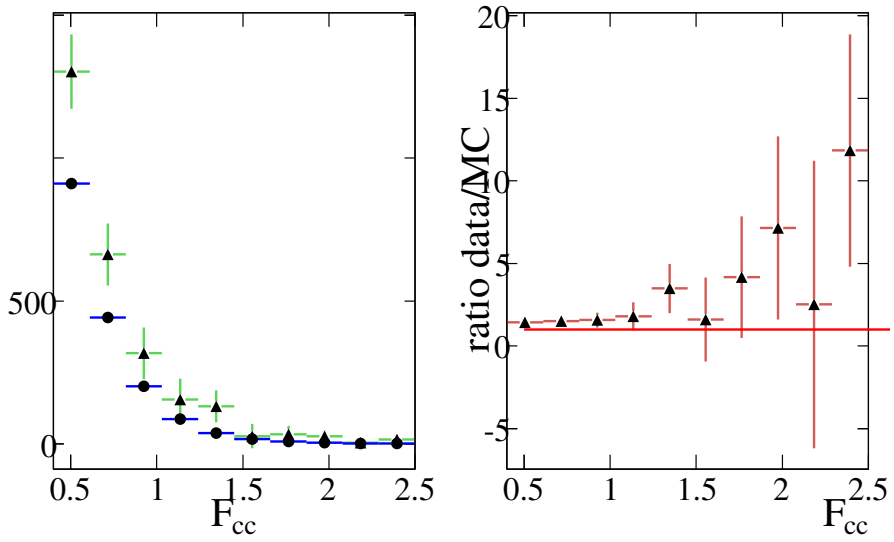

Figure 13.15: RS distribution for F_{cc} variable. Left: In ($\triangle$) (OnPeak-OffPeak) data, ($\bullet$) MC $B\bar{B}$. Right: ratio $\frac{(OnPeak-OffPeak)data}{B\bar{B}}$ with $F_{cc} > 0.4$

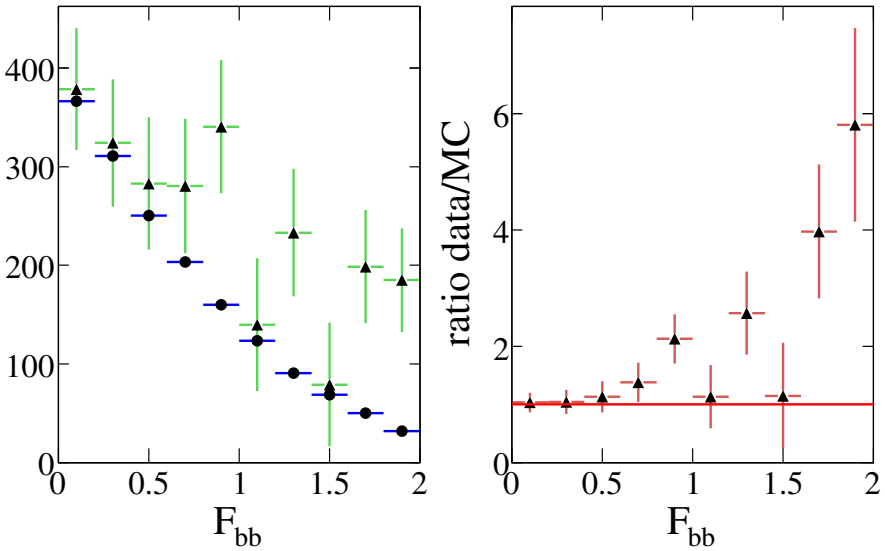

Figure 13.16: RS distribution for F_{bb} variable. Left: In ($\triangle$) (OnPeak-OffPeak) data, ($\bullet$) MC $B\bar{B}$. Right: ratio $\frac{OnPeak-OffPeak)data}{B\bar{B}}$ with $F_{cc} > 0.4$

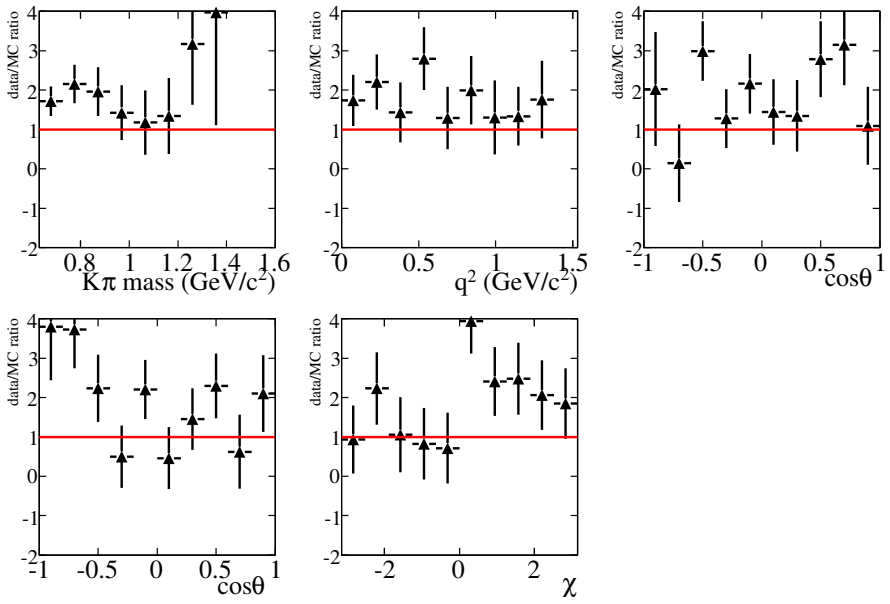

Figure 13.17: Ratio data/MC for $cos\theta_\pi, m_{K\pi}, q^2$ *and* $cos\theta_e$ with $F_{cc} > 0.7$

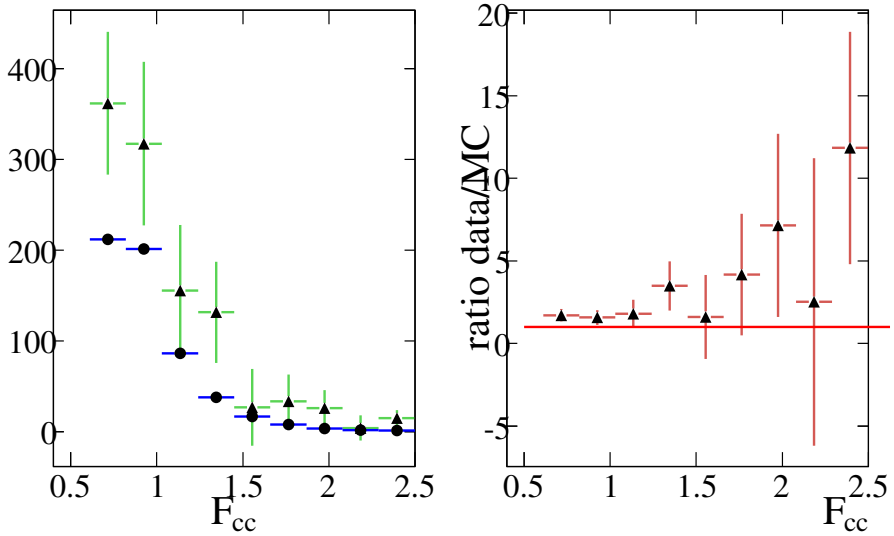

Figure 13.18: RS distribution for F_{cc} variable. Left: In (△) (OnPeak-OffPeak) data, (•) MC $B\bar{B}$. Right: ratio $\frac{(OnPeak-OffPeak)data}{B\bar{B}}$ with $F_{cc} > 0.7$

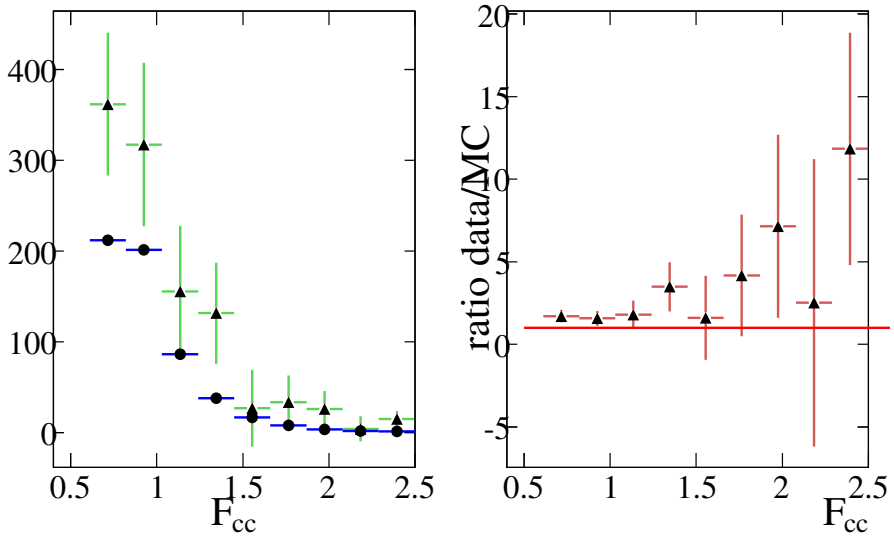

Figure 13.19: RS distribution for F_{bb} variable. Left: In (△) (OnPeak-OffPeak) data, (•) MC $B\bar{B}$. Right: ratio $\frac{OnPeak-OffPeak)data}{BB}$ with $F_{cc} > 0.7$

E - Data MC comparison for WS events for Runs 1-3 and Run 5

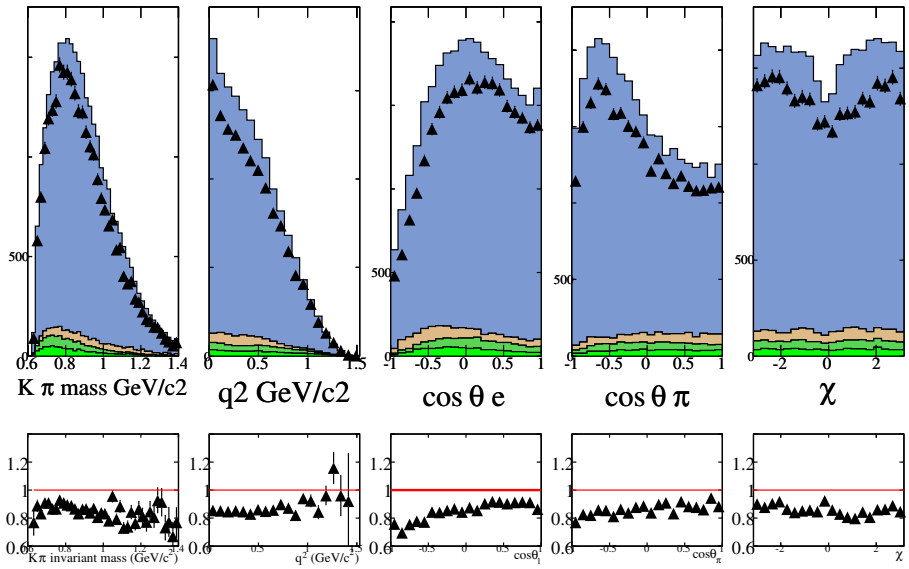

Figure 13.20: Distributions of the 5 dynamical variables for WS events in data and MC before tuning for Run123. ($\triangle$) data , MC in stacking order : $B^0\bar{B}^0, B^+B^-, uds, c\bar{c}$. Lower row: ratio data/MC for upper row plots.

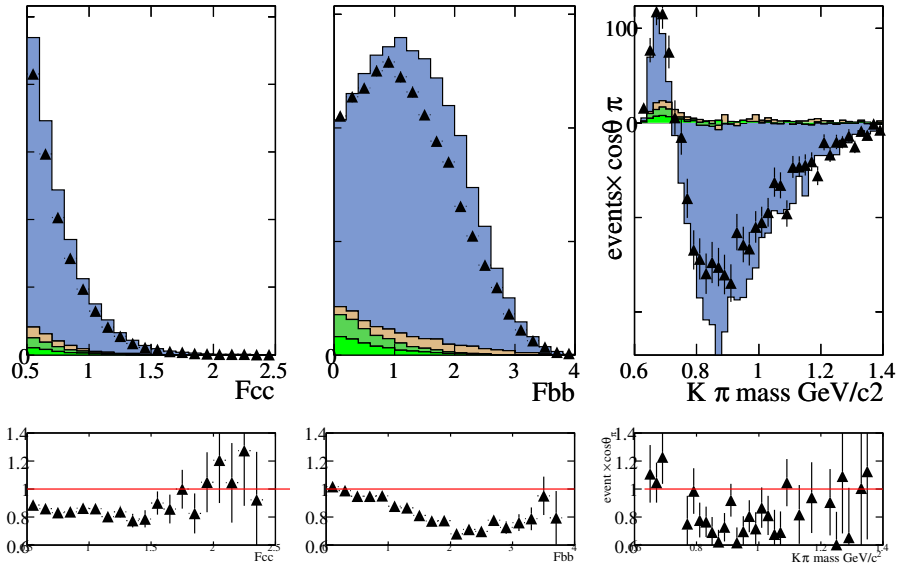

Figure 13.21: Distribution for WS data and MC for the Fisher discriminants and asymmetry variation with mass before corrections on charm for Run123. (△) data , MC in stacking order : $B^0\bar{B}^0, B^+B^-, uds, c\bar{c}$. Lower row: ratio data/MC for upper row plots.

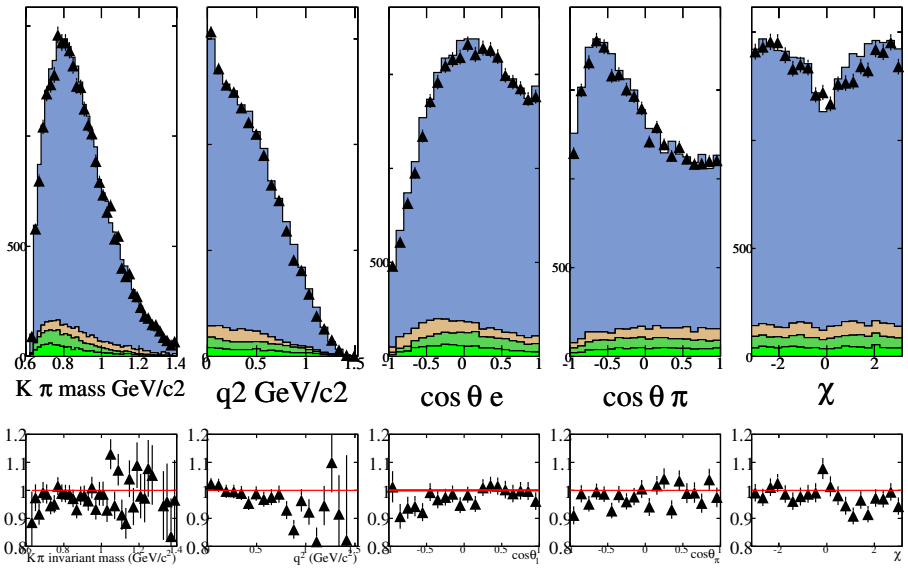

Figure 13.22: Distributions of the 5 dynamical variables for WS events in data and MC after tuning correction for charm for Run123 . (△) data , MC in stacking order : $B^0\bar{B}^0, B^+B^-, uds, c\bar{c}$. Lower row: ratio data/MC for upper row plots.

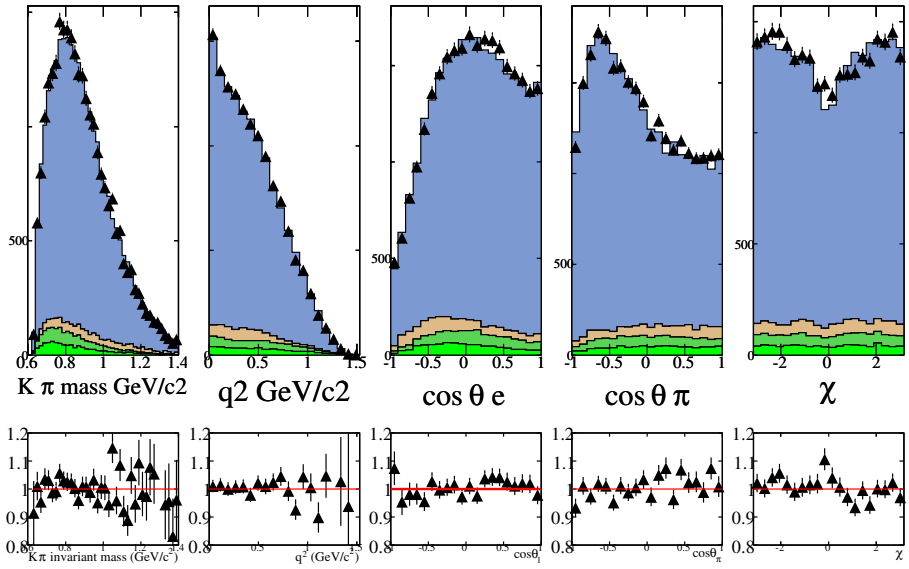

Figure 13.23: Distribution for WS data and MC for the 5 dynamical variables after renormalisation of the charm contribution for Run123. (△) data , MC in stacking order : $B^0\bar{B}^0, B^+B^-, uds, c\bar{c}$. Lower row: ratio data/MC for upper row plots.

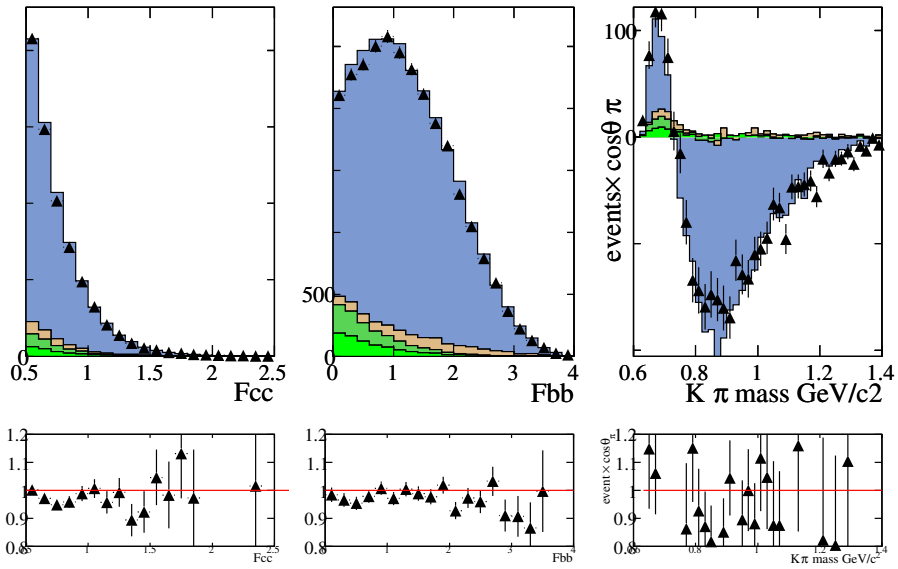

Figure 13.24: Distribution for WS data and MC for the Fisher discriminants and asymmetry variation with mass after tuning corrections on charm for Run132 . (△) data , MC in stacking order : $B^0\bar{B}^0, B^+B^-, uds, c\bar{c}$. Lower row: ratio data/MC for upper row plots.

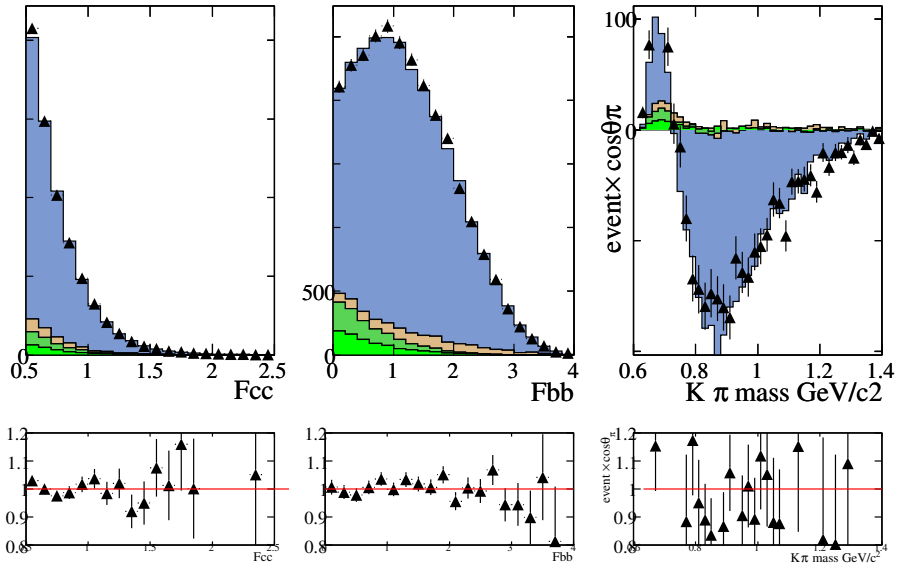

Figure 13.25: Distribution for WS data and MC for the Fisher discriminants and asymmetry variation with mass after renormalisation of the charm contribution for Run123. (△) data , MC in stacking order : $B^0\bar{B}^0, B^+B^-, uds, c\bar{c}$. Lower row: ratio data/MC for upper row plots.

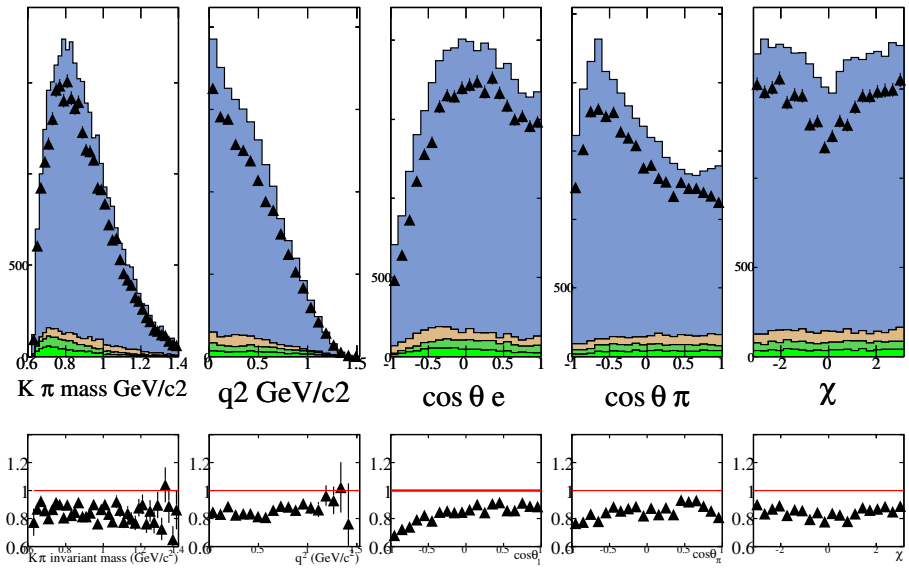

Figure 13.26: *Distributions of the 5 dynamical variables for WS events in data and MC for Run5. (△) data , MC in stacking order : $B^0\bar{B}^0, B^+B^-, uds, c\bar{c}$. Lower row: ratio data/MC for upper row plots.*

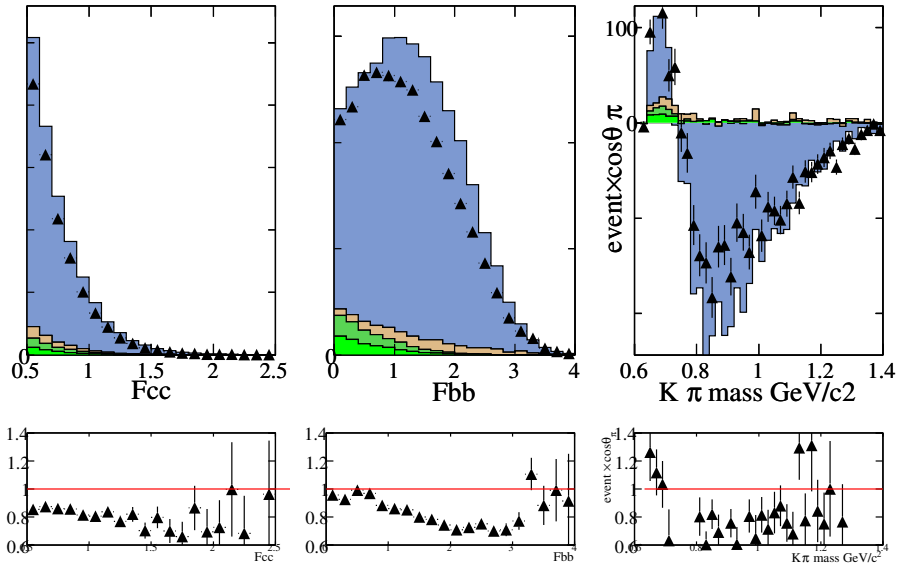

Figure 13.27: *Distribution for WS data and MC for the Fisher discriminants and asymmetry variation with mass after corrections on charm and B decays for Run5. (△) data , MC in stacking order : $B^0\bar{B}^0, B^+B^-, uds, c\bar{c}$. Lower row: ratio data/MC for upper row plots.*

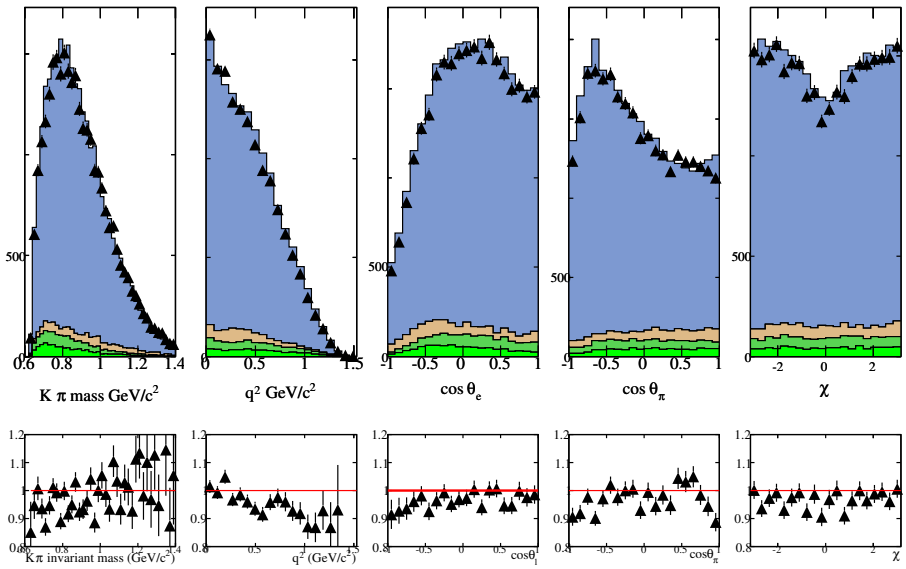

Figure 13.28: Distributions of the 5 dynamical variables for WS events in data and MC for Run5. (△) data , MC in stacking order : $B^0\bar{B}^0, B^+B^-, uds, c\bar{c}$. Lower row: ratio data/MC for upper row plots.

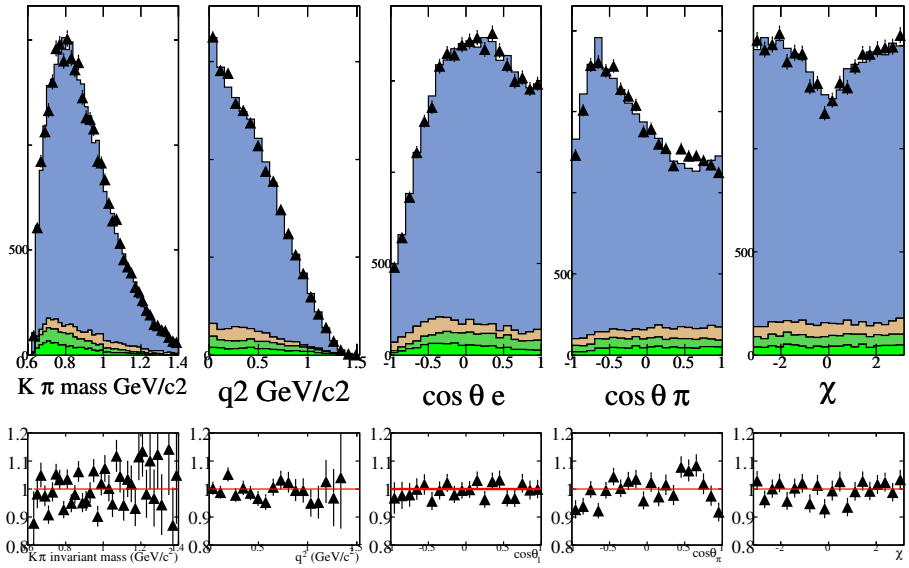

Figure 13.29: Distribution for WS data and MC for the 5 dynamical variables after renormalisation of the charm contribution for Run5. ($\triangle$) data , MC in stacking order : $B^0\bar{B}^0, B^+B^-, uds, c\bar{c}$. Lower row: ratio data/MC for upper row plots.

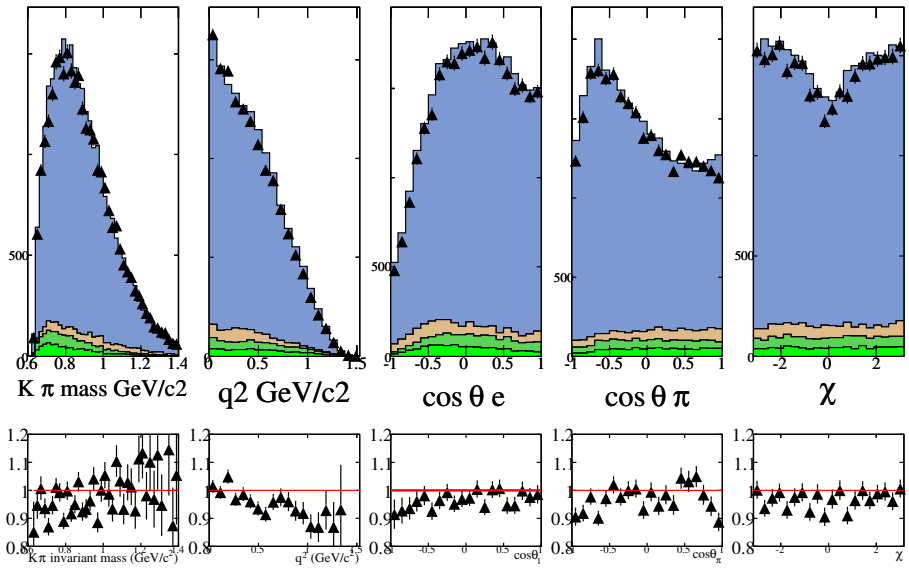

Figure 13.30: Distribution for WS data and MC for the Fisher discriminants and asymmetry variation with mass after corrections on charm and B decays for Run5. ($\triangle$) data , MC in stacking order : $B^0\bar{B}^0, B^+B^-, uds, c\bar{c}$. Lower row: ratio data/MC for upper row plots.

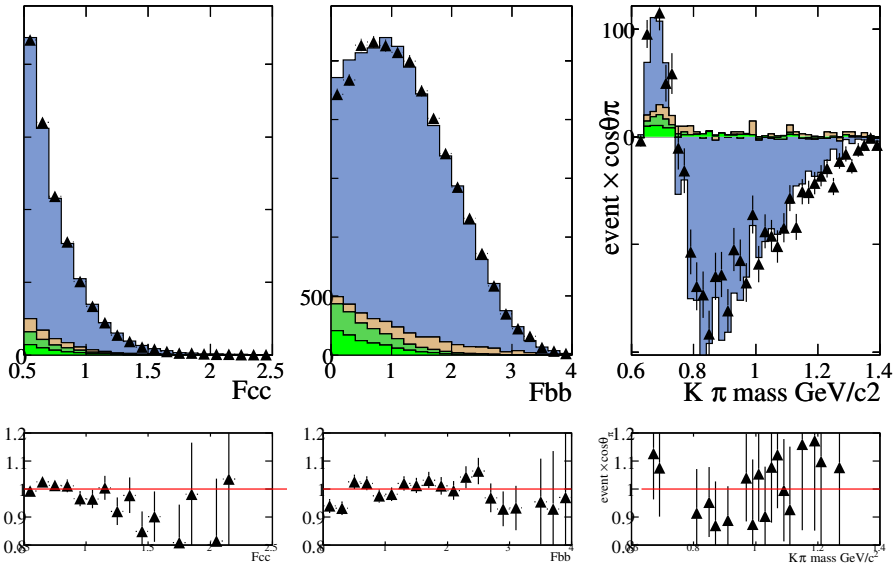

Figure 13.31: Distribution for WS data and MC for the Fisher discriminants and asymmetry variation with mass after renormalisation of the charm contribution for Run5. (△) data , MC in stacking order : $B^0\bar{B}^0, B^+B^-, uds, c\bar{c}$. Lower row: ratio data/MC for upper row plots.

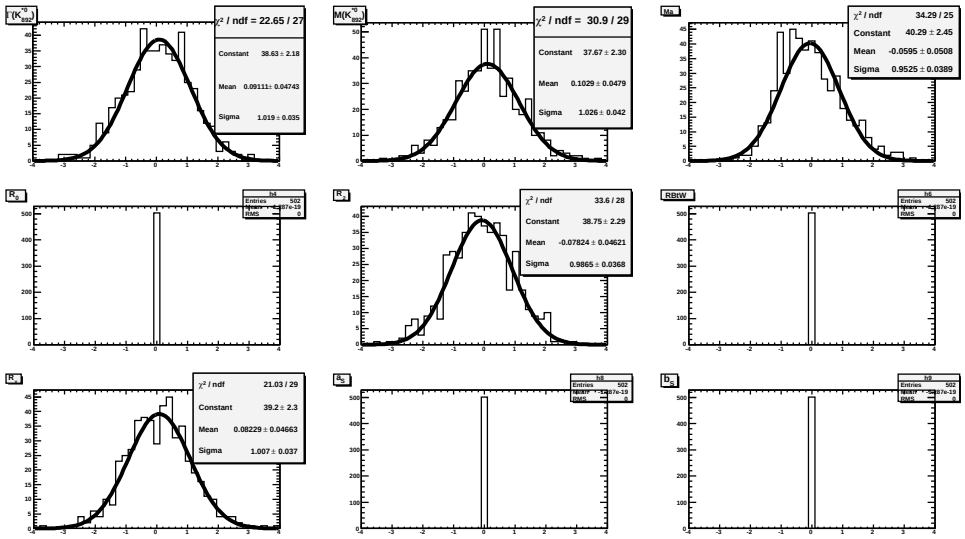

Figure 13.32: PULLS for P-wave fit for case where control samples has 10 times more statistics than the "data" sample.

F - PULL plots Fit stability analysis

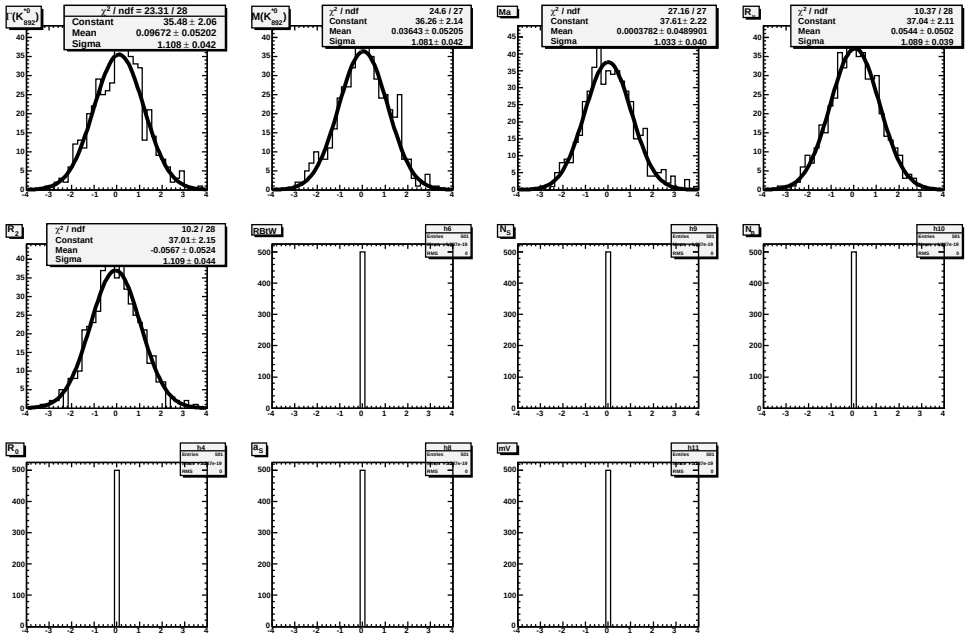

Figure 13.33: PULLS for P-wave fit.

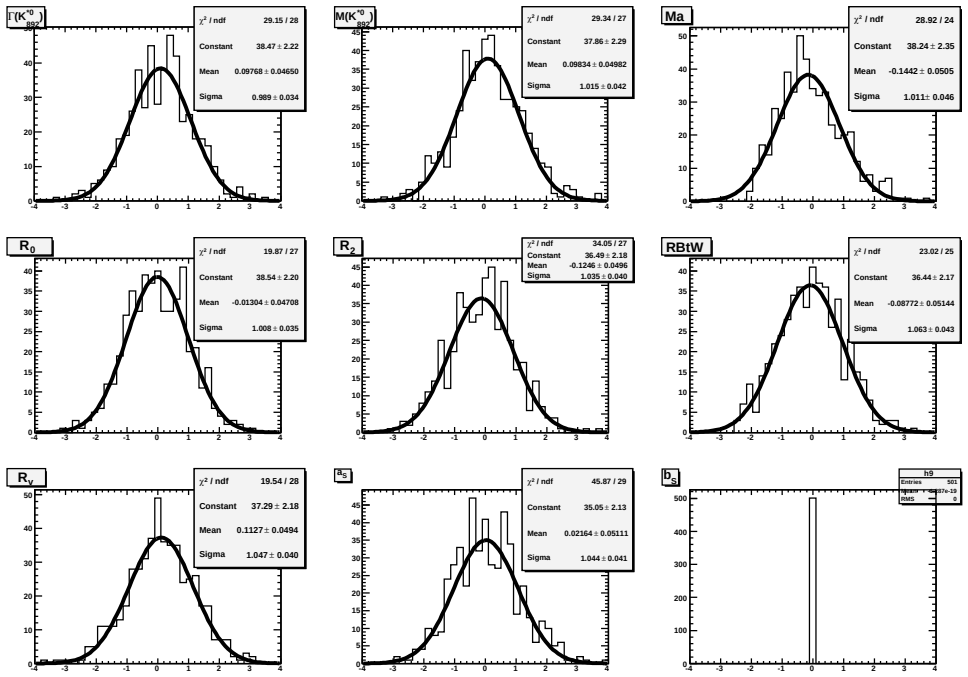

Figure 13.34: PULLS for SP-wave fit for case where control samples has 10 times more statistics than the "data" sample.

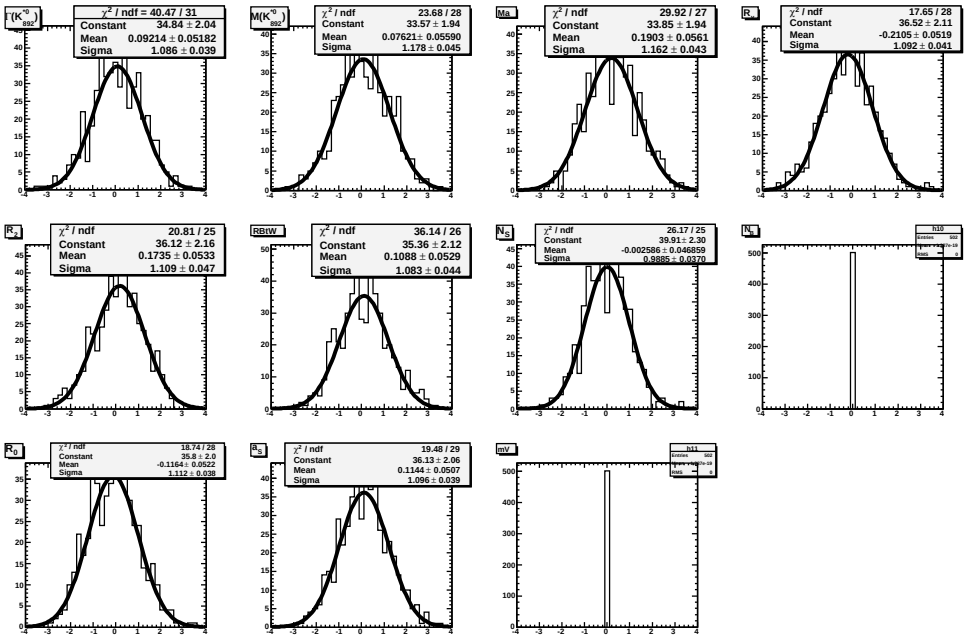

Figure 13.35: PULLS for SP-wave fit.

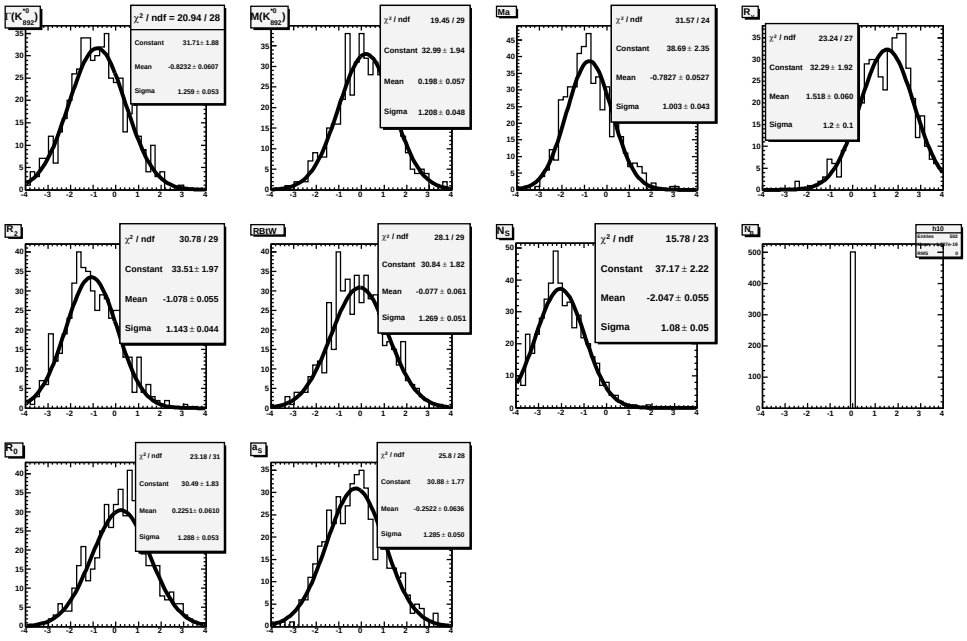

Figure 13.36: PULLS for the case where background is introduced in data and control. Background sample in control has similar statistics as background in data. No action is taken to control background fluctuations.

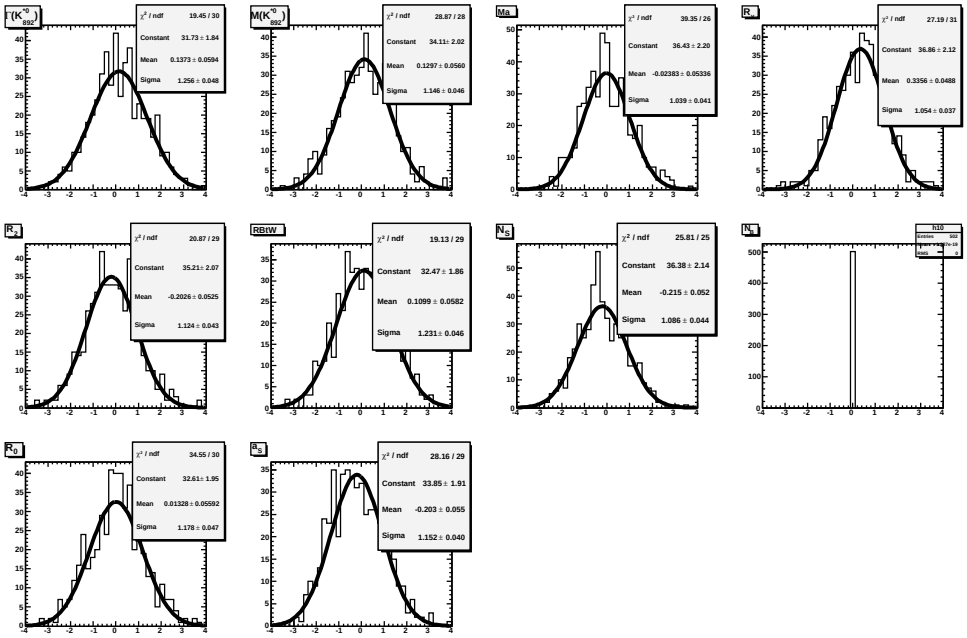

Figure 13.37: PULLS for the case where background is introduced in data and control. Background sample in control has similar statistics as background in data. Smoothing is performed in background control sample.

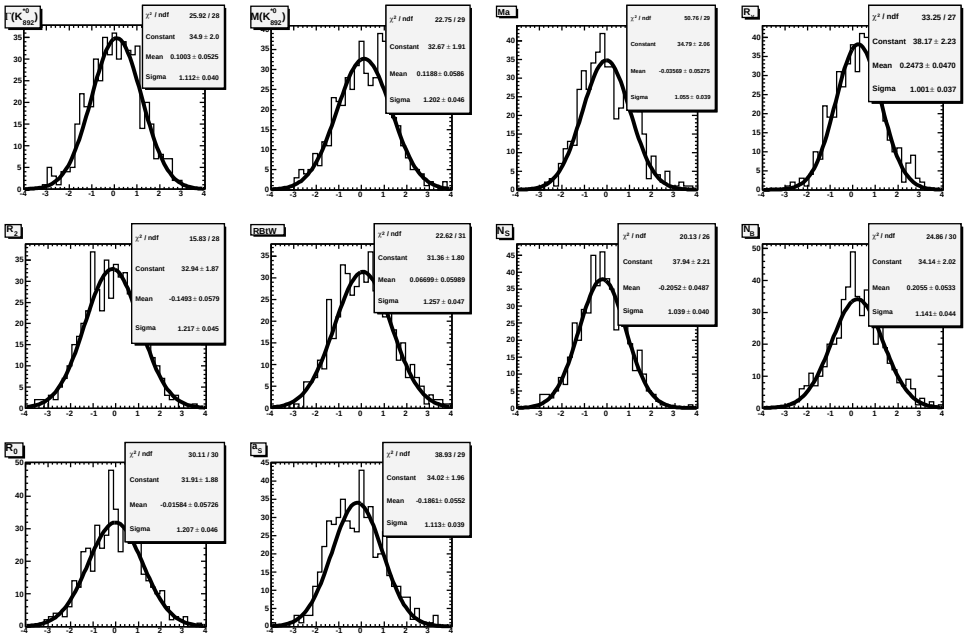

Figure 13.38: Signal sample has S+P signal distribution and background component. Signal control sample has an S+P distribution. Background control sample is smoothed

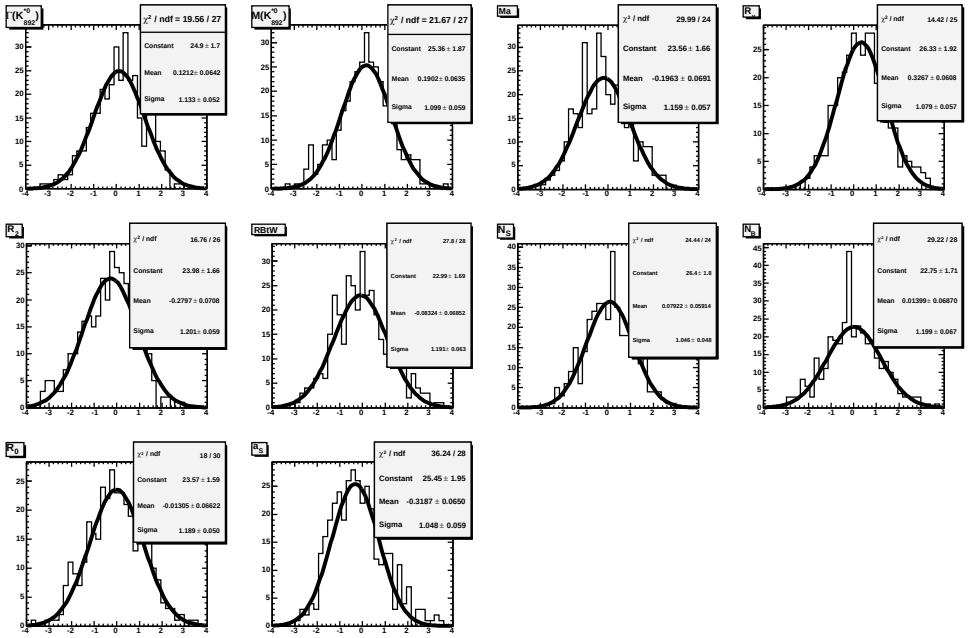

Figure 13.39: Pull distributions for and S+P-wave fitted using a composed control sample obtained from a P-wave and a phase space distributions. Background is smoothed

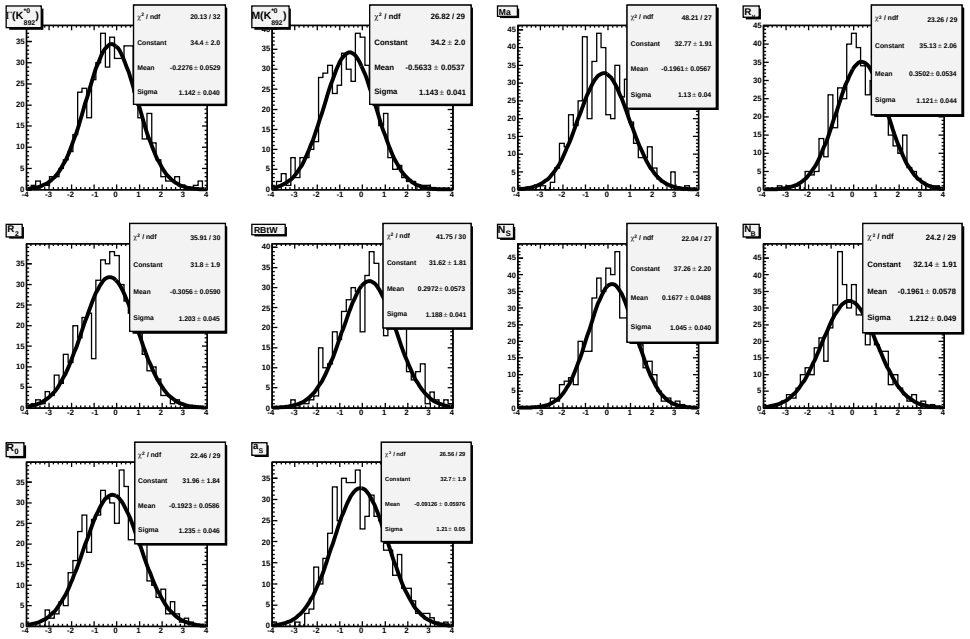

Figure 13.40: PULLS for SP-wave fit with control sample corrected for EvtGen mass feature. Background is smoothed

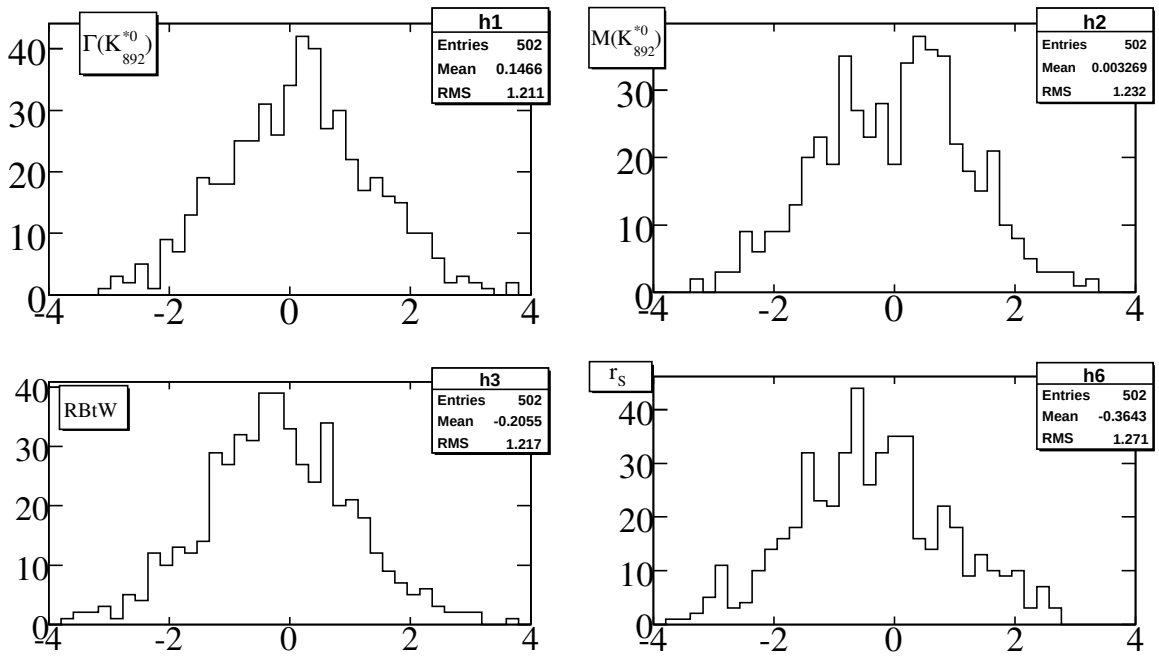

Figure 13.41: *PULLS for P-wave parameters and for relative strength of the S-wave*

G - PULLS for fit of the S-wave phase in 20 bins assuming LASS parameterization for the S-wave

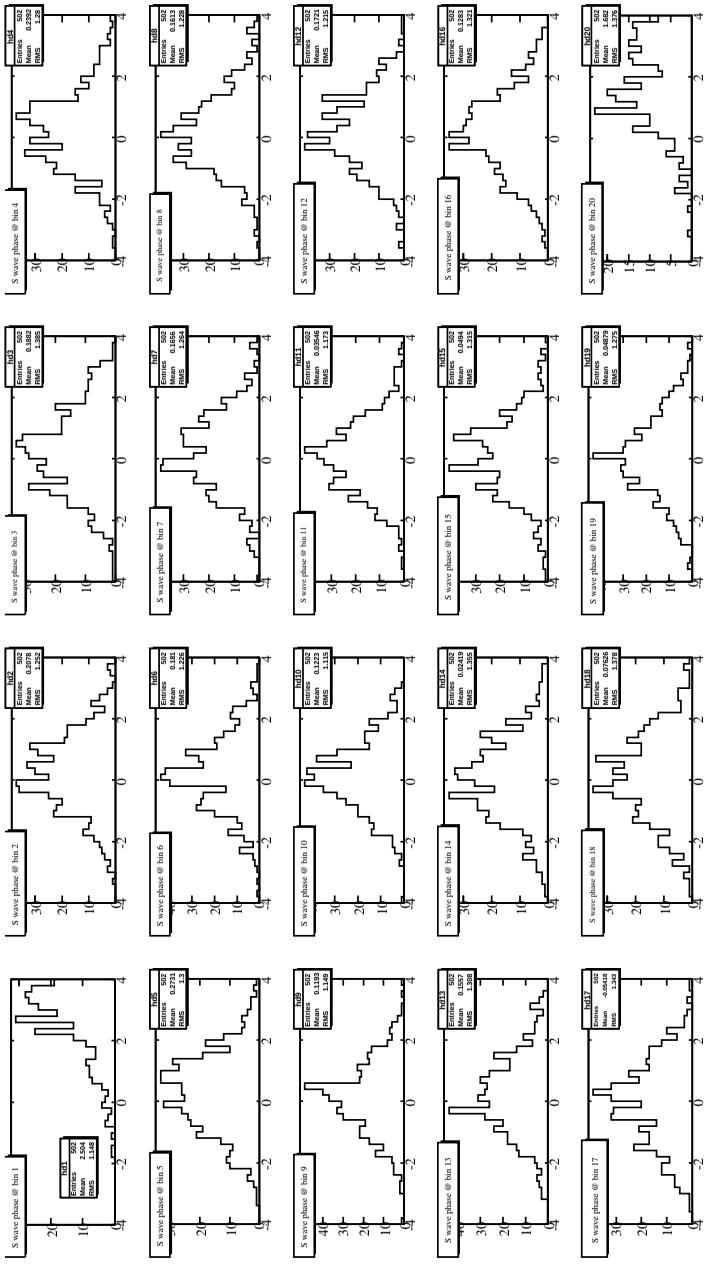

Figure 13.42: *PULLS for the 20 phase points of the S-wave measured*

H - Statistical correlation matrix for Fit of the S-wave phase in 20 bins assuming LASS parameterization for S-wave

1.000																			
0.222	1.000																		
-0.209	-0.266	1.000																	
-0.284	-0.388	0.096	1.000																
-0.268	-0.318	0.112	0.092	1.000															
-0.407	-0.458	0.162	0.241	0.151	1.000														
-0.410	-0.440	0.162	0.235	0.207	0.268	1.000													
-0.294	-0.362	0.129	0.186	0.161	0.238	0.186	1.000												
-0.210	-0.289	0.101	0.145	0.125	0.183	0.182	0.048	1.000											
-0.208	-0.426	0.135	0.194	0.164	0.239	0.233	0.191	0.064	1.000										
-0.068	-0.303	0.084	0.121	0.100	0.144	0.139	0.116	0.099	0.023	1.000									
-0.033	-0.240	0.063	0.092	0.075	0.107	0.103	0.086	0.069	0.117	-0.128	1.000								
-0.025	-0.182	0.048	0.070	0.057	0.081	0.079	0.066	0.053	0.077	0.094	-0.244	1.000							
-0.030	-0.147	0.040	0.059	0.048	0.069	0.067	0.056	0.044	0.065	0.037	0.100	-0.320	1.000						
-0.032	-0.113	0.034	0.048	0.040	0.058	0.056	0.047	0.038	0.055	0.039	0.013	0.107	-0.346	1.000					
-0.011	-0.090	0.025	0.035	0.029	0.042	0.040	0.035	0.027	0.042	0.030	0.026	-0.001	0.094	-0.310	1.000				
0.050	-0.059	0.009	0.013	0.009	0.012	0.012	0.013	0.013	0.026	0.024	0.019	0.016	0.000	0.054	-0.217	1.000			
0.255	-0.046	-0.028	-0.034	-0.037	-0.058	-0.059	-0.034	-0.019	0.000	0.023	0.023	0.018	0.012	0.005	0.025	-0.074	1.000		
0.206	-0.203	0.010	0.026	0.012	0.013	0.010	0.021	0.025	0.065	0.067	0.059	0.045	0.034	0.025	0.023	0.038	0.045	1.000	
0.070	-0.339	0.063	0.100	0.077	0.108	0.102	0.093	0.078	0.132	0.107	0.087	0.066	0.052	0.040	0.034	0.033	0.062	0.058	1.000
0.021	-0.257	0.053	0.082	0.065	0.092	0.088	0.077	0.064	0.104	0.080	0.065	0.050	0.039	0.030	0.025	0.023	0.036	0.075	0.042
0.009	0.132	-0.026	-0.044	-0.036	-0.051	-0.050	-0.043	-0.036	-0.056	-0.042	-0.033	-0.026	-0.020	-0.016	-0.013	-0.010	-0.013	-0.031	-0.046

Table 13.7: *Matrix correlation for FIT to variation of the S-wave phase where the S-wave expression is similar to the one used in elastic scattering.*

I - Study of the vector pole mass

We have also fitted the pole mass m_V assuming the single pole parameterization of the corresponding form factor and using BaBar Runs 1-5.
The mass of this pole is expected to be below the mass of the $D_s^{*+}(J^P = 1^-)$ which is equal to $2.1 GeV/c^2$ because of contributions from higher mass states.
It has never been measured before in this channel. In the $(D_s^+ \to K^-K^+e^+\nu_e)$ analysis [42] a scan of the NLL disitribution was compatible with these expectations. but the uncertainty on m_V was too large to give a measurement. In the other channels $(D^0 \to K^-e^+\nu_e)$ [41] the value $m_V = 1.884 \pm 0.012 \pm 0.015\ GeV/c^2$ is obtained.
A priori, the value of m_V in the $D \to K^*e^+\nu_e$ can be different from the one measured in $D \to Ke\nu_e$ because the hadronic final state is different.

Letting free the value of m_V in the fit does not change really the fitted values for the parameters other than r_V (which is correlated with m_V). We found $m_V = 1.53^{+0.064}_{-0.058} GeV/c^2$, and in this case $r_V = 1.31 \pm 0.031$. This represents over 4σ difference from the expected m_V. Table 13.8 shows the values for the other parameters fitted if we fit or not m_V.

Parameter	m_V fitted	m_V not fitted
$\Gamma(K^{*0}(892))\ MeV/c^2$	45.85 ± 0.22	45.84 ± 0.23
$M(K^{*0}(892))\ MeV/c^2$	894.43 ± 0.08	894.41 ± 0.08
$r_{BW}(GeV/c)^{-1}$	3.63 ± 0.13	3.71 ± 0.14
$m_A\ (GeV/c^2)$	$2.64^{+0.11}_{-0.10}$	$2.72^{+0.11}_{-0.10}$
r_2	0.808 ± 0.020	0.828 ± 0.020
r_S	0.2447 ± 0.0046	0.2432 ± 0.0044
a_S	2.77 ± 0.09	2.77 ± 0.09

Table 13.8: *Results obtained on BaBar data for Runs1-5 when fitting or not the parameter* m_V

We have made several tests of the fit program to check its stability, these include:

- 400 fits to toy distributions, they show no problem with the fit mechanics and indicate that $m_V = 1.79 \pm 0.2\ GeV/c^2$ whereas the generated value is $1.8\ GeV/c^2$. These fits were done using toy distributions with 70k signal events and 32k bkg events in the data sample. Distributions of fitted values for the form factor parameters are presented in Figure 13.43.

- a fit to the full Monte Carlo signal distribution gives expected results ($m_V = 2.10 \pm 0.17\ GeV/c^2$).

From the distribution given in Figure 13.43 one can note a different behaviour for m_V as compared with the other quantities (m_a, r_V, r_2). Whereas as the latter are relatively Gaussian with a central value well separated from zero this is not the case for m_V.
In the fit to m_V and m_A we use:

$$m_V = 1.266 + \lambda_V^2,\ m_A = 1.266 + \lambda_A^2; \tag{13.3}$$

(13.4)

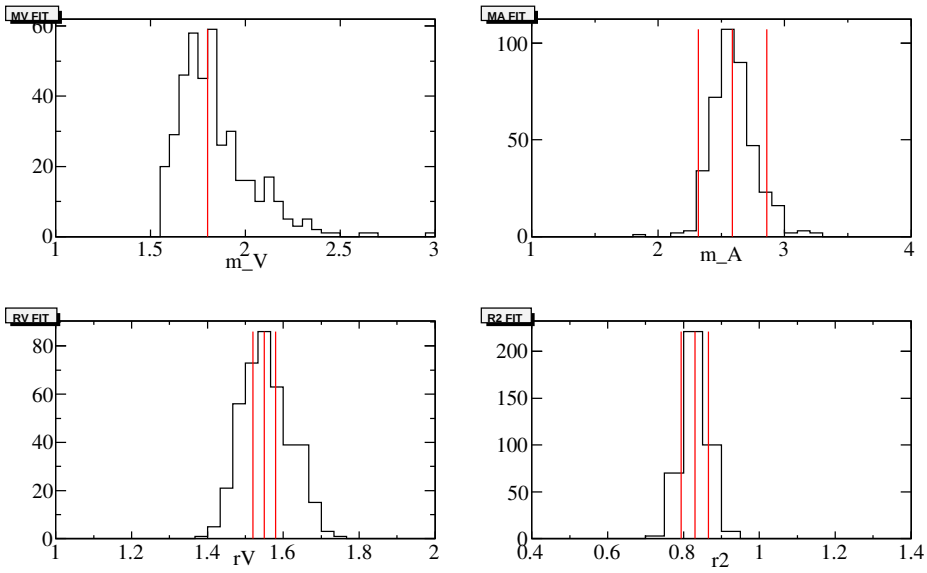

Figure 13.43: *Distribution of the fitted form factor parameters using Toy distributions where the data sample has 70k signal events and 32k bkg events. For the m_V plot the vertical line represents the exact value of this pole. For the other plots the vertical lines represent the exact value for the parameter as well as an estimation of the expected 1σ deviation in a fit where m_V would be a fixed parameter.*

This is to avoid unphysical behaviour of the decay rate expressions from the parameterization of the form factors:

$$\frac{1}{1 - q^2/m^2} \tag{13.5}$$

must be positive therefore $m > q_{max} = (m_D - m_K - m_\pi) = 1.24\ GeV/c^2$.
The Pull distributions for λ_V and λ_A are displayed in Figure 13.44 upper plots. In the lower plots of the same Figure we show the distribution of estimated uncertainties on λ_V and λ_A from the fit. There is a large dispersion.

In addition, because of the pole dependance of the form factor, a low fitted value for m_V is correlated with a low value for the estimated uncertainty as shown in Figure 13.45.

We made tests with the data sample as well, looking for possible sources of biases in selections cuts, in background estimation and in corrections tuning to Monte Carlo signal or background. These tests are presented below and none of them changed significantly the fitted value of m_V.

Generic variations tests:

- Reject events with lepton candidates in opposite hemisphere

- Correct for PHOTOS effect

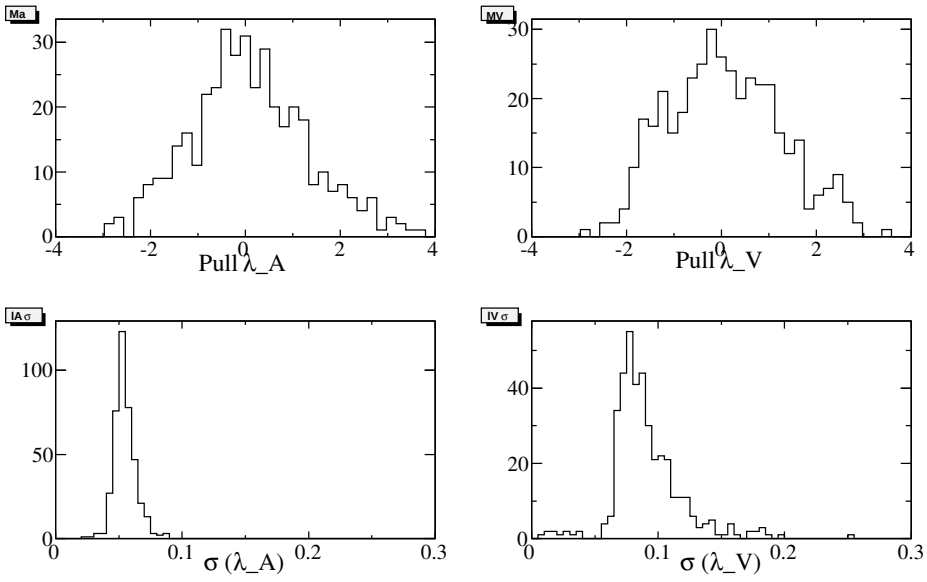

Figure 13.44: *Upper plots: Pull distribution for λ_A et λ_V. Lower plot: Distribution of the uncertainties for each of the above parameters.*

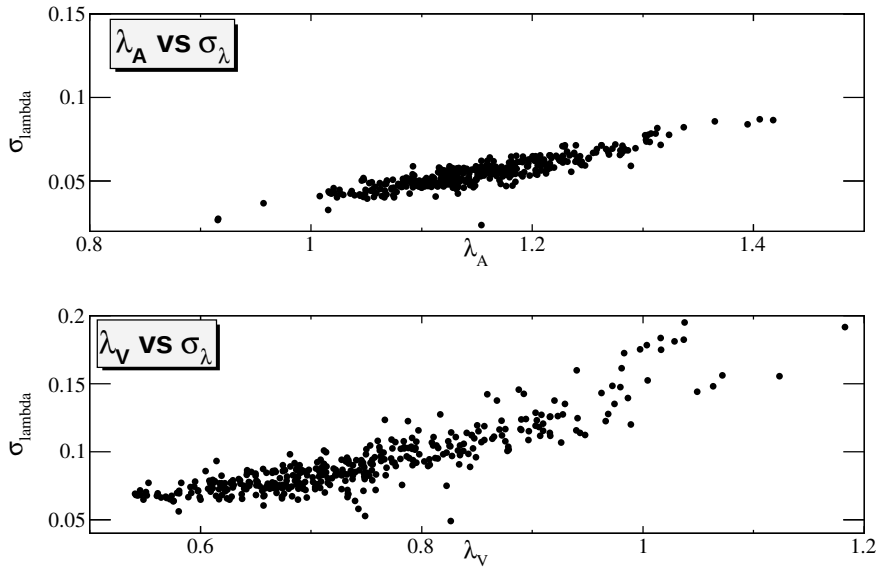

Figure 13.45: *Distribution of the correlation between fitted value of λ and associated uncertainty, for m_A (upper plot) and m_V (lower plot).*

- Cut harder in electron spectrum ($E_e > 0.6GeV/c^2$)

- Increase binning in the variable $cos\theta_e$

- Vary the signal efficiency with respect to the lepton momentum. The variation is of 10% between 0.5 and 4 GeV/c^2

Tests over Monte Carlo Signal:

- No tuning implementation
- Fit only the K^{*0} region

Tests over Monte Carlo background:

- No smoothing
- No correction of charm bkg q^2 shape
- No renormalization of $B\bar{B}$ background
- Change the amount of $B\bar{B}$ events at low $cos\theta_e$

We have also looked for incompatibilities in distributions of the lepton's direction polar angle in the laboratory, but the agreement data/MC is good.
We decide not to fit m_V and fix its value to 2.1 GeV/c^2 and associate a systematic uncertainty by varying the mass by $\pm 0.1 GeV/c^2$.

J - Agreement data-MC below the Fisher cuts

Keeping the cut on $F_{bb} > 0.$ (as used in the analysis), we look for events with F_{cc} below 0.5 and compare the agreement data/MC. This is performed for WS and RS events.

WS events for $F_{cc} < 0.5$, comparison between data and MC for $B\bar{B}$ events

We first analyze OnPeak-OffPeak data and compare it to $B\bar{B}$ MC. The total number of events kept in MC and Data are respectively 18834 ± 27 and 20962 ± 394, using OnPeak data from Runs 1-5 and all available OffPeak($34\ fb^{-1}$). The ratio data/MC is 1.1 ± 0.01.
We present in Figures 13.46 and 13.47 the distributions of F_{bb} and F_{cc} for data and MC and their ratio. There is good agreeement for the F_{bb} variable at the 5% level, while for F_{cc} the MC has $10 - 20\%$ deviations compared to data. We do not correct the F_{cc} distribution for $B\bar{B}$ events as in the final sample used in the analysis the remaining fraction of $B\bar{B}$ events is small.

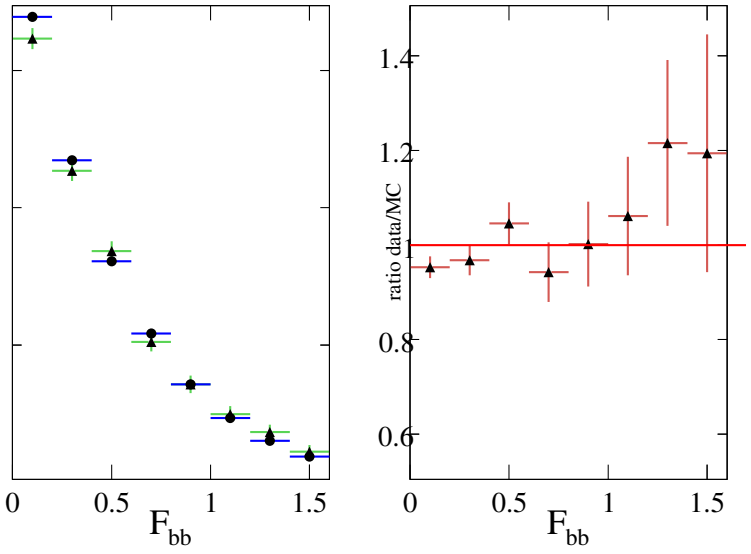

Figure 13.46: *WS F_{bb}. Left Plot: ($\triangle$) OnPeak-OffPeak, ($\bullet$) $B\bar{B}$. Right Plot: ratio (OnPeak-OffPeak) over ($B\bar{B}$).*

We present in Figure 13.48 the ratio data/MC for the 5 decay variables. There is in general a good agreeement.

WS events for $F_{cc} < 0.5$, comparison between data and MC for all events We compare the MC and data samples of Run4, where the $B\bar{B}$ MC has been renormalized according to OnPeak-OffPeak and where the charm bkg component has been tuned. The tuning corrections are those applied to MC used elsewhere in the analysis. Figures 13.49 and 13.50 show the agreement data-MC for all events below the F_{cc} cut. We observe a good agreement for most variables with the exception of the trend observed in the q^2 variable (this same behaviour was observed for WS events with $F_{cc} > 0.5$ and considered in the evaluation of systematic uncertainties). There is as well a 5% effect for the F_{bb} variable. we present in Table 13.9 the number of events for each MC component and for data after all corrections to MC are applied.

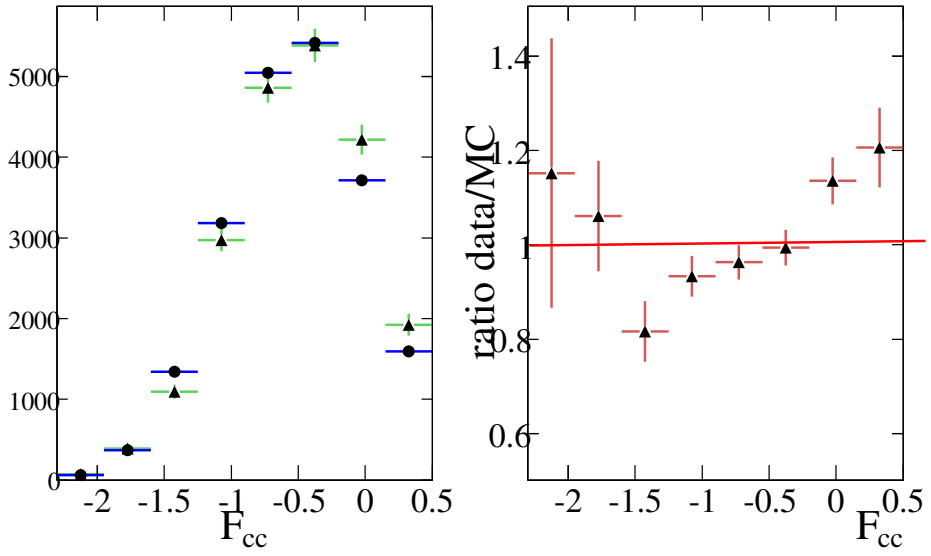

Figure 13.47: *WS F_{cc} . Left Plot: (△) OnPeak-OffPeak, (•) $B\bar{B}$. Right Plot: ratio (OnPeak-OffPeak) over ($B\bar{B}$).*

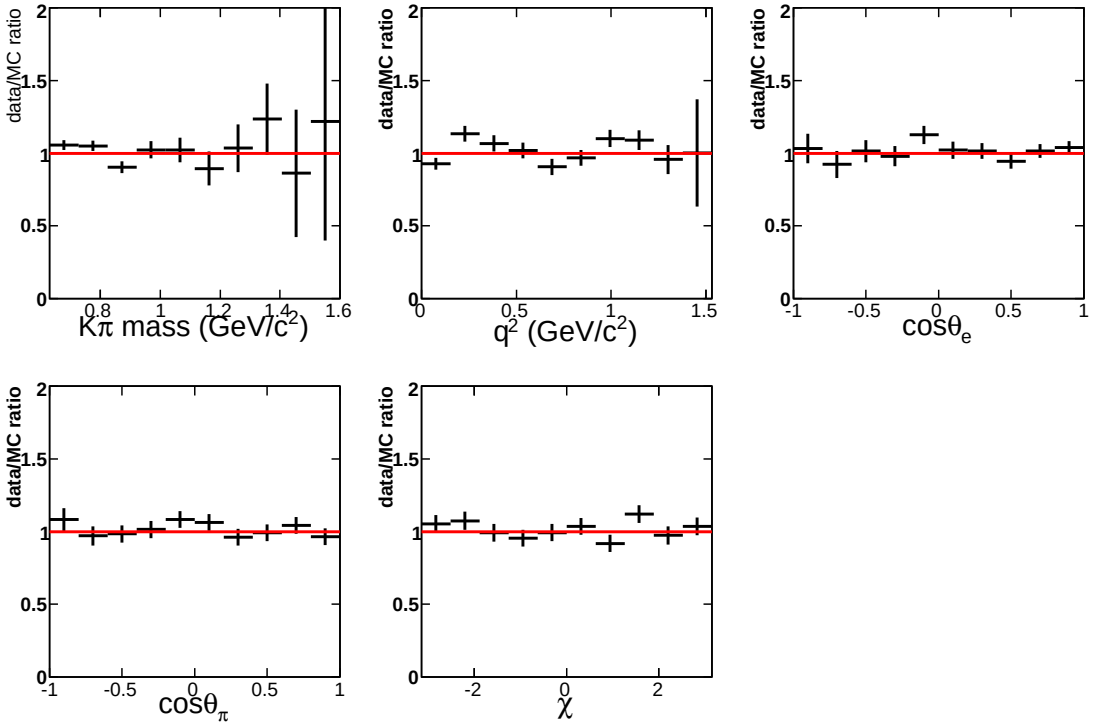

Figure 13.48: *ratio data/MC for $B\bar{B}$ WS events below the F_{cc} cut for the 5 kinematic variables (Runs1-5).*

RS events for $F_{cc} < 0.5$, comparison between data and MC for $B\bar{B}$ events We first analyze OnPeak-OffPeak data and compare it to $B\bar{B}$ MC. The total number of events kept in MC and Data are respectively 18834 ± 27 and 20962 ± 394, using OnPeak data from Runs 1-5 and all available OffPeak($34\ fb^{-1}$). The ratio data/MC is 1.08 ± 0.02. We present

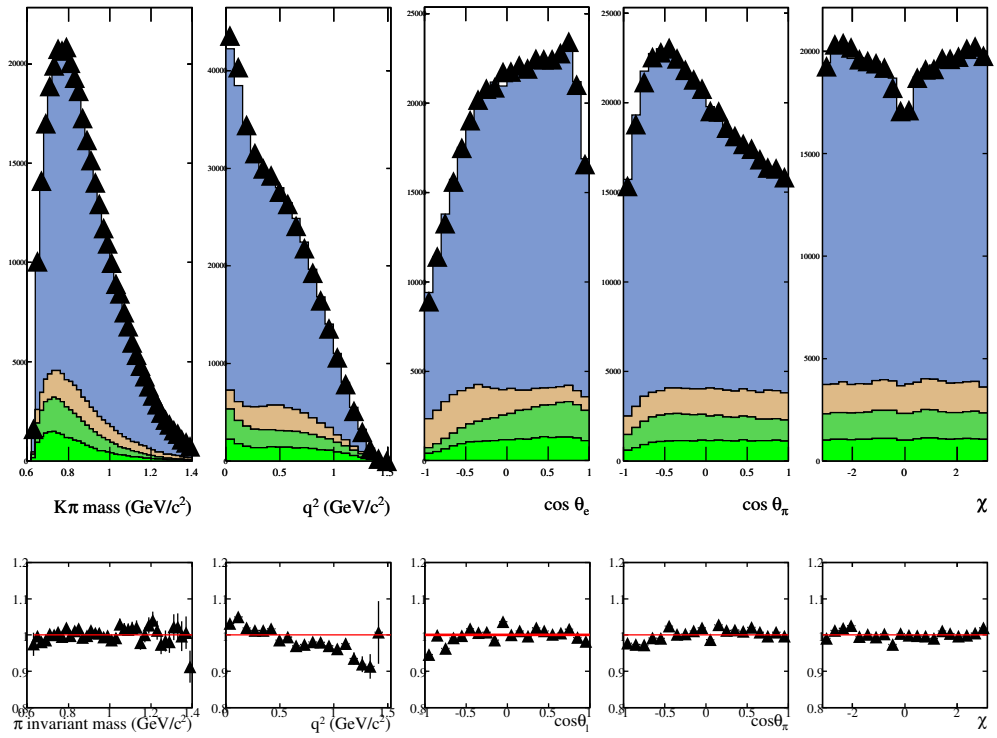

Figure 13.49: *Run 4 distributions of the 5 dynamical variables for WS events in data and MC below the F_{cc} cut after tuning and form factor corrections. ($\triangle$) data , MC in stacking order : $B^0\bar{B}^0, B^+B^-, uds, c\bar{c}$. Lower row: ratio data/MC for upper row plots.*

in Figures 13.51 and 13.52 the distributions of F_{bb} and F_{cc} for data and MC and their ratio. There is good agreeement for the F_{bb} variable at the 5% level except for the region of high F_{bb} (zone with less stats) where there is an important disagreement, while for F_{cc} we observe the same disagreement observed in WS events. We do not correct the F_{cc} distribution for $B\bar{B}$ events. We present in Figure 13.53 the data/MC ratio for the distributions of the 5 kinematic variables. There is a good agreement.

RS events for $F_{cc} < 0.5$, comparison between data and MC for all events We compare the MC and data samples of Run4, where the $B\bar{B}$ MC has been renormalized according to OnPeak-OffPeak and where the charm bkg component has been tuned. The tuning corrections are those applied to MC used elsewhere in the analysis. We present in Figures 13.54 and 13.55 the comparison between data and MC. The agreement is good for the 5 kinematic variables. The signal MC has been tuned the same way as explained in the BAD and reweighted according to the results found in the fit to BaBar Runs 1-5 for a S+P wave fit. The background has beend reweighted by 0.98 and the rate of signal defined to be $N_{data} - \sum_{i=1}^{flavours} N_i^{bkgMC}$. The 0.98 weight is found so to have a good agreement data/MC in the F_{cc} discriminant variable.
Besides the agreement for the 5 kinematic variables, we observe however the same trend as in WS events for data/MC ratio in the F_{bb} variable.
Overall we consider that the tuned signal and bkg MC are in good agreement with data distributions below the F_{cc} cut.

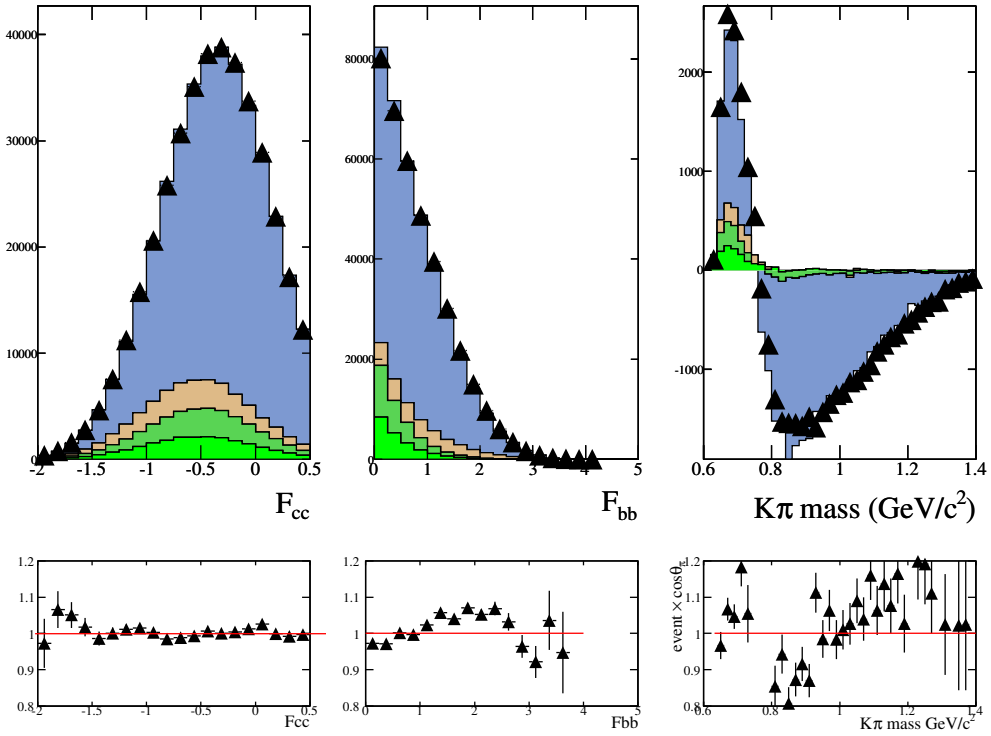

Figure 13.50: *Distribution for WS data and MC below the F_{cc} cut for the Fisher discriminants and asymmetry variation with mass after tuning,form factor corrections on charm decays and after its renormalization. (△) data , MC in stacking order : $B^0\bar{B}^0, B^+B^-, uds, c\bar{c}$. Lower row: ratio data/MC for upper row plots.*

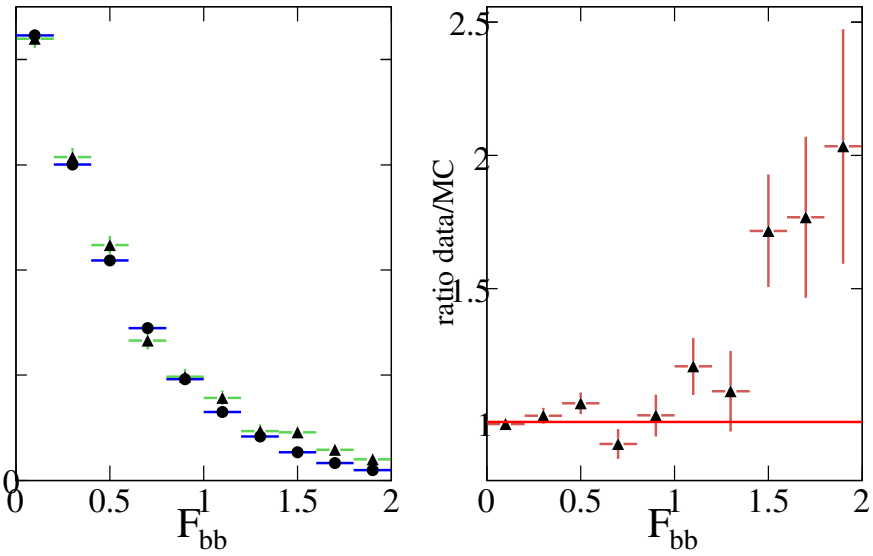

Figure 13.51: *RS F_{bb}. Left Plot: (△) OnPeak-OffPeak, (•) $B\bar{B}$. Right Plot: ratio (OnPeak-OffPeak) over ($B\bar{B}$).*

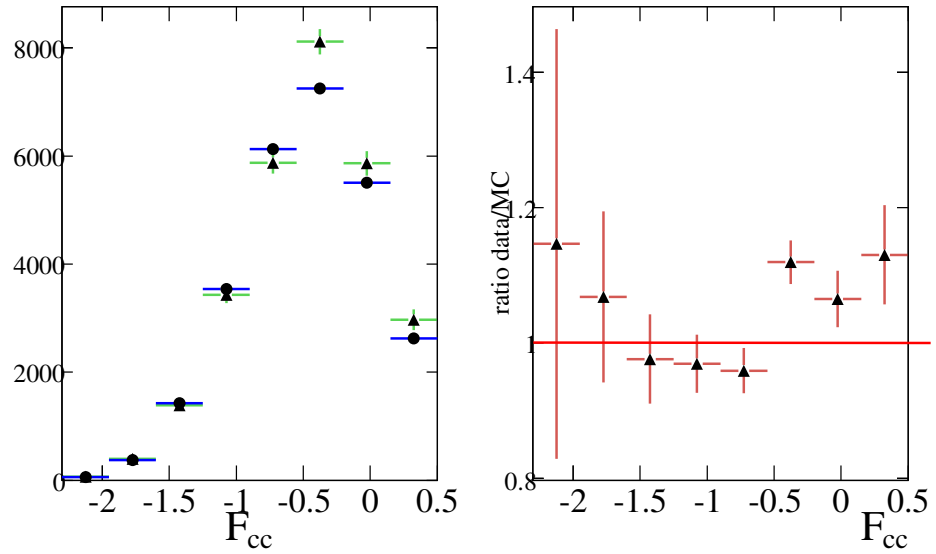

Figure 13.52: *it RS F_{cc} . Left Plot: (△) OnPeak-OffPeak, (●) $B\bar{B}$. Right Plot: ratio (OnPeak-OffPeak) over ($B\bar{B}$).*

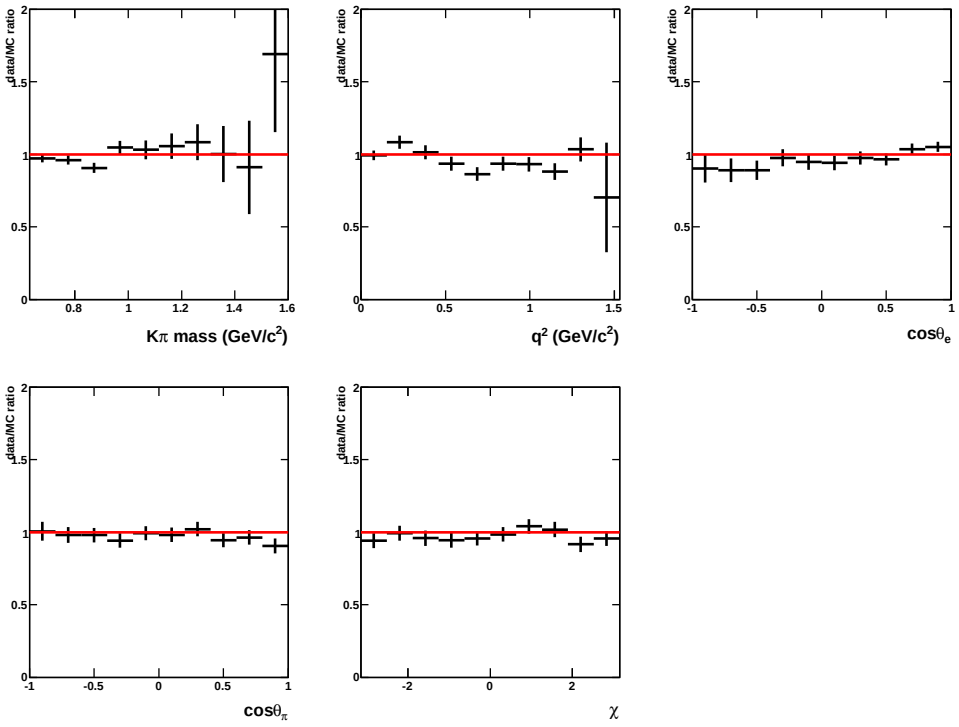

Figure 13.53: *ratio data/MC for $B\bar{B}$ RS events below the F_{cc} cut for the 5 kinematic variables.*

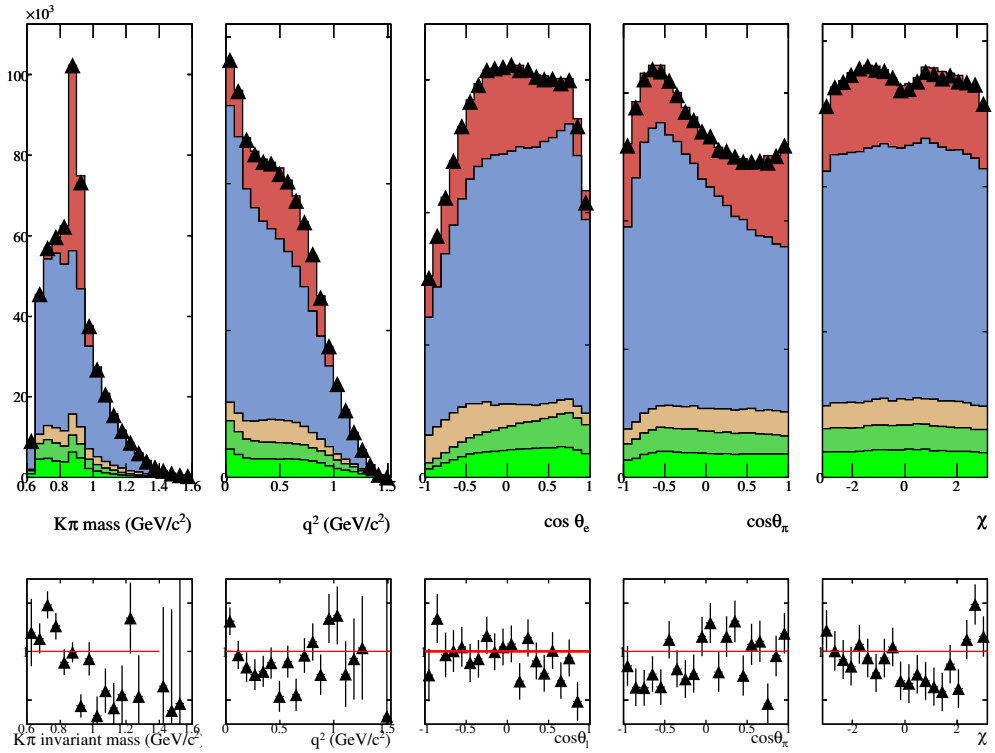

Figure 13.54: *Upper plots:Comparison data/MC for RS events below the F_{cc} cut for the 5 kinematic variables. Color code: red(signal),blue(charm bkg), light brown(uds bkg), dark green(B^+B^- bkg), light green($B^0\bar{B}^0$). Lower plots: Corresponding data/MC ratios, vertical scale goes from 0.97 to 1.03.*

	Data	Signal MC	$c\bar{c}$ bkg MC	B^+B^- MC	B^0B^0 MC	uds MC	total MC
WS	386441 ± 622	0.	310207 ± 532	26452 ± 96	21246 ± 87	28652 ± 165	386568 ± 571
RS	545493 ± 739	98609 ± 156	344756 ± 566	33237 ± 108	36392 ± 115	34710 ± 184	547704 ± 635

Table 13.9: *Distribution of events for WS and RS for data and all MC components for $F_{cc} < 0.5$. MC samples are reweighted as explained in the text.*

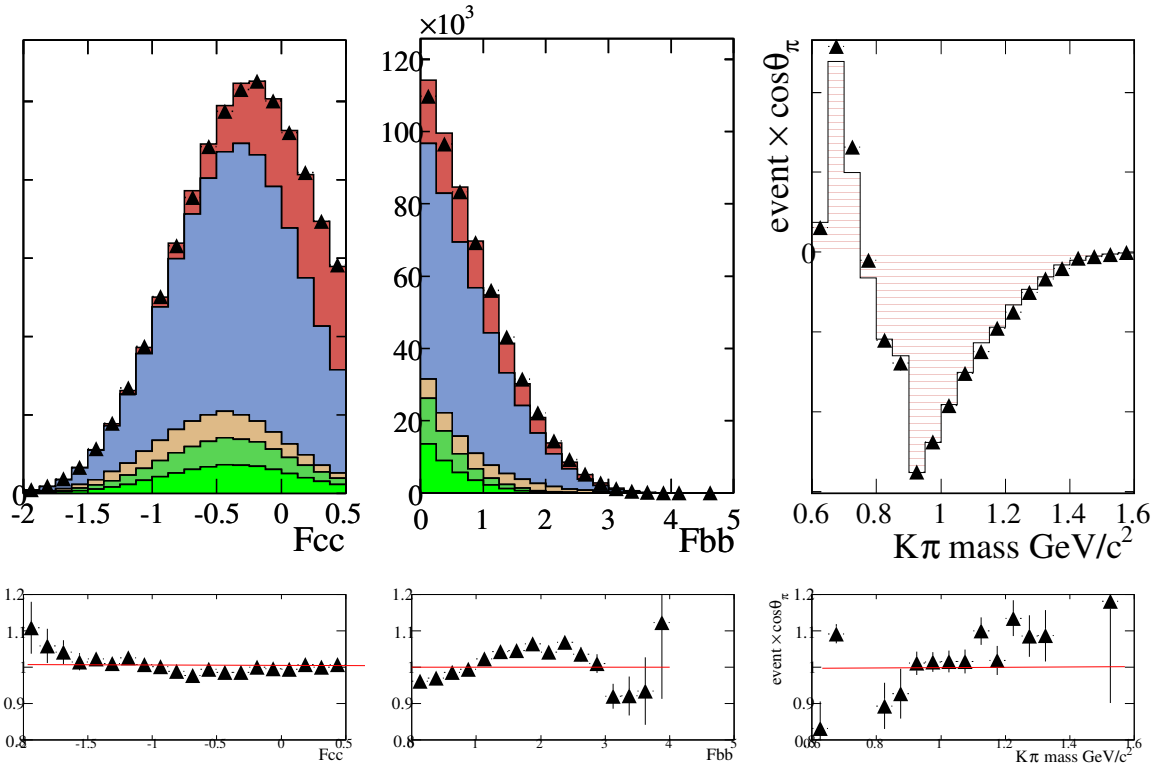

Figure 13.55: *Upper plots: Comparison data/MC for RS events below the F_{cc} cut for the Fisher discriminant variables and for the variation of $cos\theta_\pi$ with the $k\pi$ mass. Color code: red(signal),blue(charm bkg), light brown(uds bkg), dark green(B^+B^- bkg), light green($B^0\bar{B}^0$). Lower plots: Corresponding data/MC ratios.*

Bibliography

[1] C.B. Lang, Fortsch. Phy. 26(1978) 509;

[2] K.M. Watson, Phys. Rev. **95** 228 (1954);

[3] M. Jamin, J.A. Oller and A. Pich, Nucl. Phys. **B622** 279 (2002);

[4] B. Moussalam, [hep-ph/0407246];

[5] B. Borasoy,[hep-ph/0703297];

[6] A. Pich, [hep-ph/9502366];

[7] S. Adler and R.F. Dashen, Current Algebras (1968);

[8] M.A. Shifman, A.I. Vainstein and V.I.Zakharov, Nucl. Phys **B147** (1979) 385;

[9] V. Bernard, N. Kaiser and U.G. Meissner, Nucl. Phys. **B357** 129 (1991);
V. Bernard, N. Kaiser and U.G. Meissner, Phys. Rev. **D43** 2757 (1991);

[10] J. Bijnens, P. Dhonte and P. Talavera, JHEP 0405:036, 2004;

[11] B. Ananthanarayan, P. Büttiker and B. Moussallam, Eur. Phys. J. **C22** 133, 2001;

[12] S. Fajfer, J. Kamenic, Phys. Rev. **D 72** (2005) 034029; [hep-ph/0506051] and [hep-ph/0601028]

[13] W.-M. Yao *et al.*, Review of Particle Physics, Journal of Physics **G33** 1 (2006);

[14] C. Amsler *et al.*, Review of Particle Physics, Physics Letters **B667** 1 (2008);

[15] D. Aston *et al.*, Nucl. Phys. **B296** 493 (1988);

[16] R. Gupta, Introduction to Lattice QCD, [hep-let/9807028];

[17] P. Estabrooks *et al.*, Nucl. Phys. **B133** 490 (1978);

[18] P. Büttiker, S. Descotes-Genon, B. Moussallam, Eur. Phys. J. **C33** 409 (2004), [arxiv:hep-ph/0310283];

[19] W. Dunwoodie , private communication, $http://www.slac.stanford.edu/\ wmd/kpi_swave/kpi_swave_fit.note$;

[20] D. Epifanov *et al.*, Belle Collaboration, Phys. Lett. **B654** 65 (2007);

[21] M. Jamin, A. Pich and J. Portoleś, Phys. Lett. **B664** 78 (2008);

[22] J.M. Link *et al.*, FOCUS Collaboration, Phys. Lett. **B653** 1 (2007);

[23] E.M. Aitala *et al.*, Fermilab E791 Collaboration, Phys. Rev. **D73**, 032004 (2006);

[24] P. L. Frabetti *et al.*, E687 Collaboration, Phys. Lett. **B307** 262 (1993);

[25] J. M. Link *et al.*, FOCUS Collaboration, Phys. Lett. **B535** 43 (2002);

[26] J. M. Link *et al.*, FOCUS Collaboration, Phys. Lett. **B621** 72 (2005);

[27] : S. Descotes-Genon, private communication;

[28] L. Rosselet *et al.*, Phys. Rev. **D15** 574 (1977);

[29] S. Pislak *et al.*, BNL-E865 Collaboration, Phys. Rev. Lett. **87** 221801 (2001);

[30] J.R. Batley *et al.*, NA48/2 Collaboration, Eur. Phys. J. **C54** 411 (2008);

[31] A. Schenk, Nucl. Phys. **B363**, 97 (1991);

[32] B. Ananthanarayan *et al.*, Phys Rep. **353/4**,207 (2001) Appendix D and S.Descotes, N.H. Fuchs, L. Girlanda, J. Stern, Eur. Phys. J. **C24**, 469 (2002);

[33] M. R. Shepherd *et al.*, CLEO Collaboration, Phys. Rev. **D74** 052001 (2006);

[34] J.Y. *et al.*, CLEO Collaboration, arXiv:0810.3878;

[35] E. M. Aitala *et al.*, E791 Collaboration, Phys. Rev. Lett. **89** 121801 (2002);

[36] N. Cabibbo and A. Maksymowicz, Phys Rev. **137**, B438 (1965);

[37] A. Pais and S. B. Treiman, Phys. Rev. **168** 1858 (1968);

[38] C. L. Y. Lee, M. Lu and M. B. Wise, Phys. Rev. **D46** 5040 (1992);

[39] J. D. Richman and P. R. Burchat, Rev. Mod. Phys. **67**, 893 (1995).

[40] D. Epifanov *et al.*, Belle Collaboration, Phys. Lett. **B654** 65 (2007);

[41] B. Aubert *et al.*, BaBar Collaboration, Phys. Rev. **D76** 052005 (2007);

[42] B. Aubert *et al.*, BaBar Collaboration, Phys. Rev. **D78** 051101 (2008);

[43] D. Aston *et al.*, LASS Collaboration, Nucl. Phys. **B296** 253 (1988);

[44] J.G. Korner and G.A. Schuler, Z. Phys. C46 (1990) 93;

[45] B. Aubert *et al.*, *BABAR* Collaboration, Nucl. Instr. and Methods A **479**, 1 (2002).

[46] *PEP II - An Asymmetric B Factory, Conceptual Design Report*, SLAC-418, LBL-5379 (1993).

[47] P.F. Harrison, *et al.*, *BABAR* Collaboration, *The BABAR physics book: Physics at an asymmetric B factory.*, SLAC-R-0504 (1998).

[48] J. Seeman *et al.*, *Results and Plans of the PEP-II B Factory*, SLAC-PUB-10547, Contribution to EPAC 2004 (2004).

[49] B. Aubert *et al.*, *BABAR* Collaboration, *The First Year of the BABAR experiment at PEP-II*, BABAR-CONF-00/17, Contribution to XXX^{th} International Conference of High Energy Physics, Osaka (Japan) (2000).

[50] C. Bozzi *et al.*, Nucl. Instr. and Method A **453**, 78 (2000).

[51] V. Re *et al.*, Nucl. Instr. and Method A **511**, 1 (2003).

[52] V. Re *et al.*, Nucl. Instr. and Method A **501**, 14 (2003).

[53] G. Sciolla *et al.*, Nucl. Instr. and Method A **419**, 310 (1998).

[54] M. H. Kelsey *et al.*, Nucl. Instr. and Method A **536**, 206 (2004).

[55] I. Adam *et al.*, IEEE Trans. Nucl. Sci. 45, 657 (1998).

[56] I. Adam *et al.*, SLAC-PUB-8783 (2001).

[57] B. Lewandowski *et al.*, Nucl. Instr. and Method A **494**, 302 (2002).

[58] F. Anulli *et al.*, Nucl. Instr. and Method A **409**, 542 (1998).

[59] P. Billior, Nucl. Instr. and Method A **225**, 225 (1984).

[60] http://www.slac.stanford.edu/BFROOT/www/Physics/Tools/Pid/Selectors/r18a/selectors.html.

[61] T. Brandt, "Likelihood based electron identification", *BABAR* analysis document #391.

[62] http://www.slac.stanford.edu/ lange/EvtGen/;

[63] http://tmva.sourceforge.net/;

[64] K. Cranmer, Kernel Estimation in HEP, hep-ex/0011057 (2000);

[65] A. Bonvicini *et al.*, CLEO Collaboration, Phys. Rev. **D78** 052001 (2008);

[66] S. Dobbs *et al.*, CLEO Collaboration [arXiv:hep-ex:0712.1020];

[67] A. Abada *et al.*, SPQcdR Collaboration [arXiv:hep-lat/0209116v1] (2002)

[68] J. Gill for the UKQCD Collaboration, [arXiv:hep-lat/0109035v3] (2001)

Abstract/Resumé

Abstract

We use $347.5 fb^{-1}$ of data recorded by the BaBar detector at the PEPII electron-positron collider to study the $D^+ \rightarrow K^-\pi^+e^+\nu_e$ decay channel. The hadronic final state is described by the sum of S and P-waves.

Using the LASS parameterization for the S-wave phase, we measure the scattering length parameter a_S and the effective range term b_S. In this fit the other parameters entering this parameterization as the mass and width of the $K_0^*(1430)$) are fixed to the values provided by LASS.

We find $a_S = 1.78 \pm 0.15 \pm 0.19\ (GeV/c)^{-1}$ and $b_S = -1.93 \pm 0.69 \pm 0.69\ (GeV/c)^{-1}$. We have in this fit parameterized the S-wave amplitude until the $K_0^*(1430)$ using a linear expression and have fitted both terms of the expansion (r_S and $r_S^{(1)}$). We find $r_S = 0.477 \pm 0.025 \pm 0.022$ and $r_S^{(1)} = 0.15 \pm 0.06 \pm 0.06$. In the same fit, we obtain also the $K^{*0}(892)$ parameters (mass,width and barrier factor) as well as the form factor ratios at $q^2 = 0$ ($r_V = \frac{V(0)}{A_1(0)}$, $r_2 = \frac{A_2(0)}{A_1(0)}$) and the value of the axial-vector pole mass parameterizing A_1 and A_2.

We find $m(K^{*0}(892)) = 895.0 \pm 0.1 \pm 0.5\ MeV/c^2$, $\Gamma(K^{*0}(892)) = 45.79 \pm 0.23 \pm 0.21\ MeV/c^2$, $r_{BW} = 4.20 \pm 0.23 \pm 0.39\ GeV/c$, $r_V = 1.480 \pm 0.016 \pm 0.026$, $r_2 = 0.824 \pm 0.020 \pm 0.020$ and $m_A = 2.68^{+0.11}_{-0.10} \pm 0.16\ GeV/c^2$.

We determine B($D^+ \rightarrow K^-\pi^+e^+\nu_e$) = $(4.03 \pm 0.03 \pm 0.04 \pm 0.09) \times 10^{-2}$, B($D^+ \rightarrow \bar{K^{*0}}e^+\nu_e$)$\times$ B($\bar{K^{*0}} \rightarrow K^-\pi^+$)=$(3.81 \pm 0.03 \pm 0.04 \pm 0.09) \times 10^{-2}$. The S-wave contribution to the $K^-\pi^+e^+\nu_e$ decay channel is equal to $(5.68 \pm 0.21 \pm 0.24\ \%)$.
The value of the hadronic form factor A_1 at $q^2 = 0$ is $A_1(0) = 0.6270 \pm 0.0027 \pm 0.0032 \pm 0.0076$.

In a second approach, we measure the S-wave phase variation from threshold up to 1.6 GeV/c^2 for several values of the $K\pi$ mass. We also fit parameters for a signal model where the S-wave amplitude is proportional to the $K\pi$ elastic scattering amplitude. We find compatibility with the afore mentioned results.

We look for other contributions for this decay channel, namely the ($J^P = 1^-$) $K^*(1410)$ and fit both its relative strength to the dominant $K^{*0}(892)$ and relative phase. We find evidence for this resonance at more than 5 sigma, considering only statistical uncertainties.

These measurements, in the same manner as those obtained by the LASS collaboration, are sensitive to the difference between the phase of the S and P waves. Comparing directly, versus the $K\pi$ mass, the measured difference between the phase of the two waves shows that results from the two experiments agree.

On utilise $347.5 fb^{-1}$ de données recueillies par le détecteur BaBar opérant sur le collisionneur électron-positron PEP-II pour étudier le canal de désintégration $D^+ \rightarrow K^-\pi^+e^+\nu_e$. L'état hadronique final est décrit par la somme d'une onde P et d'une onde S.

En utilisant la paramétrisation de LASS pour l'onde S, nous mesurons à la fois le paramètre a_S de la longueur de diffusion de l'onde S et le terme de portée effective b_S. Dans ce fit, les autres paramètres de l'onde S (masse et largeur du $K_0^*(1430)$) sont fixés à des valeurs fournies par LASS.

On obtient les valeurs $a_S = 1.78 \pm 0.15 \pm 0.19\ (GeV/c)^{-1}$ et $b_S = -1.93 \pm 0.69 \pm 0.69\ (GeV/c)^{-1}$. Dans ce fit, nous avons paramétré l'amplitude de l'onde S jusqu'à la masse du $K_0^*(1430)$) en utilisant une expression linéaire et nous avons fitté les deux paramètres de cette expression (r_S et $r_S^{(1)}$).Nous avons obtenu $r_S = 0.477 \pm 0.025 \pm 0.022$ et $r_S^{(1)} = 0.15 \pm 0.06 \pm 0.06$. Dans le même fit, on obtient également les paramètres du $K^{*0}(892)$ (masse, largeur et le facteur de Blatt-Weisskopf) ainsi que les rapports entre les facteurs de forme à $q^2 = 0$ ($r_V = \frac{V(0)}{A_1(0)}$, $r_2 = \frac{A_2(0)}{A_1(0)}$) et la valeur de la masse du pôle axial-vecteur contribuant à A_1 et A_2.

On obtient $m(K^{*0}(892)) = 895.0 \pm 0.1 \pm 0.5\ MeV/c^2$, $\Gamma(K^{*0}(892)) = 45.79 \pm 0.23 \pm 0.21\ MeV/c^2$, $r_{BW} = 4.20 \pm 0.23 \pm 0.39\ GeV/c$, $r_V = 1.480 \pm 0.016 \pm 0.026$, $r_2 = 0.824 \pm 0.020 \pm 0.020$ et $m_A = 2.68^{+0.11}_{-0.10} \pm 0.16\ GeV/c^2$.

On détermine le rapport d'embranchement B($D^+ \rightarrow K^-\pi^+e^+\nu_e$) = $(4.03 \pm 0.03 \pm 0.04 \pm 0.09) \times 10^{-2}$ et B($D^+ \rightarrow \bar{K^{*0}}e^+\nu_e) \times$ B($\bar{K^{*0}} \rightarrow K^-\pi^+$)=$(3.81 \pm 0.03 \pm 0.04 \pm 0.09) \times 10^{-2}$. La contribution de l'onde S pour ce canal est de ($5.68 \pm 0.21 \pm 0.24$ %). Le facteur de forme hadronique A_1 à $q^2 = 0$ vaut $A_1(0) = 0.6270 \pm 0.0027 \pm 0.0032 \pm 0.0076$.

Une seconde approche nous permet de mesurer les variations de la phase de l'onde S depuis le seuil jusqu'à 1.6 GeV/c^2 en supposant que l'amplitude de l'onde S est proportionnelle à celle de la diffusion $K\pi$ élastique. On obtient des résultats compatibles avec ceux mentionnés précédemment.

On recherche d'autres contributions pour ce canal de désintégration, notamment ($J^P = 1^-$) $K^*(1410)$ et on fitte à la fois son intensité et sa phase relative au $K^{*0}(892)$. On obtient des effets de cette résonance à plus de 5 sigma en ne considérant que les incertitudes statistiques.

De même que ceux obtenus par l'expérience LASS, ces mesures sont sensibles à la différence entre les phases des ondes S et P. La comparaison entre les mesures de cette différence obtenues par les deux expériences et en fonction de la masse $K\pi$ montre un bon accord.

Remerciements

Je tiens tout d'abord à remercier le Laboratoire de l'Accélérateur Linéaire de m'avoir accueilli pour la réalisation de cette thèse de doctorat. Je remercie Guy Wormser d'avoir présidé mon jury de thèse.
Je remercie Jochen Dingfelder ainsi que Marcello Rotondo d'avoir accepté le rôle de rapporteurs. Merci également à Sébastien Descotes-Genon d'avoir accepté de faire partie de mon jury de thèse ainsi que sa disponibilité pour les nombreuses discussions autour de mon sujet de thèse.

Patrick, je tiens à te remercier vivement pour tout ce que tu as fais pour moi pendant ma thèse. Merci pour ta rigueur et ton professionnalisme. J'ai beaucoup appris avec toi. Merci de m'avoir montré comment être un physicien et de m'avoir guidé à travers ce grand travail.

Je remercie très chaleureusement le groupe du LAL : Anne-Marie, Marie-Hélène, Achille, Denis, Michel, Nicolas, Bogdan et Gilbert ainsi que Justine et Viola (qui ont malheureusement fini par partir) de m'avoir accueilli avec amitié.

Un grand merci à Achille de m'avoir accueilli au sein du master NPAC, ce qui a fini par me mener à cette thèse. Merci pour son écoute, sa franchise et pour le foot du dimanche.

Merci aux jeunes du LAL (mes copains dans cette galère) : Dimitris, Viola, Justine, Yasmine, Aurélien, Denis, Francesco, pour votre amitié et votre capacité de me faire sortir de mon stress quotidien.

Merci aux copains de voyage de ces années de thèse à Paris : le kernel Yasmine et Viola (shoukran et grazie), merci d'être toujours là, pour les bières à Bourg-la-Reine (zone 3 du RER B), pour les mails débiles et pour tout le reste. Merci aussi à tous les autres copains de ces quatre années à Paris : Marcel, Clément, Andreas et tous ceux du LAL, pour votre amitié, pour les fêtes, pour les bons repas et tout votre soutien.

Merci tout particulièrement à Yasmine d'avoir été une vraie amie pendant trois ans et pour son soutien crucial (PS : il faudra décider qui garde la machine à expresso).

Un grand merci à la famille Duretz pour m'avoir toujours soutenu et pour votre amitié pendant tout ce temps. Um grande obrigado para a minha família, para os meus pais, por me terem permitido todas as liberdades de escolha ao longo da minha vida e por todo o apoio que sempre me deram. Obrigado por tudo. Lamento não ter estado mais presente para vocês durante estes três últimos anos.

Et surtout Séverine, qui arrive par une quelconque magie à me soutenir pendant les mauvaises periodes, et sans qui rien de cela n'aurait eu de sens.